



HAL
open science

Global observations of ocean surface winds and waves using spaceborne synthetic aperture radar measurements

Huimin Li

► **To cite this version:**

Huimin Li. Global observations of ocean surface winds and waves using spaceborne synthetic aperture radar measurements. Atmospheric and Oceanic Physics [physics.ao-ph]. Ecole nationale supérieure Mines-Télécom Atlantique, 2019. English. NNT : 2019IMTA0138 . tel-02164506

HAL Id: tel-02164506

<https://theses.hal.science/tel-02164506>

Submitted on 25 Jun 2019

HAL is a multi-disciplinary open access archive for the deposit and dissemination of scientific research documents, whether they are published or not. The documents may come from teaching and research institutions in France or abroad, or from public or private research centers.

L'archive ouverte pluridisciplinaire **HAL**, est destinée au dépôt et à la diffusion de documents scientifiques de niveau recherche, publiés ou non, émanant des établissements d'enseignement et de recherche français ou étrangers, des laboratoires publics ou privés.

THESE DE DOCTORAT DE

L'ÉCOLE NATIONALE SUPERIEURE MINES-TELECOM ATLANTIQUE
BRETAGNE PAYS DE LA LOIRE - IMT ATLANTIQUE
COMUE UNIVERSITE BRETAGNE LOIRE

ECOLE DOCTORALE N° 602
Sciences de la Mer et du littoral
Spécialité : Océanographie, Physique et Environnement

Par

Huimin LI

Global observations of ocean surface winds and waves using spaceborne synthetic aperture radar measurements

Thèse présentée et soutenue à Plouzane, le 7 juin, 2019

Unité de recherche : LabSTICC

Thèse N° : 2019IMTA0138

Rapporteurs avant soutenance : Composition du Jury :

Douglas VANDEMARK
Professor, University of New Hampshire

Harald JOHNSEN,
Professor, University of Tromsø

Douglas VANDEMARK
Professor, University of New Hampshire/ Rapporteur

Harald JOHNSEN
Professor, University of Tromsø/ Rapporteur

Paco LOPEZ-DEKKER
Professor, Delft University of Technology/ Examineur

René GARELLO
Professor, IMT Atlantique/ Président

Ronan FABLET
Professor, IMT Atlantique/Directeur de thèse

Bertrand CHAPRON
Researcher, IFREMER/Co-directeur de thèse

Alexis MOUCHE
Researcher, IFREMER/Co-directeur de thèse

Acknowledgements

First, I really appreciate the China Scholarship Council (CSC) for giving me the opportunity to pursue my PhD at Ifremer, France.

I would like to express my sincere gratitude to my thesis advisors, Dr. Bertrand Chapron and Dr. Alexis Mouche for their continuous support and help on my Ph.D study and the related research. Their immense knowledge and scientific curiosity have motivated me to expand and pursue my study interests. Their guidance has helped me conduct the studies and write this thesis for all the time. I could not have finished my PhD study without their aid and advice.

In addition, I would like to thank Prof. Ronan Fablet, for his assistance in completing the doctoral processes. I am grateful for his kind support, particularly every time I seek for help.

My sincere thanks also goes to Dr. Justin Stopa in University of Hawaii at Manoa, who gave me a lot of help and advice in advancing my PhD study and writing the papers. Through the entire PhD, his questions has driven me to widen my research from various perspectives.

I also would like to thank all the colleagues in LOPS-SIAM, Ifremer for all the help after I joined the lab, and for the assistance in accessing to the laboratory and research facilities. Without they precious support it would not be possible to conduct this research here. I thank my fellow labmates in LOPS-SIAM for all the fun we have had in the last four years.

I am grateful to Chen Wang for keeping me company in getting through the hard time and his relentless encouragement to strive for brilliance. Also, I thank all my good friends in France and in China for their support.

Last but not the least, I would like to thank my family: my parents and my younger brother for supporting me spiritually throughout pursuing my doctorate and my life in general. I cannot imagine how my life will be without their care and support.

Contents

Acknowledgements	i
Abstract	iii
List of Figures	viii
List of Tables	xiii
I Background and study of the existing SAR parameters	1
1 Background	2
1.1 Motivations and objectives	2
1.2 Publications	2
1.3 Overview of the satellite measured sea surface winds and waves	3
1.4 Thesis outline	10
2 SAR imaging of the ocean surface	12
2.1 Radar backscattering	12
2.2 SAR basics	18
2.3 SAR imaging principle for a point target	22
2.4 SAR transformation of ocean waves	23
3 Status and challenges in SAR winds	32
3.1 Method of SAR wind retrieval	33
3.2 Assessment and re-calibration of S-1 NRCS	36
3.3 Challenges in S-1 wind retrieval	49
3.4 Summary	52
4 Azimuth cutoff of polarimetric SAR images	54
4.1 Single-polarized azimuth cutoff w.r.t. wind vectors	55
4.2 Quad-pol data set	57
4.3 Polarized SAR azimuth cutoff	59
4.4 Azimuth cutoffs from simulations	63
4.5 Summary	68

II	A new SAR parameter and its applications in wind/wave study	71
5	A new SAR parameter: MACS and its directionality	72
5.1	Definition of MACS	73
5.2	Characteristics of IMACS ⁽¹⁾ w.r.t. winds	78
5.3	Spatial pattern of IMACS ⁽¹⁾	82
5.4	Summary	87
6	Statistics of MACS magnitude and derived RAR MTF	89
6.1	Speckle noise of MMACS ⁽⁰⁾	90
6.2	Statistics of noise-free MMACS ⁽⁰⁾	92
6.3	RAR modulation derived from MMACS ⁽⁰⁾	96
6.4	Summary	100
7	Investigation of global ocean waves using SAR MACS	102
7.1	Introduction of wave spectra climate	103
7.2	Extraction of the MACS profile	104
7.3	MACS variation with wind speed	107
7.4	Global wave characteristics from MACS profile	108
7.5	Summary	115
8	Conclusion and perspectives	117
8.1	Conclusion	117
8.2	Future Work	120
A	Sea state impact on wind retrieval	122
A.1	Collocated wind and wave dataset	122
A.2	Sea state impact	123
	Bibliography	129
	References	129

Abstract

The ocean plays significant roles in shaping features of the Earth. The ocean controls the Earth's weather and long-term climate patterns. It also has great impacts on our societies through water/food supply and product delivery. Only by studying the characteristics and dynamics of the ocean can we better project its influence on the humankind. Among the numerous exploration techniques, spaceborne synthetic aperture radar (SAR), independent of the solar illumination and cloud cover, has been widely used to observe the atmospheric and oceanic phenomena. Air-sea interactions govern the sea surface roughness (gravity-capillary waves) which determines the magnitude of the radar backscattering. Despite of being complex and non-linear, the modulation of the sea surface roughness by ocean waves is also mapped on the SAR images, providing a unique source of two-dimensional ocean swell spectra measurements from space. As consequence, many different applications, such as swell tracking, assimilation of wave spectra into operational wave forecasting systems or more recently wave-ice interactions studies have benefited from SAR observations. However, since Envisat/ASAR (2002-2012) which provided 10-year acquisitions over open ocean, SAR systems have been significantly improved, offering new perspectives for ocean applications. This thesis deals with the potential of these new missions to fully exploit their capabilities and to, possibly, provide guidance for future concept missions.

To this aim, this thesis mainly deals with the latest European (Copernicus program) SAR constellation mission Sentinel-1(S-1) constellation (S-1A in April 2014 and S-1B in April 2016). These two C-band SAR ensures continuity with the past European missions for waves measurements thanks to the so-called Wave Mode and new capabilities. In particular, S-1 wave mode acquires SAR vignettes over the global ocean at higher resolution than Envisat/ASAR and alternately at two different incidence angles to increase the swell sampling. This thesis also explores the GaoFen-3 (Chinese mission) and Radarsat-2 (Canadian mission) to extend the incidence angle range and investigate the polarization diversity benefits. Finally, the 10 years of Envisat/ASAR data are also considered to explore the temporal trend of global wind/waves.

In Part I, the commonly used SAR parameters are reviewed, including the Normalized radar cross-section (NRCS) and azimuth cutoff. NRCS has been extensively used in the microwave remote sensing to describe the backscattering magnitude of the imaged area. A series of calibration steps are required to obtain the proper NRCS. Thus, prior to any geophysical applications, NRCS of Sentinel-1 (S-1) wave mode (WV) acquisitions is first assessed. It is found in this thesis that WV

NRCS is poorly calibrated, in particular for WV2 at larger incidence angle. This is because there is no strategic acquisitions over the corner reflectors to consistently calibrate NRCS. Two different re-calibration methods: rainforest and ocean calibration are carried out and both achieved comparable performance. The ocean calibration turns out to be more efficient and easy to implement from the operational point of view. Following the NRCS re-calibration, wind speed is then derived using an input wind direction and compared with the S-1 level-2 products. It exhibits better agreement with the collocated buoy wind speed, particularly over the low winds range. Despite of the improved NRCS quality with re-calibration, NRCS is still subject to other impact factors, such as presence of geophysical phenomena and signal-to-noise ratio.

Azimuth cutoff is another parameter that has been proven useful in the wind retrieval. Azimuth cutoff is advantageous because it is directly estimated from SAR image spectra and free of calibration steps. It can be taken as a complementary to NRCS and accounts for the sea state impact on wind speed. In addition to its wind dependence, the azimuth cutoff is also analyzed regarding its polarization dependence based on data acquired by Radarsat-2 and Gaofen-3. In general, azimuth cutoff is greater in VH than in HH, which in turn larger than VV. The comparison of azimuth cutoff between SAR measurements and the simulation out of collocated ocean wave spectra is conducted on a case-by-case basis. The statistical disagreement mainly lies in the cross-polarized azimuth cutoff that SAR measurements show larger values. The greater azimuth cutoff is speculated to associate with the higher sensitivity of cross-polarization to the wave breaking. Further theoretical investigations are required to fully interpret the SAR mapping principles for cross-polarization measurements. This shall lead to the possibility of quantifying the contributions of wave breaking by combining the polarized azimuth cutoff.

One of the main limitations of existing SAR system is their unique viewing angle. To overcome this issue, one can combine complementary (different sensitivity to azimuth look angle) radar parameters. For instance, the use of both Doppler centroid anomaly (DCA) and NRCS has proven to help constraining the wind speed and direction inversion. However, due to issues in the attitude systems of S-1, its accuracy is still under improvement. Another possible solution is to move toward more advanced SAR mission concepts such as STEREOID to get both diversity in viewing angles and radar parameters. Here, based on the existing SAR, a new SAR parameter is defined to complement NRCS and azimuth cut-off. In addition, it could possibly replace DCA as existing SAR mission requirements hardly fit the mandatory accuracy needed for ocean applications from Doppler. This new parameter is termed as MACS and defined from the SAR image cross Spectra. Part II of this

thesis is dedicated to this new parameter.

MACS is first defined by filtering the cross-spectra around range-traveling intermediate ocean waves (15-20 m) since these waves are strongly coupled with the local winds. By definition, MACS is expected to reflect both magnitude and direction of the mapped intermediate waves. It is a complex quantity and dependent on the radar configurations (radar center frequency, polarizations and incidence angles). Imaginary part of MACS (IMACS) is found to be a signed quantity relative to the wind direction (from upwind to downwind). IMACS also shows asymmetry with respect to the radar line-of-sight direction. Analogous to the DCA, MACS can be used together with NRCS to establish an independent wind algorithm. The self-derived winds from SAR measurements shall benefit further studies, such as wave inversion, assessment of finescale wind/wave/current interaction, et al.

As a follow-up study to the IMACS dependence on winds, the possibility of using MACS to examine the modulation transfer function (MTF) between SAR backscatter and ocean waves is also addressed. To this end, the magnitude of MACS (MMACS) is documented with respect to the sea surface wind (wind direction dependence, up-downwind asymmetry) and radar configurations (incidence angles and polarizations). The comparison of MMACS obtained from SAR measurements and simulations shows disagreements, particularly at small incidence angle. Assuming a linear mapping for MMACS, the real aperture radar (RAR) MTF is accordingly derived by adjusting the simulation to be consistent with the measurements. The ratio of the derived to the initial RAR MTF overall increases with wind speed. And for given wind speed, this ratio is slightly larger in HH than in VV and much greater at small incidence angle. It shall be used to refine the wave spectral inversion and possibly to complement the tilt modulation based on the NRCS GMF.

More practically, MACS offers new perspectives for wind/waves analysis from routine and global SAR acquisitions but also to better characterize complex atmospheric phenomena. One-year S-1 WV data is used to demonstrate the global and seasonal variations of IMACS. In general, global patterns of IMACS are in agreement with the global winds. IMACS exhibits opposite signs from trade winds to the westerlies. Its magnitude is much greater in the respective storm tracks, which is associated to the consistently high winds. Complementary to the NRCS, IMACS is able to capture the seasonal variations of wind direction. In addition, the feasibility to use MACS computed at high spatial resolution for measuring sea surface wind field from SAR acquisitions in wide swath mode is also demonstrated in a case of polar low. In this context, IMACS should be advantageously used

to help constrain local wind retrieval schemes from various SAR measurements and help look into the fine structures of wind field over local wind events.

As described, MACS is defined to highlight the image spectral properties of the individual wave scales. The primary application of MACS shall be to investigate the global distributions of ocean waves at various wavelengths. Taking advantage of the ten-year acquisitions from Envisat/ASAR wave mode, this aspect is studied with the following results. The MACS for various wavelengths presents increasing trend with respect to the wind speed, corresponding to the wind-wave coupling. The degree of coupling depends on the wavelength: longer waves are in higher coupling with higher winds. And from the wave climate point of view, global patterns of MACS differ from the intermediate wind waves (60 m) to the long ocean waves (300 m). The signatures well represent the global distribution of winds, spatially and seasonally. In addition, it is found that the most energetic wavelengths are closely related to the local winds. In specifics, MACS signatures of longer waves are found over the storm tracks while relatively shorter waves (~ 100 m) are within the trade winds. The global wave signatures represented by MACS are expected to help evaluate the model outputs and complement studies of the wave spectral climate. The data continuation of S-1 in the coming 10 years shall allow this study to extend towards longer temporal analysis.

Based on the results presented in this thesis, future studies are anticipated in several aspects. First, given the distinct wind direction dependence of MACS, an independent wind retrieval scheme by combining NRCS and MACS will certainly enhance the usage of SAR images. This method is also expected to perform at wide swath SAR images and the fine structure of wind field over various weather events can be possibly examined. Then, this analysis technique can be readily applied to the SWIM observations aboard the CFOSAT satellite, which is capable of providing the fully two-dimensional ocean wave spectra. The MACS shall be extended to all waves directions since SWIM is not subject to the nonlinear mapping as a SAR is. In addition, the spectral analysis of individual wave scales may provide reference for data processing of the coming concept missions, such as STEREOID and SKIM. The proposed MACS shall open up a new avenue for data analyses to enhance the utility of SAR observations as well as other sensors.

List of Figures

2.1	Geometry of specular backscattering.	14
2.2	Illustration of resonant Bragg backscattering from slightly rough surface.	15
2.3	Illustration of composite backscattering from ocean surface.	17
2.4	Illustration of antenna pattern impact on radar return from a point target.	19
2.5	SAR image representation for (a) a stationary target; (b) a target moving towards the sensor; (c) a target moving away from the sensor. The red dot marks true point target position.	22
2.6	SAR imaging mechanism of surface scatterers. (a) Two stationary independent targets at different positions. (b) Mapping of a stationary scattering element A and another B at the same range position but with non-zero mean velocity. (c) Mapping of a scattering facet with a continuous distribution of distinct and independent scattering elements at different intrinsic frequency. After (K. Hasselmann et al., 1985b).	25
2.7	Variation of tilt MTF relative to (a) incidence angle at wind speed of 7 m/s and wind direction of 45°; (b) wind speed at incidence angle of 40° and wind direction of 45°; (c) wind direction at incidence angle of 40° and wind speed of 7 m/s. 0° wind direction denotes upwind (wind blowing towards the radar looking direction). Theoretical values are derived using formula in (W. R. Alpers et al., 1981). The GMF-based tilt MTF is calculated using CSARMOD in (A. Mouche & Chapron, 2015a).	28
3.1	Flowchart of the wind retrieval from a SAR image. 'wdir' is wind direction and 'DCA' is Doppler centroid anomaly. 'U10' is the neutral wind speed at 10 m height. Solid lines represent determined processes and dashed lines are alternatives.	33
3.2	Histogram of incidence angles for (a) WV1 and (b) WV2, receptively. Bin size of incidence angle is 0.22°. (c) Normalized histogram of latitude at given incidence angle for WV1. Bin size of latitude is 2°. Solid lines are for Ascending pass and dashed lines are for Descending pass. Colors represent different incidence angles. Products acquired at latitude higher than 55° have been filtered out to avoid ice contamination.	37
3.3	NRCS at 12 ms ⁻¹ relative to wind direction for (a) WV1 at incidence of 23.4°; (b) WV2 at incidence of 36.4°. Black dots are S-1A measurements and red lines are fit to S-1A observed NRCS in form of Eq.(3.1). Blue line is the predicted CMOD5.N for given incidence angle and wind speed. For wind direction, 0° indicates upwind and 180° is downwind.	39
3.4	NRCS difference ($\sigma_{SAR}^0 - \sigma_{CMOD5.N}^0$) as function of wind speed for given incidence angle for (top) WV1; (bottom) WV2. Solid line is mean NRCS difference with bin size of 1 ms ⁻¹ . The error bar represents 1 standard deviation of NRCS difference within each bin. Colors denote count of data points.	40
3.5	(a) An example of processing one imagette into subimages of 10 km by 10 km (WV2 image acquired on November 10, 2017 at 22:21:41 UTC). (b) Histogram of γ^0 over sub-image I (blue solid line) and fit (red dashed line) with Eq.(3.4). The bin size of γ^0 is 0.1 dB. The vertical dashed line represents position of fitted A_1 coefficient.	42
3.6	(a) Map of processed IW and WV points. Colors denote number of processed IW points. The solid circle represents position of WV data points (WV1 in red and WV2 in black). (b) Weekly count of data points for WV and IW, respectively.	43

3.7	(a) Variation of γ^0 relative to elevation angle. Histogram of γ^0 for (b) all IW data; (c) IW data filtered around WV2 elevation angle; (d) WV1; (e) WV2. The fit formula to histogram is given in Eq.(3.4), plotted by black dashed lines. The fitted A_1 coefficients are annotated in subplots.	44
3.8	(Top) Variation of $\Delta\sigma^0$ relative to wind speed (a) WV1; (b) WV2. (Bottom) The corresponding number of observations for given wind speed.	45
3.9	The same as Figure 3.3 but for re-calibrated NRCS. The scatters are re-calibrated NRCS using rain-forest method. Black line (marker of right triangle) 'Fit I' represents rain-forest calibration method and red line (marker of vertical line) 'Fit II' for ocean calibration.	46
3.10	Re-calibrated NRCS residuals ($\sigma_{SAR}^0 - \sigma_{CMOD5.N}^0$) relative to wind speeds. Data (in color) are re-calibrated NRCS by ocean calibration method. Black lines are the replica of Figure 3.4 and blue (red) lines are mean re-calibrated NRCS residuals using Amazon rain-forest (ocean calibration) method. The wind speed bin is 1 ms^{-1} . The error bar represents 1 standard deviation of NRCS difference within each bin.	47
3.11	Temporal evolution of correction constant obtained by ocean calibration method per cycle for (a) S-1A and (b) S-1B (top). The corresponding number of imagerettes per cycle is given in the bottom panel. Any cycle with acquisitions less than 1000 is excluded. The fact that S-1B operated in HH polarization results in the interruption from mid-March to June in 2017.	49
3.12	(Top) Scatter plot of retrieved wind speed from re-calibrated NRCS using CMOD5.N relative to buoy wind speed for (a) WV1; (b) WV2. The buoy wind direction is input as <i>a priori</i> to CMOD5.N. (Bottom) The ocean wind field of S-1 Level-2 products derived from ESA-calibrated NRCS using CMOD-IFR2 are plotted with respect to buoy wind speed for (c) WV1; (d) WV2. Red lines are least-squared linear regression for all collocation data points and dashed red lines are linear fit to data points with buoy wind speed higher than 4 m/s.	50
4.1	VV-polarized azimuth cutoff relative to wind direction at wind speed of $12 \text{ m} \cdot \text{s}^{-1}$ for (left) WV1 and (right) WV2. Solid line is fit to the SAR measurements. Note the different maximum value along y-axis.	55
4.2	Azimuth cutoff relative to wind speed for (upper) VV-polarization WV1/WV2 and (bottom) HH-polarization WV1/WV2, respectively. Color denotes the data count.	56
4.3	(a) The geographic position of Gaofen-3 WM data across the globe. Color denotes incidence angle [$^\circ$]. (b) Histogram of incidence angles in bin size of 2°	59
4.4	A case of Gaofen-3 WM product acquired on February 1, 2017 at UTC 4:25:26. Incidence angle is 30.4° . (Left) Image of normalized backscattering for (a) VV; (b) HH; (c) VH polarization. (Right) Real part of SAR image cross-spectra for (d) VV; (e) HH; (f) VH polarization.	60
4.5	(Top) Azimuth cutoff of HH relative to VV polarization for five incidence angles of Gaofen-3 data set. (Bottom) Azimuth cutoff of VH relative to VV polarization. The solid lines are the mean fit for each incidence angle. The dashed lines are the one-to-one curves.	61
4.6	Azimuth cutoff in HH-pol (a) and in VH-pol (b) relative to VV-pol based on the 21 Radarsat-2 data. Color denotes incidence angle.	62
4.7	(Left) Simulated SAR image cross-spectra for three polarization channels: (a) VV; (c) HH; (e) VH. (Right) The corresponding azimuth cutoff estimation for three polarization channels: (b) VV; (d) HH; (f) VH. The input ocean wave spectrum is Elfouhaily spectrum at wind speed of 7 m/s and wind direction of 45° with inverse wave age of 0.35. Incidence angle is set as 36°	65

LIST OF FIGURES

4.8 (Top) Comparison of azimuth cutoff from SAR measurements and nonlinear SAR transformation for (a) VV-pol, (b) HH-pol and (c) VH-pol. Solid line is one-to-one curve and dashed line is the least-squared linear regression. Color denotes data density. (Bottom) The corresponding data count of simulated azimuth cutoff in bin size of 25 m for each polarization. 66

4.9 Azimuth cutoff residual (SAR-simulation) relative to the collocated ECMWF wind speed for (a) VV; (b) HH; (c)VH. Solid black line is the mean azimuth cutoff residual. Color denotes data count. 68

4.10 Polarization difference of azimuth cutoff relative to the ECMWF wind speed for (a) HH-VV; (b) VH-VV. Solid line is for SAR measurements and dashed line is for the simulation results. 69

5.1 (a) Flowchart of SAR image cross-spectral estimate; (b) simplified view of individual look extraction based on Doppler bandwidth spectrum. (c) An example of SAR image acquired by S-1A. Incidence angle is 23.8°. (d) The corresponding imaginary part of SAR cross-spectra computed for $\Delta t = 1\tau$ 74

5.2 A schematic view on extent of intermediate radial waves denoted by 'A' over which to compute MACS. The limits of wavelength used here is 600 m in azimuth and between 15 m and 20 m in range. The dotted circles represent wavelengths of 100 m and 20 m from inner to outer. 75

5.3 (Top) Probability density function (PDF) of collocated radial wind speed between S1A/B and ECMWF for HH and VV, WV1 and WV2, respectively; (bottom) PDF of correspondingly equalized dataset (denoted as Data I). The wind speed bin used here is 1 m/s. Data with wind greater than 20 m/s has been excluded due to lack of enough points. Positive radial winds correspond to upwind direction. 77

5.4 IMACS⁽¹⁾ relative to radial wind speed for (a) WV1-HH; (b) WV2-HH; (c) WV1-VV; (d) WV2-VV based on the equalized Data I. 'N' is the number of points used in each plot. The color represents latitude. The solid black line marks the mean curve to the observations. Positive radial wind speeds denote upwind configuration. 78

5.5 (a) Scatter plot of IMACS⁽¹⁾ relative to wind direction at wind speed of 7 m/s. Binned average of IMACS⁽¹⁾ (solid), IMACS_{+A}⁽¹⁾ (dashed) and IMACS_{-A}⁽¹⁾ (dotted) are also plotted. (b) Δ IMACS _{\pm} ⁽¹⁾ (IMACS_{+A}⁽¹⁾-IMACS_{-A}⁽¹⁾) at 7 m/s. (c) Δ IMACS _{\pm} ⁽¹⁾ relative to wind direction for various wind speeds. Wind direction of 0° denotes upwind. 80

5.6 (a) NRCS representation acquired by S-1A Interferometric Wide swath (IW) on 29 December, 2016 at 15:03 UTC over a Polar Low. ECMWF forecast winds at 15h00 UTC are superimposed as arrows with colors denoting wind speed. (b) IMACS⁽¹⁾ computed over moving window. (c) IMACS⁽¹⁾ along two transects depicted by two black lines in plot (b). 81

5.7 Seasonal global map of IMACS⁽¹⁾ based on data acquired by S-1A WV1 over ascending pass from December 2016 to November 2017. The negative IMACS⁽¹⁾ corresponds to upwind direction with wind roughly blowing from the east to the west. Data are averaged on a spatial bin of 2° in both longitude and latitude. 84

5.8 Probability Density Function (PDF) of (a) NRCS and (b) IMACS⁽¹⁾ over the east Equatorial Current area (marked by red rectangle in Figure 5.7(a)) are presented for four seasons. The wind rose of collocated ECMWF winds is also depicted for (c) season of JJA; (d) season DJF. 85

LIST OF FIGURES

5.9 Seasonal average of (a) IMACS⁽¹⁾, (b) collocated ECMWF wind direction and (c) projected radial wind speed relative to latitude along the transect of 90°E shown as vertical black line in Figure 5.7(a). Data are averaged over latitude bin of 2°. The gray arrow denotes SAR flight direction over ascending pass. Wind convention is the same with Figure 5.7. 86

5.10 Inter-seasonal standard deviation of IMACS⁽¹⁾ computed from seasonal average given in Figure 5.7. 87

6.1 (a) The solid lines represent best fit to SAR-measured MMACS⁽⁰⁾ for wind directions along the range ($\pm 10^\circ$), containing contribution of noise. Dashed lines are polynomial fit to the observations in an effort to infer noise floor, which is equal to MMACS⁽⁰⁾ at wind speed of 0 m/s. (b) noise-free MMACS⁽⁰⁾ after deducting global noise floor. Positive winds are upwind (wind blowing against the antenna). 91

6.2 The left panel is NRCS as function of wind direction at 9 m/s in (a) WV1; (b) WV2. The right panel is MMACS⁽⁰⁾ in (c) WV1; (d) WV2. The dashed line represents the mean and solid line marks fit curve in form of Eq.(6.1) to the observations. The wind direction of 0° is upwind and 180° downwind. 93

6.3 Two-dimensional plot of MMACS⁽⁰⁾ for (a) HH WV1; (b) VV WV1; (c) HH WV2; (d) VV WV2. The radius is wind speed with circles from inner to outer of 5 m/s, 10 m/s and 15 m/s, respectively. The color represents MMACS⁽⁰⁾. Wind direction of 0° corresponds to upwind (wind blows against the antenna pointing direction). 94

6.4 (Top) UCA of (a) NRCS; (b) MMACS⁽⁰⁾; (bottom) UDA of (c) NRCS; (d) MMACS⁽⁰⁾ as function of wind speed. 96

6.5 (a) RAR modulation estimated using empirical GMF of NRCS by $M_r = \frac{1}{\sigma_0} \frac{\partial \sigma_0}{\partial \theta}$. The solid lines are results with CSARMOD and dashed lines are with CMOD5. (b)(c) Comparison of MACS⁽⁰⁾ between SAR measurements and simulations for incidence of 23° and 36.5°, respectively. 98

6.6 Ratio of derived RAR MTF to the empirical as function of radial wind speed based on assumption of negligible velocity bunching. 100

7.1 (Top) Global data density of wave mode acquisitions at spatial resolution of 2.5° by 2.5° and monthly data count of global ASAR data. Ascending products collected from 2003 to 2012 are used here. (Bottom) Monthly data density in March 2003 and March 2004. 105

7.2 Examples of ENVISAT/ASAR wave mode images for definition of range MACS profile. (Top) Normalized backscattering for four cases. (Middle) The corresponding SAR image spectra are plotted. Color represents the normalized image spectral magnitude. The circles from inner to the outer are 400 m, 200 m 100 m and 50 m respectively. (Bottom) The range MACS profile is extracted relative to wavenumber. 106

7.3 MACS derived for various wavelengths. (a) MACS for wavelength of 62.5 m relative to wind speed. Color denotes data counts and solid black line is the mean fit. (b) MACS relative to wind speed for various wavelengths between 47 m and 257 m. (c) MACS variations relative to inverse wave age (wind speed/wave phase speed). Only winds in the radar looking direction (upwind and downwind) with a variation of 2° are included in the analysis. 107

7.4 (Left) Peak wavelength at given wind speed is plotted for various iwa. Peak wavelength is derived from Elfouhaily spectrum. (Right) Wavelength resolution of Level-1B SAR image spectra products. 107

7.5	(Left) Estimates of averaged MACS for given wavelength. Bars are histogram of MACS at 602.6 m over A2 during the season MAM. Vertical red line indicates the median value and black line is the mean value. (Right) Comparison of range MACS profile using mean and median values.	109
7.6	Seasonal average of MACS for three selected wavelengths in the panels of (a) 62.50 m; (b) 168.4 m; (c) 342.0 m. Both latitude and longitude are binned into 2.5° by 2.5°. Color denotes MACS and note that the color bar dynamics vary in the three columns. Blank spaces are due to lack of SAR observations.	110
7.7	(Top) MACS profiles averaged over the Pacific Ocean (150°W-145°W) along latitude are shown for four seasons: (a) DJF; (b) MAM; (c) JJA and (d) SON. Color bar denotes MACS in log scale. (Middle) MACS profile relative to wavenumbers for three latitudes in (a). Total average in (e) and seasonal average for (f) A1; (g) A2; (h) A3. Dashed vertical lines indicates position of detected peak wavenumber with color corresponding to seasons. (Bottom) Seasonal average of global peak wavenumber derived over latitude and longitude bin of 2.5°. Color denotes peak wavenumber k_p [rad · m ⁻¹].	112
7.8	(Top) The geographic position of six area of interest. (Left) Monthly time series of MACS profile (color in log scale) over six area of interest (A1-A6) and detected k_{rp} (black solid line). The vertical blank space is due to lack of observations during that month. (Right) The frequency spectra of time series of range peak wavenumber. Note that A1-A3 correspond to the three transects in the Pacific Ocean in Figure 3.	114
A.1	Map of collocation dataset between S-1 WV and buoys. The red asterisk denotes collocations for WV1 and the blue for WV2. Spatially overlapped WV1 and WV2 do not coincide in time.	123
A.2	Wind speed residual ($U^{SAR}-U^{buoy}$) relative to collocated buoy wind speed for (a) WV1 and (b) WV2. The error bars are 1 standard deviation about the average (black solid lines) and red solid lines represent least-squared linear regression. The linear fit slope is annotated on top left corner in red.	124
A.3	(Top) Wind speed residual ($U^{SAR}-U^{buoy}$) is shown relative to collocated buoy H_s for (a) WV1 and (b) WV2. The error bars are 1 standard deviation about the average (black solid lines) and red solid lines represent linear regression. (Bottom) Histogram with bin of 0.25 m for WV1 in (c) and WV2 in (d), respectively.	125
A.4	Wind speed residual ($U^{SAR}-U^{buoy}$) relative to azimuth cutoff for (a) WV1 and (b) WV2. Error bars are 1 standard deviation about the average (black solid lines) and red solid lines represent linear regression.	126
A.5	NRCS as function of wind speed WV1/WV2 at top/bottom (only upwind direction with variation of ±5°). (a)/(d) S-1A observations; (b)/(e) the predicted using a neural network with wind speed and wind direction as input; and (c)/(f) the predicted using a neural network with wind speed, wind direction and azimuth cutoff as input. The color denotes azimuth cutoff [m]. Bias and RMSE are calculated by the predicted NRCS relative to the S-1A observations.	127

List of Tables

- 3.1 Mean NRCS residual 48
- 4.1 Azimuth cutoff at $15 \text{ m} \cdot \text{s}^{-1}$ 57
- 4.2 Details of Radarsat-2 Fine Quad-pol products. 58
- 5.1 Number of data included in this study. 77

Part I

Background and study of the existing SAR parameters

Chapter 1

Background

1.1 Motivations and objectives

Space-borne synthetic aperture radar (SAR) can provide extensive and continuous observations of the ocean surface under all-weather conditions. Since the launch of SeaSat-A, SAR observations have been widely used in various maritime applications. Wave mode is an imaging mode that is dedicated to global wave measurements. It has been used to routinely collect SAR vignettes over the global ocean from ERS-2 to Envisat/ASAR to today's Sentinel-1 constellation. In the meantime, fully polarimetric images have also been available to provide complementary imaging of ocean surface. The contemporary massive ocean data archive is invaluable to observations of the basic elements on the sea surface: wind and waves, among others. Taking advantage of the present SAR acquisitions, this thesis focuses on deriving the wind and wave information and the following points are addressed.

1. Assessment of the normalized radar cross-section for Sentinel-1 wave mode
2. Investigation of sea state impact on wind speed retrieval at two incidence angles
3. A new radar parameter, MACS, is proposed to complement SAR surface wind retrievals
4. MACS offers new perspectives on interpreting the global patterns of wind and waves
5. MACS helps improve real aperture radar modulation transfer function estimates
6. Study global wave spectral climate from MACS profile using the ten-year Envisat/ASAR
7. Preliminary analysis of polarimetric SAR mapping through azimuth cutoff

1.2 Publications

In achieving the objectives listed above, the following papers in Chapter 3-7 are prepared:

1.3. Overview of the satellite measured sea surface winds and waves

1. Li Huimin, Mouche Alexis, Stopa Justin E., Chapron Bertrand, Calibration of the normalized radar cross-section for Sentinel-1 wave mode, *IEEE Transactions on Geoscience and Remote Sensing*, vol. 57, no. 3, pp. 1514-1522, March 2019. doi: 10.1109/TGRS.2018.2867035
2. Li Huimin, Mouche Alexis, Stopa Justin E., Impact of Sea State on Wind Retrieval from Sentinel-1 Wave Mode data, *IEEE Journal of Selected Topics in Applied Earth Observations and Remote Sensing*, vol. 12, no. 2, pp. 559-566, Feb. 2019. doi: 10.1109/JS-TARS.2019.2893890
3. Li Huimin, Mouche Alexis, Wang He, Stopa Justin E., Chapron Bertrand, Polarization dependence of azimuth cutoff from Quad-pol SAR images, submitted to *IEEE Transactions on Geoscience and Remote Sensing*, in revision.
4. Li Huimin, Chapron Bertrand, Mouche Alexis, Stopa Justin E., A new ocean SAR cross-spectral parameter: definition and directional property using the global Sentinel-1 wave mode measurements, *Journal of Geophysical Research - Oceans*, 124, 1566-1577, Feb 2019.
5. Li Huimin, Mouche Alexis, Stopa Justin E., Chapron Bertrand, A new ocean SAR cross-spectral parameter: magnitude statistics and its application in deriving the real aperture radar modulation transfer function, in preparation.
6. Li Huimin, Mouche Alexis, Stopa Justin E., Chapron Bertrand, New investigation of ten-year Envisat/ASAR wave mode for global ocean waves, in preparation.
7. Li Huimin, Chapron Bertrand, Mouche Alexis, SAR Cross-Spectral Analysis of Radial Intermediate Waves: Directional Properties. IEEE International Geoscience and Remote Sensing Symposium, Valencia, 2018, pp. 5827-5830.

1.3 Overview of the satellite measured sea surface winds and waves

The ocean covers approximately 71% of the Earth's surface and contains almost 97% of the Earth's water. It plays significant roles in shaping the global weather and long-term climate. Comprehensive observations of the global ocean are necessary to understand its geophysical dynamics. This includes a wide range of oceanic and atmospheric variables, such as the oceanic current, sea surface salinity, ocean biology, precipitation, sea surface temperature, wind and waves, etc. Of which, the sea surface wind and waves are the most basic elements on the vast ocean surface.

Sea surface wind is caused by atmospheric pressure gradient. Surface waves are then generated under the forcing of sea surface wind. These two variables are highly correlated and both are important to local air-sea interactions. Observations are needed to better understand the wind-wave coupling and their roles in the air-sea interactions. In the context of global atmosphere and ocean interaction, their climate signatures at regional or global scale are also desired. To date, the winds and waves are usually measured using two types of systems: *in situ* and remote sensing sensors.

The traditional *in situ* instruments are able to regularly provide observational records, but are limited to sparse locations in space and it is difficult and expensive to deploy many sensors over a large area on the ocean. Plus they are subject to fragile damage associated with environmental events or human activities. As such, despite accurate observational records at the location of interest, it is not feasible to gather *in situ* measurements that cover the entire region, not to mention the globe.

Remote sensing measurements can be grouped in terms of their mounted positions, such as ship-borne, airborne, spaceborne etc. Among others, spaceborne remote sensing systems are capable of continuously providing observations of sea surface wind and waves at global scale. This was first demonstrated with the pioneering launch of the SeaSat-A satellite in 1978. It carried a Ku-band (center frequency 14.599 GHz) scatterometer sensor, an Ku-band (center frequency 13.56 GHz) radar altimeter and an L-band (center frequency 1.275 GHz) SAR sensor. Unfortunately, the satellite mission was terminated by a massive power failure only after 105 days of operation. Yet, the large data set collected over this short duration still proved the ability of spaceborne radars to accurately measure sea surface winds and waves (Jones et al., 1981). In this sense, the SeaSat-A is a visionary mission, being the precursor for the subsequent ocean satellite systems.

1.3.1 Satellite observations of ocean winds

Spaceborne satellites are effective and economical means of observing global ocean winds. Active radars, including scatterometer, SAR and altimeter are the main sensors to measure sea surface winds. These radars rely on the sea surface roughness to measure the surface wind at 10 m elevation (hereafter U10) (Quilfen & Bentamy, 1994; Hersbach et al., 2007; Hersbach, 2008; A. Mouche & Chapron, 2015a). Among which, each sensor has its strong and weak points.

Scatterometers have multiple viewing antennas and are able to resolve the absolute wind direction. Typical errors of the inferred wind vectors are 1 m/s for wind speed from various scatterometers and

1.3. Overview of the satellite measured sea surface winds and waves

less than 20° for wind direction (Bentamy et al., 2013; Stoffelen & Anderson, 1997). The winds are usually available at spatial resolution of 12.5 km or 25 km (Bentamy et al., 2013; Freilich & Dunbar, 1999; Stoffelen & Anderson, 1997). Since SeaSAT-A, several scatterometers have been launched. These include the wind scatterometer on ERS satellite (ERS-1: 1991-2000 and ERS-2: 1995-2011), the SeaWinds instrument on QuikSCAT (2001-2009), the SCAT instrument on Oceansat-2 (2009-2014), the ISS-RapidScat on International Space Station (2014-2016) and the ASCAT on MetOp satellites (MetOp-A launched in 2006 and MetOp-B in 2012). The next generation MetOp satellites have been approved and are going to be launched soon.

While a SAR has only one fixed antenna, in consequence, it cannot resolve the wind direction. With the input wind direction as *a priori*, SAR is able to provide the wind speed at much higher spatial resolution up to hundred meters (Lehner et al., 1998; Horstmann et al., 2002). The derived fine-scale SAR winds can complement the scatterometer measurements to better resolve the spatial variability of local wind fields. The typical errors of derived wind speed are 1 m/s (Lehner et al., 1998; Lin et al., 2008). It is worth pointing out that wind direction can be partly resolved (180° ambiguity still exists) by SAR images when wind streaks are present. Past and present SAR missions include C-band sensors on ERS-1/2 (1991-2011), Radarsat-1 (1995-2016), ENVISAT (2002-2012), Radarsat-2 (2007-), Sentinel-1 (2014-) and X-band sensor (center frequency: 9.65 GHz) on TerraSAR-X satellite (2007-now) and TanDEM-X (2010-now).

In addition to the two radars mentioned above, the radar altimeter is another instrument that can obtain wind speed records. The wind speed can help correct the simultaneously measured significant wave height and can also be used for climatological studies given the long duration of altimeter missions (I. R. Young et al., 2011). There are a many of altimeters that have been launched, including: GEOSAT (1986-1990), ERS-1 (1991-2000), TOPEX/Poseidon (1992-2006), ERS-2 (1995-2011), Jason-1 (2001-2013) and Jason-2 (2008-now), Cryosat-2 (2010-now), HY-2 (2011-2016) and SARAL (2013-now).

In remote sensing, a geophysical model function (GMF) is generally used to infer the wind speed and direction from these radar measurements. It relates the Normalized Radar Cross Section (NRCS) to radar configurations (radar wavelength, polarization as well as incidence angle) and sea surface wind (wind speed and direction). Several families of GMF have been proposed to aid the wind retrieval from radar measurements at different bands (X-, ku-, C-band). Among which, C-band GMF is widely used in virtue of the numerous data archive. Though it has been continu-

ously updated to improve its performance in wind retrieval (Quilfen & Bentamy, 1994; Hersbach et al., 2007; Hersbach, 2008; A. Mouche & Chapron, 2015a), the accuracy is still subject to multiple impact factors. For example, the atmospheric instability (Hoffman & Louis, 1990) and presence of upper oceanic current (Plagge et al., 2012) shall both modify the local sea surface roughness. These influence on sea surface roughness leads to a modified NRCS, different from the ambient NRCS generated by the local winds. In addition to that, the modulation of wind generated small scale roughness by ocean swell can also influence the mean radar backscattering. All these NRCS modifications would accordingly translate to biases in the wind retrieval. In particular, the sea state impact has been examined by (Stopa et al., 2017) using the advanced SAR (ASAR) aboard ENVISAT. Since ASAR operated only at one incidence angle ($\sim 23^\circ$), analyses using scatterometers were extrapolated to investigate sea state impact dependence on incidence angle. It was found that this impact decreases with increasing incidence angle (Stopa et al., 2017), consistent with the previous findings (Quilfen et al., 2004). This impact is expected to be compensated in order to obtain the accurate wind from both SAR and scatterometers.

On top of that, it should also be noted that most of the present active radars operate at co-polarization (VV or HH). The co-polarized radar return is notoriously prone to signal saturation at high winds (>25 m/s), restricting their applications in extreme weather events (for example tropical cyclones). With the increasing availability of fully polarimetric acquisitions, it was recently documented that cross-polarized backscatter is not subject to the saturation issue (B. Zhang & Perrie, 2012). This opens up a new avenue for monitoring the high winds conditions using spaceborne radar observations. Now, quasi-routine acquisitions over tropical cyclones have been initiated by S-1 constellation during the hurricane season. This capability shall be further enhanced with the coming S-1C&D, the next generation Metop as well as the radarsat constellation mission (launch expected in May 2019).

In addition to the active radars, passive radiometers have recently been demonstrated to be capable of monitoring high wind conditions, particularly over the tropical cyclones (Reul et al., 2017). And microwave radiometers work quite differently from the radar (Zhao et al., 2018), depending on the brightness temperature to sense the wind strength. The brightness temperature is closely related to the surface emissivity affected by surface whitecaps. As the winds intensify particularly over cyclone conditions, whitecap coverage greatly increases, changing the brightness temperature. With careful corrections, the local winds can then be derived. The radiometers can provide wide-swath observations at spatial resolution of 40 km and have been shown to give reliable measurements

on the wind structures of hurricanes. By combining with the active radar measurements, it shall improve forecasting for tropical cyclones.

1.3.2 Satellite measurements of ocean waves

Ocean waves are the most common phenomena on the sea surface and cover a wide range of wavelengths and directions. They are caused by the sea surface wind, generated by the friction between the wind and the water. As the wind blows, ocean waves gain energy from the wind and gradually grow. After the wind blowing over an area (fetch) for a certain time (duration), the sea state reach equilibrium with the local winds (Phillips, 1985; Juszko et al., 1995). Properties of local sea state can be fully characterized by the two-dimensional ocean wave spectrum, describing the wave energy distribution with respect to the wavelength and direction (Phillips, 1985). All statistical parameters of ocean waves can be accordingly derived from the ocean wave spectrum. In fact, spaceborne satellites provide quite different measurements of ocean waves, depending on the platform. On one hand, the integrated significant wave height (hereafter H_s) is systematically measured by the radar altimeters. While SAR is the one of the few spaceborne sensors that are able to observe the two-dimensional ocean wave spectrum, based on which the integrated variables can be accordingly derived, such as H_s , peak wavelength and direction, mean wavelength and direction, etc.

A radar altimeter is an active radar, looking at down nadir direction. It transmits the radar pulses and records the travel time of the signal to the ocean surface. Since radar altimeters operate at nadir, radar backscattering can be well described by the specular reflection theory (Barrick, 1968; G. R. Valenzuela, 1978). After a series of atmospheric corrections, the significant wave height can be derived from the slope of the return radar pulse (Brown et al., 1981; Wingham et al., 2004; Phalippou & Enjolras, 2007). To reduce the uncertainty, a number of radar return pulses are usually averaged to produce one estimate of H_s about every 7 km along the satellite track. Altimeters on various satellites have been launched, including: GEOSAT (1986-1990), ERS-1 (1991-2000), TOPEX/Poseidon (1992-2006), ERS-2 (1995-2011), Jason-1 (2001-2013) and Jason-2 (2008-now), Cryosat-2 (2010-now), HY-2 (2011-2016) and SARAL (2003-now). The accuracy of altimeter measurements is generally on the order of 0.5 m or $\pm 10\%$ of the wave height in the range from 1 m to 20 m (Staabs & Bauer, 1998; Queffelec & Bentamy, 2007).

Though the global H_s can be obtained, other parameters, such as the peak wavelength and wave di-

rection are currently not available from the radar altimeters. By comparison, SAR has the potential to routinely measure the two-dimensional ocean wave spectrum. Since ERS-1/2, a dedicated imaging mode for ocean waves measurements, called wave mode, has been operating over the global ocean. Each wave mode vignette is acquired every 100 km or 200 km along the flight direction. The wave mode data set is designed to provide extensive wave measurements at global scale. To better interpret the wave mode data, an analytic formulation of the SAR forward mapping is fundamental (W. R. Alpers et al., 1981; K. Hasselmann et al., 1985b). The mapping transformation of ocean waves has been the subject of many studies over past decades. In general, an ocean wave SAR image is formed by two independent processes: RAR imaging of ocean waves and the motion effects of velocity bunching. A closed-form of SAR imaging relation from ocean wave spectrum to SAR image spectrum has been proposed in (K. Hasselmann & Hasselmann, 1991b). Later, SAR image cross-spectrum between two sub-looks is formulated relative to the ocean wave spectrum in (Engen & Johnsen, 1995; Bao & Alpers, 1998).

With the closed-form transformation in hand, the inversion of ocean wave spectrum from SAR image spectrum is then addressed by several studies (K. Hasselmann & Hasselmann, 1991b; Engen & Johnsen, 1995; S. Hasselmann et al., 1996). The inversion scheme is usually classified into two types of schemes. The first is developed at the Max Planck Institut (MPI), proposed by (K. Hasselmann & Hasselmann, 1991b) and later updated in (S. Hasselmann et al., 1996). This method relies on a twoloop cost function minimization procedure. *A priori* structure of the wave spectrum (wavenumber and the spectral shape of each wave systems) is taken as input. The wavenumber, wave height, and wave propagation direction of each partition is then adjusted iteratively to improve the agreement of the observed with the predicted image spectra. (Heimbach et al., 1998) used three-year ERS-1 wave mode data set to assess performance of the MPI scheme relative to the wave model outputs. (Violante-Carvalho et al., 2005) further carried out a validation test with the directional buoy measurements and demonstrated the good performance of this inversion scheme. However, the primary drawback of this scheme is that it requires *A priori* wave spectra, which are not always available.

The second scheme is a straightforward inversion scheme (Krogstad et al., 1994). It only makes use of the quasi-linear part of SAR image spectrum and then directly derives the ocean wave spectrum with the input modulation function. This inversion scheme has been applied to the operational inversion for wave mode of ENVISAT/ASAR (2002-2012) and Sentinel-1 (2014-). Quality of the retrieved ocean wave spectrum has been assessed for ENVISAT/ASAR by (J.-G. Li & Holt, 2009;

J.-G. Li & Saulter, 2012) and for Sentinel-1 in (Husson et al., 2016), showing satisfactory results from a statistical point of view.

It is worth mentioning that polarimetric SAR observations have been used in attempt to obtain more wave information. (Engen et al., 2000) demonstrated the feasibility of estimating the RAR MTF by combing co-polarized (VV and HH) measurements. (B. Zhang et al., 2010) used fully polarimetric SAR images to validate the independent wave retrieval algorithm bypassing input of the difficult-to-measure RAR MTF. These studies evidenced the possibility to extract more information on ocean waves from polarized SAR measurements. Now the Chinese Gaofen-3 (launched in 2016) is collecting wave mode vignettes with fully polarimetric modes. And launch of a second Gaofen-3 sensor is also under discussion. In addition, the coming Radarsat constellation mission that carries three fully polarimetric SAR is going to be launched soon (G. Zhang et al., 2018). Abundant wave information shall be systematically provided. Moreover, it will have the capacity to view a point over 90% of the global open ocean every 24 hours. This capacity shall allow to create the image series that highlight the changes over time, which is useful to monitor the wave variations at daily scale.

Unlike the SAR sensors, SWIM aboard the recently launched CFOSAT, is a real aperture radar. Its imaging process of ocean waves is a linear process. It has been demonstrated to be capable of measuring quality two-dimensional ocean wave spectra at relatively high resolution. In combination with the winds field from the scatterometer on board CFOSAT, studies towards the wind-wave interaction shall be intriguing.

In addition to the microwave sensors, recently, the multispectral camera has been demonstrated to capture wave patterns. This technique relies on the sun reflections to sense the tilting ocean waves. Using the acquisitions from slightly different angles and at slightly different times, (Kudryavtsev et al., 2017) determined the two-dimensional ocean wave spectra and inferred the speed of oceanic current according to the wave-current interaction theory. However, this instrument is deterred by the cloud cover. Combination of the microwave and multispectral sensors (for example, OptiSAR) shall great benefit the continuous observations of ocean surface and better understand the wind-wave-current interactions.

1.4 Thesis outline

This dissertation is dedicated to exploring new potential methods for refining wind and wave observation from SAR images. Such methods should enhance usage of SAR data and bring new perspectives for SAR wind/wave retrieval. To better describe the work involved in this thesis, it is divided into two parts and organized as follows.

Part I begins with a brief introduction on SAR backscattering from the ocean surface and SAR mapping transformation of ocean waves in Chapter 2.

In Chapter 3, the wind retrieval scheme from SAR measurements is reviewed. The widely used parameter to infer wind field is the Normalized Radar Cross Section (NRCS). Prior to any geophysical application, its calibration quality is first evaluated for S-1 wave mode. The NRCS is found to be poorly calibrated. Two re-calibration methods are then implemented by examining the backscattering profile over Amazon rain-forest and ocean calibration. NRCS of Sentinel-1 constellation is fully re-calibrated using the ocean calibration considering its high efficiency and accuracy. The retrieved wind speed based on which exhibits better agreement with buoy observations in comparison to the level-2 products. Possible improvements to refine the algorithm are also discussed in this chapter.

Azimuth cutoff, another parameter has been demonstrated useful in wind retrieval. For example, it is feasible to account for the sea state impact in the wind speed retrieval. Yet, these studies are mostly based on co-polarized observations, foremost VV-polarization. With the increasing number of quad-polarized SAR images, the polarimetric azimuth cutoff analysis becomes possible. Taking advantage of the acquisitions from Radarsat-2 and Gaofen-3, the analyses are covered in Chapter 4.

Though NRCS and azimuth cutoff have been demonstrated to work in the wind retrieval, the prerequisite of *a priori* wind direction is as yet resolved. This issue might be overcome with the proposed parameter, MACS, defined based on the SAR image cross-spectra. Part II of this thesis is dedicated to exploring the properties of MACS and its applications in SAR wind/wave observations.

In Chapter 5, the definition of MACS is detailed. Its dependence on wind speed and direction is first documented. This confirms the possibility of using MACS to resolve the wind direction ambiguity in deriving high-resolution wind fields from SAR images. More importantly, MACS

can be employed to look into the global signatures of ocean winds. A one-year analysis, from Sentinel-1 Wave Mode data, is further reported to quantify the regional and seasonal variations of MACS.

Then in Chapter 6, the magnitude of MACS (MMACS) is addressed in terms of wind speed and direction. Its dependence on polarization as well as incidence angle is also demonstrated. It is found that MMACS greatly differs between SAR measurements and simulations. Assuming a quasi-linear mapping formulation for MMACS, a refined RAR MTF is derived by adjusting the simulations to be consistent with SAR-MMACS .

Since MACS is defined to highlight the image spectra of isolated wave scales, the global patterns of MACS at various wavelengths are expected to depict the spatial distribution of differing ocean waves. Chapter 7 then follows to address this point by analyzing MACS of various wavelengths based on the ten-year Envisat/ASAR data archive. The wind-wave coupling is examined for different wave scales. The global patterns of three MACS, typical of wind sea and long waves are illustrated and compared. The temporal variations of MACS profile are also analyzed at six locations of interest across the globe.

Conclusion and the perspectives are given in Chapter 8.

Chapter 2

SAR imaging of the ocean surface

Contents

1.1 Motivations and objectives	2
1.2 Publications	2
1.3 Overview of the satellite measured sea surface winds and waves	3
1.3.1 Satellite observations of ocean winds	4
1.3.2 Satellite measurements of ocean waves	7
1.4 Thesis outline	10

Progresses in scattering theory of electromagnetic (EM) waves lay the groundwork for development of microwave remote sensing of ocean surfaces. The key to interpreting radar return data is to associate it with geophysical phenomena. The complexity of wave-roughened ocean surface imposes additional difficulties in understanding the radar backscattering. To tackle this, simplified assumptions are needed so that ocean surface backscatter can be described by the linear statistics. Based on which, several fundamental microwave backscattering models have been proposed to solve the EM scattering problem.

The ocean surface can be considered as a complex distributed target with statistical surface descriptors that vary both in time and space. This randomness yields uncorrelated scatterers of different scales contributing to the radar return. Under certain linearized assumptions, great progress has been achieved towards interpreting the radar backscattering. In this chapter, we briefly introduce key radar imaging principles for ocean surfaces as well as the SAR mapping transformation of moving ocean waves.

2.1 Radar backscattering

According to linear wave theory, ocean waves are assumed to be homogeneous and Gaussian processes. The EM surface scattering can therefore be approximated by the analytic solutions. In terms

of the approximation criteria, the surface scattering is categorized into three types of solutions. The first is referred to as specular scattering, applicable to the smooth and undulating surface with large horizontal dimension compared to the incident radar wavelength. Kirchhoff and the physical optics are the most widely used formulation in specular scattering. The second is resonant scattering, which is applied to the slightly rough surface equivalent to the incident radar waves. Small perturbation method is one of the standard approach. The third is a combination of the two mentioned methods. These models have been reviewed in detail elsewhere (G. R. Valenzuela, 1978; Ulaby, 1982).

Since the rough surface can be described statistically, the scattering field is also a statistical quantity. Therefore, the ensemble averages of scattering field are usually calculated to represent the mean values. Normalized radar cross-section (NRCS, hereafter it is used interchangeably with σ^0) is often used to quantify the scattering field from rough surface, written as (Ulaby, 1982):

$$\sigma^0 = 4\pi R^2 \frac{\langle |E_s|^2 \rangle}{\langle |E_i|^2 \rangle} \quad (2.1)$$

where R is the distance between the receiving radar and center of the scattering area. $\langle \rangle$ represents the ensemble average over the scattering area. E_s is the total scattered power from the scattering area and E_i is the total incident (transmitted) power.

For given incident radar power, each scattering model predicts differing scattered power from the rough surface, dependent on the conditions of ocean surface. This then corresponds to distinct scattering coefficient σ_0 of each model. In the following, the analytic formulations of σ^0 in the case of specular, Bragg and composite scattering are introduced, respectively.

2.1.1 Specular scattering

When both the horizontal dimension and radius of curvature of the imaged surface are much larger than the incident EM wavelength, specular scattering can be invoked to predict the scattering mechanism. The incident wave is assumed to impinge upon an infinite plane, tangent to the given point on the surface. The scattering field is from the surface slope in the radar line-of-sight direction. Schematic view of the specular scattering is shown in Figure 2.1. The scattering field is computed by physical optics or the Kirchhoff method.

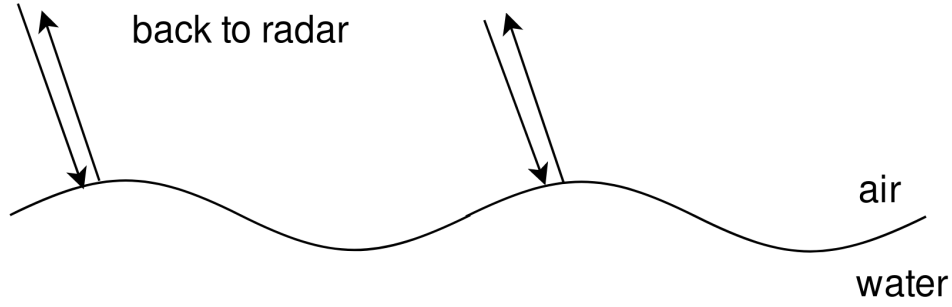


Figure 2.1: Geometry of specular backscattering.

According to (G. R. Valenzuela, 1978; Ulaby, 1982), the applicable surface conditions of Kirchhoff method can be expressed as

$$rk_r \cos^3 \theta \gg 1 \quad (2.2)$$

where r is the local radius of curvature of the illuminated ocean surface. k_r is the wavenumber of incident radar waves and θ is the radar incidence angle relative to the normal of ocean surface.

(Barrick, 1968) derived an analytic formulae to predict the backscattering σ^0 from the finitely conductive rough surface in terms of the physical optics approximation. The magnitude of σ^0 is proportional to the sea surface slope, written as:

$$\sigma^0 = \frac{\pi}{\cos^4 \theta} p(s_x, s_y) |R(0)|^2 \quad (2.3)$$

where $p(s_x, s_y)$ is the joint probability density of the two-dimensional slope of the rough ocean surface at the specular point. The sea surface slope s is computed as the first derivative of the vertical sea surface height by $s_x = \frac{\partial h}{\partial x}$ and $s_y = \frac{\partial h}{\partial y}$. h is the vertical sea surface height. $R(0)$ is the Fresnel reflection coefficient for the normal incidence angle. As formulated, the backscattering only contains backscattering contributions from the ocean surface facets normal to the radar line-of-light direction (Hagfors, 1964).

Assuming a Gaussian-distributed random ocean surface, the formula in Eq. (2.3) can be further simplified. And the σ^0 for upwind configuration (radar antenna looks against the wind) can be written as:

$$\sigma^0 = \frac{|R(0)|^2}{2 s_u s_c} \sec^{\theta} \exp(-\tan^2 \theta / 2s_u^2) \quad (2.4)$$

where s_u^2 and s_c^2 are the mean-squared sea surface slopes at upwind and crosswind direction, respectively. This simplification has been proved to be valid by various radar observations (Barrick,

1972). One can easily find that this scattering coefficient is independent of polarization because multiple scattering and shadowing effect are both excluded here.

The surface backscattering from ocean surface is specular only at near normal incidence angle. The scattering starts to diffuse with increasing incidence angle due to the augmenting contributions from the sea surface roughness (capillary waves of wavelength equivalent to the incident radar waves).

2.1.2 Resonant scattering

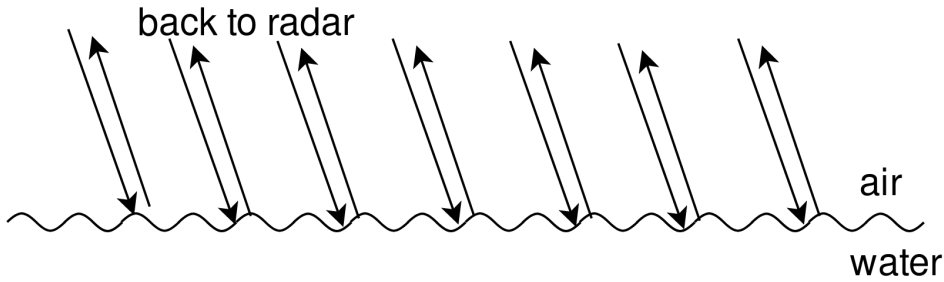


Figure 2.2: Illustration of resonant Bragg backscattering from slightly rough surface.

When both the standard deviation and correlation length of sea surface height are much smaller than the incident EM wavelength, a different surface scattering model is supposed to be devised. This is the case for most of the spaceborne radars, who operate at incidence angle higher than 18° . The radar waves interact with the short capillary waves traveling along the line-of-sight direction with wavenumber of

$$k_w = 2k_r \sin\theta \quad (2.5)$$

where k_r is wavenumber of incident radar waves. That is to say, the wave scale responsible for radar scattering echoes the radar wave scale. The backscattering σ^0 is proportional to the variance spectrum of short capillary waves on ocean surface. This resonant scattering mechanism was first outlined by (Rice, 1951) and identified by (Crombie, 1955) using measurements of 22.1 m radio waves over the sea. The Doppler shift generated by the capillary waves is equal to their frequency, showing two peaks travelling at opposite directions (one moves towards the radar and one moves away).

According to the perturbation theory in (Rice, 1951), the first-order backscattered σ^0 from the ocean surface is (Wright, 1968):

$$\sigma_{(1)}^0(\theta)_{pq} = 4\pi k_r^4 \cos^4\theta |g_{pq}^{(1)}(\theta)|^2 W(2k_r \sin\theta, 0) \quad (2.6)$$

where the subscript pq denotes polarization state of incident and backscattered EM waves, respectively. $W(k_x, k_z)$ is the two-dimensional spectral density of the ocean surface capillary waves. The incident radar wave is in the $x - z$ plane with z being the vertical direction. $g_{pq}^{(1)}(\theta)$ is the first-order scattering coefficients. For horizontal polarization (G. R. Valenzuela, 1978):

$$g_{HH}^{(1)}(\theta) = \frac{\epsilon_r - 1}{[\cos\theta + (\epsilon_r - \sin^2\theta)^{1/2}]^2} \quad (2.7)$$

and for vertical polarization

$$g_{VV}^{(1)}(\theta) = \frac{(\epsilon_r - 1)[\epsilon_r(1 + \sin^2\theta) - \sin^2\theta]}{[\epsilon_r \cos\theta + (\epsilon_r - \sin^2\theta)^{1/2}]^2} \quad (2.8)$$

where ϵ_r is the relative dielectric constant of the ocean. The cross-polarized scattering coefficients (VH and HV) are zero when only the first-order contribution is considered. Details of the second-order backscattering σ^0 can be found in (Ulaby, 1982).

When high-order solutions are considered, radar backscattering from slightly rough ocean surface contains contributions from various wave components. This is why radar backscattering can be used to infer characteristics of ocean surface waves. In addition to backscattering σ^0 , Doppler spectrum is also important in radar remote sensing. To first order, Doppler spectrum has only two frequency peaks corresponding to the frequency of capillary waves $\pm\omega_B$. At high-order, Doppler spectrum has broader band centered around the first-order capillary peaks.

For resonant scattering model, the basic scatterers are the short gravity-capillary waves. The resonant interactions between incident radar wave and ocean waves are mostly second order or even higher order contributions. In the case of low wind and low sea state, capillary waves are the dominant scatterers. Tilting and hydrodynamic processes by longer waves might slightly broaden the Doppler spectrum of radar return. However, as the wind and sea state increase, the sea surface becomes more and more rougher. High order contributions to the backscattering accordingly becomes prominent. In that context, the typical composite or two-scale scattering model should be applied.

2.1.3 Composite scattering

As stated above, both specular and Bragg scattering have strict application criteria, which is only valid for rough surface with either large or small horizontal dimension. But the natural ocean

2.1. Radar backscattering

surface usually contains a number of wave scales, even a continuous distribution of ocean waves. To predict the scattering solutions from such kind of surface, the ocean surface is assumed to consist of two types of independent scales: one is large and one is small, in comparison to the incident radar waves. Figure 2.3 gives an illustration of two-scale ocean surface.

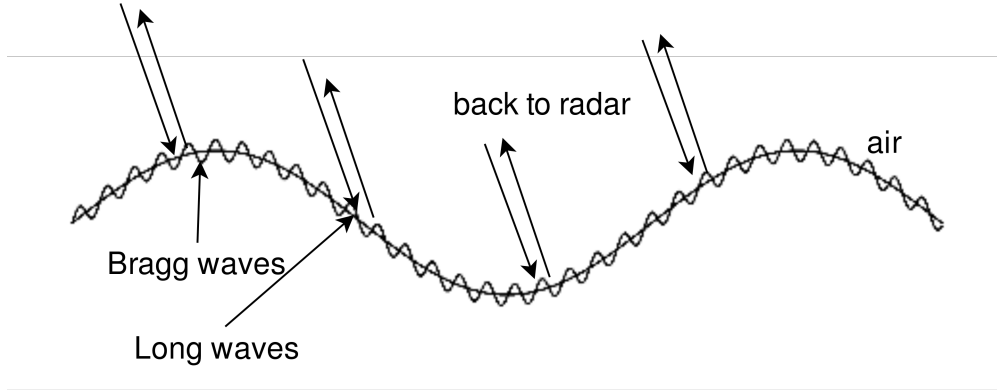


Figure 2.3: Illustration of composite backscattering from ocean surface.

This decomposition yields the composite or two-scale scattering model. It expresses the ocean surface as short capillary waves riding on the longer waves, which are generated by two independent processes. In the model, it is assumed that the ocean surface is composed of an infinite number of slightly rough facets. Each individual facet is composed of short capillary waves, tilted by the slope of undulating longer waves. This tilt results in the local incidence angle θ_i being different from the nominal incidence angle θ . The local incidence angle reads as $\theta_i = \cos^{-1}[\cos(\theta + \psi)\cos\delta]$ with ψ being the slope angle in the incidence plane and δ in the plane perpendicular to the incidence plane. The backscattering σ^0 of each slightly rough facet for horizontal polarization (HH) is (Wright, 1968; G. R. Valenzuela, 1978)

$$\sigma^0(\theta_i)_{HH} = 4\pi k_r^4 \cos^4 \theta_i \left| \left(\frac{\alpha \cos \delta}{\alpha_i} \right)^2 g_{HH}^{(1)}(\theta_i) + \left(\frac{\sin \delta}{\alpha_i} \right)^2 g_{VV}^{(1)}(\theta_i) \right|^2 \cdot W(2k_r \alpha, 2k_r \gamma \sin \delta) \quad (2.9)$$

and for vertical polarization (VV):

$$\sigma^0(\theta_i)_{VV} = 4\pi k_r^4 \cos^4 \theta_i \left| \left(\frac{\alpha \cos \delta}{\alpha_i} \right)^2 g_{VV}^{(1)}(\theta_i) + \left(\frac{\sin \delta}{\alpha_i} \right)^2 g_{HH}^{(1)}(\theta_i) \right|^2 \cdot W(2k_r \alpha, 2k_r \gamma \sin \delta) \quad (2.10)$$

and for the cross-polarization (VH, HV):

$$\sigma^0(\theta_i)_{VH(HV)} = 4\pi k_r^2 \cos^4 \theta_i \left(\frac{\alpha \sin \delta \cos \delta}{\alpha_i^2} \right)^2 \left| g_{VV}^{(1)}(\theta_i) - g_{HH}^{(1)}(\theta_i) \right|^2 \cdot W(2k_r \alpha, 2k_r \gamma \sin \delta) \quad (2.11)$$

where $\alpha_i = \sin\theta_i$ and $\alpha = \sin(\theta + \psi)$ and $\gamma = \cos(\theta + \psi)$. $g_{HH}^{(1)}(\theta)$ and $g_{VV}^{(1)}(\theta)$ is the first-order scattering coefficients given in Eq.(2.7) and Eq.(2.8), respectively.

Thus, the total backscattering σ^0 from an area of ocean surface is the weighted sum of each facet scattering over the distribution of ocean surface slopes, obtained by

$$\sigma^0(\theta)_{pq} = \int_{-\infty}^{+\infty} d(\tan\psi) \int_{-\infty}^{+\infty} d(\tan\delta) \sigma^0(\theta_i)_{pq} p(\tan\psi, \tan\delta) \quad (2.12)$$

where $p(\tan\psi, \tan\delta)$ is the joint probability density function of surface slopes of the longer ocean waves. Accordingly, one can find that VV backscattering is less sensitive to the tilt of surface slopes in comparison to HH polarization (K. Hasselmann et al., 1985b).

Though, composite scattering model is able to predict the increasing σ^0 and the decreasing polarization ratio $\sigma_{VV}^0/\sigma_{HH}^0$ as wind speed increases (G. R. Valenzuela, 1978). It is not sufficient to reproduce observed polarization ratio variation relative to wind direction (A. A. Mouche et al., 2005, 2006a). In the last decade, progresses in the domain of approximate scattering theory has led to better interpretation of the backscattering σ^0 from ocean surface. In particular, (A. A. Mouche et al., 2007a) proposed an improvement to local and resonant curvature approximation theory and reproduced the azimuth modulation of polarization ratio. Comparable results have been reported by (Kudryavtsev et al., 2003; Johnsen et al., 2008). Radar measurements for both HH and VV polarized backscattering show consistency with these model results.

Space-borne SARs usually operate at incidence angles higher than 18° . Therefore, composite scattering theory is generally applicable. But given the complexity of ocean surface, more effort is still required to better interpret SAR imaging of moving ocean surfaces.

2.2 SAR basics

In the context of remote sensing, a SAR sensor is mounted aboard a moving aircraft or satellite. This is to make best use of the Doppler shift in order to achieve the high spatial resolution, which is characteristic of a SAR sensor. A SAR usually points the radar beam approximately perpendicular to the sensor's flight direction. It transmits radar pulses and records the return signal from the Earth's surface. In this section, how a SAR works and the processing methods to form high-resolution images are briefly reviewed.

2.2.1 Resolution

Two-dimensional backscattering signal are required to form a SAR image. In the SAR coordinate, one dimension, range direction, is along the radar antenna pointing direction (denoted by x – axis). The range distance between SAR and the scatterer determines the traveling time of radar signal. The return signal is placed in the right position according to the time delay along this dimension. Pulse compression technique is widely used to achieve high resolution in the range axis. The range resolution is therefore proportional to the reciprocal of pulse bandwidth B as (Jackson & Apel, 2004):

$$R_r = \frac{c}{2B} \tag{2.13}$$

where c is the speed of light. B is related to the radar center frequency.

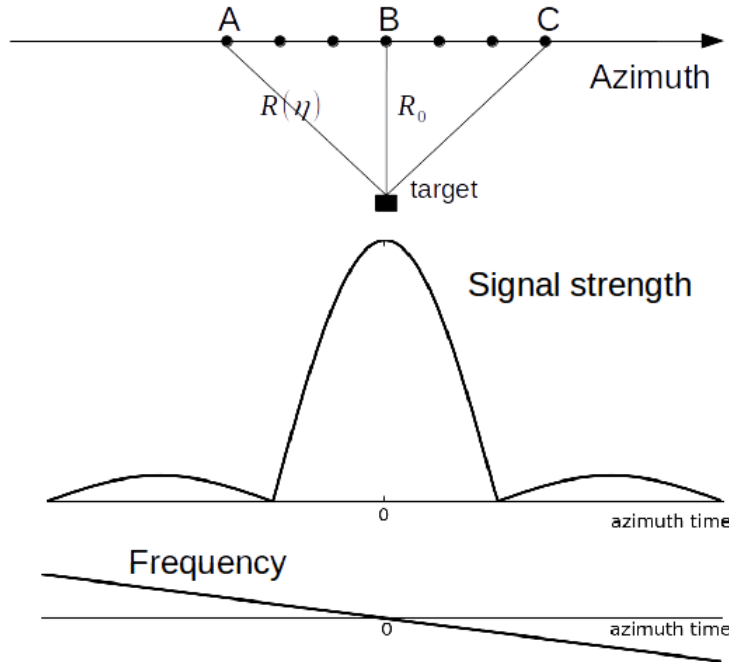


Figure 2.4: Illustration of antenna pattern impact on radar return from a point target.

While the other dimension, azimuth direction, is in the flight direction of a SAR (denoted by y – axis). As the sensor advances along its motion vector, SAR transmits subsequent pulses and records the return signal. The received signal is processed and placed in the right position along the y – axis. The SAR received signal has an additional phase shift in comparison to the transmitted pulses. This phase shift is given by the distance between SAR and the point target $R(\eta)$, written as:

$$\phi = -\frac{4\pi}{\lambda} R(\eta) \tag{2.14}$$

where η is time in azimuth. The approximation $R(\eta) = \sqrt{R_0^2 + V^2\eta^2} \approx R_0 + \frac{V^2\eta^2}{2R_0}$ is used for the special zero squint case. R_0 is the shortest slant range distance and V is the platform velocity. As a result, the instantaneous Doppler shift is (Madsen, 1989)

$$f_D = \frac{1}{2\pi} \frac{d\phi}{d\eta} = -\frac{2V^2}{\lambda R_0} \eta \quad (2.15)$$

from which, one can find that Doppler shift and azimuth time are one-to-one correspondent. As the sensor moves forwards, a point target is illuminated by a sequence of radar pulses. While strength of each pulse varies in terms of its position within the azimuth beam pattern. A schematic view of signal variation in azimuth is given in Figure 2.4. In general, only the received signal from main lobe of the azimuth pattern is considered in the SAR processing algorithm. Yet, contributions from the side lobe would produce azimuthal ambiguities on the processed image. The Doppler shift is determined by radial component of the relative velocity between the imaged target and the sensor. When the sensor is approaching the target, the Doppler shift is positive and becomes negative when the sensor is moving away. The Doppler shift is zero when the target is in the center of antenna beam since their relative velocity is zero.

The maximum Doppler shift occurs at the edge of the main lobe with $\eta = \frac{\lambda R_0}{VL}$, where L is the antenna length. The bandwidth of Doppler shift then writes $f_{Dmax} = 2V/L$. As such, resolution of the azimuth time η is (Madsen, 1989)

$$\delta\eta = \frac{1}{f_{Dmax}} = \frac{L}{2V} \quad (2.16)$$

and accordingly, the azimuth resolution is

$$R_a = V \cdot \delta\eta = \frac{L}{2} \quad (2.17)$$

As shown, SAR azimuth resolution is ideally half of the antenna length, independent of the radar altitude. By virtue of the high-resolution along two dimensions, SAR images are believed to have better performance in the discrimination of surface features.

2.2.2 SAR processing

Though SAR data are recorded in the two-dimensional time domain, they are often transformed into frequency domain to increase high processing efficiency. In processing the azimuth signal to achieve high resolution, one important parameter is the Doppler centroid, which is the Doppler shift when the imaged point target is in the antenna bore-sight direction. It is an essential input in the procedure of Range Cell Migration Correction (RCMC) and azimuth compression (Cumming & Wong, 2005). After range compression and RCMC, a matched filter is often used to focus the data in the azimuth direction in order to register the results to zero Doppler. The phase of stationary point targets can be canceled by the matched filter, leaving only a linear phase term that corresponds to the unique azimuth position of each target. And it is zero when the point target is right in the bore-sight direction.

It should be noted that different SAR processing algorithms have been specifically developed for different applications or imaging modes. Range Doppler algorithm (RDA) (Wu et al., 1982; SMITH, 1991) is widely used to achieve block processing efficiency by implementing in frequency domain along both range and azimuth direction. Another key feature of this algorithm is that it is able to accommodate range variation of the signal (Cumming & Wong, 2005). However, limitations of the RDA are also obvious. The computation load is high if an accurate RCMC operation is required and it is also difficult to deal with the secondary range compression (SRC) when the squint angle is non-zero (Cumming & Wong, 2005). The chirp scaling algorithm (CSA) is then developed to overcome these limitations (Raney et al., 1994). Neither RDA or CSA is as yet adequate to compensate the range time dependence for wide apertures or high squint cases. As such, a new algorithm, the *omega-K* algorithm (ωKA) corrects range dependence of range-azimuth coupling through a special implementation in the two-dimensional frequency domain (Cumming & Wong, 2005; Bamler, 1992). All these three algorithms are particularly applicable to the stripmap mode, in which each point target is illuminated by the complete antenna footprint. With the growing need of larger swath, another imaging mode is developed, the Scanning SAR (ScanSAR). With the operation of ScanSAR, a new processing algorithm is proposed, called SPECAN algorithm. SPECAN can yield SAR images with swath up to 500 km but at reduced resolution around 50 m.

At present, a SAR sensor can alternate among various imaging modes. For example, Sentinel-1 has four exclusive imaging modes with two of them belonging to the stripmap mode and the others being the ScanSAR mode (or TOPSAR). Accordingly, the SAR processing facility is equipped with

various algorithms to process all kinds of acquisitions.

2.3 SAR imaging principle for a point target

In this section, the SAR imaging principle is demonstrated by simulating the radar response over a point target. Several simulation algorithms have been proposed to construct the SAR images from the stationary surface as well as the moving ocean surface (W. Alpers, 1983; Franceschetti et al., 1998, 2002; Liu & He, 2016). Among which, the inverse omega-k algorithm presented in (Liu & He, 2016) is chosen to compute the SAR raw data considering its computational efficiency. Details are referred to in (Liu & He, 2016).

Here, the simulation size of a SAR image is set to be 256×256 in both range and azimuth direction. Altitude of the SAR sensor is 708 km and the velocity is 7.6 km/s. In addition, the pulse repetition frequency (PRF) is 1650 Hz, the range sampling rate is 54.6 MHz and incidence angle is 30° . As such, the resulting spatial spacing is 4.6 m in the azimuth and 5.4 m in the range. The simulation procedure is based on a point target positioned in the center of SAR image with various velocity properties. Three simulation procedures are carried out here with the simulated SAR images shown in Figure 2.5.

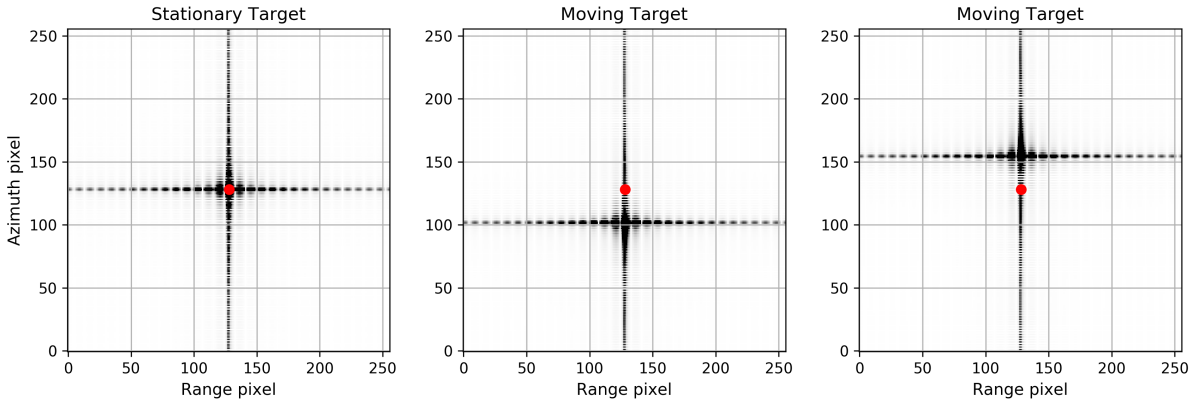


Figure 2.5: SAR image representation for (a) a stationary target; (b) a target moving towards the sensor; (c) a target moving away from the sensor. The red dot marks true point target position.

Figure 2.5(a) presents the simulated SAR raw data over a stationary point target positioned at (256, 256) marked by the red dot. Given its zero velocity, there is no additional Doppler shift in the backscattering signal. This stationary target is thus registered at the original position where it is. While a SAR flies over a moving target, its non-zero velocity shall induce an additional Doppler shift in addition to the SAR's velocity. This additional Doppler shift displaces the point target

forward or backward, depending on its relative moving direction to the SAR. In Figure 2.5(b), the point target is moving toward the sensor, yielding an additional positive Doppler shift. It is then registered at the forward position in comparison to its original position. On the contrary, when the point target is moving away from the sensor, the negative Doppler shift corresponds to a backward displacement as shown in Figure 2.5(c).

Quantitatively, the displacement is proportional to the slant range to velocity ratio and the relative velocity between the target and the sensor. In this simulation, velocity of the point target is set as 0.5 m/s and range to velocity ratio is 107.56 s^{-1} . As such, the expected displacement along the azimuth is 53.78 m. Considering the azimuth resolution of 4.606 m, the imaged target is supposed to be positioned approximately 11.7 pixels forward or backward. As shown in Figure 2.5, the point target is positioned by 12 pixels forward or backward, which roughly conforms to the expectation. The displacement of a moving point target on SAR image plane can be equally applied to the case of ocean surface.

In the context of SAR imaging over ocean surface, the moving ocean waves would induce additional Doppler shift. As a result, each target will be displaced in the image plane along the azimuth by a certain distance, which distorts the capability of SAR in resolving the full two-dimensional ocean wave field. This distortion yields the non-linearity of SAR imaging of ocean waves and is depicted in the following section.

2.4 SAR transformation of ocean waves

In this section, the forward mapping relation from ocean wave spectrum to SAR image spectrum is presented in detail. The backscattering properties from moving ocean surface is first described, followed by the SAR transformation relation of ocean waves.

2.4.1 Backscattering of moving ocean surface

Numerous efforts have been devoted to interpreting the SAR imaging relation of ocean waves (K. Alpers W.and Hasselmann, 1978; W. Alpers & Rufenach, 1979; W. R. Alpers et al., 1981; TUCKER, 1985). A consistent SAR ocean imaging theory has been summarized and presented in (K. Hasselmann et al., 1985b). Later, a series of studies have derived the nonlinear mapping from

ocean wave spectrum to SAR image spectrum (K. Hasselmann & Hasselmann, 1991b; Krogstad et al., 1994; Engen & Johnsen, 1995; Bao & Alpers, 1998). These established the basis to inverse ocean wave spectrum from SAR measured image spectrum.

Space-borne SAR is often operated at incidence angle ranging from 20° to 50° , right in the resonant scattering regime. As introduced above, resonant scattering occurs on the facets, satisfying the condition that their vertical displacements is on the order of a radar wavelength. In deriving the EM backscattering field, an assumption has to be made that complex reflectivity at different scattering facets on the ocean surface are distinct and uncorrelated. According to (K. Hasselmann et al., 1985b), this assumption applies for spatial scales that are larger than radar wavelength but smaller than a SAR resolution. Thus, it is reasonable to consider the reflectivity field within a SAR resolution as spatially white.

Based on the spatially white hypothesis, the covariance function of the complex reflectivity for moving ocean surface is:

$$\langle r(\vec{x}, t) \cdot r(\vec{x} + \vec{\zeta}, t + \tau) \rangle = \sigma^0(\vec{x}, t) R(\vec{x}, t; \tau) \delta(\vec{\zeta}) \quad (2.18)$$

where $\langle \rangle$ denotes ensemble average and $\sigma^0(\vec{x}, t)$ is the cross-section. R is the normalized correlation function and $\delta(\vec{\zeta})$ expresses the spatially white property of $r(\vec{x}, t)$. The time lag τ describes variation of the complex reflectivity during the SAR integration time T_i . While the variable t denotes the variation of R and σ^0 along the more slowly changing long waves with the typical periods of 10 s.

In the context of two-scale model, the ocean surface is decomposed of small-scale capillary waves and longer waves. As such, it is convenient to consider a scattering facet advected with the orbital velocity of underlying long waves. For a given facet, the reflectivity can be expressed as:

$$r(\vec{x}, t) = r_0(\vec{x}) \exp(j\omega_d t + ja_\omega t^2) \quad (2.19)$$

where

$$\omega_d = 2k_r v_r, \quad a_\omega = 2k_r a_r \quad (2.20)$$

v_r and a_r are the line-of-sight component of long-wave orbital velocity and its acceleration, respectively. k_r represents the wavenumber of incident radar wave. The linear term arises from the averaged orbital velocity of long waves and the quadratic terms comes from the variance of orbital velocity over the SAR integration time. The linear Doppler would induce displacements in azimuth

direction by the distance of

$$\Delta x = \frac{R_0}{V} v_r \quad (2.21)$$

and the quadratic term smears the SAR image by

$$\delta x^2 = \frac{1}{3} \left(\frac{R_0}{V} a_r \frac{T_i}{2} \right)^2 \quad (2.22)$$

The smearing effect is often regarded as the variation of azimuth displacements Δx during the SAR integration time.

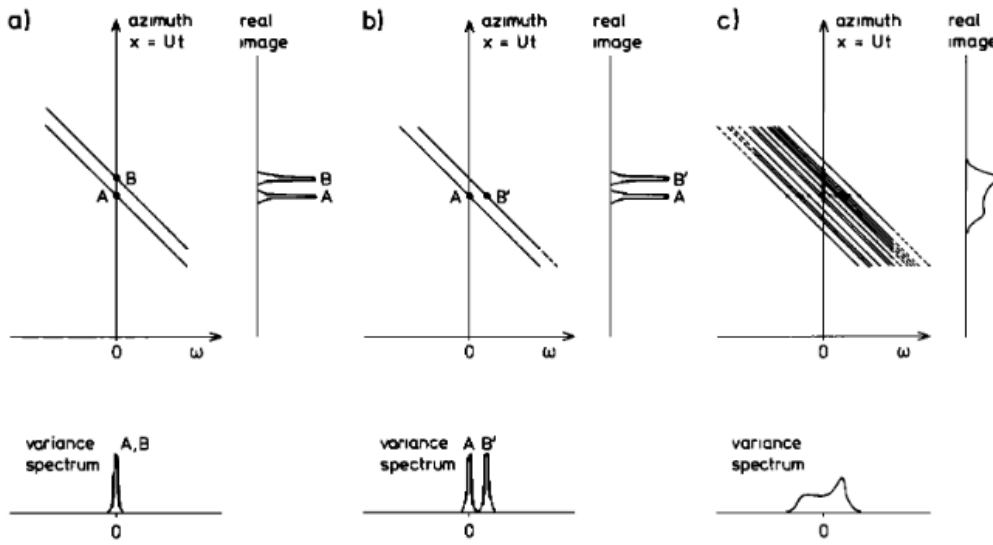


Figure 2.6: SAR imaging mechanism of surface scatterers. (a) Two stationary independent targets at different positions. (b) Mapping of a stationary scattering element A and another B at the same range position but with non-zero mean velocity. (c) Mapping of a scattering facet with a continuous distribution of distinct and independent scattering elements at different intrinsic frequency. After (K. Hasselmann et al., 1985b).

From the ocean surface reflectivity map $r(\vec{x}, t)$, its normalized variance spectrum can be written as:

$$\tilde{R}(\vec{x}, T_i; \omega) = \langle |\tilde{r}(\vec{x}, T_i; \omega)|^2 \rangle T_i / 2\pi \sigma^0 \quad (2.23)$$

where

$$\tilde{r}(\vec{x}, T_i; \omega) = T_i^{-1} \int_{-\infty}^{\infty} r(\vec{x}, t) H(t, \omega) \exp^{-j\omega t} dt \quad (2.24)$$

H represents a weighting function of antenna pattern, which varies with time and frequency. The quantity $\tilde{R}(\vec{x}, T_i; \omega)$ can be associated with the SAR image impulse response function (IRF) through

$$\langle I(x) \rangle = \int N^2 \sigma^0(x', T_i) \tilde{R}(\vec{x}', T_i; \omega) dx' \quad (2.25)$$

in which

$$N = T_i^{-1} \int H(Vt') H\left(\frac{R_0\omega}{2k_r V} - Vt'\right) dt' \quad (2.26)$$

for the case of single look processing. $\sigma^0(x', T_i)$ is the averaged cross-section for given facet over the SAR integration time.

Response of the SAR image IRF to various reflectivity variance spectra is then demonstrated. Figure 2.6 displays the structure of variance spectrum and SAR image IRF for three cases. The azimuth position determined through Doppler history is demonstrated in Figure 2.6(a). Two stationary targets (A and B), positioned separately along the azimuth are accordingly mapped on the image plane. While a moving target (B') at the same position as target A is displaced along the azimuth on the image plane. The motion of target B' induces an additional Doppler shift in the backscattering signal. This results in the mapping of B' into the displacement relative to its true position. The displacement distance is proportional to the radial component of target velocity, as shown in Figure 2.6(b). In reality, the ocean surface is composed of a continuous distribution of surface scatterers instead of the distinct ones. Figure 2.6 therefore shows mapping of a scattering facet with scatterers at the same position but moving at different velocities. These components are directly mapped into an identical distribution on the image plane. This represents the image smearing caused by the variability of the scatterers even within one scattering facet.

The interpretation of SAR imaging principles of ocean waves has been the subject of many studies, both from theoretical and experimental point of view (K. Alpers W.and Hasselmann, 1978; K. Hasselmann et al., 1985b; K. Hasselmann & Hasselmann, 1991b; Engen & Johnsen, 1995). As introduced, SAR backscattering can be described by the two-scale scattering model. In specifics, the small-scale roughness is responsible for the mean scattering field. And these short Bragg waves are in turn modulated by the undulating longer waves. The assumption that the capillary waves and longer waves are independent generally holds. Two basic modulation processes are effectively to form a SAR image of ocean waves: real aperture radar and velocity bunching modulation.

2.4.2 Real aperture radar modulation

Linear tilt and hydrodynamic modulation constitute the Real Aperture Radar (RAR) modulation. In terms of linear wave theory, the surface elevation is expressed as:

$$\eta(\vec{x}, t) = \sum_{\vec{k}} \eta_{\vec{k}} \exp[j(\vec{k} \cdot \vec{r} - \omega t)] + c.c. \quad (2.27)$$

where *c.c.* stands for the complex conjugate. The variation of backscattering can be accordingly written as:

$$\sigma(\vec{x}, t) = \bar{\sigma} \left\{ 1 + \sum_{\vec{k}} m_{\vec{k}} \exp[j(\vec{k} \cdot \vec{r} - \omega t)] + c.c. \right\} \quad (2.28)$$

where $\bar{\sigma}$ is the averaged backscattering over SAR imaged area, ω is the wave angular frequency and $\omega = \sqrt{gk}$ based on the ocean wave dispersion relation in deep water condition. Further, the backscattering modulation is linearly related to wave amplitude through:

$$m_{\vec{x}} = T_{\vec{x}}^R \eta_{\vec{x}} \quad (2.29)$$

where $T_{\vec{x}}^R$ is the RAR modulation transfer function (MTF), consisting of tilt and hydrodynamic modulation:

$$T_{\vec{x}}^R = T_{\vec{x}}^t + T_{\vec{x}}^h \quad (2.30)$$

The magnitude of tilt modulation has been derived theoretically by (W. R. Alpers et al., 1981), which is a constant for given incidence angle. Then, a straightforward estimate methodology from SAR images is presented in (Jacobsen & Hgda, 1994). However, it is inadequate to utilize a RAR modulation without considering its dependence on local wind speed and direction, therefore Kerboal (Kerbaol, 1997) proposed to employ the geophysical model function (GMF) such as CMOD family to calculate the RAR MTF for given radar configuration and surface winds. Here, the tilt modulation of theoretical estimate and GMF estimate are compared in Figure 2.7.

The variation of tilt MTF relative to incidence angle is shown in Figure 2.7(a) at wind speed of 7 m/s and wind direction of 45° for both HH and VV polarization. The theoretical values of tilt MTF are calculated after (W. R. Alpers et al., 1981). Tilt MTF is generally larger in HH than in VV polarization (W. R. Alpers et al., 1981; Engen et al., 2000). In addition, the theoretical tilt MTF is a constant at given incidence angle and independent of wind speed and direction given its

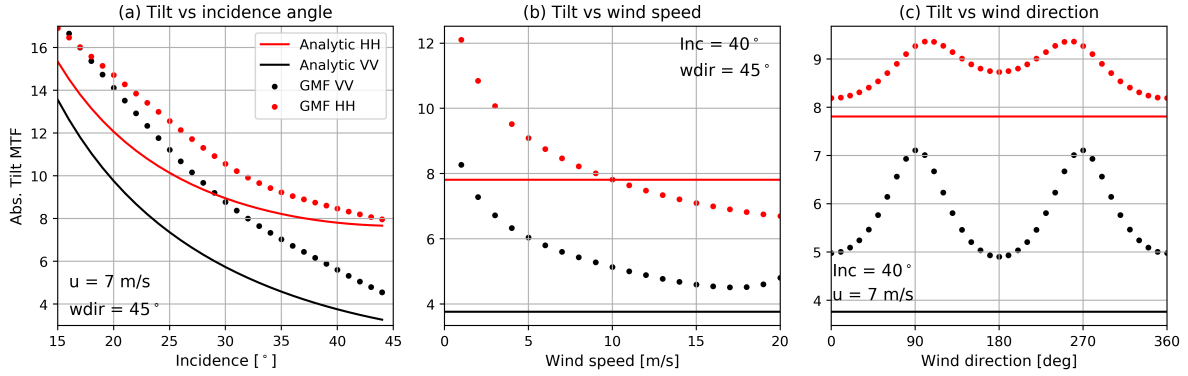


Figure 2.7: Variation of tilt MTF relative to (a) incidence angle at wind speed of 7 m/s and wind direction of 45°; (b) wind speed at incidence angle of 40° and wind direction of 45°; (c) wind direction at incidence angle of 40° and wind speed of 7 m/s. 0° wind direction denotes upwind (wind blowing towards the radar looking direction). Theoretical values are derived using formula in (W. R. Alpers et al., 1981). The GMF-based tilt MTF is calculated using CSARMOD in (A. Mouche & Chapron, 2015a).

sole dependence on SAR incidence angle, as shown in Figure 2.7(b) (c). For incidence angle of 40°, the GMF-based tilt MTF decreases with increasing incidence angle and reaches the maximum at crosswind direction. The theoretical tilt MTF is mostly smaller than the GMF-based estimates. Because only few case studies have been carried out to infer RAR MTF from SAR measurements, it is still inadequate to determine their respective accuracy. Nevertheless, the RAR MTF derived from GMF can account for wind speed and direction variation, carrying more information than the analytic formula.

Further, hydrodynamic component in the RAR modulation is derived considering the interaction between short and long swell. The detailed form is deduced in (W. R. Alpers et al., 1981) for a simple Phillips k^{-4} wave spectrum, written as:

$$T_x^h = -4.5k\omega \frac{\omega - i\mu}{\omega^2 + \mu^2} \quad (2.31)$$

where μ is the relaxation rate to describe the response of short waves to long waves modulation. To first order, both tilt and hydrodynamic modulation are linear function with respect to the sea surface slope. The RAR image can be interpreted as instantaneous representation of the sea surface geometry. A SAR image is then formed by the motion effects of long waves.

2.4.3 Velocity bunching

A SAR finds its azimuthal position by recording the phase history of backscattering during the integration time (W. R. Alpers & Bruening, 1986). Since SAR processing is to position a stationary target at zero Doppler, the orbital velocity of long waves would induce an additional Doppler shift relative to the stationary scatterers. In consequence, these moving scatterers would be displaced by a certain distance forward or backward along azimuth of SAR image plane in terms of their moving direction.

The displacement distance is proportional to wave orbital velocity. From linear wave theory, the orbital velocity is

$$v_r = \sum_{\vec{k}} T_{\vec{x}}^v \eta_{\vec{x}} \exp(j\vec{k} \cdot \vec{r}) + c.c. \quad (2.32)$$

where the range velocity transfer function is expressed by

$$T_{\vec{x}}^v = -\omega (\sin\theta \cos\phi + j \cos\theta) \quad (2.33)$$

where ϕ is wave propagation direction relative to SAR line-of-sight and θ is SAR incidence angle. Note that this orbital velocity is the average over the SAR integration time during which a point target stays within the SAR antenna pattern. For simplicity, the instantaneous orbital velocity in the center of SAR integration time is taken since the SAR integration time (~ 0.6 s) is relatively short compared to long wave period (> 6 s).

2.4.4 The non-linear SAR transformation

It is a common assumption that the RAR formulation is independent of the motion effects. Considering a multiplicative noise model of SAR return, the RAR intensity image can be expressed as:

$$I(\vec{x}', t) = I^R(\vec{x}', t) n(\vec{x}', t) \quad (2.34)$$

where $n(x, t)$ represents the multiplicative noise superimposed on the backscattering intensity. In terms of the motion effects, each pixel on RAR image is accordingly mapped to form the SAR

image. This process can be written as,

$$I^S(\vec{x}, t) = \int I(\vec{x}', t) h[\vec{x} - \vec{x}' - \Delta(\vec{x}', t)] d\vec{x}' \quad (2.35)$$

h is referred to as the SAR mapping function and describes the imaging mechanism that displaces a scattering facet on the RAR image plane into a different position on the SAR image plane. An analytic approximation to the mapping function h is necessary to derive a closed-form expression of SAR image (Krogstad et al., 1994),

$$h(\vec{x}) = \frac{1}{\sigma_x \sigma_y} e^{-\pi^2 x^2 / (2\sigma_x^2)} e^{-\pi^2 y^2 / (2\sigma_y^2)} \quad (2.36)$$

where the variables $\Delta(\vec{x}', t)$, σ_x , σ_y denote the azimuthal displacements and smearing spread in the azimuth (x) and range (y) direction, respectively. For simplicity, further assumption that the range smearing can be neglected and $\sigma_y = 0$ is therefore employed. This range shift is then proportional to the sea surface elevation and orbital velocity (Krogstad et al., 1994).

The Fourier components I_k^S on a SAR image can be calculated by applying a Fourier Transform to the basic mapping relation in Eq.(2.35),

$$I_k^S = \int d\vec{x} e^{-j\vec{k} \cdot \vec{x}} I^S(\vec{x}, t) = \int d^2x I^R(\vec{x}', t) e^{-jk_x(x' + \Delta_x(\vec{x}', t))} e^{-jk_y(y' + \Delta_y(\vec{x}', t))} \quad (2.37)$$

According to the derivations in (Krogstad et al., 1994; Engen & Johnsen, 1995), the SAR image cross-spectrum may be written as,

$$P(\vec{k}, t) = \frac{1}{(2\pi)^2} \int d\vec{x} e^{-j\vec{k} \cdot \vec{x}} G(\vec{x}, \vec{k}) - \delta(\vec{k}) \quad (2.38)$$

$$G(\vec{x}, \vec{k}, t) = \langle I \rangle^{-2} \left\langle I^R(\vec{x}, t) I^R(\vec{0}, 0) e^{-j\vec{k}[\Delta(\vec{x}, t) - \Delta(\vec{0}, 0)]} n(\vec{x}, t) n(\vec{0}, 0) \right\rangle \quad (2.39)$$

Given the assumption that the intensity image I^R and the white noise n are independent, one can obtain:

$$\left\langle n(\vec{x}, t) n(\vec{0}, 0) \right\rangle = \langle n \rangle^2 + \sigma_n^2 \delta(\vec{x}) \delta(t) \quad (2.40)$$

where σ_n is the variance of the speckle noise. As such, the G -function can be formulated as:

$$G(\vec{x}, \vec{k}, t) = \langle I \rangle^{-2} \left\langle I^R(\vec{x}, t) I^R(\vec{0}, 0) e^{-j\vec{k}[\Delta(\vec{x}, t) - \Delta(\vec{0}, 0)]} \right\rangle \times \left(\langle n \rangle^2 + \sigma_n^2 \delta(\vec{x}) \delta(t) \right) \quad (2.41)$$

By exploiting the properties of speckle noise, SAR image cross-spectrum can be grouped as two types: $t = 0$ and $t \neq 0$. In the case of $t = 0$, the standard SAR image spectrum is obtained by

$$P(\vec{k}, 0) = \frac{\langle I^2 \rangle}{\langle I \rangle^2} + \sigma_n^2 P_0(\vec{k}, 0) \quad (2.42)$$

where the un-speckled SAR image spectrum is

$$P_0(\vec{k}, 0) = \langle I \rangle^{-2} \int d\vec{x} e^{-j\vec{k}\cdot\vec{x}} \langle I^R(\vec{x}, 0) I^R(\vec{0}, 0) e^{-j\vec{k}[\Delta(\vec{x}, 0) - \Delta(\vec{0}, 0)]} \rangle \quad (2.43)$$

While in the case of $t \neq 0$, the SAR image cross-spectrum is

$$P(\vec{k}, t) = P_0(\vec{k}, t) \quad (2.44)$$

Assuming that the smearing term σ_x and σ_y in Eq.(2.36) is small in comparison to the ocean wavelength of interest, and range bunching effect is negligible, the G -function can be written as

$$G(\vec{x}, \vec{k}, t) = e^{k_x^2 [\rho_{vv}(\vec{x}, t) - \rho_{vv}(\vec{0}, 0)]} \times [1 + \rho_{II}(\vec{x}, t)] \quad (2.45)$$

where the cross terms between RAR modulation and velocity bunching are neglected as well as the high-order terms. The correlation functions are associated with the ocean wave spectrum $S(\vec{k})$ through

$$\rho_{aa}(\vec{x}, t) = \frac{1}{(2\pi)^2} \int d\vec{k} e^{j\vec{k}\cdot\vec{x}} \left\{ N_a(\vec{k}, t) S(\vec{k}) + N_a^*(-\vec{k}, t) S^*(-\vec{k}) \right\} \quad (2.46)$$

where the subscript a represents I for RAR modulation in Eq.(2.30) or v for velocity bunching MTF in Eq.(2.33) and

$$N_{aa}(\vec{k}, t) = \frac{1}{2} |T^{aa}(\vec{k})|^2 e^{-j\omega t} \quad (2.47)$$

Another advantage of SAR image cross-spectrum is the introduction of phase shift through ωt during the time interval t . This feature is widely used to resolve the propagation ambiguity of ocean swell in the wave spectrum inversion.

Chapter 3

Status and challenges in SAR winds

Contents

2.1	Radar backscattering	12
2.1.1	Specular scattering	13
2.1.2	Resonant scattering	15
2.1.3	Composite scattering	16
2.2	SAR basics	18
2.2.1	Resolution	19
2.2.2	SAR processing	21
2.3	SAR imaging principle for a point target	22
2.4	SAR transformation of ocean waves	23
2.4.1	Backscattering of moving ocean surface	23
2.4.2	Real aperture radar modulation	27
2.4.3	Velocity bunching	29
2.4.4	The non-linear SAR transformation	29

High-resolution SAR imageries can complement scatterometer observations, providing local variability of sea surface wind field. The wind vector is also a key parameter for the ocean wave spectral inversion. Accurate wind retrieval from SAR images is therefore of great significance. In this chapter, the SAR wind retrieval algorithm is reviewed. As a first step, radiometric calibration of normalized radar cross-section (NRCS) is evaluated prior to inferring the geophysical quantity. The challenges of the present wind retrieval algorithms are discussed and inspire the following studies outlined in this thesis. This chapter is based on the papers '*Calibration of the normalized radar cross-section for Sentinel-1 wave mode*' and '*Impact of Sea State on Wind Retrieval from Sentinel-1 Wave Mode data*'.

3.1 Method of SAR wind retrieval

In this section, the methods widely used to derive wind speed from SAR measurements are described. The importance or description of each component in the retrieval algorithm is then accordingly given.

3.1.1 Algorithm of SAR wind retrieval

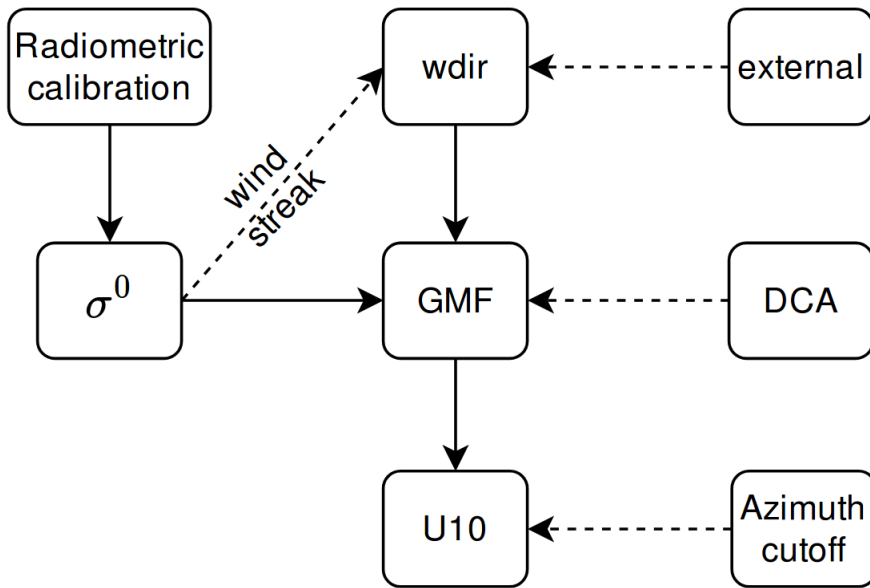


Figure 3.1: Flowchart of the wind retrieval from a SAR image. 'wdir' is wind direction and 'DCA' is Doppler centroid anomaly. 'U10' is the neutral wind speed at 10 m height. Solid lines represent determined processes and dashed lines are alternatives.

Since the launch of Seasat-A in 1978, numerous wind retrieval algorithms from SAR measurements have been proposed and developed. As outlined in Chapter 1, many subsequent SAR missions have been operational in orbit. In spite of varying radar configurations (incidence angle, polarization, wavelength), the principle of wind retrieval remains the same. In general, an empirical function relates the SAR observable to both radar configurations and environmental conditions and a so-called Geophysical Model Function (GMF) is built. This function is then used to infer winds from a given measurement.

Figure 3.1 presents the basic flowchart of wind retrieval from SAR data. NRCS is the most straightforward SAR measurement, thus, most of the retrieval algorithms are developed based on the NRCS. The co-polarized NRCS where a SAR transmits and receives the signal in the same po-

larization is still widely used. Though extraction of wind direction with the help of wind streaks has been demonstrated feasible, the signal of wind streaks is not always visible on the SAR image. As a result, the essential wind direction in the retrieval algorithm usually comes from the external input, such as weather model output or measurements from other in-situ and remote instruments (Stopa & Mouche, 2017a).

In addition to the NRCS, the Doppler Centroid Anomaly (DCA) estimated from the SAR backscattering signal has also been found to exhibit a unique relationship with surface wind (Chapron et al., 2005). DCA can be interpreted as the averaged orbital velocity of line-of-sight ocean waves weighted by the local radar return. Over the regions with strong surface current, the estimated DCA is composed of actions from both surface wind and current. This forms the basis to infer features of oceanic current from single-antenna SAR (Collard et al., 2009a; Rouault et al., 2010). Yet, by consequence, the retrieved wind speed that combines NRCS and DCA can be greatly biased. Nevertheless, over the regions without strong surface current, the introduction of DCA in the wind retrieval algorithm does improve the accuracy and lessen its reliance on *a priori* wind direction (A. A. Mouche et al., 2012).

As shown in Figure 3.1, azimuth cutoff, a parameter derived from the SAR image spectrum can also be used to refine the wind speed retrieval. In fact, there are growing number of studies that have addressed this subject (Grieco et al., 2016; Corcione et al., 2018). It is found that azimuth cutoff also depends on the local sea state in addition to the winds. As such, many studies have been carried out to extract wave information based on the azimuth cutoff (Shao et al., 2016a; Stopa et al., 2015a).

Recently, the potential of cross-polarized (VH or HV) SAR images in monitoring high winds conditions has been well proven (B. Zhang et al., 2011a). Several new GMF relating cross-polarized NRCS to winds have been proposed in the literature (Hwang et al., 2015; A. A. Mouche et al., 2017). Given the insensitivity of cross-polarized NRCS to changing wind direction, the combination of both co- and cross-polarized backscattering enables the derivation of wind speed and direction independently from SAR observations.

3.1.2 GMF of CMOD5.N

The empirical GMF, CMOD5.N, was developed for global applications for use of the C-band scatterometer on board ERS-2 satellite and the Advanced Scatterometer (ASCAT) (Hersbach, 2008). CMOD5.N performs better than its predecessor CMOD5 with higher accuracy in the wind retrieval (Carvajal et al., 2014; Jagdish et al., 2018). It is routinely used for operational ocean surface wind produced by the OSI-SAF (Ocean and Sea Ice - Satellite Application Facilities) (Ocean and Sea Ice SAF, 2016). CMOD5.N is valid for incidence angles ranging from 18° to 60°, covering the two incidence angles of WV. CMOD5.N relates the NRCS to the incidence angle, wind speed and wind direction (relative to radar line-of-sight), and polarization under neutral atmospheric stability with the following equation (Hersbach, 2008):

$$\sigma^0 = B_0[1 + B_1\cos(\phi) + B_2\cos(2\phi)] \quad (3.1)$$

where ϕ is the wind direction relative to the antenna look angle. B_0 is the dominant term determining scale of NRCS for given wind speed. B_1 incorporates the up-downwind asymmetry of NRCS, while B_2 expresses the up-crosswind asymmetry of NRCS. The three terms are all functions of incidence angle, wind speed, and wind direction. Coefficients for each term are given in (Hersbach, 2008). It is used throughout the rest of the manuscript to predict NRCS for given S-1A incidence angle and collocated ECMWF (European Centre for Medium-Range Weather Forecasts) winds on a case-to-case basis.

3.1.3 Radiometric calibration of S-1 NRCS

Over the ocean, the normalized radar cross section (NRCS or σ^0 used inter-changeably through this work) responds primarily to the ocean surface wind vector. Proper calibration of WV NRCS is necessary in order to accurately estimate geophysical quantities such as oceanic wind speeds (Horstmann et al., 2003; Lehner et al., 2000) and sea state parameters, such as significant wave height (Schulz-Stellenfleth & Lehner, 2002; Stopa et al., 2017; H. Wang et al., 2017) or ocean swell spectrum (Chapron et al., 2001). In general, the radiometric calibration of NRCS is performed by comparing the backscatter from ground targets with known NRCS that are concurrently measured by transponders (Shimada et al., 2009; Sharma et al., 2017) or routine acquisitions over the reference distributed targets such as Amazon rain-forest (Crapolicchio et al., 2012; Gupta et al., 2017).

At C-band the NRCS is a function of radar polarization, incidence angle as well as environmental conditions such as the wind field (A. Mouche & Chapron, 2015a). For a given polarization and wind speed, the NRCS decreases with increasing incidence angle. As such, the signal-to-noise ratio decreases with incidence angles, leading to possible contamination of thermal noise at high incidence angle and under low wind conditions. A proper noise-correction is therefore essential to obtain an accurate NRCS. The radiometric calibration of S-1A, taking noise-correction into account is expressed as (European Space Agency, 2017) :

$$\sigma^0 = \frac{DN^2 - \eta_i}{A_i^2} \quad (3.2)$$

where $DN = \sqrt{(I^2 + Q^2)}$ is the digital number of ESA Level-1 Single Look Complex (SLC) product. η is the de-noise Look-Up-Table (LUT) provided in annotation file and A_i is the calibration LUT for σ^0 as function of azimuth and range pixel, also annotated in the Level-1 products. Multiple calibration procedures are incorporated in A_i , containing area normalization factor, calibration constant and geophysical calibration. Among which, the geophysical calibration constant, the NRCS difference between SAR measurements and simulated NRCS using CMOD-IFR2 from collocated ECMWF winds in the range of [4 m/s, 10 m/s], is provided by the Sentinel-1 Mission Performance Center for WV1 and WV2, respectively (Collecte Localisation Satellites (CLS), 2017).

Here, we compute a single σ^0 per imagette at a resolution of 20 km by 20 km. The noise equivalent sigma-nought (NESZ) is further removed from NRCS in Eq. (3.2). The maximum of NRCS histogram for collocated ECMWF wind speed lower than 1 ms^{-1} is taken as the NESZ. The NESZ-corrected NRCS is used throughout rest of this manuscript unless particularly stated. Images with negative NRCS are not included in the analysis because the backscattered signal is lower than than thermal noise.

3.2 Assessment and re-calibration of S-1 NRCS

Prior to any geophysical applications over the ocean, it is essential to assess the accuracy of its radiometric calibration. In this section, the accuracy of S-1 calibrated NRCS is firstly evaluated. Given the results, two different and complementary methods for re-calibration are demonstrated and compared. The first method relies on the use of the Amazon rain-forest through the Gamma-nought parameter γ^0 (Crapolicchio & Lecomte, 1999; PCS Team, 1999; Gupta et al., 2017) whereas

the second is an evaluation over open ocean (Verspeek et al., 2013). In the end, ocean calibration is chosen to re-calibrate the long-time series of S-1 NRCS.

3.2.1 Collocated Sentinel-1A and ECMWF wind speed

The lack of sufficient acquisitions over ground transponders or the limited acquisitions over the rain-forest makes routine calibration difficult. Therefore, an alternative method can be used to quantitatively assess NRCS calibration through comparisons with the an empirical Geophysical Model Function (GMF) combined with collocated 10 meter height wind (U10) from the European Centre for Medium-range Weather Forecasts (ECMWF) forecast. Here the collocated data set is presented.

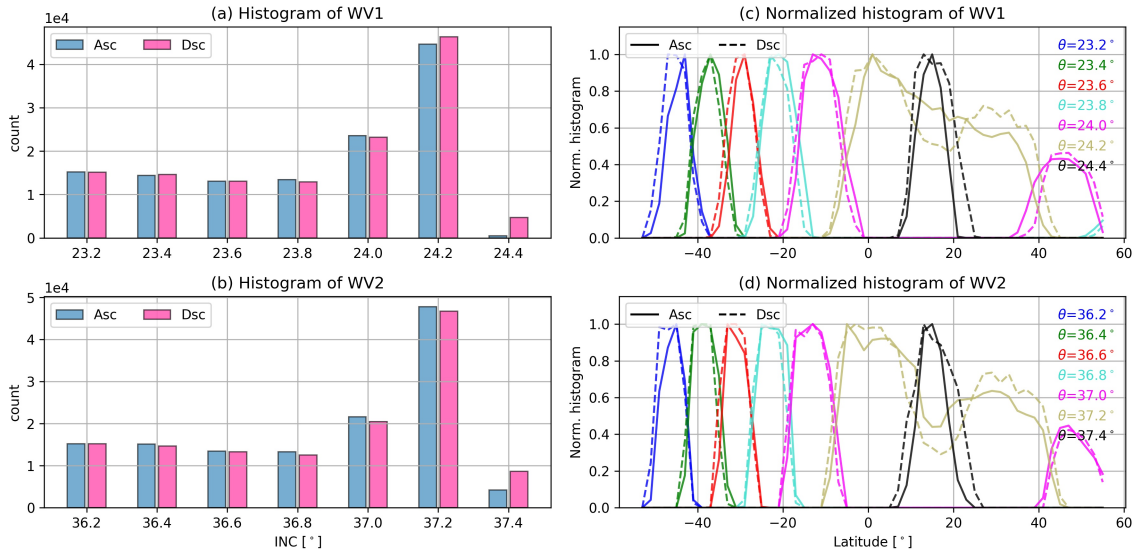


Figure 3.2: Histogram of incidence angles for (a) WV1 and (b) WV2, receptively. Bin size of incidence angle is 0.22° . (c) Normalized histogram of latitude at given incidence angle for WV1. Bin size of latitude is 2° . Solid lines are for Ascending pass and dashed lines are for Descending pass. Colors represent different incidence angles. Products acquired at latitude higher than 55° have been filtered out to avoid ice contamination.

S-1 WV alternates between WV1 (centered at 23.8°) and WV2 (at 36.8°) with a new 'leap frog' approach (European Space Agency, 2018). Each vignette is acquired every 100 km along the flight direction (Torres et al., 2012). S-1 WV can only be operated in single polarization (either VV or HH) for a given acquisition. The WV at VV polarization is the default mode over global ocean. Here we use 27,000 images acquired between June 2016 and June 2017 by S-1A WV1 and WV2 at VV polarization, respectively. This period was chosen to avoid processor updates, such as one

that occurred in May 2016, and to maintain the consistency of instrument calibration. We also limit the data to latitudes less than 55° to avoid any possible sea-ice contamination. Each WV imagette is collocated with ECMWF forecast winds from operational forecast model. The wind data set is considered 'nowcast' and is a compiled data set of the ECWMF forecast initialized every 6 hours. The ECWMF winds are available every 3 hours on a spatial grid of 0.25° . The collocation takes the nearest point both in space and in time, resulting in maximum spatial distance of 12.5 km and maximum temporal difference being 1h30.

A $\pm 0.7^\circ$ incidence angle variation is observed for S-1 WV1 and WV2 along the orbit. Figure 3.2 (a) and (b) present histogram of collocated data set binned by incidence angle for WV1 and WV2, respectively with bin size of 0.2° . For each incidence bin, the numbers of products are regular (around 15,000) at incidence smaller than 24.0° (37.0°) for WV1 (WV2). Note that 24.2° (37.2°) for WV1 (WV2) has the maximum of acquisitions around 41,000. Only about 5,000 imagettes are acquired at incidence of 24.4° (37.4°) for WV1 (WV2). Ascending and descending passes have similar data counts (except 24.4° (37.4°) for WV1 (WV2)).

Incidence angles are not evenly distributed across the globe. This is shown by the normalized histograms in Figure 3.2 (c) and (d), where latitude bin size is 2° . There is an incidence angle dependence on latitude for both ascending and descending passes. Both ascending and descending passes have similar spread over latitude per incidence. Incidence angle generally increases from the south to the north. In particular, the highest incidence angles plotted as black lines (24.4° for WV1 and 37.4° for WV2) are distributed between the Equator (0°) and 20° N. Incidence angles of 24.2° for WV1 and 37.2° for WV2 have the largest spread over 10° S to 40° N. Since wind speed and direction vary greatly with latitude (Atlas et al., 1996), WV1 and WV2 data are analyzed separately throughout this work. Ascending and descending passes are merged and analyzed as a single dataset since we did not find any differences related to the orbit configuration.

3.2.2 Assessment of the NRCS

S-1A WV NRCS is assessed for given wind speed and incidence angle by comparing with the predicted value from CMOD5.N. The deviations are then quantified by NRCS residual between SAR measurements and CMOD5.N prediction.

First we evaluate the S-1A NRCS relative to wind direction for given wind speed and incidence

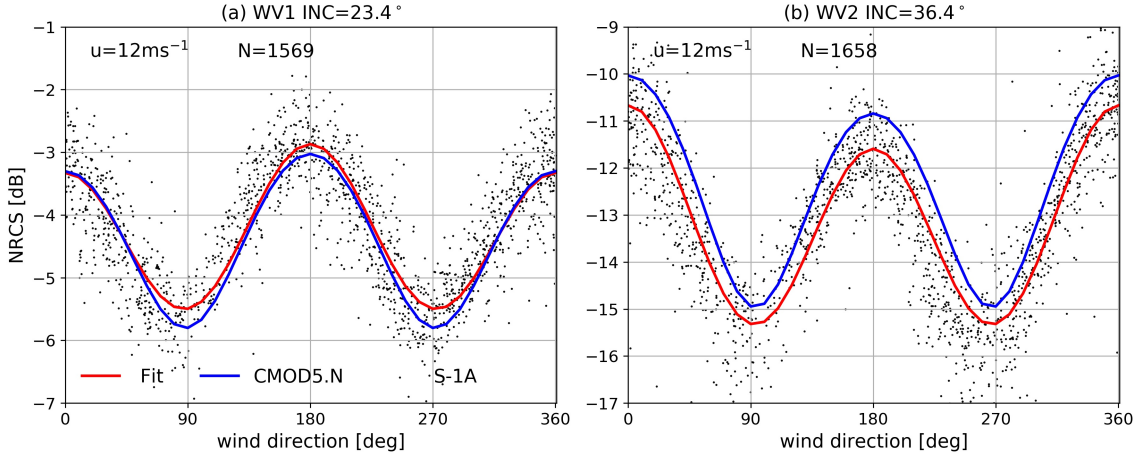


Figure 3.3: NRCS at 12 ms^{-1} relative to wind direction for (a) WV1 at incidence of 23.4° ; (b) WV2 at incidence of 36.4° . Black dots are S-1A measurements and red lines are fit to S-1A observed NRCS in form of Eq.(3.1). Blue line is the predicted CMOD5.N for given incidence angle and wind speed. For wind direction, 0° indicates upwind and 180° is downwind.

angle. U_{10} of 12 ms^{-1} is used to illustrate the comparison of S-1A NRCS with the CMOD5.N prediction. We choose $U_{10}=12 \text{ ms}^{-1}$ because it is a compromise between sufficiently high signal-to-noise ratio and adequate collocation pairs. In addition, working with incidence angles of 23.4° and 36.4° ensures a narrow spread over latitudes as well as relatively uniform wind direction across $[0^\circ, 360^\circ]$. NRCS with respect to wind direction is shown on Figure 3.3 (a) for WV1 and on Figure 3.3 (b) for WV2. Within each direction bin of 10° , 50 data points are randomly selected if there are more than 50 samples. Otherwise, all data points are used for that bin. This equalization method is used to remove biases induced by nonuniform distribution of wind direction (Stopa & Mouche, 2017b). This results in 1569 and 1658 points (marked by 'N') for WV1 and WV2, respectively for $U_{10}=12 \text{ ms}^{-1}$. The random selection taken in the equalization procedure has been repeated for several times and we found the nearly identical results.

As shown in Figure 3.3 (a), the fit to S-1A measurements are overall in good agreement with CMOD5.N curve for WV1. In particular, S-1A NRCS are slightly greater than CMOD5.N estimate approximately by about 0.3 dB at crosswind (wind direction of 90°). Similar trend is found for other incidence angles of WV1. By contrast, as shown in Figure 3.3 (b), S-1A NRCS is constantly smaller than the CMOD5.N estimate across all wind directions for WV2. The NRCS residual ($\sigma_{SAR}^0 - \sigma_{CMOD5.N}^0$) at crosswind is -0.4041 dB and -0.6545 dB at upwind. Similar trend has been found for wind speeds higher than 7 ms^{-1} for other incidence angles of WV2. This suggests that the WV has not been properly calibrated for WV2 and wind speeds would be consistently underestimated.

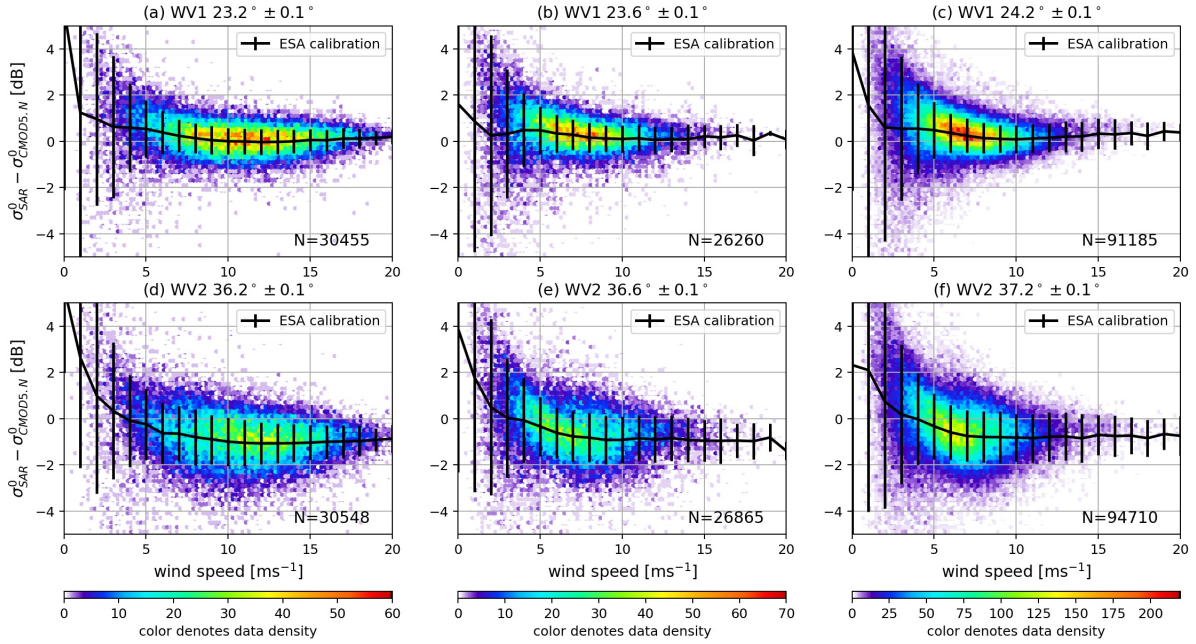


Figure 3.4: NRCS difference ($\sigma_{SAR}^0 - \sigma_{CMOD5.N}^0$) as function of wind speed for given incidence angle for (top) WV1; (bottom) WV2. Solid line is mean NRCS difference with bin size of 1 ms⁻¹. The error bar represents 1 standard deviation of NRCS difference within each bin. Colors denote count of data points.

CMOD5.N is now systematically used to calculate the expected NRCS for each S-1A imagette based on collocated ECMWF winds and given incidence angle. The NRCS residuals ($\sigma_{SAR}^0 - \sigma_{CMOD5.N}^0$) relative to U10 at three incidence angles for WV1 (WV2) are presented in the upper (lower) panels of Figure 3.4. The main similarities between WV1 and WV2 are the slightly decreasing NRCS residual with increasing wind speed up to 7 ms⁻¹ before remaining steady at higher winds. The NRCS residuals for WV1 and WV2 are different when $U10 > 7$ ms⁻¹. Overall the average NRCS residual is approximately 0 dB for all WV1 and -0.8 dB for WV2 when considering all incidence angles. In particular, for $U10 = 12$ ms⁻¹, there are NRCS residuals of 0.05 dB for WV1 (incidence angle of 23.6°) and -0.88 dB for WV2 (incidence of 36.6°) (see Figure 3.4(b),(e)). In addition, the standard deviation exhibits similar variation trend with the mean residual. The greater variability at low wind speed (<3 ms⁻¹) is mostly due to limited number of observations.

The negative NRCS residuals are unexpected for WV2. There are several possible sources of error to verify, including accuracy of radiometric calibration for WV2, bias of NESZ correction as well as errors in collocated ECMWF winds. The bias of NESZ could be ruled out because higher wind speed corresponds to higher signal-to-noise ratio and consequently leads to negligible noise contribution. Indeed the contribution of thermal noise to NRCS is expected to decrease with increasing wind speed, making it impossible to reproduce the increasing deviation. As for biases

induced by the ECMWF winds, WV1 and WV2 used the same data source, so that any errors in the ECMWF winds should be equally translated into NRCS residuals for both WV1 and WV2. However, we do not see this behavior. Therefore the calibration is likely the best candidate for causing the NRCS discrepancies. In the following, we apply two different methods to re-calibrate S-1A WV NRCS and compare their respective performances.

3.2.3 Re-calibration of NRCS

In this section, two re-calibration methods are carried out. First the γ^0 profile over the Amazon rain-forest is examined and then the NRCS residuals over the open ocean.

Re-calibration over rain-forest

For radiometric calibration of most scatterometers and SARs (Crapolicchio & Lecomte, 1999; Long & Skouson, 1996; Hawkins et al., 1999), the Amazon rain-forest is used as a reference distributed target to monitor variation of backscattering during missions lifetime. For C-band radar, this target could be considered as a rough surface, which equally scatters the incident radar electromagnetic waves in all directions. Therefore the backscatter has small incidence angle dependence and can be characterized by (Hawkins et al., 1999):

$$\gamma^0 = \sigma^0 / \cos(\theta) = \beta^0 \tan(\theta) \quad (3.3)$$

where γ^0 , σ^0 and β^0 are three different forms to represent the backscattering signal. In terms of the isotropic properties of the rain-forest, γ^0 can be approximated to be incidence angle independent (Crapolicchio & Lecomte, 1999). This property together with the stability of rain-forest allow us to directly compare measurements from different imaging modes of S-1A that have large range of incidence angles.

IW γ^0 is chosen as reference to re-calibrate WV because IW is well calibrated against ground corner reflectors (Schwerdt et al., 2016). Besides, the comparison of IW NRCS with CMOD5.N using collocated ECMWF winds for various incidence angles shows good consistency with mean NRCS residual around 0.1 dB (not shown). Adopting the common test site used by scatterometer community (PCS Team, 1999), we collect IW acquisitions from 4°S to 9°S in latitude and from 73°W to

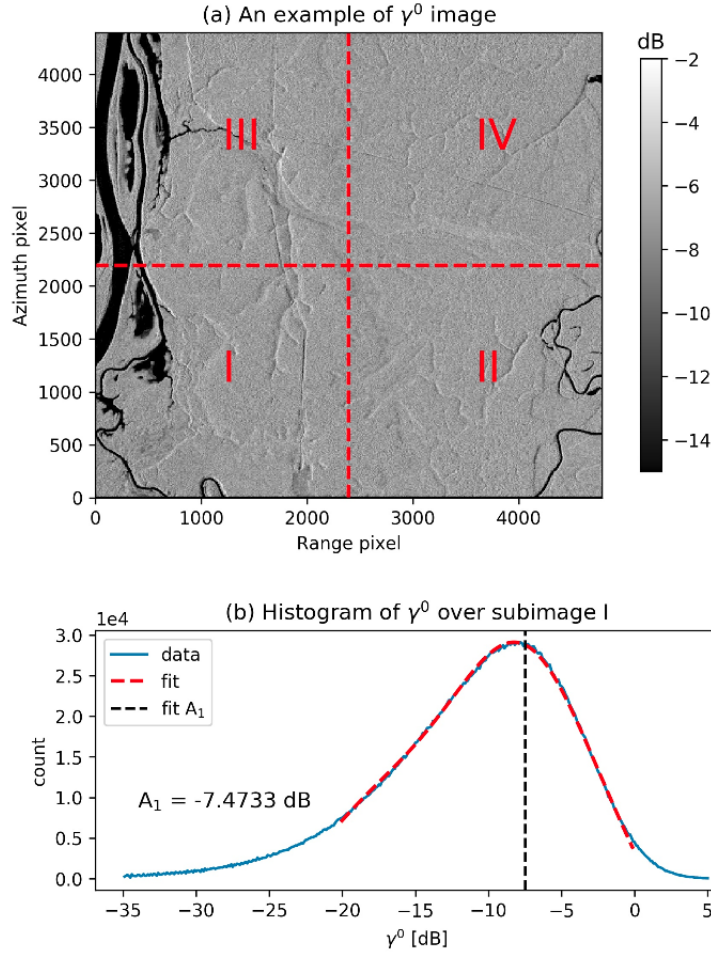


Figure 3.5: (a) An example of processing one imagette into subimages of 10 km by 10 km (WV2 image acquired on November 10, 2017 at 22:21:41 UTC). (b) Histogram of γ^0 over sub-image I (blue solid line) and fit (red dashed line) with Eq.(3.4). The bin size of γ^0 is 0.1 dB. The vertical dashed line represents position of fitted A_1 coefficient.

59°W in longitude between June 2016 and June 2017. In total, 425 IW Ground Range Detected (GRD) products are used, each with spatial coverage of 250 km by 250 km. In contrast, there are fewer acquisitions by WV over this test site. Most of the WV images are located in the eastern South America of relatively high heterogeneity, which would induce spatial variability in radar backscatter. To assure the spatial homogeneity of imaged area, we manually screened 366 products acquired by WV1 and 338 by WV2 over rain-forest. Both IW and WV products are processed into sub-images of 10 km by 10 km. An example of WV2 imagette is shown in Figure 3.5 (a). For each sub-image, histogram of γ^0 is computed and fitted with a normal distribution plus a second-order polynomial, expressed as (PCS Team, 1999):

$$F(x) = A_0 \cdot \exp\left[-\frac{(x - A_1)^2}{2A_2^2}\right] + A_3 \cdot x^2 + A_4 \cdot x + A_5 \quad (3.4)$$

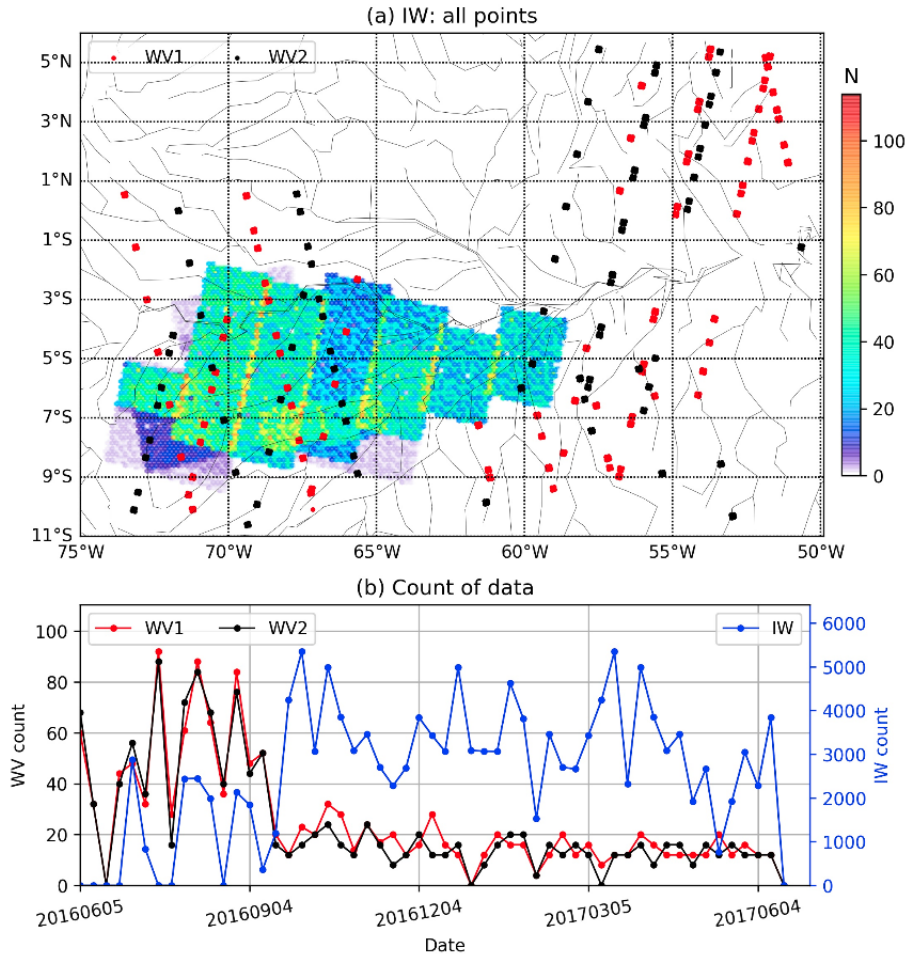


Figure 3.6: (a) Map of processed IW and WV points. Colors denote number of processed IW points. The solid circle represents position of WV data points (WV1 in red and WV2 in black). (b) Weekly count of data points for WV and IW, respectively.

where x denote γ^0 and A_i are six coefficients to be determined, which are determined by non-linear least squares method. Figure 3.5 (b) is an example of γ^0 histogram over the sub-image I in Figure 3.5 (a). The coefficient A_1 is then taken as the reference γ^0 over this sub-image. The same procedure is applied to all WV and IW products.

The geographical positions of processed IW and WV data are presented in Figure 3.6 (a). As shown, IW data are densely located in the west, while points of WV are sparsely distributed throughout. The weekly count of data points is shown in Figure 3.6 (b). Although there is one to two orders of magnitude difference in the number of data counts between WV and IW, both show regular acquisition number during the study period, without obvious seasonal variation. This could to an extent avoid a temporal bias caused by nonuniform acquisitions.

As theoretically derived, γ^0 over Amazon rain-forest is approximately a constant for VV polar-

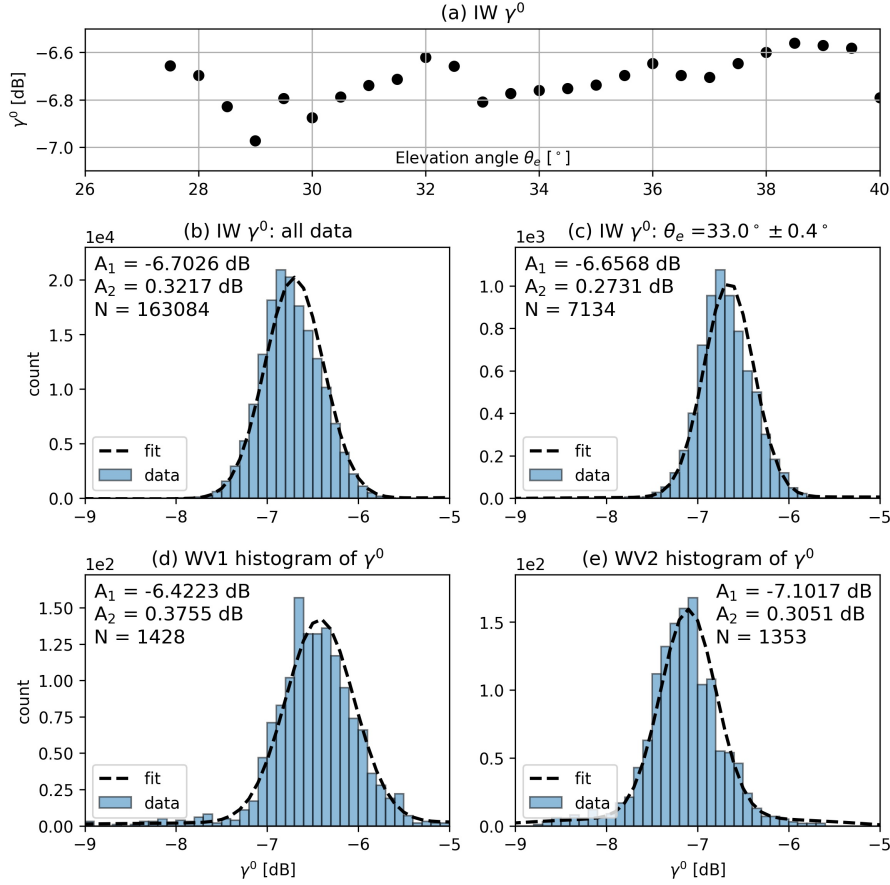


Figure 3.7: (a) Variation of γ^0 relative to elevation angle. Histogram of γ^0 for (b) all IW data; (c) IW data filtered around WV2 elevation angle; (d) WV1; (e) WV2. The fit formula to histogram is given in Eq.(3.4), plotted by black dashed lines. The fitted A_1 coefficients are annotated in subplots.

ization, independent of elevation angle or incidence angle (Hawkins et al., 1999). Though, it is preferable to compare the γ^0 observed at the same elevation angle in purpose to maintain the same antenna elevation pattern. Elevation angle of IW varies between 27.5° and 40.5° , covering WV2 (32.6°) but does not cover WV1 (21.6°). For WV2, a filtering of elevation angle within $32.6^\circ \pm 0.4^\circ$ is accordingly applied to processed IW data points. While for WV1, we use a different strategy. IW γ^0 relative to elevation angle is shown in Figure 3.7 (a). It is worth noting that the γ^0 does exhibit variation with elevation angle, which might be caused by the inadequate correction of inter-beam as well as beam-to-beam gain offset of azimuth antenna pattern as reported in (Schwerdt et al., 2016). Here, we choose to use all IW Level-1 data given the small variability of γ^0 , assuming that the γ^0 dependence on the elevation angle is negligible.

We present the histograms of γ^0 for all IW points, filtered with respect to elevation angle, WV1, and WV2, in Figure 3.7 (b-e). The formula in Eq. (3.4) is employed to fit the histogram and shown as black dashed lines. The fitted coefficient A_1 is also annotated in the plots. By compar-

ing A_1 in Figure 3.7(b) and (d), there is a difference of 0.2803 dB between IW and WV1, while 0.4449 dB between filtered IW and WV2 (Figure 3.7c,e). A seasonal variation on the order of 0.15 dB (Crapolicchio & Lecomte, 1999) has been commonly observed by scatterometers. However, this cannot explain the difference found here. For simplicity, the seasonal variation is not considered for the moment in this re-calibration process. In order to make the γ^0 consistent between IW and WV1, a deduction of 0.2803 dB is required which is equivalent to be divided by a factor of 1.0667 in linear units. Similarly, for WV2 γ^0 a deduction of -0.4449 dB is equivalent to be divided by 0.9026 in linear units.

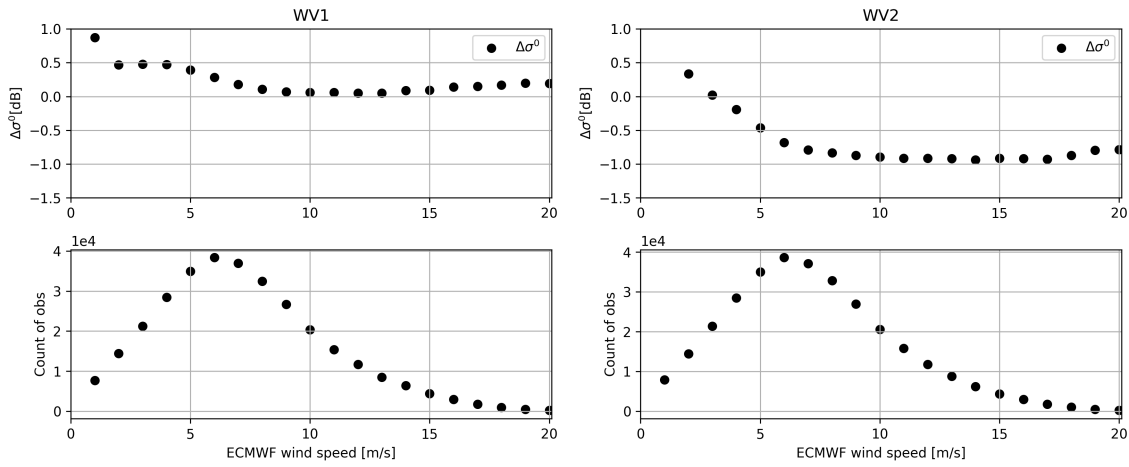


Figure 3.8: (Top) Variation of $\Delta\sigma^0$ relative to wind speed (a) WV1; (b) WV2. (Bottom) The corresponding number of observations for given wind speed.

Ocean calibration

Although the γ^0 profile over Amazon rain-forest could serve to re-calibrate WV NRCS, few WV products limits its routine application. A more practical method taking advantage of the numerous acquisitions over open ocean is therefore advantageous. The ocean calibration procedure (Verspeek et al., 2013) is widely used in scatterometer community to derive the NRCS corrections. It is more feasible since it only needs a few days of collocated pairs to compute the correction constant.

The ocean calibration algorithm is applied to the collocated dataset between S-1A and ECMWF winds. The dataset is split into wind speed bins of 1 ms^{-1} and wind direction bin of 10° . Within each wind speed bin, one out of thirty-six of the collocated pairs is randomly selected to equalize wind direction bin. This varying threshold considerably preserves the proportion of dataset relative to wind speed. An averaged NRCS residual is calculated per wind speed, which is further weighted

by the occurrence of this wind speed to compute the final NRCS residual. It is worth noting here that only the cases with collocated ECMWF wind speed higher than 1 ms^{-1} are used to estimate the final NRCS residual. Based on the collocated dataset, the final NRCS residuals are 0.2730 dB for WV1 and -0.5750 dB for WV2, which correspond to a correction constant of 1.0649 for WV1 and 0.8760 for WV2 to divide in linear unit. These ocean correction constants are comparable with those obtained using Amazon rain-forest calibration method. This confirms the robustness of the ocean calibration procedure for SAR WV data.

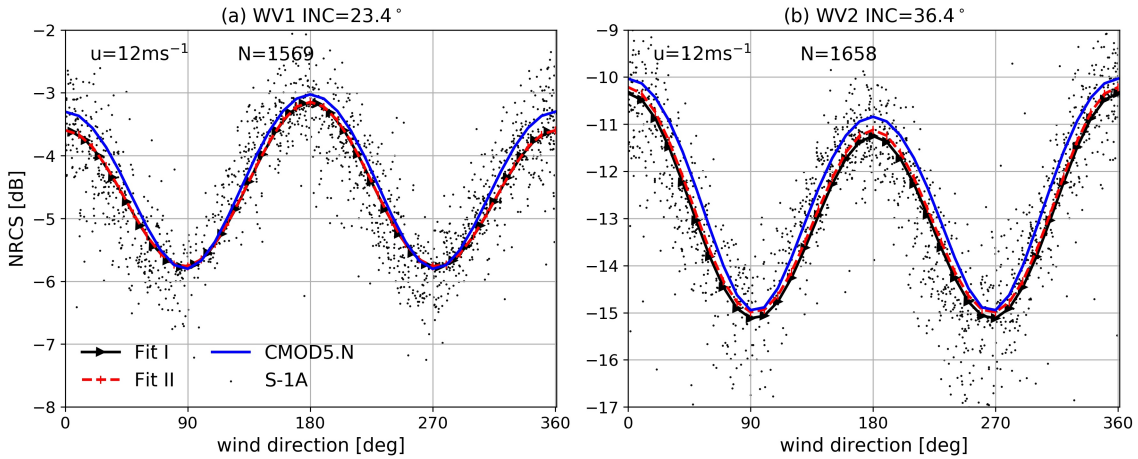


Figure 3.9: The same as Figure 3.3 but for re-calibrated NRCS. The scatters are re-calibrated NRCS using rain-forest method. Black line (marker of right triangle) 'Fit I' represents rain-forest calibration method and red line (marker of vertical line) 'Fit II' for ocean calibration.

3.2.4 Assessment of the re-calibrated NRCS

It should be noted that both re-calibration methods are not devoted to seeking an absolute radiometric calibration constant for WV. Its purpose is to tune an additional correction factor based on ESA provided NRCS. As expressed in Eq. (3.3), the two backscattering coefficients γ^0 and σ^0 in linear unit share the same radiometric calibration constant. As such, the additional factors are supposed to be further divided by ESA-calibrated σ^0 to obtain the re-calibrated NRCS.

Figure 3.9 presents the re-calibrated NRCS curve relative to wind direction at wind speed of 12 ms^{-1} as shown in Figure 3.3. Both rain-forest calibration (black lines) and ocean calibration (red lines) are plotted. It is found that the agreement between re-calibrated NRCS and CMOD5.N based estimates improves in contrast to Figure 3.3. Particularly for WV2, the NRCS residual is reduced to about -0.24083 dB for rain-forest method and -0.1109 dB for ocean calibration at cross-wind (wind direction of 90°). This improvement is further quantified by the re-calibrated NRCS

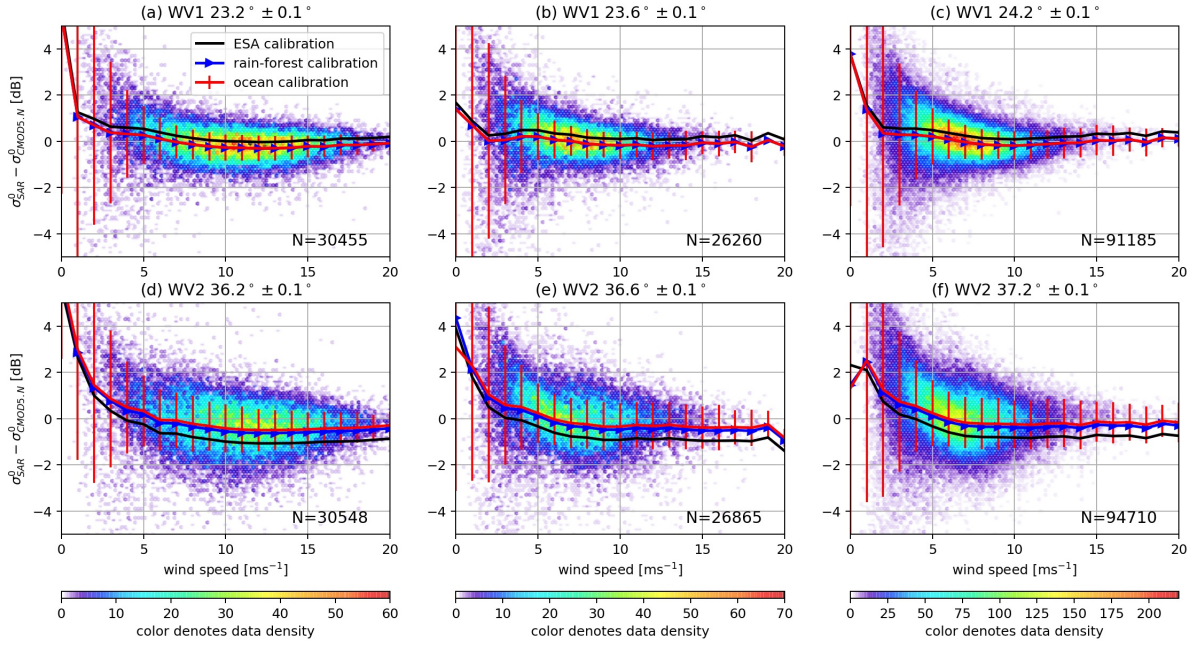


Figure 3.10: Re-calibrated NRCS residuals ($\sigma_{SAR}^0 - \sigma_{CMOD5.N}^0$) relative to wind speeds. Data (in color) are re-calibrated NRCS by ocean calibration method. Black lines are the replica of Figure 3.4 and blue (red) lines are mean re-calibrated NRCS residuals using Amazon rain-forest (ocean calibration) method. The wind speed bin is 1 ms⁻¹. The error bar represents 1 standard deviation of NRCS difference within each bin.

residuals shown in Figure 3.10. The black lines are identical to Figure 3.4 for reference. For WV1, the fit for rain-forest calibration (blue line with right triangle) are superimposed by the fit lines of ocean calibration (red with error bar). The error bar represents standard deviation of NRCS difference within each bin. The outliers when $U_{10} > 15$ ms⁻¹ in Figure 3.10 (e) are caused by the limited number of data points. By comparison, both re-calibrated NRCS residuals using either rain-forest or ocean calibration demonstrate reduced deviation from zero, particularly at high wind. For WV2 in Figure 3.10 (d-f), the mean NRCS residuals show varying trend relative to wind speed with incidence angles. For incidence angles of 36.6° and 37.2° in Figure 3.10(e) and (f), the residual is close to zero with negligible variation on the order of -0.05 dB. However, clearly decreasing NRCS residuals with increasing wind speed is still found at 36.2° in Figure 3.10 (d). The reasons responsible for this variation are discussed in the next section. To summarize the overall performance of both re-calibration methods, the mean NRCS residuals of the whole dataset before and after re-calibration are listed in Table 3.1. The two re-calibration methods have comparable performance and improve the mean residual for both WV1 and WV2 in comparison to ESA calibration.

Table 3.1: Mean NRCS residual

NRCS Residual	WV1 [dB]	WV2 [dB]
ESA calibration	0.2541	-0.6052
rain-forest calibration	-0.0241	-0.1642
ocean calibration	-0.0169	-0.0352

3.2.5 Re-calibration of S-1A and S-1B wave mode

Two re-calibration methods including gamma-zero profile examination over rain-forest and ocean calibration, were implemented. The ocean calibration method is more efficient and practical to perform since it only needs several days of collocations to get a robust estimate of the NRCS difference between S-1 NRCS and the predicted NRCS (Verspeek et al., 2013). As a follow-up, a correction constant is calculated per cycle for both S-1A and S-1B and presented in Figure 3.11. WV of both S-1A and S-1B show non-negligible fluctuation in the derived calibration constant. NRCS residual for WV1 is consistently positive, while WV2 has negative residual value. In particular, large variance of NRCS residual is primarily related to updates of radiometric calibration constant in the Instrument Processing Facilities (IPF) (Collecte Localisation Satellites, 2018). For example for S-1A, update of IPF to version 2.71 on 15 May, 2016 (cycle 79) causes a clear drift of NRCS residual. Notice that S-1B operates at HH-polarization from mid-March to June in 2017. Thus there are no data available during that period as shown in Figure 3.11(b) since only VV polarization is considered in this analysis.

As introduced in (H. Li et al., 2018), an additional noise is also removed from ESA-provided NRCS. It is 0.0001 (0.0002) for WV1 and 0.001565 (0.0008) for WV2 of S-1A (S-1B) in linear unit, respectively. Taking this additional noise removal into account, the overall re-calibrated NRCS is:

$$\sigma^0 = (\sigma_{ESA}^0 - \eta_a) / C_{OC} \text{ [linear]} \quad (3.5)$$

where σ_{ESA}^0 denotes ESA-calibrated NRCS in Eq.(3.2) and C_{OC} is the correction factor converted to linear unit. Here, we choose to directly apply the correction factor per cycle for both S-1A and S-1B. Re-calibrated NRCS will be used to infer wind speed throughout rest of this paper unless particularly stated.

3.3. Challenges in S-1 wind retrieval

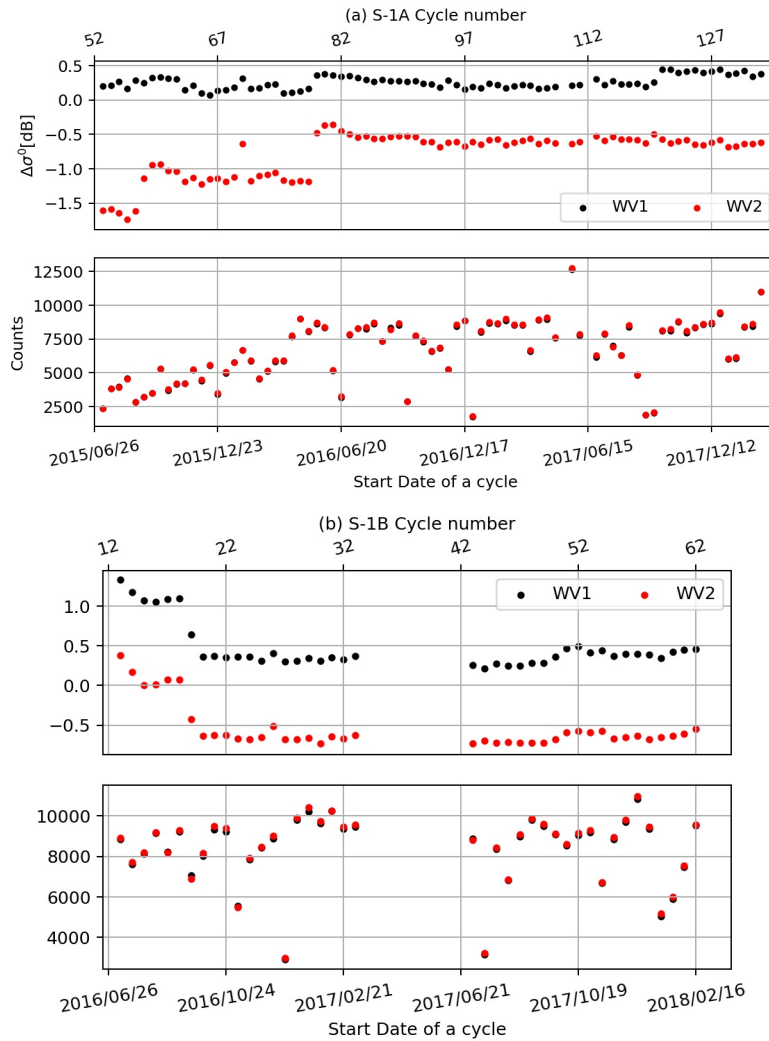


Figure 3.11: Temporal evolution of correction constant obtained by ocean calibration method per cycle for (a) S-1A and (b) S-1B (top). The corresponding number of imagerettes per cycle is given in the bottom panel. Any cycle with acquisitions less than 1000 is excluded. The fact that S-1B operated in HH polarization results in the interruption from mid-March to June in 2017.

3.3 Challenges in S-1 wind retrieval

In this section, the status of wind retrieval from S-1 WV images is first described. The problems and challenges in the present retrieval algorithm is then discussed.

3.3.1 Wind retrieval based on re-calibrated NRCS

CMOD5.N is used to derive wind speed from re-calibrated NRCS based on assumption of neutrally stable atmospheric condition. Wind direction measured by buoy is input to CMOD5.N. SAR re-

3.3. Challenges in S-1 wind retrieval

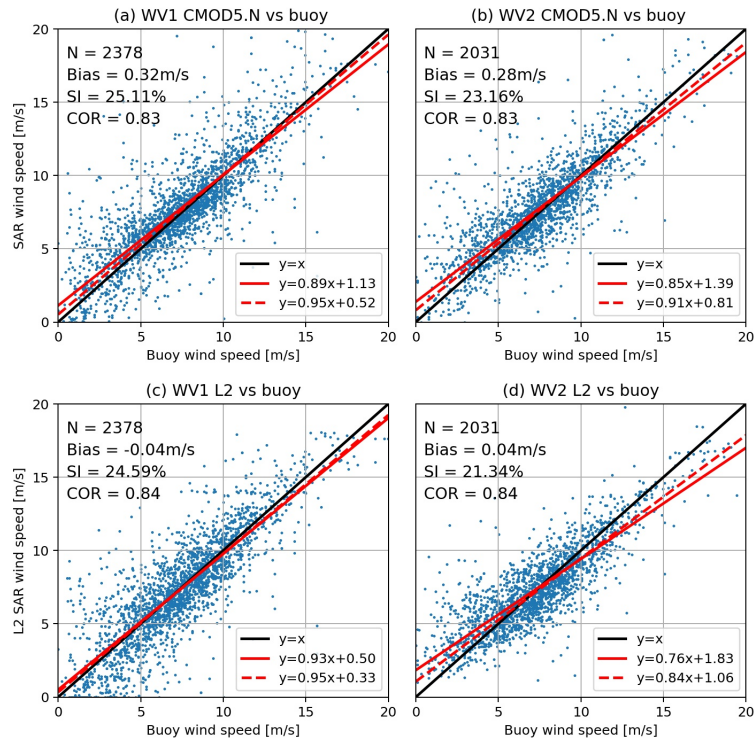


Figure 3.12: (Top) Scatter plot of retrieved wind speed from re-calibrated NRCS using CMOD5.N relative to buoy wind speed for (a) WV1; (b) WV2. The buoy wind direction is input as *a priori* to CMOD5.N. (Bottom) The ocean wind field of S-1 Level-2 products derived from ESA-calibrated NRCS using CMOD-IFR2 are plotted with respect to buoy wind speed for (c) WV1; (d) WV2. Red lines are least-squared linear regression for all collocation data points and dashed red lines are linear fit to data points with buoy wind speed higher than 4 m/s.

retrieved U10 is firstly compared to collocated buoy wind speed in Figure 3.12 for WV1 and WV2, respectively. The standard error metrics are given in top left corner. Retrieved wind speeds of both WV1 and WV2 are overall in good agreement with buoy measurements. Specifically, biases of SAR retrieved wind speed are 0.32 m/s for WV1 and 0.28 m/s for WV2. Scatter index (SI) is on the similar level for these two incidence angles. Slopes of least-squared linear fit to all winds pairs (red solid line) is 0.89 and 0.85 for WV1 and WV2, respectively. The less steeper fit than one-to-one curve is in primary caused by the greater SAR U10 at low wind speed (<4 m/s). This is confirmed by fitting data points with buoy wind speed larger than 4 m/s and finding the linear regression slopes are closer to one-to-one curve: 0.96 for WV1 and 0.91 for WV2. This is because the noise removal particularly at low winds is not sufficient to obtain a noise-free NRCS.

To better outline the improvements of wind speed retrieval using the re-calibrated NRCS, we also show the Level-2 (L2) ocean wind field in Figure 3.12(c)(d) for comparison. L2 wind speed is derived from ESA-calibrated NRCS using CMOD-IFR2 with ECMWF wind direction as input.

The wind speed biases are smaller than those derived using CMOD5.N and the overall error metrics are similar. For example, the root mean square error (RMSE) is around 2 m/s, comparable to typical errors on SAR wind retrieval (Horstmann et al., 2003; Lu et al., 2018). Yet, improvements by using CMOD5.N are obvious. First, there are fewer points with retrieved U10 being 0 m/s for WV1. The gathering of L2 U10 around 0 m/s is induced by the lower sensitivity of CMOD-IFR2 at low wind speed than CMOD5.N. This 0 m/s winds cluster also influences the linear fit to have a larger slope. Second, for WV2 the re-calibrated U10 partly resolves the U10 overestimate U10 at low wind speed of L2 products. This results in linear fit of re-calibrated U10 closer to the one-to-one curve. These improvements further confirm the necessity to re-calibrate NRCS using CMOD5.N for S-1 WV.

It should be noted that the S-1 L2 wind algorithm takes ECMWF model wind direction as input. In comparison to the buoy measurements, model wind has relatively coarser spatial and temporal resolution. In addition, accuracy of ECMWF wind direction tends to be poor, particularly at low wind conditions. These aspects might result in lower accuracy of retrieved L2 wind speed.

3.3.2 Possible improvements in wind retrieval

Though C-band GMFs have been continuously updated to improve its performances in wind retrieval (Quilfen & Bentamy, 1994; Hersbach et al., 2007; Hersbach, 2008; A. Mouche & Chapron, 2015a), the retrieval accuracy is still subject to multiple impact factors. For example, atmospheric instability (Hoffman & Louis, 1990) and presence of upper oceanic current (Plagge et al., 2012) shall both modify local sea surface roughness. These influence on sea surface roughness leads to a modified NRCS, different from the NRCS generated by local winds. In addition, the modulation of wind generated small scale roughness by ocean swell can also influence the mean radar backscattering. All these NRCS modifications would accordingly impact wind retrieval.

A match-up dataset between S-1 WV and NDBC buoys allows to evaluate performance of wind speed retrieval from re-calibrated NRCS. The retrieved wind speeds are overall in good agreement with buoy observations as in Figure 3.12. In addition, the concurrent wind and wave measurements from NDBC buoys help to investigate the sea state impact on wind retrieval. As shown in the Appendix A, weaker sea state impact is observed at higher incidence angle. This impact should also be taken into account in the operational wind retrieval.

3.4. Summary

In addition, the lack of accurate satellite AOCS (Attitude and Orbital Control System) information hampers the S-1 DCA interpretation, as the geometric DC accuracy is not sufficient. Notably, the estimated DC is latitude dependent, that is being said, its relationship with winds differs from low to high latitude. It further hinders the application of DCA in refining the wind retrieval from SAR measurements. Thus, other comparable variables which can be independently derived from a SAR image and have distinct relationship with the wind direction is demanded. As such, they should be advantageously used to help constrain the local wind retrieval schemes from SAR measurements.

Recently, several studies have been published, attempting to include azimuth cutoff in the wind retrieval (Shao et al., 2016a; Corcione et al., 2018). As a parameter directly derived from the SAR image spectrum, azimuth cutoff has been found, to first order, associated with the local winds like NRCS does. Being a spectral parameter, its relationships relative to winds differ with polarizations. Yet, this difference has not been well addressed from the SAR imaging point of view.

Further, the cross-polarization should also be involved in the wind retrieval in effort to lessen the dependence on the *a priori* wind direction. Since the combination of both co- and cross-polarized channels has been proven efficient in wind retrieval over the extreme winds ($> 25m/s$), its potential to observe the intermediate wind conditions needs explored. With the increasingly available quad-pol SAR products, this aspect is expected to advance the wind retrieval in the future.

3.4 Summary

High-resolution wind field is essential to investigate local winds variability over the global ocean. SAR can provide wind observations up to hundreds of meters in spatial resolution. Although SAR wind retrieval algorithms have been widely studied, improvements are still required.

Accurate radiometric calibration of a SAR is fundamental to various applications for land and ocean studies. In this chapter, we assessed radiometric calibration accuracy of S-1A WV through comparisons of SAR-measured NRCS with CMOD5.N prediction over open ocean and at global scale. WV1 and WV2 exhibit distinct calibration accuracy: WV1 is overall consistent with CMOD5.N predictions while WV2 shows a considerable deviation from CMOD5.N. Two re-calibration methods are then carried out by examining the γ^0 profile over Amazon rain-forest as well as ocean calibration. These two methods give comparable correction constants for WV1 and WV2, respectively. When the corrections are applied, the NRCS residuals between re-calibrated NRCS and CMOD5.N

3.4. Summary

predicts are greatly reduced towards zero. By comparison, ocean calibration is more advantageous than the rain-forest calibration method, showing greater improvement of NRCS residuals as well as being more practical to implement.

As such, NRCS of both S-1A and S-1B has been revisited using ocean calibration method throughout the whole mission operational duration. The retrieved wind speeds from re-calibrated NRCS are overall in good agreement with buoy observations, showing distinct improvements in comparison to ESA-provided wind speed.

As demonstrated in the appendix, the weaker sea state impact is observed at higher incidence angle. More importantly, azimuth cutoff is found to be an effective variable in accounting for the sea state impact on wind speed retrieval since it is easily measured from SAR image spectrum. A new NRCS GMF including azimuth cutoff would benefit more accurate wind speed retrieval from SAR measurements. Yet, as pointed out above, azimuth cutoff has been reported to exhibit different relationship with sea surface winds/waves for polarimetric images. This aspect will be discussed in the following chapter in preparation to better interpret the polarimetric imaging of ocean surface.

Chapter 4

Azimuth cutoff of polarimetric SAR images

Contents

3.1	Method of SAR wind retrieval	33
3.1.1	Algorithm of SAR wind retrieval	33
3.1.2	GMF of CMOD5.N	35
3.1.3	Radiometric calibration of S-1 NRCS	35
3.2	Assessment and re-calibration of S-1 NRCS	36
3.2.1	Collocated Sentinel-1A and ECMWF wind speed	37
3.2.2	Assessment of the NRCS	38
3.2.3	Re-calibration of NRCS	41
3.2.4	Assessment of the re-calibrated NRCS	46
3.2.5	Re-calibration of S-1A and S-1B wave mode	48
3.3	Challenges in S-1 wind retrieval	49
3.3.1	Wind retrieval based on re-calibrated NRCS	49
3.3.2	Possible improvements in wind retrieval	51
3.4	Summary	52

Though basic understanding on the SAR imaging mechanism of ocean waves has been achieved, challenges still remain. A large number of quad-polarized SAR images are analyzed here to help assess how the standard SAR imaging transformation applies to all polarization channels. The analyses based on quad-polarized Radarsat-2 and Gaofen-3 products, document the distinct dependence of azimuth cutoff on polarization and incidence angle. Especially, for cross-polarized VH measurements, azimuth cutoff estimates are generally larger than co-polarized HH ones, the latter already being larger than values estimated under VV configuration. This trend increases with the incidence angle. The systematic comparisons between SAR measurements and simulations further demonstrate that the present SAR nonlinear transformation may not properly take into account

the differing coherence times associated to the multi-polarized SAR-ocean scenes. In particular, to reproduce the large azimuth cutoff parameters obtained from cross-polarized images, a reduced coherence time shall be expected. This measurable sensitivity shall enhance the capabilities of polarized SAR systems to derive more precise ocean surface properties, especially the influence of wave breakers, by combining both the co- and cross-polarization measurements. This chapter is based on the paper entitled '*Polarization dependence of azimuth cutoff from Quad-pol SAR images*'.

4.1 Single-polarized azimuth cutoff w.r.t. wind vectors

In this section, the azimuth cutoff dependence on wind vectors (wind speed and direction) is illustrated using SAR images acquired by S-1 WV.

4.1.1 Wind direction

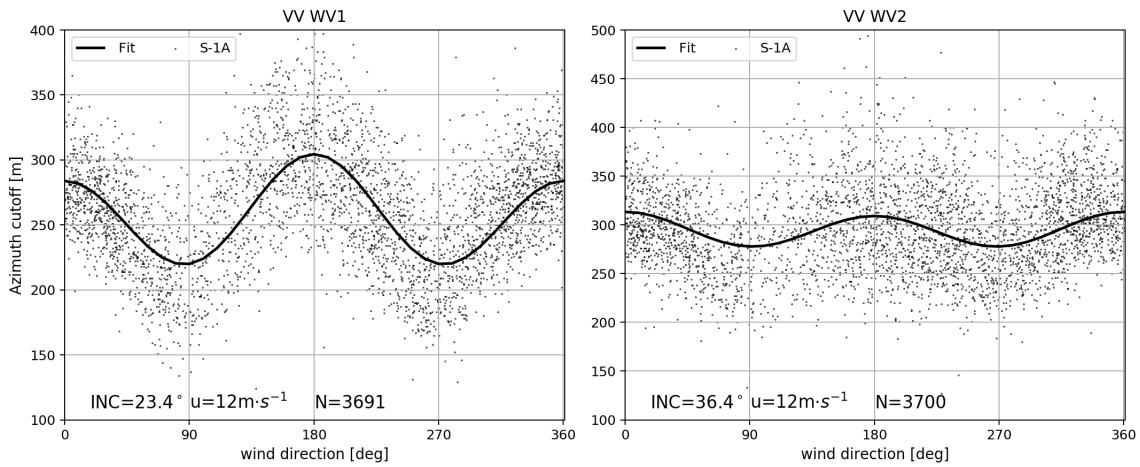


Figure 4.1: VV-polarized azimuth cutoff relative to wind direction at wind speed of $12 \text{ m} \cdot \text{s}^{-1}$ for (left) WV1 and (right) WV2. Solid line is fit to the SAR measurements. Note the different maximum value along y-axis.

As a comparison to Figure 3.3, the wind speed of $12 \text{ m} \cdot \text{s}^{-1}$ is also chosen here to depict the azimuth cutoff variation with respect to wind direction as in Figure 4.1. Azimuth cutoff is determined by both the range-to-velocity ratio and variance of the orbital velocity. Since WV2 has larger range-to-velocity ratio, a larger azimuth cutoff is thus expected for given winds. As shown in Figure 4.1, azimuth cutoff of WV2 is greater than that of WV1 across the entire wind direction range.

Comparable to NRCS, azimuth cutoff also exhibits sine-like dependence on wind direction. Specifically, the azimuth cutoff is the smallest in the crosswind and increases toward both upwind and

downwind. It is worth noting that azimuth cutoff reaches the maximum at downwind for WV1 while upwind for WV2 as shown in Figure 4.1. In addition, the modulation depth is much greater for WV1, suggesting the higher sensitivity of radar return to the wave modulation at lower incidence angle. This in turn is associated with the greater RAR modulation for WV1.

4.1.2 Wind speed

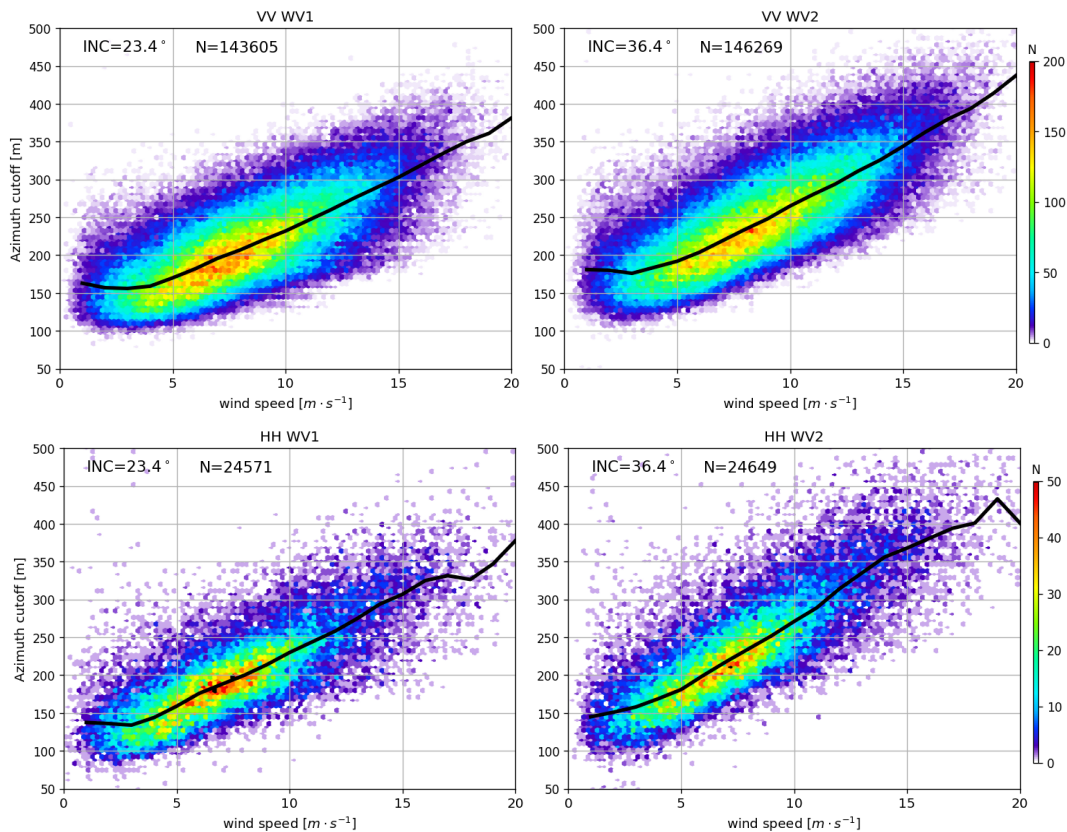


Figure 4.2: Azimuth cutoff relative to wind speed for (upper) VV-polarization WV1/WV2 and (bottom) HH-polarization WV1/WV2, respectively. Color denotes the data count.

The wind speed dependence of azimuth cutoff is explored in Figure 4.2 for both VV and HH polarization. For given wind speed and polarization, azimuth cutoff is larger at WV2 than at WV1 because of the greater range-to-velocity ratio. For given wind speed at WV2, it is clear that azimuth cutoff is larger in HH polarization than in VV polarization. For example, Table 4.1 lists the azimuth cutoff at wind speed of $15 \text{ m} \cdot \text{s}^{-1}$ for the two polarizations and incidence angles. For WV1 at lower incidence angle, azimuth cutoff is comparable in VV and HH polarization. While for WV2, HH azimuth cutoff is larger by 21 m.

The polarization dependence of azimuth cutoff is statistically clear in Figure 4.2, though the VV-

Table 4.1: Azimuth cutoff at $15 \text{ m} \cdot \text{s}^{-1}$.

Pol	VV-WV1	VV-WV2	HH-WV1	HH-WV2
AC	303.0 m	344.0 m	307.0 m	368.0 m

and HH-polarized SAR images are not acquired simultaneously over the same ocean scene. With the technical development, formulation of multi-polarized SAR images are possible. They are acquired at negligible time difference $O(1 \text{ ms})$ over the identical area, namely sea state. In the following, taking advantage of the increasingly available quad-pol data, the polarimetric azimuth cutoff is thus explored.

4.2 Quad-pol data set

In this section, the quad-pol data used to analyze the azimuth cutoff are presented, including Radarsat-2 and Gaofen-3. The collocated WaveWatch III ocean wave spectra are also described.

4.2.1 Radarsat-2

Radarsat-2 was launched in 2007 and carries a C-band SAR sensor (radar frequency of 5.4 GHz). Among various imaging modes, the quad-pol mode transmits H and V pulses alternatively and receive H and V simultaneously, forming four polarimetric combinations, namely HH, VV, HV and VH. The term HV represents transmitting H pulse H and receiving V and hereinafter. In this chapter, we use Fine Quad-pol mode products, with swath of about 25 km by 25 km and nominal spatial resolution of 4.7 m (range direction) and 4.8 m (azimuth direction). In this study, a total number of 21 Fine Quad-pol products acquired by Radarsat-2 are used, acquired between 2009 and 2016. The incidence angles ranges from 19° to 49° . Table 4.2 presents the detailed information (acquisition time, incidence angle and geographic position) of these Radarsat-2 products.

4.2.2 Gaofen-3

The Chinese Gaofen-3 satellite also carries a C-band SAR sensor (radar frequency of 5.3 GHz), launched in August 2016. It can support acquisitions in 12 imaging modes. Among which, wave

Table 4.2: Details of Radarsat-2 Fine Quad-pol products.

Time (UTC)	Inc [°]	Lat/Lon	Time (UTC)	Inc [°]	Lat/Lon
2013-10-07 19:51:52	19.3	34.20N/30.84W	2011-12-26 18:23:23	25.6	57.17N/177.78W
2015-10-28 06:48:34	19.4	48.48N/5.66W	2009-02-28 05:47:58	32.2	51.20N/178.80E
2013-06-28 16:11:48	20.8	17.60N/152.39W	2009-08-22 14:31:05	33.2	46.17N/124.54W
2016-09-13 01:59:59	20.9	46.44N/125.43W	2011-11-28 18:40:49	33.3	55.18N/175.24E
2011-12-19 18:27:32	20.9	57.16N/177.65W	2011-12-30 06:02:15	35.3	55.18N/175.12E
2016-09-13 01:59:56	20.9	46.24N/125.37W	2012-11-29 18:36:40	37.3	55.17N/175.17E
2012-11-27 05:49:47	21.9	55.17N/175.04E	2012-11-23 06:06:25	39.1	55.17N/175.16E
2009-01-11 02:25:04	23.2	46.15N/131.08W	2011-12-19 18:28:18	44.3	55.17N/175.07E
2009-03-17 14:39:15	23.2	46.19N/124.56W	2011-12-02 18:24:08	47.5	55.19N/175.03E
2011-12-02 18:23:23	25.6	57.15N/177.78W	2011-12-26 18:24:08	47.5	55.17N/175.02E
2012-05-01 02:48:21	48.2	38.05N/129.99W			

mode (WM) is dedicated to observations of ocean waves. It acquires one imagette every 50 km along the flight direction. Each WM image has swath of approximately 5 km by 10 km (depending on the incidence angle) with nominal spatial resolution of 4 m. It is operated in quad-polarization (VV, VH, HH, HV) and at various incidence angles, ranging from 20° to 50°.

In this chapter, we use Level-1 Single Look Complex (SLC) WM products obtained from January to October in 2017. In total, about 7,000 products have been collected during this period. The geographic distribution of these data is shown in Figure 4.3(a). As pointed out in (H. Wang et al., 2018), WM can only operate up to 50 minutes per orbit due to power limitations. Therefore, the data are not uniformly distributed across the globe and most of the data are acquired over the north Pacific Ocean. There are no clear dependence of incidence angle on latitude. Histogram of incidence angles in bin size of 2° is given in Figure 4.3(b). Note that the incidence angle of $36^\circ \pm 1^\circ$ has the maximum number of images around 1,700. There are 7 incidence angles with more than 400 acquisitions ($22^\circ \pm 1^\circ$, $30^\circ \pm 1^\circ$, $34^\circ \pm 1^\circ$, $36^\circ \pm 1^\circ$, $40^\circ \pm 1^\circ$, $42^\circ \pm 1^\circ$, $48^\circ \pm 1^\circ$).

4.2.3 WW3 ocean wave spectrum

For our purpose, a match-up data set between Gaofen-3 and WW3 ocean wave spectrum has been created. The ocean wave spectra are generated by WW3 spectral wave model using wind forcing from operational European Centre for Medium-Range Weather Forecasts (ECMWF) output and the parameterization in (Ardhuin et al., 2010). They are available on a global spatial grid of 0.5° in both

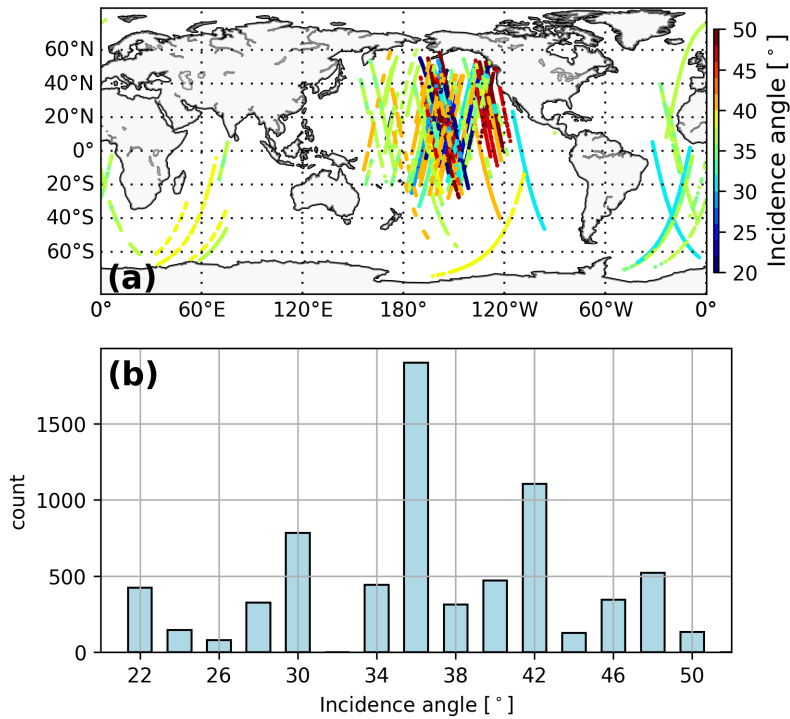


Figure 4.3: (a) The geographic position of Gaofen-3 WM data across the globe. Color denotes incidence angle [°]. (b) Histogram of incidence angles in bin size of 2°.

latitude and longitude and temporal interval of 30 mins. The WW3 wave spectrum composes of 24 directions and 32 wavenumber bins from $0.0056 \text{ rad}\cdot\text{m}^{-1}$ to $2.0632 \text{ rad}\cdot\text{m}^{-1}$. This corresponds to wavelength ranging from 1,122 m to 3.045 m. The minimum wavelength is comparable to the spatial resolution of Gaofen-3 WM. This assures the azimuth cutoff from Gaofen-3 measurements and simulations out of WW3 spectra is comparable.

4.3 Polarized SAR azimuth cutoff

The polarimetric azimuth cutoff computed from Quad-pol SAR observations is demonstrated from a case study and statistical point of view, respectively.

4.3.1 A Case study

Figure 4.4 shows a case of Gaofen-3 WM acquired on February 1, 2017 at UTC 4:25:26. Incidence angle is 30.4° . The normalized backscatter intensity for VV, HH and VH polarization is given in Figure 4.4(a)(d)(g), respectively. All three images exhibit clear wavy signatures. The pattern on

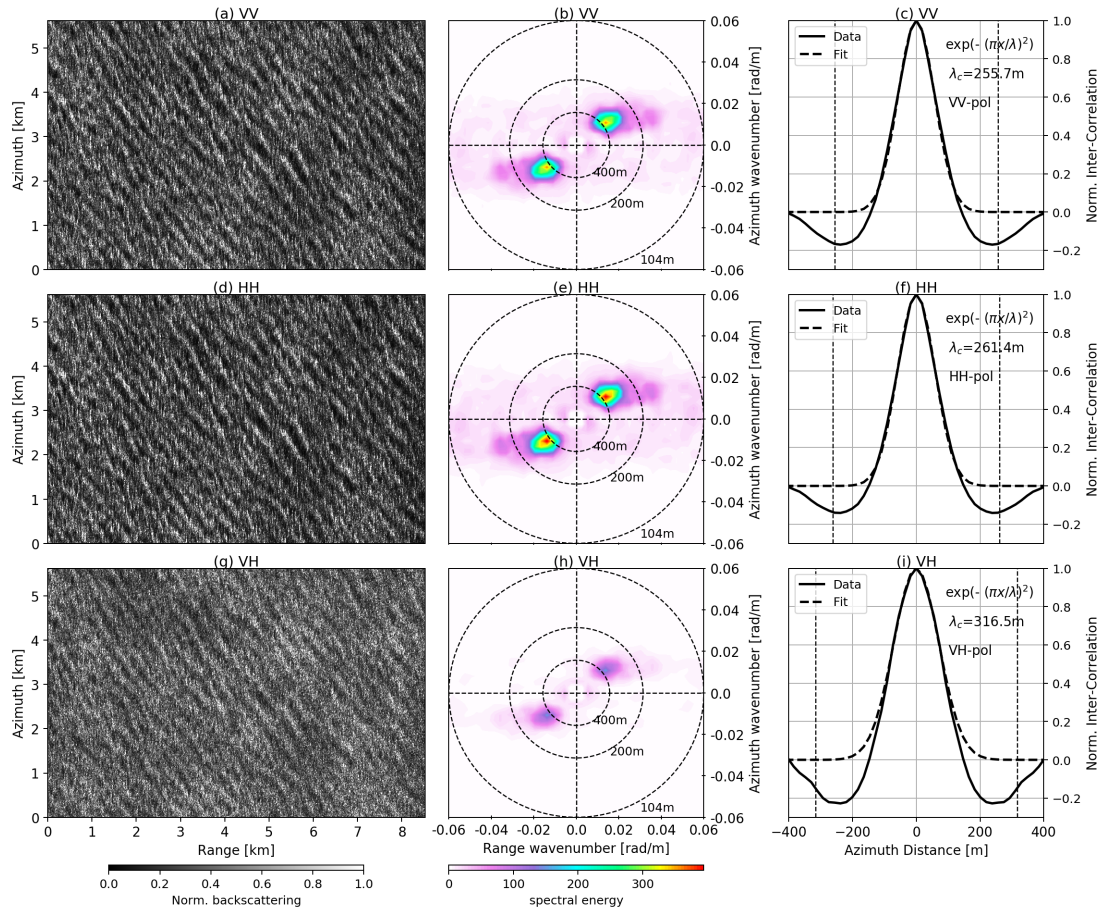


Figure 4.4: A case of Gaofen-3 WM product acquired on February 1, 2017 at UTC 4:25:26. Incidence angle is 30.4° . (Left) Image of normalized backscattering for (a) VV; (b) HH; (c) VH polarization. (Right) Real part of SAR image cross-spectra for (d) VV; (e) HH; (f) VH polarization.

the VH image in Figure 4.4(e) is slightly blurred compared to VV and HH polarization. The real parts of SAR cross-spectra for each polarization are shown in Figure 4.4(b)(e)(h). Peak wavelength is around 350 m. Image spectral magnitude of HH polarization is larger than VV. By comparison, the VH spectrum is much smaller, which is partly related to the lower RAR MTF. These variations of spectral energy are consistent with the simulation results in Figure 4.7.

Azimuth cutoffs are estimated by fitting a Gaussian function to the inter-correlation, as shown in the right panel of Figure 4.4. The HH-pol azimuth cutoff is slightly larger than the VV-pol estimate. This can still be related to the larger HH-pol RAR MTF, in agreement with the above simulated results, Figure 4.7. We would expect a smaller VH azimuth cutoff, as the VH RAR MTF may be expected to be much smaller (A. Mouche & Chapron, 2015b). This is not the case. Smearing effects, likely associated to shorter life times of VH scatters, seem to dominate, as the image contrast is apparently more blurred. VH cutoff parameter provides the largest value, Figure 4.4.

4.3.2 Statistical azimuth cutoff

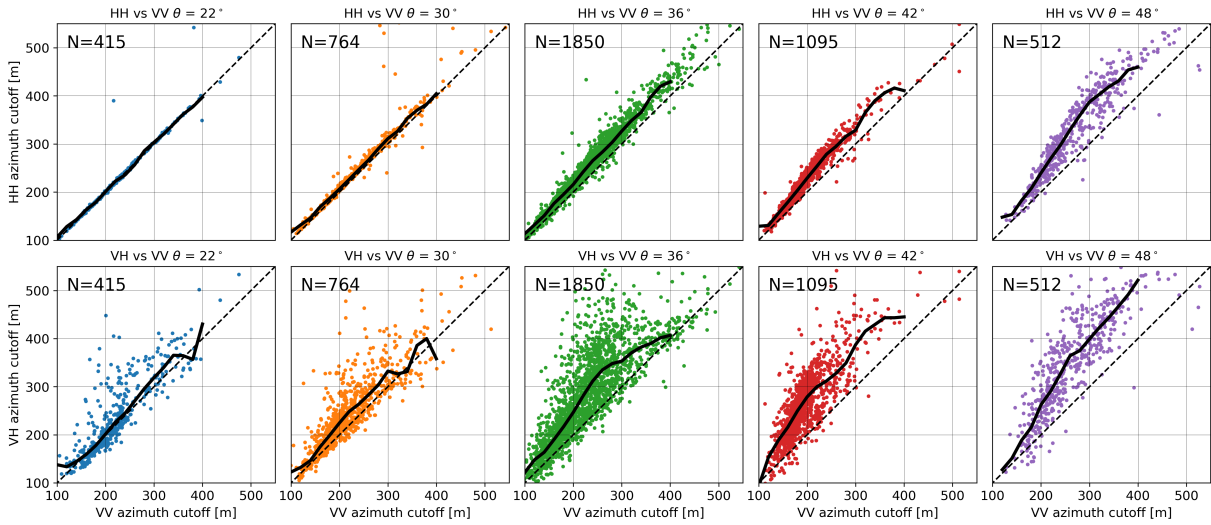


Figure 4.5: (Top) Azimuth cutoff of HH relative to VV polarization for five incidence angles of Gaofen-3 data set. (Bottom) Azimuth cutoff of VH relative to VV polarization. The solid lines are the mean fit for each incidence angle. The dashed lines are the one-to-one curves.

To emphasize the differing azimuth cutoff sensitivity to polarization, both HH and VH estimates are displayed relative to VV. Figure 4.5 top panel gives HH versus VV azimuth cutoff based on the Gaofen-3 data set. The five incidence angles with more than 400 images (22° , 30° , 36° , 42° , 48°) are plotted, respectively. The mean fit is given (solid line) at each incidence angle. As found with the large data set, HH azimuth cutoff parameters are generally larger than VV ones, and the deviation increases with the incidence angle. At low incidence angle of 22° , the mean fit line is closer to the one-to-one curve. This result must be related to the overall weak polarization sensitivity between VV and HH backscatter measurements at low incidence angles (A. A. Mouche et al., 2006b, 2007b). As the incidence angle increases, the mean fit line deviates from the one-to-one relationship. Particularly, at incidence angle of 48° , the HH azimuth cutoff first show a more rapid increase before leveling off when compared to high VV values. While this increasing HH azimuth cutoff may be expected from simulations, it shall also be recalled that larger scalar backscatter contributions (Kudryavtsev et al., 2013), likely associated to breaking events, impact HH measurements. Accordingly, smearing effects, associated to these breaking events, are certainly acting to contribute to increase the HH cutoff values compared to VV ones.

Figure 4.5, bottom panel, shows VH azimuth cutoffs with respect to VV ones, for the five different incidence angles. Clearly, VH azimuth cutoff is almost always larger than VV. As found for HH cases, the mean fit also increases with incidence angle. Note that the mean fit lines are also slightly

4.3. Polarized SAR azimuth cutoff

higher than the one-to-one curve for low incidence angles, Figure 4.5 top panel. For incidence angle larger than 36° , the deviation increases. As compared to HH, the increasing trend is distinct, with VH almost exhibiting constant offset compared to VV. Note, the VH azimuth cutoff is largely more scattered than HH for all incidence angles.

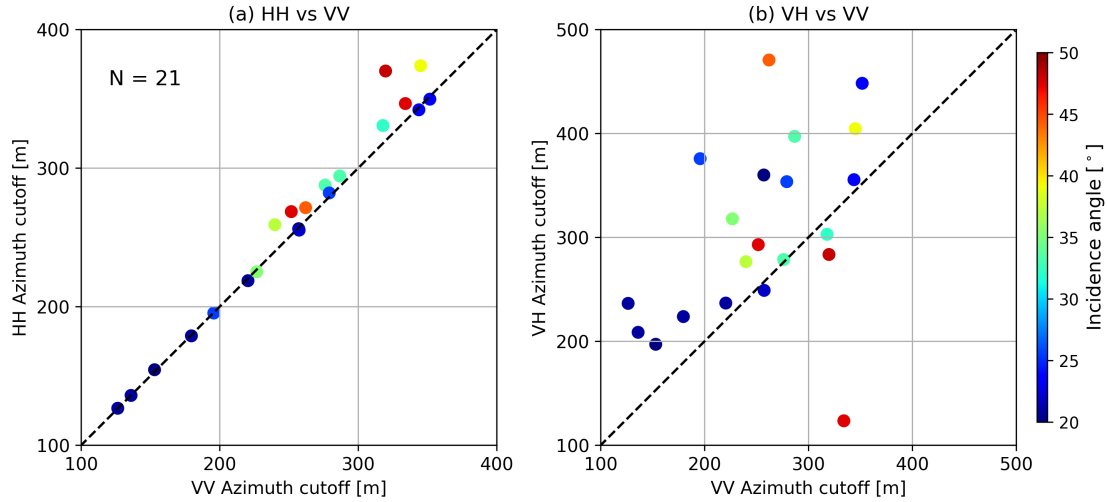


Figure 4.6: Azimuth cutoff in HH-pol (a) and in VH-pol (b) relative to VV-pol based on the 21 Radarsat-2 data. Color denotes incidence angle.

Figure 4.6 displays azimuth cutoff estimates from the Quad-pol Radarsat-2 data set for HH versus VV in (a) and VH versus VV in (b). Again, confirming the previous results, the azimuth cutoff increases with incidence angle. At moderate incidence angles, $[19^\circ, 25^\circ]$, co-polarized VV and HH azimuth cutoffs can be well well considered as identical given the negligible difference (<10 m). With increasing incidence angle, 30° (in green and red), HH azimuth cutoffs are larger than VV, consistent with Gaofen-3 data in Figure 4.5. As also found, VH azimuth cutoff is larger than both VV or HH parameters, except one outlier. Again, this is consistent with results reported in Figure 4.5.

To summarize these comparisons, VH azimuth cutoffs are certainly expressing the impact of SAR ocean scene coherence times on smearing effects. Larger than HH estimates, already larger than VV ones, these results seem to confirm that different scattering mechanisms are to be considered, with so-called non-polarized and super-Bragg contributions associated with wave breaking events (Kudryavtsev et al., 2005; A. A. Mouche et al., 2008; Kudryavtsev et al., 2013, 2014; Hansen et al., 2016). Already key to control the polarized degree of backscatter intensity, these events may have short-life time properties., Especially under VH configuration, the detected scatters may then contribute to reduce the SAR coherence time to explain the azimuth resolution losses.

4.4 Azimuth cutoffs from simulations

In this section, we first show estimates of polarimetric azimuth cutoff from simulated image cross-spectrum based on the nonlinear SAR-forward mapping transform. Comparisons between SAR measurements and simulations based on WW3 ocean wave spectra are then presented and discussed

4.4.1 Nonlinear SAR transformation

Assuming a multiplicative noise model to represent the backscatter intensity from a moving ocean surface, (Engen & Johnsen, 1995) derived a closed-form expression for SAR image cross-spectra between two sub-looks. Uncorrelated speckle noise largely vanishes, and phase motions of ocean waves, captured during the dwell-time interval between two sub-looks, can then be estimated. Phase motions are directional, and the 180° direction ambiguity of ocean waves is generally resolved. The nonlinear cross-spectrum can be simplified as:

$$P_S^{mn}(\mathbf{k}, \Delta t) = \int d\mathbf{x} e^{-i\mathbf{k}\cdot\mathbf{x}} e^{k_x^2[\rho_{dd}(\mathbf{x}, t) - \rho_{dd}(\mathbf{0}, 0)]} [1 + \rho_{II}(\mathbf{x}, t)] \quad (4.1)$$

where the subscript d and I in ρ_{aa} denote the velocity bunching and RAR modulation, respectively. k_x is the wavenumber along the azimuth direction. The correlation function defined in Eq. (4.1) is related to the ocean wave spectrum $S(\mathbf{k})$ through

$$\rho_{aa}(\mathbf{x}, \Delta t) = \frac{1}{(2\pi)^2} \int d\mathbf{k} e^{i\mathbf{k}\cdot\mathbf{x}} \cdot \frac{1}{2} \left[|M_a(\mathbf{k})|^2 e^{-i\omega\Delta t} S(\mathbf{k}) + |M_a(-\mathbf{k})|^2 e^{i\omega\Delta t} S(-\mathbf{k}) \right] \quad (4.2)$$

where M_a represents the modulation transfer function (MTF) for RAR or velocity bunching. In this study, we use the following form of MTF for velocity bunching (K. Hasselmann & Hasselmann, 1991a; Chapron et al., 2001):

$$M_d = \frac{R}{V} \omega (\sin\theta \cos\phi + j \cos\theta) \quad (4.3)$$

where R/V is the slant-range to velocity ratio of SAR sensor. The RAR MTF is expressed by:

$$M_I = -ik_y \frac{1}{\sigma_0} \frac{\partial \sigma_0}{\partial \theta} \quad (4.4)$$

The co-polarized (VV, HH) σ_0 is empirically derived using the CSARMOD (A. Mouche & Chapron, 2015b) and cross-polarized (VH) by the model in (Hwang et al., 2015; A. Mouche & Chapron, 2015b; A. A. Mouche et al., 2017). According to the reciprocity theorem (G. Valenzuela, 1967), VH and HV backscatter intensities are expected to be the same. Thus, only VH polarization is analyzed throughout this chapter. It is worth noting that azimuth cutoff parameter reflects the expected random time-evolution of the radar detected scatterers during the SAR-integration time. The time-evolution shall include orbital motions, but also local accelerations over the integration time (K. Hasselmann & Hasselmann, 1991a). Since the integration time of space-borne SAR is of the order of 0.6 seconds, the specific acceleration of long waves is generally neglected (K. Hasselmann et al., 1985a), and a catch-all time coherency parameter possibly considered. A finite scene coherence time will relate to smearing effects, acting to reduce the along-track resolution associated with both the unresolved random scatter motions and the limited scatter lifetime during the SAR integration time. To estimate this contribution, the ratio between azimuth cross-spectrum profiles obtained for different look separation time can be performed. The idea is to make use of the expected extremely short life time of the wind generated ripples and breakers to evaluate, if there is, increasing impact on the overall smearing of the SAR scene. Expecting different scattering mechanism associated to each polarization configuration (Kudryavtsev et al., 2014), it will be demonstrated that a more direct estimation can be obtained.

Left panel of Figure 4.7 shows simulated SAR image cross-spectra for three polarization channels (VV, HH and VH). The time coherency is not adjusted, and the simulations serve to analyze the cut-off sensitivity to the different RAR MTFs. The input ocean wave spectrum is Elfouhaily spectrum (Elfouhaily et al., 1997) at wind speed of 7 m/s and wind direction of 45° with inverse wave age of 0.35. The R/V ratio is set as 92.5 s and incidence angle is 36° . Peak wavelength is around 256 m. Comparing the three simulated cross-spectra, one can find that HH spectrum exhibits the largest spectral energy at a given wavenumber, in line with the expected largest RAR MTF in HH pol. Note, the input velocity bunching is the same for all three polarization channels.

To estimate the azimuth cutoff parameter, a widely used method is to fit the inter-correlation of SAR cross-spectrum by a Gaussian function (Kerbaol et al., 1998a), as given in the right panel of Figure 4.7. Note that the inter-correlation function is generally complex, as coherent wave motions contribute to shift the resulting SAR sub-look images, i.e. the cross-spectra have non-zero imaginary contributions. Accordingly, the real part is used to estimate azimuth cutoff with asymmetry relative to the azimuth distance (Stopa et al., 2015a) (see their Figure 14). As mentioned

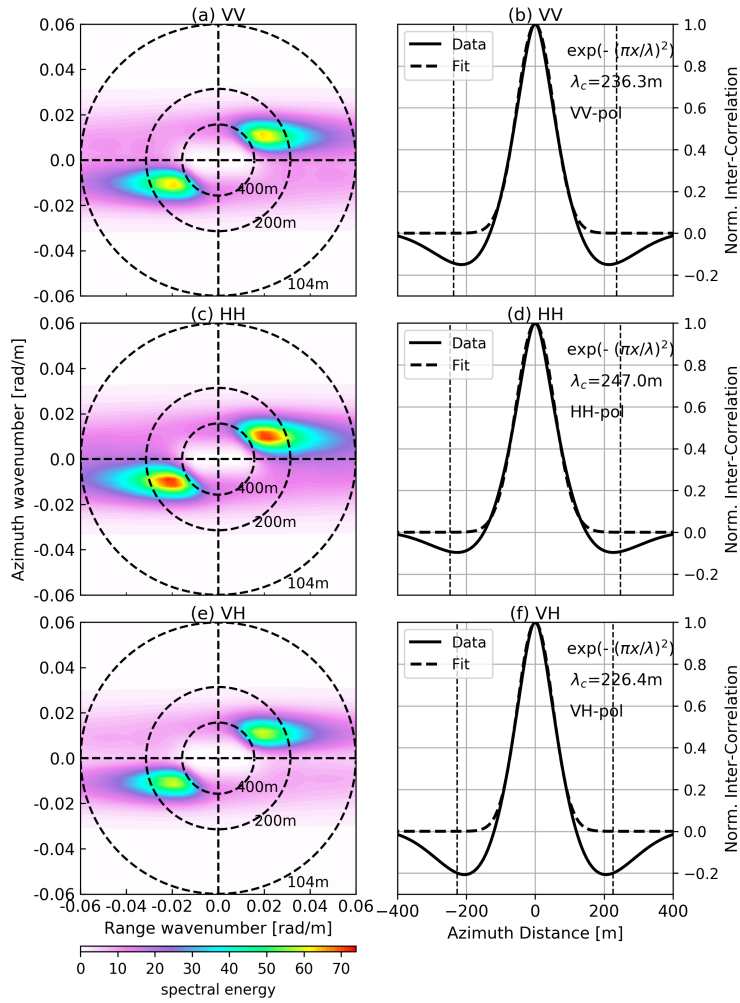


Figure 4.7: (Left) Simulated SAR image cross-spectra for three polarization channels: (a) VV; (c) HH; (e) VH. (Right) The corresponding azimuth cutoff estimation for three polarization channels: (b) VV; (d) HH; (f) VH. The input ocean wave spectrum is Elfouhaily spectrum at wind speed of 7 m/s and wind direction of 45° with inverse wave age of 0.35. Incidence angle is set as 36° .

above, this shift is key to resolve the 180° direction ambiguity. In this study, we do not focus on ocean wave retrieval, and the absolute value of the cross-spectrum is considered to estimate the inter-correlation function.

Using different MTFs, the simulated azimuth cutoff is certainly supposed to vary with polarization, as shown in Figure 4.7. While HH RAR MTF shall improve the wave imaging process, random motions are found to impact more significantly the resolution loss in the azimuth direction. This is a relative effect. For short scales, the HH SAR spectrum is indeed relatively more attenuated than the initially lower VV SAR spectrum. For the same reason, the simulated azimuth cutoff in VH is the smallest, Figure 4.7(f), following the smallest RAR MTF definition. As performed, these simulations do not consider the impact of time coherency, and under this assumption, the simulation

suggest that azimuth cutoff parameters shall only differ from the definition of the different RAR MTFs.

4.4.2 Comparison of SAR and simulation

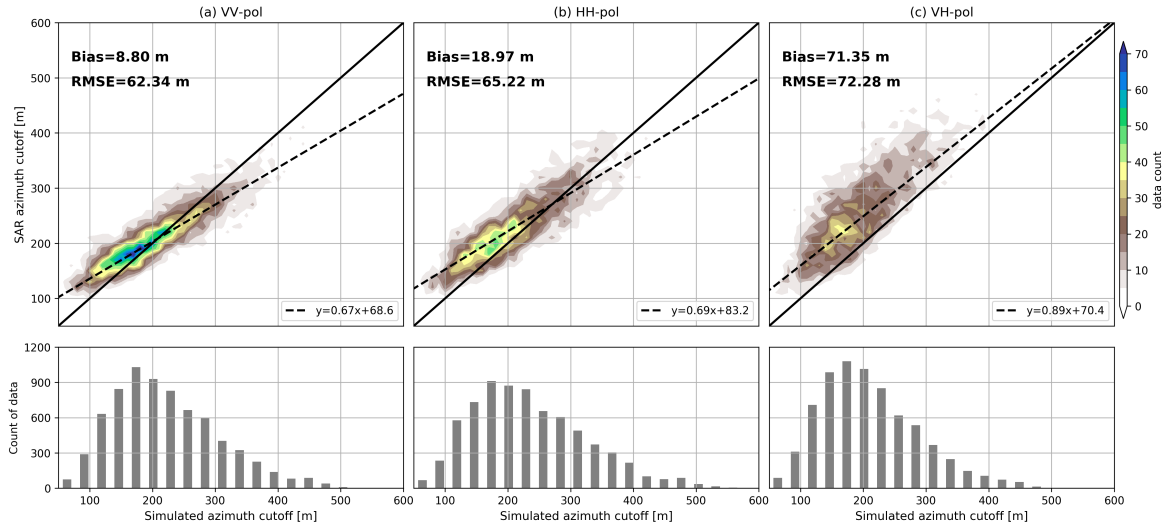


Figure 4.8: (Top) Comparison of azimuth cutoff from SAR measurements and nonlinear SAR transformation for (a) VV-pol, (b) HH-pol and (c) VH-pol. Solid line is one-to-one curve and dashed line is the least-squared linear regression. Color denotes data density. (Bottom) The corresponding data count of simulated azimuth cutoff in bin size of 25 m for each polarization.

As demonstrated in Section 4.4.1, azimuth cutoff parameters from simulated SAR image cross-spectra already display polarization sensitivity. In this section, neglecting a time coherence effect, we further systematically evaluate nonlinear SAR transformation. NRCS GMF of CSARMOD (A. Mouche & Chapron, 2015b) is used to estimate RAR MTF for co-pol VV and HH measurements and Hwang’s GMF (Hwang et al., 2015) is used to determine the VH MTF. For each Gaofen-3 product, the collocated WW3 ocean wave spectrum is used to perform a forward SAR-spectral transform. Azimuth cutoffs are then estimated from these simulation results.

For VV polarization, Figure 4.8(a) presents comparisons between SAR-measured azimuth cutoffs and from simulations Eq.(4.1). All Gaofen-3 data are used. As obtained, the simulations are in overall good agreement with SAR measurements. The total bias (SAR - simulation) is 8.80 m with root-mean-square-error (RMSE) of 62.34 m. The linear regression slope is 0.67, comparable to previous reported results (Stopa et al., 2015a) (see their Figure 4). The simulated azimuth cutoff are underestimated for low sea conditions (small azimuth cutoff) and overestimated for high sea

state conditions (large azimuth cutoff). This might in part be attributed to the poor fit of Gaussian function to the SAR inter-correlation under low sea state conditions (Stopa et al., 2015a).

For HH polarization, results are presented in Figure 4.8(b). The total bias (SAR - simulation) is 18.97 m, larger than that of VV-pol, Figure 4.8(a). RMSE is also larger, 65.22 m. The linear regression slope is still comparable to the VV polarization case. HH azimuth cutoff is seemingly much higher than simulated ones for low sea state (azimuth cutoff smaller than 150 m). With increasing sea state, SAR observations and simulated results become more consistent.

The VH configuration is given Figure 4.8(c). Most of the scatter points are now above the one-to-one curve, i.e. SAR-measured VH azimuth cutoff is likely larger than a simulated one. This also reflects in a large total bias (SAR-simulation) of 71.35 m. In comparison to VV and/or HH, VH azimuth cutoff exhibits variability with higher RMSE of 72.28 m. In short, the remarkable deviation between SAR-measured and simulated VH-pol azimuth cutoff shall certainly help to assess the short-life time of VH scatters.

To further diagnose the deviation between SAR measurements and simulations, we associate azimuth cutoff residuals (SAR-simulation) with collocated ECMWF wind speed, Figure 4.9. Azimuth cutoff residual decreases with increasing wind speed for both VV and HH. The interception point with zero residual is 7 m/s for VV and 9 m/s for HH. This corresponds to the higher intercept terms for HH in Figure 4.8(b). Note, the analysis is limited to wind speed lower than 15 m/s and more data will be collected to address the results for higher wind speed. As expected, the azimuth cutoff residual is thus wind speed dependent. As foreseen, a more careful examination of the azimuth cutoff residual might provide means to both refine the RAR MTFs and to properly take into account short life time scatters, to help constrain the ocean wave spectral retrieval algorithm. The mean VH azimuth residual slightly varies between 45 m and 60 m and exhibits an increasing trend with wind speed lower than 12 m/s. Compared to co-pol VV and HH measurements, VH residual has larger spread for a given wind speed, suggesting higher variability as shown in Figure 4.8. This demonstrates that the present SAR forward transform is not suited to interpret cross-polarized observations.

Considering the good performance of VV-forward SAR transform to reproduce measured azimuth cutoff parameters in VV, it is chosen as reference to evaluate the polarization difference (PD) between SAR measurements and simulations. Figure 4.10(a)(b) display results for HH-VV and VH-VV, as function of the wind speed. Solid line is for SAR-measured PD and dashed line for simulated

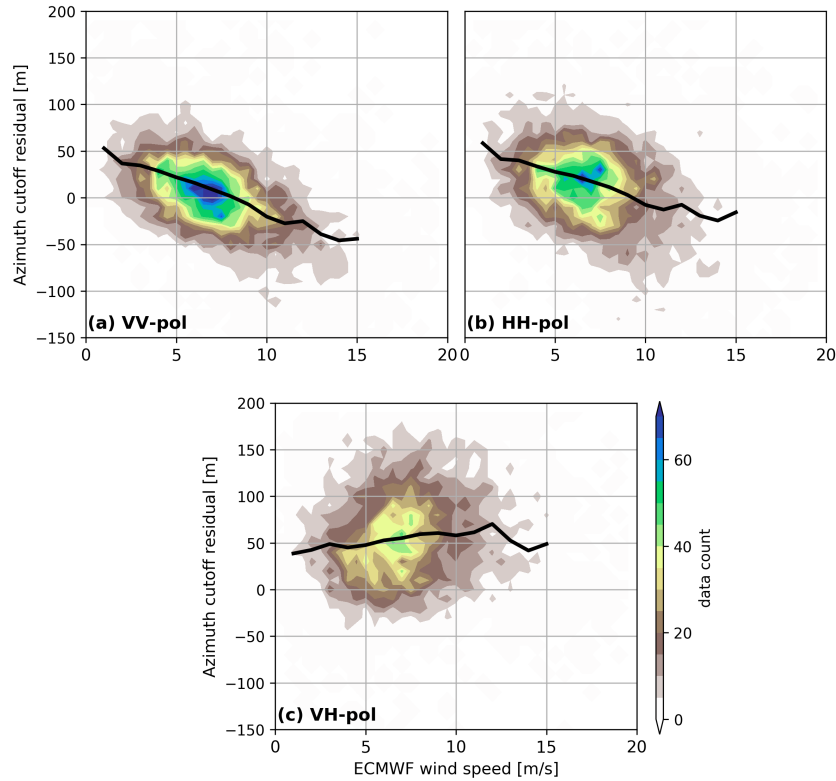


Figure 4.9: Azimuth cutoff residual (SAR-simulation) relative to the collocated ECMWF wind speed for (a) VV; (b) HH; (c) VH. Solid black line is the mean azimuth cutoff residual. Color denotes data count.

PD. In Figure 4.10(a), both azimuth cutoff PD increases with the wind speed and observation-PD always larger than simulation-PD. With increasing wind speed, SAR-measured PD increased much more rapidly. At this stage, this might be attributed to the MTF impact, as the empirical HH RAR MTF could be increasingly underestimated with wind speed. For VH-VV PD analysis, Figure 4.10(b), the smaller VH RAR MTF numerically suggests a negative trend while it is found globally positive for SAR-measured PD. SAR-measured and simulated PD are comparable at very low wind speed, but strongly depart with increasing wind speed. The VH-SAR ocean scene coherence time becomes necessary to estimate smearing effects..

4.5 Summary

Over the past years, investigations mostly focused on the mean intensity properties of co- and cross-polarized high-resolution SAR measurements (Kudryavtsev et al., 2014; Hwang et al., 2015; A. A. Mouche et al., 2017; B. Zhang et al., 2011b; B. Zhang & Perrie, 2012). In particular, the cross-polarized signal reveals higher sensitivity to the sea surface roughness changes, and the occurrence of breaking waves. As such, VH-polarized SAR measurements have already been demon-

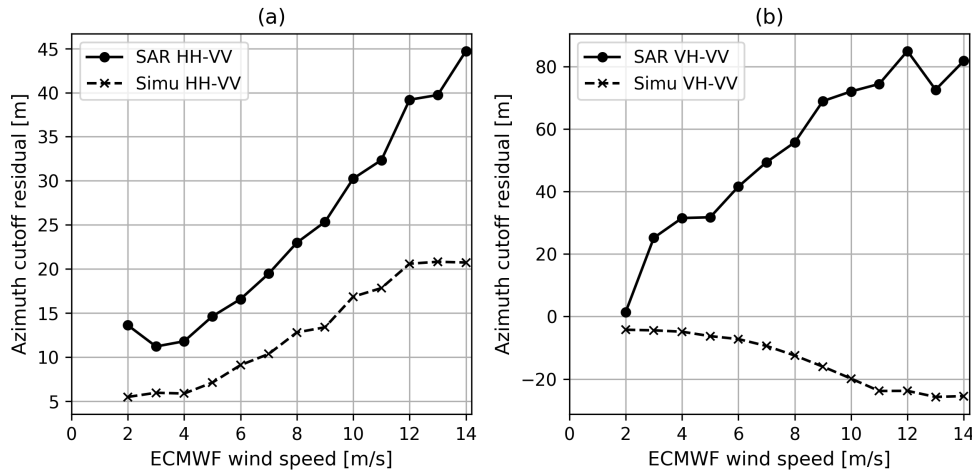


Figure 4.10: Polarization difference of azimuth cutoff relative to the ECMWF wind speed for (a) HH-VV; (b) VH-VV. Solid line is for SAR measurements and dashed line is for the simulation results.

strated to help assess extreme wind conditions (A. A. Mouche et al., 2017; B. Zhang & Perrie, 2012) and/or to depict various surface manifestations of the upper ocean dynamics (internal waves, mesoscale surface current features, and SST fronts et al) (Kudryavtsev et al., 2014). In this study, analyses are performed to better evaluate the distinct imaging capabilities of co- and cross-polarized SAR measurements. More specifically, azimuth cutoff associated with the typical SAR nonlinear imaging distortions are analyzed to document their respective polarization sensitivities.

Taking advantage of the available large number of quad-polarization products acquired by Radarsat-2 and moreover today, by the Gaofen-3 mission, statistically robust trends clearly emerge. For instance, HH azimuth cutoff parameters are generally larger compared to VV estimates, this trend increasing with incidence angle. While more contrasted, with a larger MTF, HH SAR observations are finally more impacted than VV SAR ones, with a larger sensitivity to random motions. To recall, Doppler centroid estimates, mostly governed by the correlation between local tilts and detected velocities (Chapron et al., 2005), have also been reported to be larger for HH than VV signals (A. A. Mouche et al., 2008; Saïd et al., 2015). SAR azimuth cutoff, mostly governed by the overall variance of the detected scatter motions, must thus also reflect an higher sensitivity of HH signals to random surface motions. Despite biases between SAR measurements and simulations, the co-polarized observations can be well reproduced by applying a standard SAR nonlinear forward transform.

By contrast, the increasing trend of VH azimuth cutoff relative to VV could not be attributed to an higher imaging sensitivity. Indeed, the RAR VH MTF is expected to be small compared to

4.5. Summary

co-polarized channels. As such, the SAR nonlinear forward transform does not help to interpret the present analysis. Results imply that the HV detected scatters must be associated to larger and more variable random motions. As mentioned above, cross-polarized signals are sensitive to very enhanced roughness patches, areas over which out-of-plane tilts develop (Kudryavtsev et al., 2014). These rough patches shall then further be characterized by short scene coherence time to explain the resulting VH azimuth cutoffs. Further theoretical investigations are thus required to fully interpret the SAR mapping principles for cross-polarization measurements.

Yet, this feature can already be of more direct use to refine the ocean wave spectral inversion from SAR image measurements. For future SAR polarized systems, including bi-static ones, this measurable sensitivity to both polarization and incidence angle will enhance capabilities to derive more precise ocean surface properties, especially the influence of wave breakers and local wind information, by combining co- and cross-polarization measurements.

Part II

A new SAR parameter and its applications in wind/wave study

Chapter 5

A new SAR parameter: MACS and its directionality

Contents

4.1	Single-polarized azimuth cutoff w.r.t. wind vectors	55
4.1.1	Wind direction	55
4.1.2	Wind speed	56
4.2	Quad-pol data set	57
4.2.1	Radarsat-2	57
4.2.2	Gaofen-3	57
4.2.3	WW3 ocean wave spectrum	58
4.3	Polarized SAR azimuth cutoff	59
4.3.1	A Case study	59
4.3.2	Statistical azimuth cutoff	61
4.4	Azimuth cutoffs from simulations	63
4.4.1	Nonlinear SAR transformation	63
4.4.2	Comparison of SAR and simulation	66
4.5	Summary	68

The SAR image cross-spectral analysis is extended to investigate the time coherence of radar modulations at much smaller scales than swell scales. A new parameter, the MeAn Cross-Spectra (MACS), is defined by filtering SAR cross-spectra within the shortest range-detected scales, i.e. wavelengths between 15 m and 20 m. Given the strong dependence of these intermediate ocean waves to local wind field (Juszko et al., 1995), MACS estimates shall instruct about radar modulation associated to surface waves within their equilibrium range, predominantly related to wind speed and wind direction. By definition, MACS is a complex quantity. As imaginary part of SAR cross-spectra resolves ocean swell direction, the imaginary part of MACS (IMACS) is demonstrated to capture the intermediate wave direction, in other words, wind direction. Analogous to

Doppler anomaly parameter (Chapron et al., 2005; A. A. Mouche et al., 2012), it can thus be used to reduce the wind direction ambiguity in the inversion of high-resolution wind fields. To note, as a normalized quantity, IMACS is independent of any calibration issues (as compared to NRCS and/or attitude precise knowledge). This chapter is based on the paper entitled '*A new ocean SAR cross-spectral parameter: definition and directional property using the global Sentinel-1 wave mode measurements*'.

5.1 Definition of MACS

In this section, the algorithm to estimate SAR image cross-spectra from a SAR image is presented. The new parameter MACS is then defined.

5.1.1 Estimate of SAR image cross-spectra

The relatively long aperture time, $O(1s)$, used to perform the SAR processing can be uniquely exploited. Indeed, it provides means to extract different ocean surface views (sub-looks), corresponding to different epochs, during the SAR acquisition time interval. As such, an along-track temporal correlation analysis can be performed. Resulting temporal shifts must then be associated to organized and coherent (during the acquisition time interval) line-of-sight motions. Such a property is already currently applied to efficiently eliminate incoherent speckle noise, and to help resolve the propagation ambiguity of SAR detected swell systems, longer than the azimuth cut-off (Engen & Johnsen, 1995; Chapron et al., 2001).

The method of computing SAR image cross-spectra from the Single Look Complex (SLC) data has been thoroughly described in (Johnsen & Collard, 2009). A simplified flowchart is given in Figure 5.1 (a). As shown, Sentinel-1 look-up-tables are applied to calibrate the SLC products. Two subsequent pre-processing steps are also performed to eliminate bright targets signal. The procedure 'Detrending' removes the low frequency (non-wave) signatures by low-pass filtering the input image (Johnsen & Collard, 2009). Then, each SLC imagette is split into tiles of 512×512 pixels. From each tile, a Fourier transform (FFT) is performed, and the resulting azimuthal (slow-time) spectrum is divided into three non-overlapping parts as in Figure 5.1 (b). The sub-look intensity images are obtained by applying an inverse FFT to each one of these parts. Finally, co-

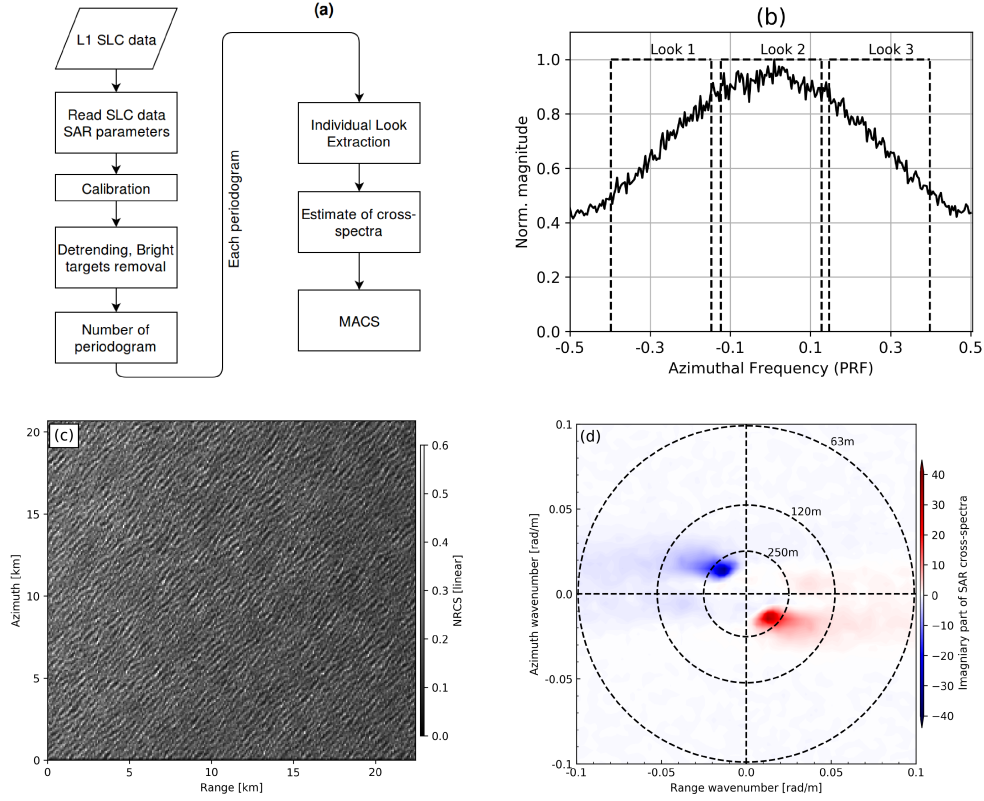


Figure 5.1: (a) Flowchart of SAR image cross-spectral estimate; (b) simplified view of individual look extraction based on Doppler bandwidth spectrum. (c) An example of SAR image acquired by S-1A. Incidence angle is 23.8° . (d) The corresponding imaginary part of SAR cross-spectra computed for $\Delta t = 1\tau$.

and cross-spectra are defined as:

$$P_s^{(m,n)}(\mathbf{k}, \Delta t) = \frac{\langle \mathcal{F}[I^{(m)}(\mathbf{x})] \cdot \mathcal{F}^*[I^{(n)}(\mathbf{x})] \rangle}{\langle I^{(m)}(\mathbf{x}) \rangle \cdot \langle I^{(n)}(\mathbf{x}) \rangle} - \delta(\mathbf{k}), \quad m, n \in [1, 2, 3] \quad (5.1)$$

where $\Delta t = |m - n|\tau$ is separation time between m -th and n -th sub-looks, τ is the time interval between two adjacent looks. In this chapter, $\tau = 0.27 \times T_a$ with T_a being SAR integration time. $\langle I^{(m)}(\mathbf{x}) \rangle$ denotes the mean intensity of the m -th look, $\mathcal{F}[\cdot]$ stands for the two-dimensional FFT operator, and the superscript $*$ is complex conjugate. $\delta(\mathbf{k})$ is a Dirac Delta function. The co-spectrum is obtained when $m = n$. Computed co- and cross-spectra for all tiles are then averaged to reduce speckle noise, leading to one co-spectra and possibly several cross-spectra (obtained for different values of Δt) for each WV image. This averaging technique is referred to as periodogram in the flowchart. Figure 5.1 (c) shows a SAR image acquired by S-1A WV1 and the corresponding imaginary part of SAR cross-spectra for $\Delta t = 2\tau$ in Figure 5.1(d). As shown, one finds that the imaginary part has opposite signs at the symmetric peaks, which is key to resolving the ocean

waves propagation ambiguity.

5.1.2 MACS of intermediate waves

Formally, the SAR nonlinear mapping writes as

$$I_{SAR}(\mathbf{x}) = \int I_{RAR}(\mathbf{x}') \delta(\mathbf{x} - \mathbf{x}' - \xi(\mathbf{x}')) d\mathbf{x}' \quad (5.2)$$

with I_{RAR} the initial detected radar intensity, ξ random shifts, and I_{SAR} the resulting SAR intensity. While this mapping is nonlinear, it still ensures the conservation of the overall mean image intensity, i.e. $\int I_{SAR}(\mathbf{x}) d\mathbf{x} = \int I_{RAR}(\mathbf{x}) d\mathbf{x}$. Accordingly, using a spatial smoothing along the azimuth direction shall best preclude undesirable nonlinear SAR processing effects. Conveniently, this filtering is carried out in the spectral domain by reducing the azimuthal wavenumber domain ($< 2\pi/600 \text{ rad} \cdot \text{m}^{-1}$). MACS parameter is then defined over intermediate range-detected waves, corresponding to filtering the cross-spectra around range (across-track) wavelength between 15 m and 20 m. The lower limit of range wavelength is set to be approximately three times the nominal S-1 line-of-sight ground resolution. It ensures that modulations of interest are sufficiently well resolved.

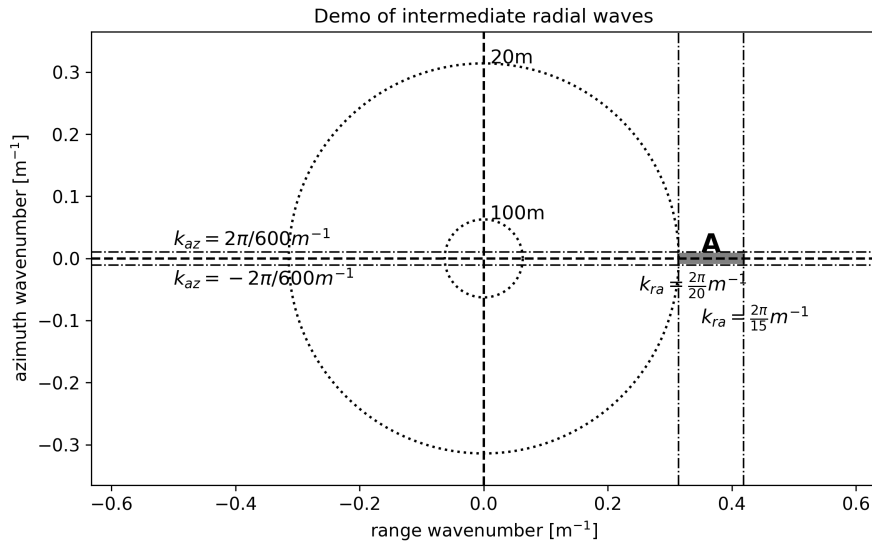


Figure 5.2: A schematic view on extent of intermediate radial waves denoted by 'A' over which to compute MACS. The limits of wavelength used here is 600 m in azimuth and between 15 m and 20 m in range. The dotted circles represent wavelengths of 100 m and 20 m from inner to outer.

A schematic view for this spectral filtering to extract intermediate range waves, and best minimize the SAR azimuthal distortion, is shown in Figure 5.2. The MeAn complex Cross-Spectral density

(MACS) over area 'A' is:

$$\text{MACS}(\bar{k}, \Delta t) = \frac{1}{N} \sum_{n=1}^N P_s^{(m,n)}(k_{az}, k_{ra}, \Delta t), \quad (k_{az}, k_{ra}) \in \mathbf{A} \quad (5.3)$$

where N is number of points within area \mathbf{A} . Cross-spectra can be calculated for different combinations of sub-looks. Throughout rest of this section, we only use MACS defined based on SAR cross-spectra computed between two adjacent sub-looks, denoted as $\text{MACS}^{(1)}$. In terms of cross-spectral transformation (Engen & Johnsen, 1995), $\text{MACS}^{(1)}$ carries both magnitude and phase information of radar backscatter modulations. Assuming that we can neglect the highly reduced contribution from velocity bunching, MACS should be related to the intermediate scale ocean wave information as viewed through the Real Aperture Radar (RAR) Modulation Transfer Function (MTF). MACS may thus contain information related to the two key different imaging contributions (hydrodynamical, tilt) and they may change relative to incidence angle and polarization. In this section, we solely concentrate on the imaginary component of MACS, denoted as $\text{IMACS}^{(1)}$.

5.1.3 Equalization of wave mode data

The Sentinel-1 (S-1) mission is a constellation of two C-band SAR sensors (S-1A and S-1B), launched by European Space Agency (ESA) in April of 2014 and 2016, respectively. Sentinel-1 ensures the continuity of SAR missions in Europe after ENVISAT/ASAR. Over the open ocean, S-1 mostly operates WaVe mode (WV) acquisitions (Torres et al., 2012). Data are publicly available on <https://scihub.copernicus.eu/>. Each imagette is acquired every 100 km following a leap-frog pattern, alternating between two incidence angles (WV1: 23.8 ° and WV2: 36.8 °, respectively). Compared to Envisat/ASAR capability, the size of each imagette has been increased to 20 × 20 km with a 5 m spatial resolution. WV can only be operated in single polarization (VV or HH). In this chapter, we use data acquired by S-1A from December 2016 to November 2017 at VV polarization. To document the polarization sensitivity, HH products acquired by S-1B from 18 March to 31 June in 2017 are considered. Numbers of data are listed in Table 5.1 in detail. It is worth mentioning that products acquired at latitude higher than 55° are filtered out to exclude possible sea-ice contamination.

A match-up dataset is systematically performed to associate the surface winds from ECMWF (European Centre for Medium-Range Weather Forecasts) and the S-1 WV acquisitions. The ECMWF

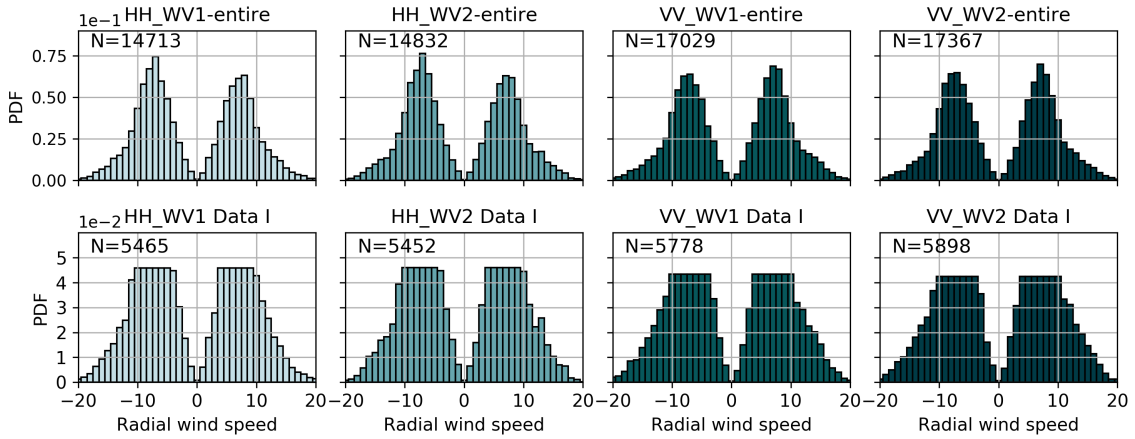


Figure 5.3: (Top) Probability density function (PDF) of collocated radial wind speed between S1A/B and ECMWF for HH and VV, WV1 and WV2, respectively; (bottom) PDF of correspondingly equalized dataset (denoted as Data I). The wind speed bin used here is 1 m/s. Data with wind greater than 20 m/s has been excluded due to lack of enough points. Positive radial winds correspond to upwind direction.

winds have spatial and temporal resolution of 0.25° and 3 hours, respectively.

Table 5.1: Number of data included in this study.

Pol	WV1	WV2
VV (S-1A 2016.12-2017.11)	350,858	350,842
VV (S-1A 2017.03-2017.06)	107,651	108,648
HH (S-1B 2017.03-2017.06)	93,915	94,671

A sub-dataset consisting of upwind/downwind (wind blowing towards/away from the radar look direction) cases is also considered. Specifically, the winds blowing towards (0°) or along (180°) the antenna look direction with a variation of $\pm 10^\circ$ are selected. The wind speed is then referred to as the radial wind speed, ranging from -20 to 20 m/s. In our conventions, positive radial wind values denote upwind conditions (wind blowing towards the antenna look direction, see Figure 5.3). The probability density function (PDF) of co-located dataset relative to the radial wind speed is shown, top panel of Figure 5.3. The bin size of radial wind speed used here is 1 m/s. The relatively nonuniform distribution of data points for intermediate wind speed (around 7 m/s) and high wind (>15 m/s) is evident. As such, we adopt the processing method described in (Stopa & Mouche, 2017a) to equalize this sub-dataset. If there are fewer than 100 data points within a radial wind speed bin, all data points are kept. Otherwise, 100 data points are randomly selected from the dataset within that radial wind speed bin. The equalized dataset is then referred to as Data I. PDFs

of Data I are plotted in bottom panel of Figure 5.3.

5.2 Characteristics of IMACS⁽¹⁾ w.r.t. winds

In this section, the dependence of IMACS⁽¹⁾ on the wind speed and direction is demonstrated based on both global wave mode measurements and a local wide-swath image over the Polar Low.

5.2.1 Directional IMACS⁽¹⁾

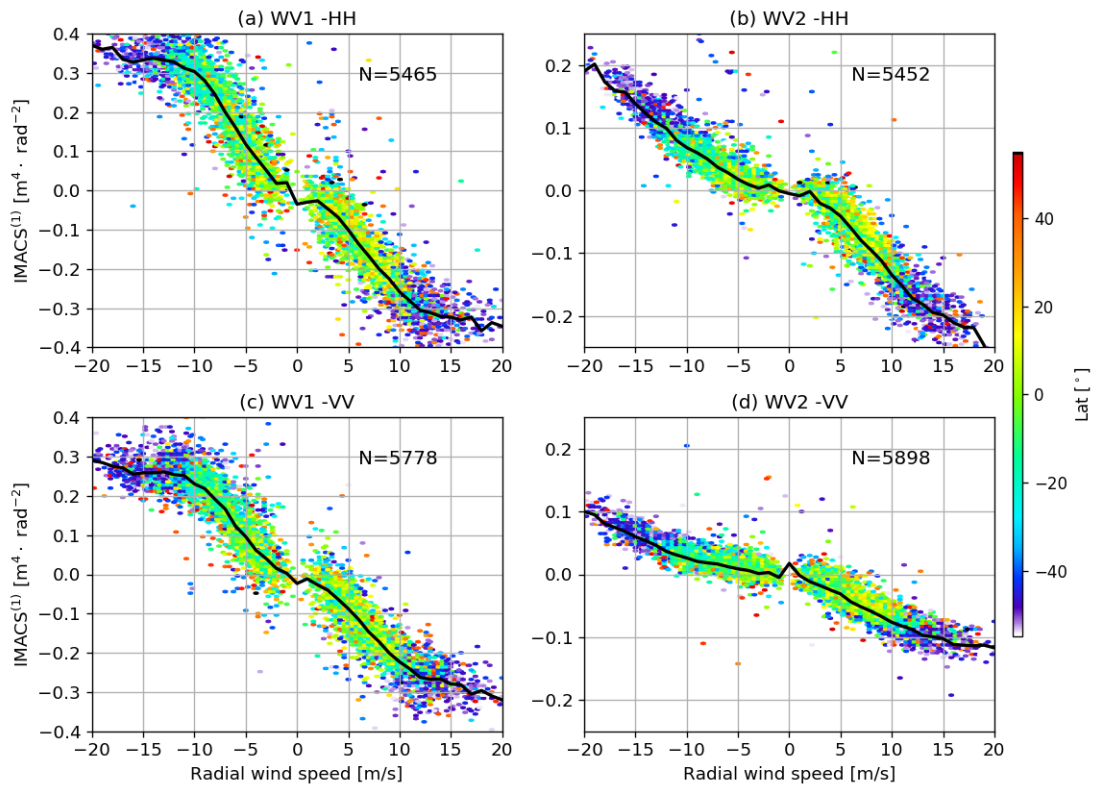


Figure 5.4: IMACS⁽¹⁾ relative to radial wind speed for (a) WV1-HH; (b) WV2-HH; (c) WV1-VV; (d) WV2-VV based on the equalized Data I. 'N' is the number of points used in each plot. The color represents latitude. The solid black line marks the mean curve to the observations. Positive radial wind speeds denote upwind configuration.

Under developed sea state conditions, propagation of intermediate waves shall mostly be in agreement with local wind direction (Juszko et al., 1995; Quilfen et al., 1999). Imaginary component of MACS⁽¹⁾, IMACS⁽¹⁾, is accordingly expected to also provide a quantitative insight on the propagation direction of intermediate (radar-detected) scales. IMACS⁽¹⁾ is displayed relative to radial

5.2. Characteristics of IMACS⁽¹⁾ w.r.t. winds

wind speed in Figure 5.4. As anticipated, IMACS⁽¹⁾ changes sign when wind direction reverses. Statistically, it is positive for downwind direction and negative for upwind.

To first order, it is a linear function of radial wind speed, up to ± 10 m/s. For WV1 in Figure 5.4(a)(c), IMACS⁽¹⁾ have nearly the same slope for upwind and downwind directions. For WV2 in Figure 5.4(b)(d), IMACS⁽¹⁾ is more sensitive under upwind conditions than for downwind ones. For a given radial wind, IMACS⁽¹⁾ is found to decrease with increasing incidence angle. At given incidence angle, IMACS⁽¹⁾ obtained in HH polarization is larger than in VV. This is expected, as HH MTFs have generally been reported larger than VV MTFs, expressing a larger sensitivity to hydrodynamical and tilt modulation effects. A slight saturation of IMACS⁽¹⁾, around wind speed higher than 10 m/s, is apparent for WV1, but not for WV2.

Quite remarkably, as shown in Figure 5.4(a), IMACS parameters share similar characteristics with Doppler Centroid Anomaly (DCA) (Chapron et al., 2005) (see their Figure 5). Indeed, both parameters are directly linked to the temporal evolution and coherency of detected sea surface scatters. The DCA encompasses all detected scales, and estimates are performed using cross-correlation between consecutive (in time) complex signals. For IMACS, it is the coherency and time evolution of filtered reflectivity modulations which are captured. As such, the cross-correlation can apply between intensity signals acquired at larger time differences. For IMACS, the cross-correlation will measure the coherency and time evolution of the filtered modulations of the intensity signals. Under a two-scale scattering model decomposition (see Appendix B in (Chapron et al., 2005), also Eq.(3) in (Johannessen et al., 2008)), such intermediate scale time evolution contribute to the DCA parameter. To first order, both parameters, DCA and IMACS, must be strongly linked, closely tracing the wind direction within a single SAR imagette. To date, the lack of accurate satellite AOCS (Attitude and Orbital Control System) information hampers S-1 DCA interpretation, as the geometric DC accuracy is not sufficient. This is not as stringent for IMACS⁽¹⁾. A precise time or Doppler origin is not required, as IMACS can isolate the ocean scene time evolution by matching detected (and filtered) modulations of intensity signals. Accordingly, IMACS⁽¹⁾ can therefore be an alternative to DCA measurements to help constrain ocean surface wind vector estimate at moderate to high spatial resolution (A. A. Mouche et al., 2012).

To note, analyses of IMACS⁽¹⁾ can also be extended to other (longer) wavelengths. For instance, over tropical hurricanes with local wind speed exceeding 30 m/s, integrating IMACS⁽¹⁾ over ocean scales of 100 m would be more appropriate.

5.2.2 Wind direction dependency of IMACS⁽¹⁾

In this section, the IMACS⁽¹⁾ dependency on wind direction is demonstrated. For simplicity, only acquisition of WV1 at VV polarization is involved. Figure 5.5 (a) displays the IMACS⁽¹⁾ relative to wind direction at wind speed of 7 m/s (dots). The mean is marked as solid curve. It closely follows a cosine function across wind direction. IMACS⁽¹⁾ reaches minimum at upwind (0°), maximum at downwind (180°). Again, azimuthal modulation of IMACS⁽¹⁾ is found similar to that of DCA, as shown in (A. A. Mouche et al., 2012). Analogous to DCA (see Fig.2(e) in (A. A. Mouche et al., 2012)), a wind retrieval algorithm using NRCS and IMACS⁽¹⁾ would reduce the possible wind solutions to two. Resolving the remaining two ambiguities is therefore crucial to develop an independent SAR wind retrieval.

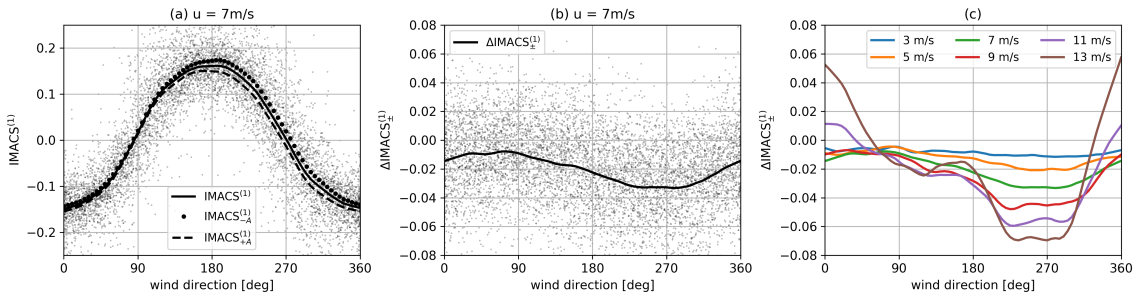


Figure 5.5: (a) Scatter plot of IMACS⁽¹⁾ relative to wind direction at wind speed of 7 m/s. Binned average of IMACS⁽¹⁾ (solid), IMACS⁽¹⁾_{+A} (dashed) and IMACS⁽¹⁾_{-A} (dotted) are also plotted. (b) Δ IMACS⁽¹⁾_± (IMACS⁽¹⁾_{+A} - IMACS⁽¹⁾_{-A}) at 7 m/s. (c) Δ IMACS⁽¹⁾_± relative to wind direction for various wind speeds. Wind direction of 0° denotes upwind.

As defined, IMACS⁽¹⁾ is concentrating on information close to the radar range direction, precisely filtering over $\pm 2\pi/600 \text{ rad} \cdot \text{m}^{-1}$ along the azimuth direction in Figure 5.2. To help discriminate the contributions between azimuthal quadrants, IMACS⁽¹⁾ is then further decomposed into two parts. The part defined over $[-2\pi/600 \text{ rad} \cdot \text{m}^{-1}, 0]$ is denoted as IMACS⁽¹⁾_{-A} and the other over $[0, 2\pi/600 \text{ rad} \cdot \text{m}^{-1}]$ is IMACS⁽¹⁾_{+A}. For wind speed at 7 m/s, these two parameters are reported in Figure 5.5(a). Estimates are different, especially for the two crosswind directions (90° and 270°). At 90°, IMACS⁽¹⁾_{+A} (dashed line) is almost identical to IMACS⁽¹⁾_{-A} (dotted line) as well as IMACS⁽¹⁾ (solid line). At 270°, the deviation between IMACS⁽¹⁾_{+A} and IMACS⁽¹⁾_{-A} increases. Variation of their deviation Δ IMACS⁽¹⁾_± versus wind direction is accordingly quantified in Figure 5.5(b). Notice that Δ IMACS⁽¹⁾_± exhibits distinct azimuthal modulation than IMACS⁽¹⁾. It is close to zero at crosswind of 90° and decreases to its minimum at 270°. This contrast between two crosswinds increases with wind speed as shown in Figure 5.5(c). At low wind speed (<3 m/s), ocean wave features are not

5.2. Characteristics of $\text{IMACS}^{(1)}$ w.r.t. winds

sufficiently well resolved due to low signal-to-noise ratio. This can explain the low contrast of $\Delta \text{IMACS}_{\pm}^{(1)}$ across wind directions at 3 m/s. With wind speed increasing, the contrast becomes pronounced. This distinguished wind direction dependence can thus help resolve the wind direction ambiguities, to provide means to obtain one single wind vector. The wind inversion scheme using $\Delta \text{IMACS}_{\pm}^{(1)}$ is beyond scope of the present thesis. Present efforts are underway (Nilsen et al., 2018), and left to further validation efforts.

5.2.3 $\text{IMACS}^{(1)}$ over a Polar Low

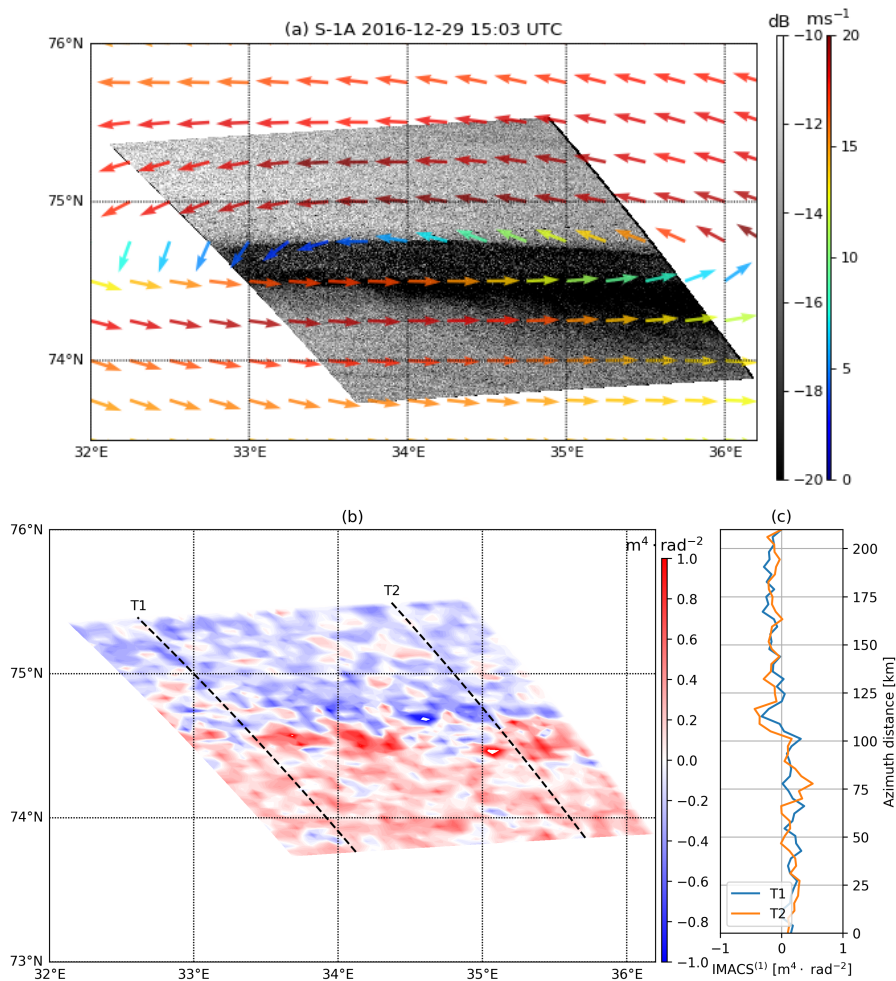


Figure 5.6: (a) NRCS representation acquired by S-1A Interferometric Wide swath (IW) on 29 December, 2016 at 15:03 UTC over a Polar Low. ECMWF forecast winds at 15h00 UTC are superimposed as arrows with colors denoting wind speed. (b) $\text{IMACS}^{(1)}$ computed over moving window. (c) $\text{IMACS}^{(1)}$ along two transects depicted by two black lines in plot (b).

Statistically, Figure 5.4, $\text{IMACS}^{(1)}$ parameters capture radial wind information. Hereafter, a particular local event is more precisely analyzed.

5.3. Spatial pattern of IMACS⁽¹⁾

Figure 5.6(a) presents a SAR image of C-band HH Normalized Radar Cross-Section (NRCS) over a polar low event. Data have been acquired by S-1A, in the Interferometric Wide swath (IW) mode, on 29 December, 2016 at 15:03 UTC. The incidence angle at near range is 41.2° and 45.5° at far range. ECMWF forecast winds at 15h00 UTC are superimposed to complement the NRCS interpretations. This event was an intense meso-scale extra tropical cyclone, quite typical over oceans at high-latitude in cold polar areas (Montgomery & Farrell, 1992; Smirnova et al., 2015). In the northern hemisphere, the winds rotate counterclockwise. Considering the SAR flight direction, towards the North in this case, it corresponds to upwind conditions (blowing against the antenna pointing) in the northern sector, and subsequently, downwind conditions in the southern sector. Given the distinct up-downwind asymmetry of NRCS at this incidence angle, a darker pattern is indeed found in the southern sector. However, at this point, it is difficult to interpret wind variation without use of external ancillary information, such as the ECMWF wind direction. By comparison, IMACS⁽¹⁾ parameters, mapped on Figure 5.6 (b), clearly provide first-order directional information of local winds. The opposite sign of IMACS⁽¹⁾ (blue to red) well captures the reversed wind direction as in Figure 5.6(a). This is better presented by the averaged IMACS⁽¹⁾ along the two transects in Figure 5.6(c). IMACS⁽¹⁾ at transect 'T1' and 'T2' has comparable magnitude, corresponding to the comparable wind speed and direction as given by ECMWF winds. In addition, magnitude of IMACS⁽¹⁾ is roughly consistent with that in Figure 5.4(b) (different incidence angles), implying the mobility of MACS analysis between various SAR imaging mode. It should also be noted that over the central part, IMACS⁽¹⁾ is not trustworthy, likely due to low signal-to-noise ratio.

5.3 Spatial pattern of IMACS⁽¹⁾

As demonstrated, IMACS⁽¹⁾ is complementary to the conventional NRCS measurements. Free from any calibration issues, IMACS⁽¹⁾ essentially contains information related to coherent time evolution of filtered radar modulations. As already mentioned, it is related to the local equilibrium part of the wind wave spectra weighted by the C-band RAR MTF. Therefore, analysis of IMACS⁽¹⁾ not only relates to local wind climate, but more directly to intermediate scale wave climate.

5.3.1 Global map of IMACS⁽¹⁾

Seasonal average of IMACS⁽¹⁾ is presented in Figure 5.7, grouped as June-July-August (JJA), and September-October-November (SON), December-January-February (DJF), March-April-May (MAM). S-1A WV1 acquisition from December 2016 to November 2017 over ascending pass is solely considered. The white areas are due to lack of observation. They are close to coastlines and over the northeast Atlantic Ocean where other acquisition modes are operated. These results are produced with observations acquired at latitude lower than 55° to avoid potential ice-sea contamination. The same convention than in Figure 5.4 is used, the negative values correspond to upwind direction (wind blowing from east to west).

In tropics (30°S – 30°N), the prevailing trade winds are blowing from the east to the west. It thus corresponds to upwind conditions for ascending passes, resulting in consistently negative IMACS⁽¹⁾ parameters. The migration of the intertropical convergence zone (ITCZ) is clearly well captured by the seasonal sign changes of IMACS⁽¹⁾. For JJA (Figure 5.7(c)) and SON (Figure 5.7(d)), ITCZ is located north of the Equator, about latitude 10°N, extending to the west Pacific Ocean. For the other two seasons, the ITCZ moves southward and locates at the Equator with shrunken zonal extension.

At mid-latitudes (30° – 60°), westerlies blow from the west to the east, i.e. downwind conditions. Accordingly, positive IMACS⁽¹⁾ are obtained. The Southern Hemisphere extra tropics are very consistent with high magnitude of IMACS⁽¹⁾. This is associated to the regular storms over this area throughout the year. During the season DJF, Figure 5.7(a), exhibits maximum IMACS⁽¹⁾ in northwest Pacific Ocean, caused by high winds of winter storms. Lack of data precludes this feature to appear over the Atlantic Ocean. As also clearly observed, boundaries between the trade winds and westerlies vary with seasons. In details, the boundary migrates southward from summer to winter, consistent with the motion of ITCZ.

5.3.2 IMACS⁽¹⁾ over the east Pacific Ocean

To further document the ITCZ migration captured by IMACS⁽¹⁾, a more local analysis is performed. It corresponds to the region delineated by a red rectangle in Figure 5.7(a), extending over the east Pacific Ocean (2°N – 12°N in latitude and 125°W – 95°W in longitude). Seasonal probability density function (PDF) of NRCS as well as IMACS⁽¹⁾ are shown Figure 5.8 (a) and (b), respectively.

5.3. Spatial pattern of $IMACS^{(1)}$

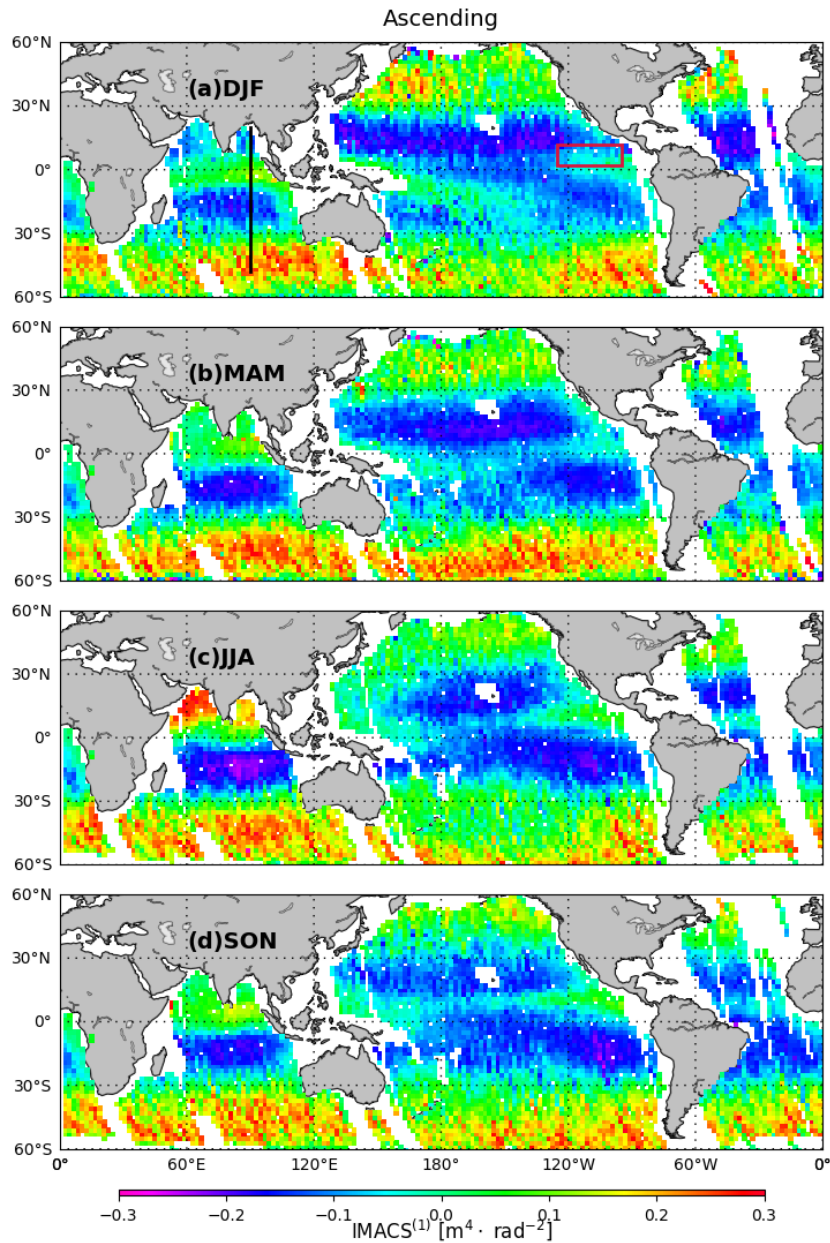


Figure 5.7: Seasonal global map of $IMACS^{(1)}$ based on data acquired by S-1A WV1 over ascending pass from December 2016 to November 2017. The negative $IMACS^{(1)}$ corresponds to upwind direction with wind roughly blowing from the east to the west. Data are averaged on a spatial bin of 2° in both longitude and latitude.

From PDF of NRCS, the maximum point is steady with seasons, being around 0.1687 (linear unit). The wider PDF in DJF and MAM implies larger spread of local winds, but gives no further details. On the contrary, PDF of $IMACS^{(1)}$ greatly differs from JJA to DJF. The maximum point in JJA and SON is located around +0.010, suggesting the prevailing winds to have small zonal components. For DJF and MAM, the maximum shifts towards -0.055, corresponding to winds blowing from the east. As obtained, PDF of $IMACS^{(1)}$ have larger spread for DJF/MAM than for JJA/SON. Given the

5.3. Spatial pattern of IMACS⁽¹⁾

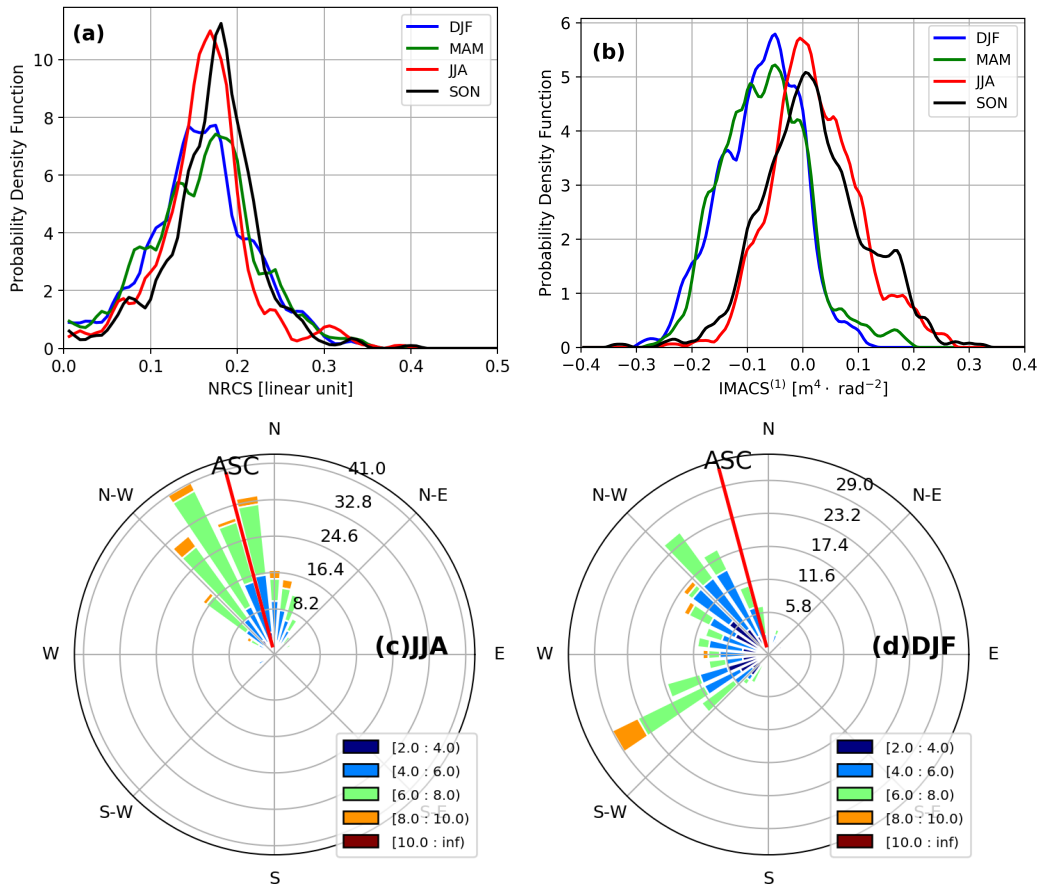


Figure 5.8: Probability Density Function (PDF) of (a) NRCS and (b) IMACS⁽¹⁾ over the east Equatorial Current area (marked by red rectangle in Figure 5.7(a)) are presented for four seasons. The wind rose of collocated ECMWF winds is also depicted for (c) season of JJA; (d) season DJF.

analogy between JJA (DJF) and SON (MAM), wind rose of collocated ECMWF forecast winds are displayed for JJA in Figure 5.8(c) and DJF in Figure 5.8(d). During JJA, most of local winds mostly blow along the SAR ascending flight direction, resulting in nearly zero IMACS⁽¹⁾, Figure 5.8(b). For DJF, winds blowing from the east are predominant and have large spread. Based on this analysis, the NRCS measurements are not sufficient to manifest the seasonal migration of ITCZ. But, combined NRCS and IMACS⁽¹⁾ may open new strategies to determine global wind/wave climatologies.

5.3.3 IMACS⁽¹⁾ along the Indian Ocean

Over the Indian Ocean, there is also a distinct seasonality captured by IMACS⁽¹⁾ estimates. North of the Equator, IMACS⁽¹⁾ is negative in DJF/MAM, positive in JJA/SON. The sign change is to be attributed to reversed winds during the monsoon season (usually occurring from July to October).

5.3. Spatial pattern of IMACS⁽¹⁾

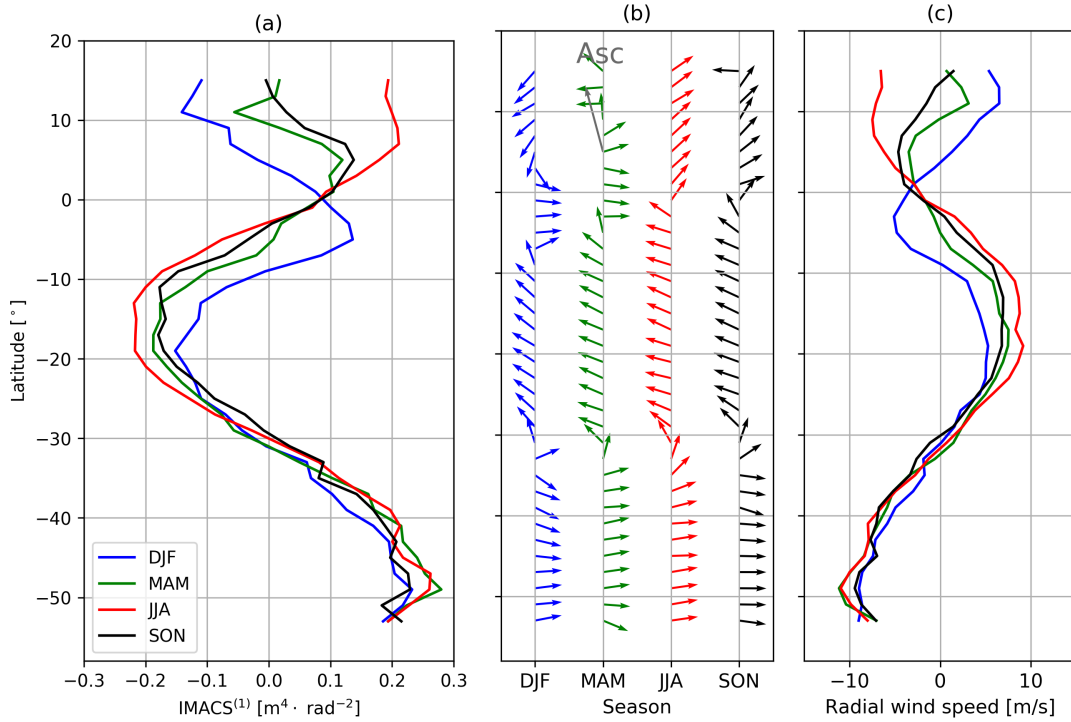


Figure 5.9: Seasonal average of (a) IMACS⁽¹⁾, (b) collocated ECMWF wind direction and (c) projected radial wind speed relative to latitude along the transect of 90°E shown as vertical black line in Figure 5.7(a). Data are averaged over latitude bin of 2°. The gray arrow denotes SAR flight direction over ascending pass. Wind convention is the same with Figure 5.7.

A different rate of sign changes of IMACS⁽¹⁾ is well captured from north to south, across the Indian Ocean. A transect at longitude 90°E is chosen to help analyze this seasonal pattern of IMACS⁽¹⁾. Seasonal average of IMACS⁽¹⁾ and wind direction along the transect are given in Figure 5.9(a)(b), respectively. During JJA (red curve) and SON (black curve), IMACS⁽¹⁾ decreases from positive to negative at latitude 5°S to reaches a negative maximum at 18°S. It then starts to increase from negative to a positive maximum at 50°S. Marked features of IMACS⁽¹⁾ during DJF (red line) and MAM (green line) are north of the Equator. During DJF, IMACS⁽¹⁾ is first negative to inverse its sign, becoming positive at latitude 3°N. The sign change from positive to negative more precisely occurs at latitude 9°S. The IMACS⁽¹⁾ variation is consistent with wind direction change shown by projected radial ECMWF winds in Figure 5.9(c).

This strong seasonal variation of IMACS⁽¹⁾ is further quantified by the inter-seasonal variability, Figure 5.10. It is computed as the standard deviation of seasonal average of IMACS⁽¹⁾. A larger variability of IMACS⁽¹⁾ occurs over the Northern Hemisphere. Around 40°N in Northern Hemisphere, the largest seasonal variability is estimated. In the Southern Hemisphere, IMACS⁽¹⁾ parameters have smaller standard deviation at 50°S. By contrast, IMACS⁽¹⁾ is largely variable, throughout

5.4. Summary

the year, at longitude between 160°W and 130°W. The Indian monsoon region also presents higher IMACS⁽¹⁾ variance. This is caused by reversed wind directions during the monsoon season, Figure 5.7. By comparison, trade wind regions over the Pacific Ocean display much lower variability. A band of increased variability is evident, centered at 10°N on the Pacific Ocean. It corresponds to wind field changes over the ITCZ, Figure 5.8. This band extends to the west Pacific Ocean. Over the Indian Ocean, a zonal band of distinct standard deviation, centered at 10°S, is also associated to wind direction changes, Figure 5.9.

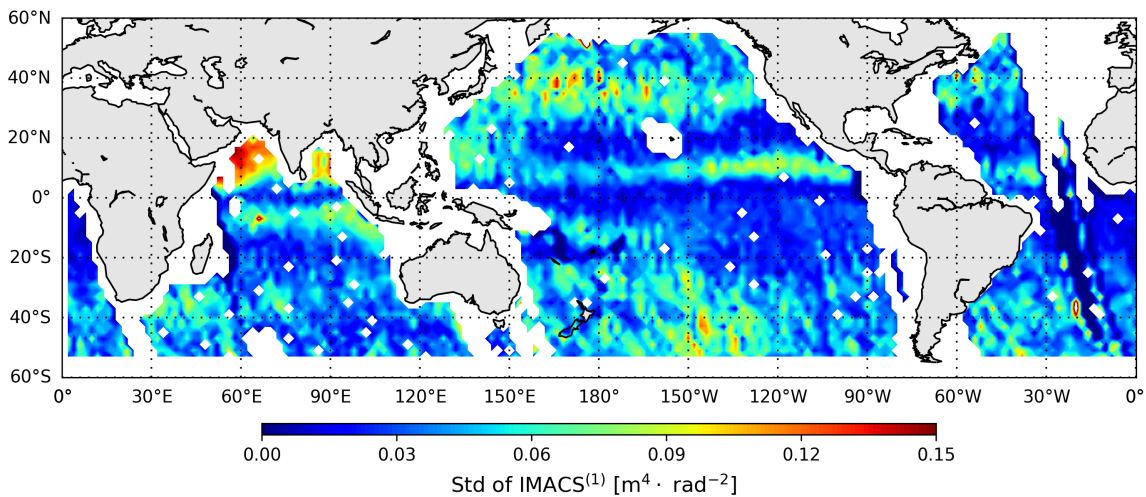


Figure 5.10: Inter-seasonal standard deviation of IMACS⁽¹⁾ computed from seasonal average given in Figure 5.7.

Due to lower operation priority of S-1A WV close to coastal areas and over the Atlantic Ocean, there are no WV data available over these regions. Nevertheless, the climatological pattern of IMACS⁽¹⁾ is consistent with previous wind and wave climate studies. IMACS⁽¹⁾ would certainly bring some new perspectives to jointly analyze wind and equilibrium wave range climate by considering an adaptive definition over various wavelengths.

5.4 Summary

To best isolate expected ocean surface wave motions, we apply an along-track temporal correlation analysis on highly resolved Sentinel-1 SAR measurements. High-pass filtered in the range direction, the time coherency of radar modulations is robustly evidenced to be a measurable geophysical quantity. Specifically, a proposed newly defined MeAn Cross-Spectra (MACS) parameter carries signed information relative to wind direction.

5.4. Summary

For upwind or downwind conditions, a signed and nearly linear variation is obtained. This result bears strong similitude with the Doppler Centroid Anomaly (DCA) sensitivity to radial wind speed (see Fig. 5b in (Chapron et al., 2005)). As understood, MACS is the result of an overall correlation between surface wave motions and filtered (radar) detected contrasts, in line with a two-scale interpretation of the wave motion bias associated to DCA measurements (see Eq. B1 in (Chapron et al., 2005), and Eq.(3) in (Johannessen et al., 2008)). Comparable to previous developments (A. A. Mouche et al., 2012), such dependencies are complementary to NRCS measurements, and open for new analysis strategies. As first anticipated and demonstrated with a Polar Low case, these two high-resolution radar quantities, i.e., NRCS and MACS (possibly DCA when available), should be advantageously used to help constrain local wind retrieval schemes from SAR measurements. Providing improved local wind estimates shall also have positive impact on SAR-wave retrieval algorithms to more precisely inform the local sea state conditions.

Moreover, given the close dependency of MACS to the strength of the local radial wind component, MACS may also have the potential to more directly help remove the wave bias contribution from DCA estimates. This step is essential to recover the geophysical Doppler information solely related to ocean surface current. In that context, MACS estimates can help bypass the need of *a priori* wind information (e.g. (Rouault et al., 2010; A. C. H. Martin et al., 2016)). Such a demonstration is beyond the scope of the present paper, and will be the focus of future studies, possibly revisiting Envisat/ASAR previous analysis. This can also establish the data processing basis for future ocean satellite mission (e.g. (A. C. Martin et al., 2018)). From its definition, MACS parameter can also be refined to encompass bi-frequency or bi-location beam instrumental configuration, as well as highly range resolved real aperture radar measurements (Nouguier et al., 2018; Ardhuin et al., 2018).

Finally, as further demonstrated in the present study, global mapping and analysis of MACS can efficiently quantify regional and seasonal wind and (intermediate) wave properties (periodicities and space-time variabilities). As such, this new parameter may support wind and wave climate studies. This aspect leads us to revisit the available ten-year archive of ENVISAT/ASAR wave mode data. Given a relatively coarser resolution (10 m) compared to Sentinel-1, the filtering operation shall certainly be adapted, i.e. possibly down to 50 m scales. This new parameter can also be used to jointly analyze wind and equilibrium wave range climate by considering an adaptive definition over various wavelengths. Still, for moderate to high wind conditions, MACS parameters will likely carry valuable information related to radial wind conditions to enhance previous attempts (Stopa et al., 2015b) to more precisely document long-term wind/wave climate properties.

Chapter 6

Statistics of MACS magnitude and derived RAR MTF

Contents

5.1	Definition of MACS	73
5.1.1	Estimate of SAR image cross-spectra	73
5.1.2	MACS of intermediate waves	75
5.1.3	Equalization of wave mode data	76
5.2	Characteristics of IMACS⁽¹⁾ w.r.t. winds	78
5.2.1	Directional IMACS ⁽¹⁾	78
5.2.2	Wind direction dependency of IMACS ⁽¹⁾	80
5.2.3	IMACS ⁽¹⁾ over a Polar Low	81
5.3	Spatial pattern of IMACS⁽¹⁾	82
5.3.1	Global map of IMACS ⁽¹⁾	83
5.3.2	IMACS ⁽¹⁾ over the east Pacific Ocean	83
5.3.3	IMACS ⁽¹⁾ along the Indian Ocean	85
5.4	Summary	87

The new parameter, MACS, captures 20 m waves traveling in the range direction is expected to provide new insights into SAR imaging processes. In particular we can assess any differences in the polarizations to improve our understanding of the radar response to the sea surface. Since we specifically define the MACS parameter to limit the effect of nonlinear SAR distortions, we can also put focus on assessing the RAR MTF relative to polarization and incidence angle.

In this chapter, we continue to explore behavior of MACS magnitude using dual-polarization data acquired by S-1A (VV polarization) and S-1B (HH polarization). Two aspects are addressed. We first document the statistical properties of MACS, including azimuthal modulation relative to wind direction, upwind-to-downwind asymmetry (UDA) and upwind-to-crosswind asymmetry (UCA) as well as polarization ratio (PR). An improved RAR modulation is then derived through comparison

with the simulated MACS based on the present SAR nonlinear transformation. This chapter is based on the paper entitled '*A new ocean SAR cross-spectral parameter: magnitude and its application in deriving the RAR MTF*'.

6.1 Speckle noise of $\text{MMACS}^{(0)}$

In this section, the reason to use $\text{MMACS}^{(0)}$ is first discussed. The removal of speckle noise from the $\text{MMACS}^{(0)}$ is then presented.

6.1.1 Usage of $\text{MMACS}^{(0)}$

By definition, MACS could be considered as RAR MTF weighted intermediate wave spectral density. As such, magnitude of MACS shall readily reveal quantitative information of RAR modulation. Better understanding of RAR modulation is crucial to improve accuracy of ocean wave spectrum inversion from a SAR image. To first-order, the intermediate waves can be considered in equilibrium range with sea surface wind. According to (Phillips, 1985), the intermediate wave spectral density is proportional to wind friction velocity, e.g. neutral wind speed. In other words, for given wind speed, spectral density of intermediate waves can be approximated as a constant, independent of radar configurations (such as incidences, polarizations and etc.). Though $\text{MMACS}^{(1)}$ is free of noise, additional decorrelation mechanisms between co-spectra and cross-spectra has been reported in (Schulz-Stellenfleth & Lehner, 2005). This would bias the derivation of RAR modulation from $\text{MMACS}^{(1)}$. As an alternative, we firstly attempted to remove noise contribution from SAR-measured $\text{MMACS}^{(0)}$. The characteristics of noise-free $\text{MMACS}^{(0)}$ as well as its application to derive RAR modulation are then discussed respectively.

6.1.2 Removal of speckle noise

The common description of a SAR intensity image is based on a multiplicative noise model. Assuming a white speckle noise as in (Engen & Johnsen, 1995), it is straightforward to find that the speckle noise contributes to SAR image variance spectrum $\text{MMACS}^{(0)}$ as a noise floor. A similar conclusion has been made in (Schulz-Stellenfleth & Lehner, 2005) but it is given in a different analytical expression. To be specific, the impact of speckle noise is related to both SAR system

transfer function and normalized variance of RAR image in the former model, while the latter only associates it to SAR spatial resolution. Both models are established on the hypothesis that a SAR has perfect sensitivity with zero thermal noise. In reality, this hypothesis is not valid. Thus, the total noise contribution including speckle noise and system thermal noise cannot be completely removed by simply deducting the analytical noise floor from $MMACS^{(0)}$. Since variance of RAR image is also hard to measure, we therefore assumed a global noise floor as in the latter model.

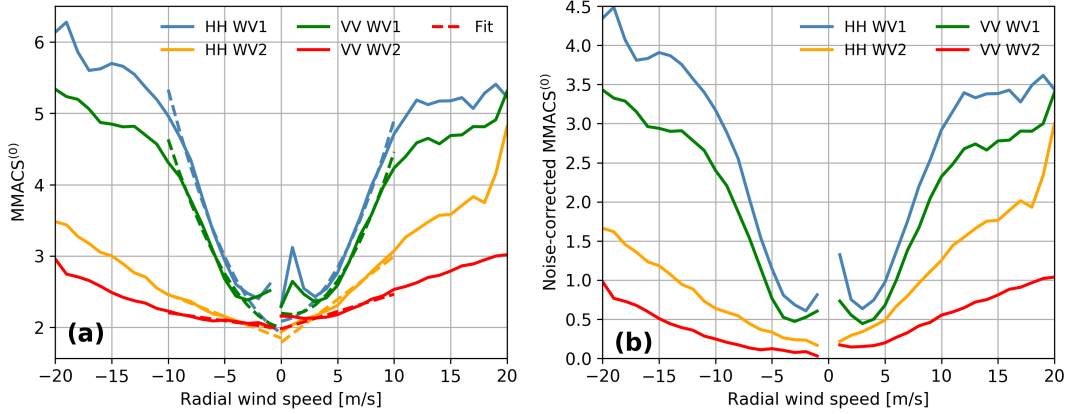


Figure 6.1: (a) The solid lines represent best fit to SAR-measured $MMACS^{(0)}$ for wind directions along the range ($\pm 10^\circ$), containing contribution of noise. Dashed lines are polynomial fit to the observations in an effort to infer noise floor, which is equal to $MMACS^{(0)}$ at wind speed of 0 m/s. (b) noise-free $MMACS^{(0)}$ after deducting global noise floor. Positive winds are upwind (wind blowing against the antenna).

In this section, we use data with wind direction on the range to determine this global noise floor. The best mean fit of SAR-measured $MMACS^{(0)}$ is presented in Figure 6.1(a). It can be seen that $MMACS^{(0)}$ decreases gradually from wind speed of 10 m/s to 4 m/s. At wind speed lower than 3 m/s, signal-to-noise ratio is low and the radar backscattering is subject to local sea state conditions. Sometimes, presence of surface surfactant or atmospheric turbulence could contaminate the surface scattering. One can find the irregular variation of $MMACS^{(0)}$ at low wind speed as shown in Figure 6.1(a). It gives rise to biases in seeking the noise floor at wind speed of 0 m/s. We carefully examine the decreasing trend of $MMACS^{(0)}$ at wind speed higher than 3 m/s and find that an extrapolation based on polynomial fit can be used to infer $MMACS^{(0)}$ at wind speed of 0 m/s. The value of $MMACS^{(0)}$ is assumed as the global noise floor independent of wind speed and is deducted from SAR measurement to obtain noise-free $MMACS^{(0)}$.

The dashed curves in Figure 6.1(a) are polynomial fit to SAR-measured $MMACS^{(0)}$ for wind speed ranging from 3 m/s to 10 m/s. It should be pointed out downwind and upwind are fitted separately, resulting in two slightly different values at wind speed of 0 m/s as shown in the plot. Average

of these two values is adopted as the final noise floor for given polarization and WV. The noise-corrected MMACS⁽⁰⁾ is accordingly shown in Figure 6.1(b). At low wind conditions, MMACS⁽⁰⁾ for WV1 still suffers from local contamination, which is not present for WV2. In the following, noise-free MMACS⁽⁰⁾ is used throughout rest of this chapter unless particularly stated.

6.2 Statistics of noise-free MMACS⁽⁰⁾

In this section, the characteristics of noise-free MMACS⁽⁰⁾ are presented in terms of the incidence angle, polarizations and wind speed and wind direction.

6.2.1 Azimuthal modulation

For microwave radars, NRCS is one measure used to describe the backscattering of illuminated sea surface. It is mainly determined by the scattering from centimeter-scale Bragg waves. To date for C-band radars, the dual-polarization NRCS has been widely studied with respect to sea surface winds and incidence angles through empirical Geophysical Model Functions (GMF) (Hersbach, 2008; A. Mouche & Chapron, 2015a). Polarization sensitivity of NRCS has also been addressed with routine SAR acquisitions (B. Zhang et al., 2011a; A. Mouche & Chapron, 2015a). The available NRCS GMF for dual-polarization C-band data allows us to examine the polarization sensitivity of empirical RAR modulation. However, the sophisticated procedures needed to derive RAR modulation from SAR observations has hindered its validation with empirical model on a statistical basis. The spectral analysis of MACS localizes the RAR modulation of intermediate waves, providing an alternative manner to directly investigate the RAR modulation. This thus facilitates the comparison of the C-band RAR MTF under various conditions: 1) polarizations, 2) incidence angles and 3) surface wind field.

NRCS and MMACS⁽⁰⁾ are plotted relative to the wind direction for dual-polarizations at given wind speed of 7 m/s in Figure 6.2. A fit to observed NRCS is carried out with the harmonics function in form of

$$\sigma_0^{PP} = a_0^{PP} + a_1^{PP} \cos(\phi) + a_2^{PP} \cos(2\phi) \quad (6.1)$$

where the superscript ^{PP} denotes polarization either VV or HH here. For WV1, both VV and HH NRCS show similar azimuthal modulation with VV NRCS slightly greater than HH NRCS. While

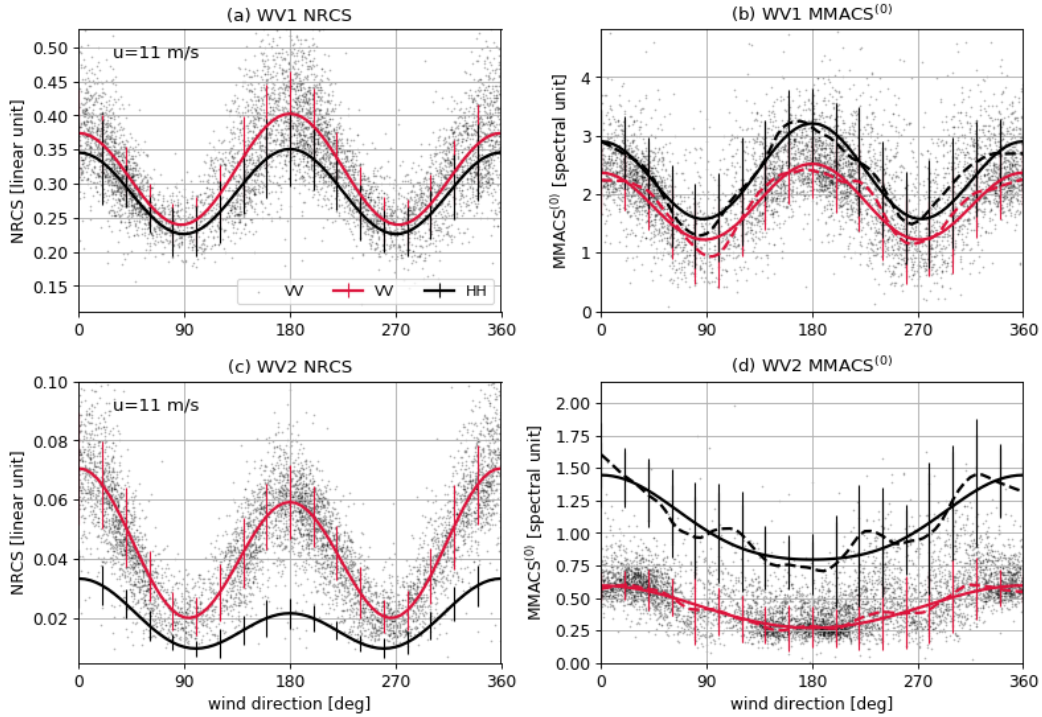


Figure 6.2: The left panel is NRCS as function of wind direction at 9 m/s in (a) WV1; (b) WV2. The right panel is $MMACS^{(0)}$ in (c) WV1; (d) WV2. The dashed line represents the mean and solid line marks fit curve in form of Eq.(6.1) to the observations. The wind direction of 0° is upwind and 180° downwind.

for WV2, NRCS in VV exhibits deeper azimuthal modulation with largely greater values than in HH. The observations agree well with the documented results that NRCS polarization difference increases with incidence angle (A. Mouche & Chapron, 2015a).

Figure 6.2(b) presents $MMACS^{(0)}$ for WV1. As shown, both VV and HH $MMACS^{(0)}$, to first order, follow similar functional curves of wind direction as NRCS does. A fit to $MMACS^{(0)}$ in form of Eq.(6.1) is carried out. HH $MMACS^{(0)}$ is slightly larger than VV, resulting from greater RAR modulation in HH than in VV (W. R. Alpers et al., 1981). In contrast to NRCS in Figure 6.2(a), HH $MMACS^{(0)}$ illustrates a deeper azimuthal modulation than that of VV. $MMACS^{(0)}$ of WV2 is given in Figure 6.2(d). With increasing incidence angle, the deviation between VV and HH $MMACS^{(0)}$ augments as the NRCS does but with greater $MMACS^{(0)}$ in HH than in VV. $MMACS^{(0)}$ of WV2 also exhibits distinguished trend with half period of cosine function. It first decreases and reaches the minimum at downwind and then increases. This great upwind/downwind asymmetry is unique to WV2 despite of wind speed (curves for other wind speeds are not shown here).

In addition, variation of standard deviation (std) for NRCS also differs from that for $MMACS^{(0)}$. In specifics, NRCS has maximum std at upwind and downwind as in Figure 6.2(a)(c). While std

of MMACS⁽⁰⁾ reaches the maximum at crosswinds and decreases to the minimum at upwind and downwind. In particular, std of NRCS does not show much polarization difference for both WV1 and WV2. However, std of HH MMACS⁽⁰⁾ is much greater than VV across all wind directions at WV2 in Figure 6.2(d). This is expected because range intermediate ocean waves would show approximately random variation at crosswind conditions.

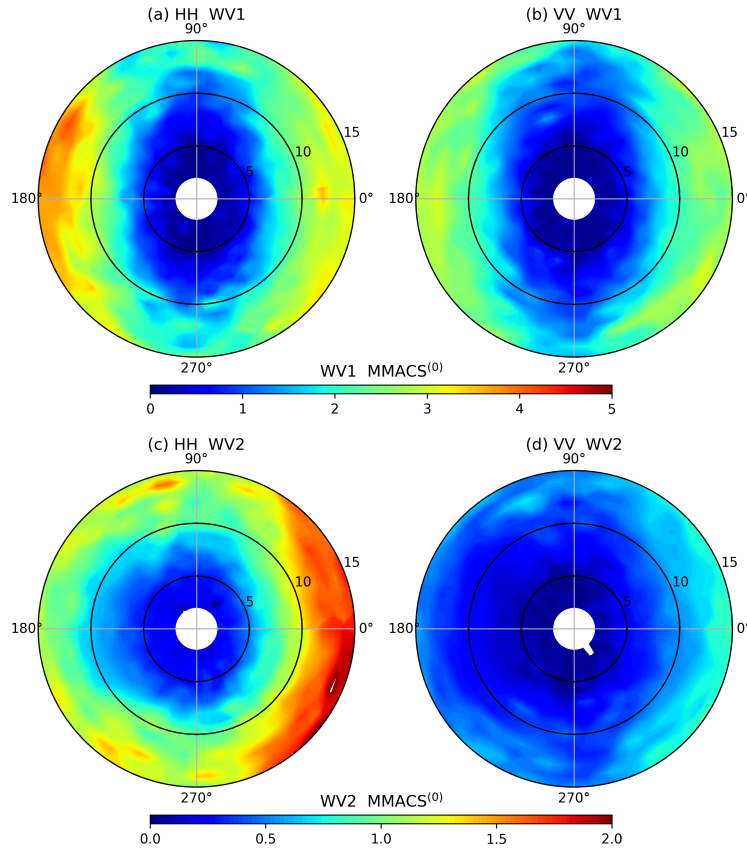


Figure 6.3: Two-dimensional plot of MMACS⁽⁰⁾ for (a) HH WV1; (b) VV WV1; (c) HH WV2; (d) VV WV2. The radius is wind speed with circles from inner to outer of 5 m/s, 10 m/s and 15 m/s, respectively. The color represents MMACS⁽⁰⁾. Wind direction of 0° corresponds to upwind (wind blows against the antenna pointing direction).

The two-dimensional plot of MMACS⁽⁰⁾ with respect to wind speed and wind direction is given in Figure 6.3. Radius represents wind speed with circles from inner to outer corresponding to 5 m/s, 10 m/s, 15 m/s, respectively. Bin size of wind speed is 1 m/s and wind direction is 5°. Data with wind speed lower than 2 m/s are not shown. Each value is obtained by averaging the valid data points within the bin based on equalized data set. MMACS⁽⁰⁾ is almost symmetric from upwind to downwind for WV1, while clearly asymmetric for WV2. To better characterize the azimuthal modulation of MMACS⁽⁰⁾, the upwind-downwind and upwind-crosswind asymmetry will be quantified and discussed in the following.

6.2.2 UDA and UCA

SAR-measured NRCS is mainly determined by backscattering from sea surface roughness composed of centimeter Bragg waves. The azimuthal modulation of NRCS is accordingly used to characterize the azimuthal distribution of Bragg waves. By similarity, MMACS⁽⁰⁾ can help reveal the azimuthal distribution of range-traveling intermediate waves.

Here, we define the Upwind-Crosswind Asymmetry (UCA) and Upwind-Downwind Asymmetry (UDA) as in (A. Mouche & Chapron, 2015a):

$$UCA^{pp} = \frac{a_0^{pp} + a_2^{pp}}{a_0^{pp} - a_2^{pp}} - 1 \quad (6.2)$$

$$UDA^{pp} = \frac{a_1^{pp}}{a_0^{pp}} \quad (6.3)$$

where a_i^{pp} are fit coefficients in form of Eq.(6.1) for NRCS and MMACS⁽⁰⁾, respectively. Figure 6.4(a) presents the UCA of NRCS relative to wind speed. Overall, NRCS UCA behaves differently between WV1 and WV2. For WV1, it gradually increases with wind speed from 0 m/s to 15 m/s. In the case of WV2, the UCA first gradually increases with wind speed and reaches its maximum at 9 m/s. It then starts to slowly decrease. In addition, the polarization sensitivity of UCA also differs with incidence angle. For WV1, no distinct deviation is found between VV UCA and HH UCA. While for WV2, UCA of NRCS in VV is greater than in HH as documented for Ku-band (Quilfen et al., 1999) and C-band (A. Mouche & Chapron, 2015a). This is because with increasing incidence angle, NRCS becomes more sensitive to non-polarized scattering associated to surface wave breaking. The relative contribution of non-polarized scattering to NRCS is larger in HH polarization, resulting in weakly distinct azimuthal distribution of NRCS in HH.

The MMACS⁽⁰⁾ UCA is given in Figure 6.4(b). It varies remarkably with wind speed for given incidence angle and polarization. For WV1, MMACS⁽⁰⁾ UCA reaches its maximum at 5 m/s and gradually increases with increasing wind speed. While it does not vary greatly for WV2. For given incidence angle, the MMACS⁽⁰⁾ UCA is distinct between HH and VV polarization at low wind speed (< 8 m/s). This difference becomes negligible for wind speed higher than 10 m/s. This might be caused by approaching RAR MTF in VV and HH polarization with increasing wind speed.

UDA of NRCS and MMACS⁽⁰⁾ are presented in Figure 6.4(c)(d). For NRCS UDA, WV1 and WV2

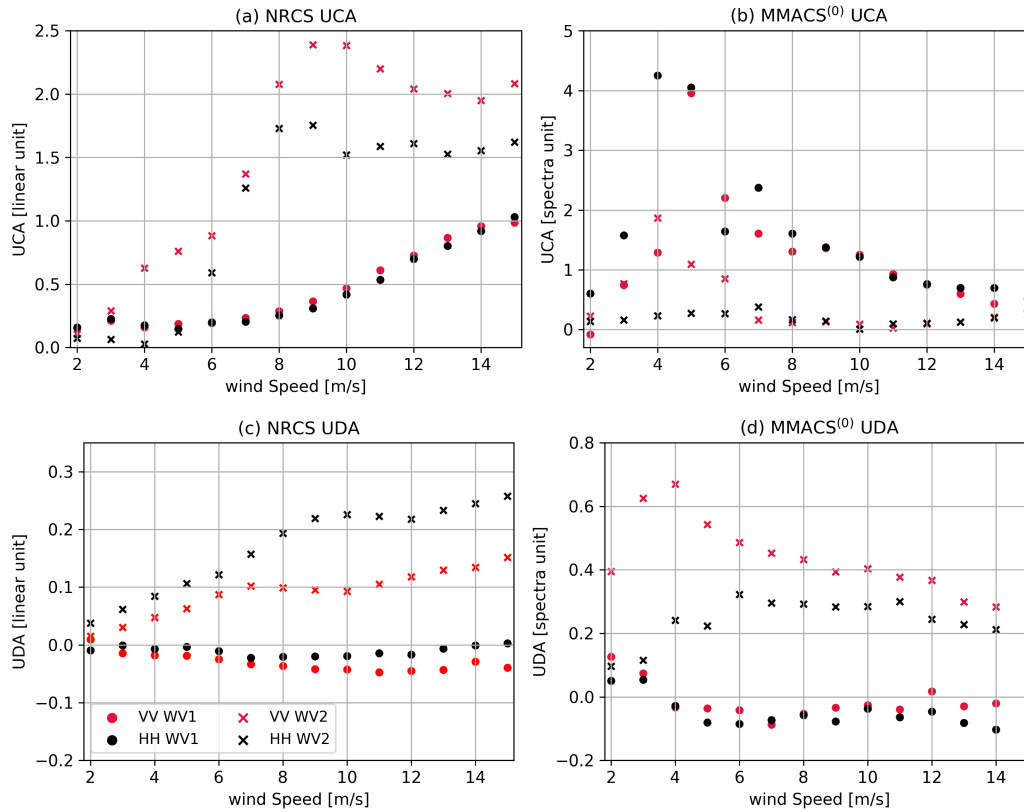


Figure 6.4: (Top) UCA of (a) NRCS; (b) MMACS⁽⁰⁾; (bottom) UDA of (c) NRCS; (d) MMACS⁽⁰⁾ as function of wind speed.

show distinct features that WV1 is mostly negative and WV2 gradually increases. The increasing slope of NRCS UDA for WV2 is larger at low wind speed (<7 m/s) and smaller at higher wind speed. In addition, NRCS UDA is greater in HH than in VV for WV2. As shown in subplot (d), MMACS⁽⁰⁾ UDA for WV1 is similar to NRCS UDA with negative values. For WV2, MMACS⁽⁰⁾ UDA is much greater in VV and in HH. This is due to the much lower level of MMACS⁽⁰⁾ in VV polarization as in Figure 6.2(d). The marked up-to-downwind asymmetry provides new qualitative insight into the RAR modulation of SAR cross-spectra for upwind and downwind direction, if not all.

6.3 RAR modulation derived from MMACS⁽⁰⁾

In the following, simulation of SAR image cross-spectra based on nonlinear transformation is introduced. We assess the agreement of MMACS⁽⁰⁾ between SAR measurements and simulation with input of empirical RAR MTF. Through comparison, an improved RAR MTF is derived and discussed.

6.3.1 Simulation of SAR image cross-spectra

To compare SAR-measured MACS with simulations, we follow the nonlinear transformation presented in (Engen & Johnsen, 1995) to compute SAR image cross-spectra. The closed-form expression of SAR cross-spectra for m th and n th look is expressed as:

$$P_S^{mn}(\mathbf{k}, \Delta t) = \int d\mathbf{x} e^{k_x^2 [\rho_{dd}(\mathbf{x}, t) - \rho_{dd}(\mathbf{0}, 0)]} [1 + \rho_{II}(\mathbf{k}, t)] \quad (6.4)$$

where the subscript dd and II denote velocity bunching and RAR modulation, respectively. k_x is the wavenumber along azimuth direction. The correlation function defined in Eq. (6.4) is related to ocean wave spectrum $S(\mathbf{k})$ through

$$\rho_{aa}(\mathbf{x}, \Delta t) = \frac{1}{(2\pi)^2} \int d\mathbf{k} e^{i\mathbf{k} \cdot \mathbf{x}} \cdot \left[\frac{1}{2} |M_a(\mathbf{k})|^2 e^{-i\omega\Delta t} S(\mathbf{k}) + \frac{1}{2} |M_a(-\mathbf{k})|^2 e^{i\omega\Delta t} S(-\mathbf{k}) \right] \quad (6.5)$$

where M_a represents the modulation transfer functions for RAR or velocity bunching. In the following, $M_d = \frac{R}{V} \omega (\sin\theta \cos\phi + j \cos\theta)$ is used and R/V is slant-range to velocity ratio of SAR. The expression of RAR modulation $M_I = ik_y M_R$ is used with $M_R = \frac{1}{\sigma_0} \frac{\partial \sigma_0}{\partial \theta}$. Here, σ_0 is calculated based on CSARMOD (A. Mouche & Chapron, 2015a) with collocated ECMWF wind and given incidence angle from S-1 product. The ocean wave spectra are generated by WAVEWATCH III (WW3) spectral wave model using wind forcing by ECMWF and the parameterizations of (Ardhuin et al., 2010). Each wave spectrum is collocated with each S-1 wave mode acquisition. The input WW3 wave spectra composes of 24 directions and 32 wavenumber bins from $0.0056 \text{ rad}\cdot\text{m}^{-1}$ to $2.0632 \text{ rad}\cdot\text{m}^{-1}$. The minimum wavelength of sea surface waves is 3.045 m, slightly smaller than S1 spatial resolution.

6.3.2 Derived RAR modulation

The RAR MTF estimated using the empirical GMF of CSARMOD (A. Mouche & Chapron, 2015a) by $M_R = \frac{1}{\sigma_0} \frac{\partial \sigma_0}{\partial \theta}$ is first plotted in Figure 6.5(a) for dual-polarizations. Modulation values of VV obtained using CMOD5.N (Hersbach, 2008) are also plotted for comparison. MMACS⁽⁰⁾ is then simulated using nonlinear transformation with empirical RAR modulation based on CSARMOD. Figure 6.5 (b)(c) present comparison of MMACS⁽⁰⁾ between SAR-measurement and simulation for WV1 and WV2, respectively. It is clear that the simulated MMACS⁽⁰⁾ is mostly underestimating

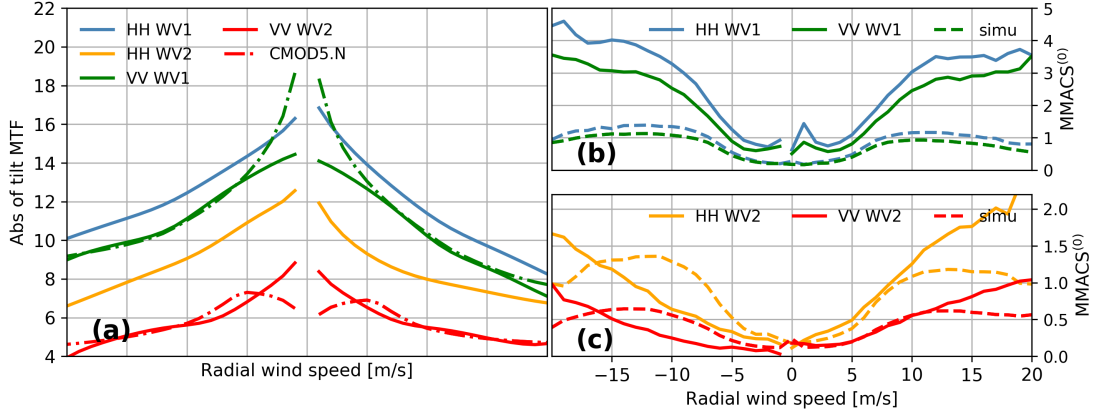


Figure 6.5: (a) RAR modulation estimated using empirical GMF of NRCS by $M_r = \frac{1}{\sigma_0} \frac{\partial \sigma_0}{\partial \theta}$. The solid lines are results with CSARMOD and dashed lines are with CMOD5. (b)(c) Comparison of $MACS^{(0)}$ between SAR measurements and simulations for incidence of 23° and 36.5° , respectively.

observations at both incidence angles. For example, for WV1 and wind speed of 10 m/s, SAR-measured $MMACS^{(0)}$ is about three times as large as the simulation. The exception is upwind for WV2. SAR-measured $MMACS^{(0)}$ and the simulated are in good agreement for wind speed lower than 10 m/s as shown in Figure 6.5(c). This suggests that empirical RAR modulation could only partly reproduce the observed RAR modulation at wind speed lower than 10 m/s. It therefore implies the deficiency of $M_R = \frac{1}{\sigma_0} \frac{\partial \sigma_0}{\partial \theta}$ in representing the true RAR modulation over a wide range of wind conditions.

The inaccurate empirical MTF in estimating RAR modulation is also traceable in theory. Local backscattering signal can be written relative to surface slope up to second order as:

$$\sigma^0(\theta + \Delta\theta) = \sigma^0(\theta) + \Delta\theta \frac{\partial \sigma^0}{\partial \tan\theta} + \frac{\Delta\theta^2}{2} \frac{\partial^2 \sigma^0}{\partial \tan^2\theta} \quad (6.6)$$

where θ is nominal incidence angle of SAR and $\Delta\theta$ is change of local incidence angle induced by surface slope. However, the $\langle \sigma^0 \rangle$ of CSARMOD or CMOD5.N is obtained by averaging SAR-measured or scatterometer-measured σ^0 to a reduced spatial resolution of 12.5 km, expressed as:

$$\langle \sigma^0(\theta) \rangle = \overline{\sigma^0(\theta)} + \frac{1}{2} \overline{\left(\frac{\partial \eta}{\partial x} \right)^2 \frac{\partial^2 \sigma^0}{\partial \tan^2\theta}} \quad (6.7)$$

where \bar{x} represents local mean and η denotes instantaneous sea surface height. The first-order tilt modulation by surface slope is averaged out by NRCS of GMFs. As such, it implies that empirical GMF cannot properly reproduce the first-order tilt modulation. However, the spectral analysis of intermediate ocean waves MACS is expected to include both first-order and second-order variation

of local backscattering signal. From Figure 6.5(b)(c), the best agreement of MMACS⁽⁰⁾ between SAR-measurement and simulation is found for upwind at WV2. We may speculate that first-order tilt modulation is more significant at smaller incidence angle and for downwind.

However, it is not straightforward to isolate the first-order tilt modulation using SAR measurements. Thus, we propose to adopt a simple method to approximate the RAR modulation based on comparisons of MACS between observations and simulations. Since MACS is defined adjacent to the range axis, it can be approximated by quasi-linear imaging, written as:

$$MACS = e^{-k_y^2 \lambda_c^2 / \pi^2} (M_d^2 + M_I^2) S(\mathbf{k}) \quad (6.8)$$

where the first exponential accounts for velocity bunching with λ_c being azimuth cutoff. The others are the same with Eq. (6.4). Azimuth cutoff mainly depends on surface wind speed (Kerbaol et al., 1998b) and slightly on incidence angle through SAR's range-to-velocity ratio. M_d is much smaller than M_I since we have constrained the azimuthal wavelength of interest greater than 600 m. Therefore, for given wind speed, variations of MMACS⁽⁰⁾ mainly arise from RAR modulation, which depends on surface wind as well as radar configurations.

Neglecting the nonlinear velocity bunching term in Eq.(6.8) for the moment, the MMACS⁽⁰⁾ can then be simplified to $MACS = F M_I^2 S(\mathbf{k})$ with F denoting the exponential factor associating to azimuth cutoff. As such, ratio of observed MMACS⁽⁰⁾ to simulated MMACS⁽⁰⁾ is equal to $(M_I^T / M_I^E)^2$ with superscript T indicating the observed RAR modulation and E empirical RAR modulation. The obtained ratio of (M_r^T / M_r^E) as function of radial wind speed is given in Figure 6.6. The ratio firstly decreases then increases with wind speed. The greater ratio of WV1 for both HH and VV implies that the empirical RAR modulation is highly underestimated. On the contrary, RAR modulation is overestimated at WV2, particularly for downwind. By comparing the up-to-downwind asymmetry of ratio, a non-tilt component almost accounts for 30% of order of magnitude of RAR modulation for WV2. However, it should be pointed out that this ratio is based on strict assumption of negligible velocity bunching. It only illustrates one potential approach to derive the RAR modulation from SAR measurements using MACS estimate. The crude approximation still provides us an insight into the insufficiency of empirical RAR estimate to reproduce up-to-downwind asymmetry. A component of particular significance at downwind is apparently missing.

The inaccurate estimate of RAR modulation using empirical GMF will lead to imprecise inversion of ocean wave spectrum from SAR images. It is accepted that RAR modulation M_R is globally

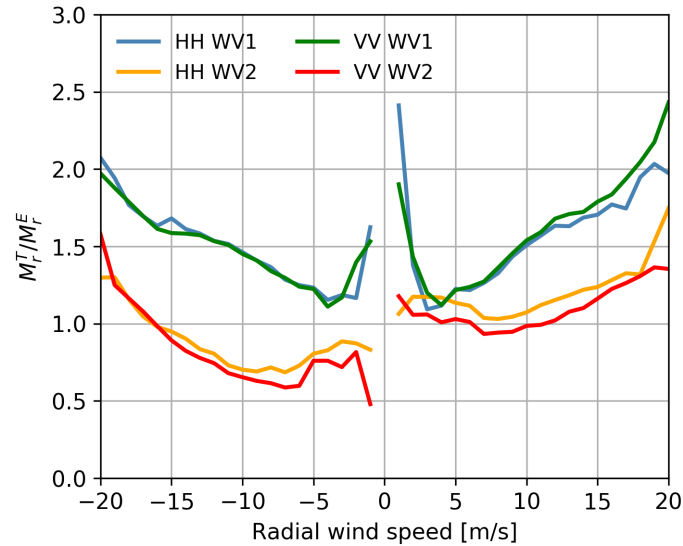


Figure 6.6: Ratio of derived RAR MTF to the empirical as function of radial wind speed based on assumption of negligible velocity bunching.

applicable to all wavenumber for given radar configuration and environmental conditions. Based on which, we consider a simple case of wind sea at 7 m/s and upwind for incidence of 23° . The empirical RAR modulation is 11.6 and the true one is tuned to be 18.6 in terms of ratio in Figure 6.6. We find that the inversed significant wave height is overestimated by 0.1 m by using the empirical RAR modulation. To date, few studies have been devoted to investigating performance of ocean swell inversion relative to wind direction. In this case, study of intermediate waves can bridge this gap thanks to the sensitivity of intermediate waves to wind speed as well as wind direction.

6.4 Summary

SAR is capable of measuring two-dimensional ocean wave spectra, based on which sea state parameters can be derived. Benefiting from the high spatial resolution as well as global coverage of S-1 WV, we focus on characteristics of intermediate ocean waves with wavelength 20 m using the collocated dataset. This is based on the new radar parameter MACS over range-traveling intermediate waves defined on SAR image cross-spectra.

MACS displays distinct dependence on wind speed and wind direction. In particular, its azimuthal modulation on wind direction gives information on spread function of ocean wave spectrum. Its up-to-downwind asymmetry can help quantify the RAR modulation, which is difficult to measure. In addition, its polarization sensitivity is valuable toward a better understanding on polarimetric

SAR imaging of ocean waves.

RAR modulation is significant to accurate ocean wave spectrum inversion from SAR images. Based on analysis of MACS relative to radial wind speed, it suggests that RAR modulation is greatly underestimated using empirical NRCS GMF. In particular, the empirical estimate also fails to capture an up-to-downwind asymmetry of RAR modulation. Adequacy of hydrodynamic modulation in accounting for this asymmetry requires considerate studies. Further, the underestimation (overestimation) of RAR modulation will translate into overestimation (underestimation) of ocean wave spectra. This study therefore provides an insight into the improvement of RAR modulation estimate by combining SAR observations and simulation results. Future studies would be devoted to addressing accurate estimate of RAR modulation both theoretically and empirically.

Chapter 7

Investigation of global ocean waves using SAR MACS

Contents

6.1	Speckle noise of MMACS⁽⁰⁾	90
6.1.1	Usage of MMACS ⁽⁰⁾	90
6.1.2	Removal of speckle noise	90
6.2	Statistics of noise-free MMACS⁽⁰⁾	92
6.2.1	Azimuthal modulation	92
6.2.2	UDA and UCA	95
6.3	RAR modulation derived from MMACS⁽⁰⁾	96
6.3.1	Simulation of SAR image cross-spectra	97
6.3.2	Derived RAR modulation	97
6.4	Summary	100

Linear ocean waves can be fully characterized by the wave spectrum (wavenumber and direction). Spaceborne synthetic aperture radar (SAR) provides measurements of the ocean wave spectra with proper treatment of the nonlinear transformation. Bypassing this complicated inversion scheme, the SAR image spectra can be filtered along the radar line-of-sight, termed as MACS profile. It reveals that the wind-wave interaction is mainly controlled by the inverse wave age, regardless of the wavelength. Global distribution of the wind sea at 62 m is closely related to the sea surface wind, while the long ocean waves (342 m) mostly exist in the storm tracks. In particular, there are four wave clusters along the latitude at 145°W, each evolving with seasons. With the impact of winter storms, ocean waves in the Northern extratropics present stronger seasonal variation. This chapter is based on the paper entitled ' *New investigation of ten-year Envisat/ASAR wave mode for global ocean waves*'.

7.1 Introduction of wave spectra climate

Ocean waves are generated by the sea surface wind, typically covering the wavelength from centimeter to hundred meters (Toba, 1972; Phillips, 1977; G. R. Valenzuela, 1976; K. Hasselmann et al., 1973). Knowledge of the global wave characteristics is essential to a wide range of marine applications. As the medium between the water and the air, ocean waves influence momentum flux transfer and play a significant role in air-sea interaction (Janssen & Viterbo, 1996; Bourassa et al., 2001; Doyle, 2002). To a broader extent, ocean wave related processes can also crucially impact global circulation and shape the coastal environment (Camus et al., 2017; X. L. Wang et al., 2014).

During the last decades, numerous studies have been conducted to study the global and regional signatures of ocean waves based on either wave model outputs, satellite observations or the combination of both (Sterl et al., 1998; I. Young, 1999; X. L. Wang et al., 2004; X. Li et al., 2011; I. R. Young et al., 2011). These subjects have greatly advanced our understanding about the spatio-temporal pattern of ocean waves (Hanley et al., 2010; Stopa et al., 2013), the presence of ocean swell (Chen et al., 2002; Jiang & Chen, 2013), response of ocean waves to global climate (Shimura et al., 2015; Reguero et al., 2019) et al. Most of these studies have focused on integrated wave field parameters (such as significant wave height, mean wave period and mean wave direction). However, these integrated parameters do not fully characterize realistic wave conditions, particularly when multi-modal wave systems exist (Portilla-Yandún, 2018). Such analyses can be complemented by a wave spectral approach, which describes the wave energy distribution over wavenumber and direction (Phillips-1977). By partitioning the full wave spectra, the integrated wave parameters from each wave system can lead to better descriptors of the local wave conditions using the reanalysis data (Portilla-Yandún et al., 2016; Portilla-Yandún, 2018). As the primary microwave imaging sensor that can provide ocean wave spectra, spaceborne SAR measurements have demonstrated an ability to provide quality wave observations, particularly for swell tracking (Collard et al., 2009b; Stopa et al., 2016) and wave-ice interaction (Ardhuin et al., 2015; Stopa et al., 2018). Recently, a global atlas of crossing swell has been presented by (X.-M. Li, 2016) based on the ten-year Envisat/ASAR data. Yet, global wave spectra for given wave component (wavenumber and direction) are rarely exploited. This might be expected to offer a new perspective for the analysis of global wave climate.

(H. Li et al., 2019) proposed a new parameter MACS by filtering the SAR image cross-spectra around the range-traveling intermediate waves (wavelength of 20 m) and demonstrated that the

global MACS variations correlate with sea surface winds. In this study, we extend this approach to a broader range of wavelengths. The ten-year wave mode data acquired by the Envisat/ASAR are analyzed. The wind-wave interaction inherent in MACS is discussed. We also demonstrate the global patterns of MACS at selected wavenumbers, from the typical wind sea to long ocean swell. The spatio-temporal features of range traveling peak wavenumber detected from the MACS profile are also investigated and discussed.

7.2 Extraction of the MACS profile

In this section, we first describe the global Envisat/ASAR wave mode data and extraction of the MACS profile. We examined the MACS variations at given wavelengths in an attempt to address the ocean wave variability with collocated wind speed and inverse wave age.

7.2.1 Envisat/ASAR wave mode

Envisat/ASAR operated for nearly a decade from November 2002 to April 2012. It is a C-band radar (center frequency of 5.4 GHz), collecting SAR images in various modes. Of which, wave mode is dedicated to observation of global ocean waves (K. Hasselmann et al., 2012), acquiring vignettes every 100 km along the track. These vignettes have a spatial footprint of 10 by 7 km and resolution of 9 by 6 m. We use only wave mode vignettes obtained at incidence angle of 23° by VV polarization in this work.

The Level-1B products of SAR image cross-spectrum, which are systematically processed from the single look complex (SLC) SAR vignettes are included in the analysis. Each image spectrum is composed of 24 discrete wavenumbers ranging from $0.008 \text{ rad}\cdot\text{m}^{-1}$ to $0.2 \text{ rad}\cdot\text{m}^{-1}$ and 36 direction (Johnsen, 2005). The ASAR wave mode acquired between January 2007 and April 2012 are collocated with the ECMWF (European Centre for Medium-Range Weather Forecasts) reanalysis wind vectors. The reanalysis product is available at spatial resolution of 0.5° every 6h (0h,6h,12h,18h). The wind vector at the nearest spatial and temporal point to the SAR passing time is assigned as the reference wind of the SAR image.

Ten-year ASAR wave mode acquisition over the ascending pass is included in this chapter. The global data density binned by 2.5° is given in Figure 7.1 top-left panel. As shown, most of the grids

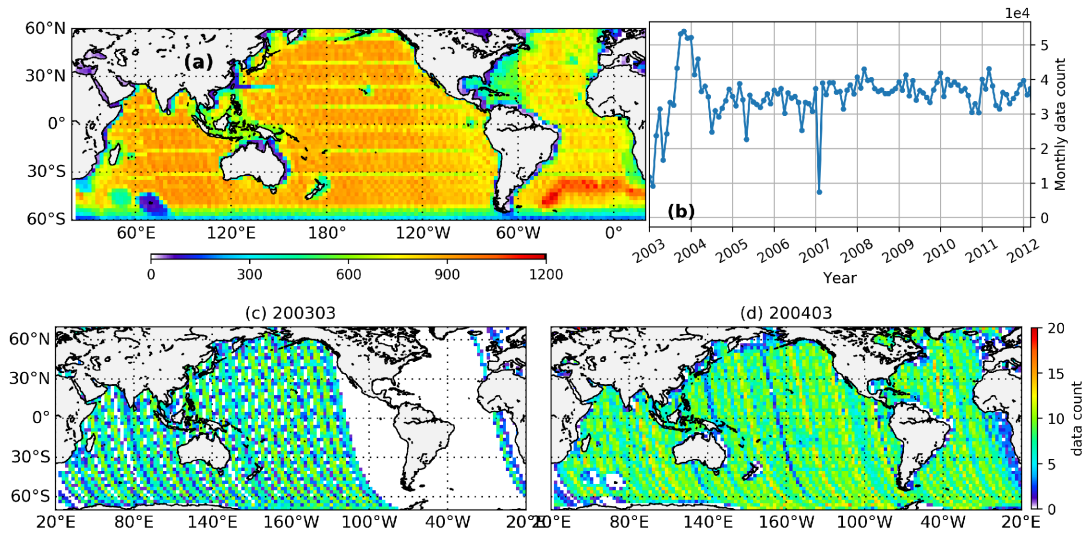


Figure 7.1: (Top) Global data density of wave mode acquisitions at spatial resolution of 2.5° by 2.5° and monthly data count of global ASAR data. Ascending products collected from 2003 to 2012 are used here. (Bottom) Monthly data density in March 2003 and March 2004.

between $\pm 50^\circ$ have more than 800 data points. The top-right panel shows the monthly data count over the globe. An abrupt decrease of data acquisition is observed in February, 2007. In addition, the first-year operation of ASAR wave mode is not globally covered as in the bottom-left plot.

7.2.2 MACS profile extraction

Since the SAR mapping of ocean waves is highly nonlinear, causing loss of information for waves traveling in the flight direction, the extraction of wave information therefore becomes complicated (Engen & Johnsen, 1995; Chapron et al., 2001). Algorithms to directly infer the integrated significant wave height from the SAR images have been proposed (Schulz-Stellenfleth et al., 2007; Stopa & Mouche, 2017b), while the inversion of wave spectra is still circumscribed by the nonlinearity. In addition to that, needs of the input wind speed and direction, either from model or observation, might add more biases in the derived ocean wave spectra (Engen & Johnsen, 1995).

Bypassing the nonlinearity of SAR mapping and the biases in the inversion algorithms, in this chapter, we extend the MACS analysis in (H. Li et al., 2019) to a wide of wavenumbers, ranging from wind sea to ocean swell. The range profile of SAR image cross-spectra is thus extracted, denoted as MACS profile hereinafter. Four examples of the extraction are shown in the Supporting Information (SI) (see Figure S1). When the peak wave directions are close to the range, the spectral

7.2. Extraction of the MACS profile

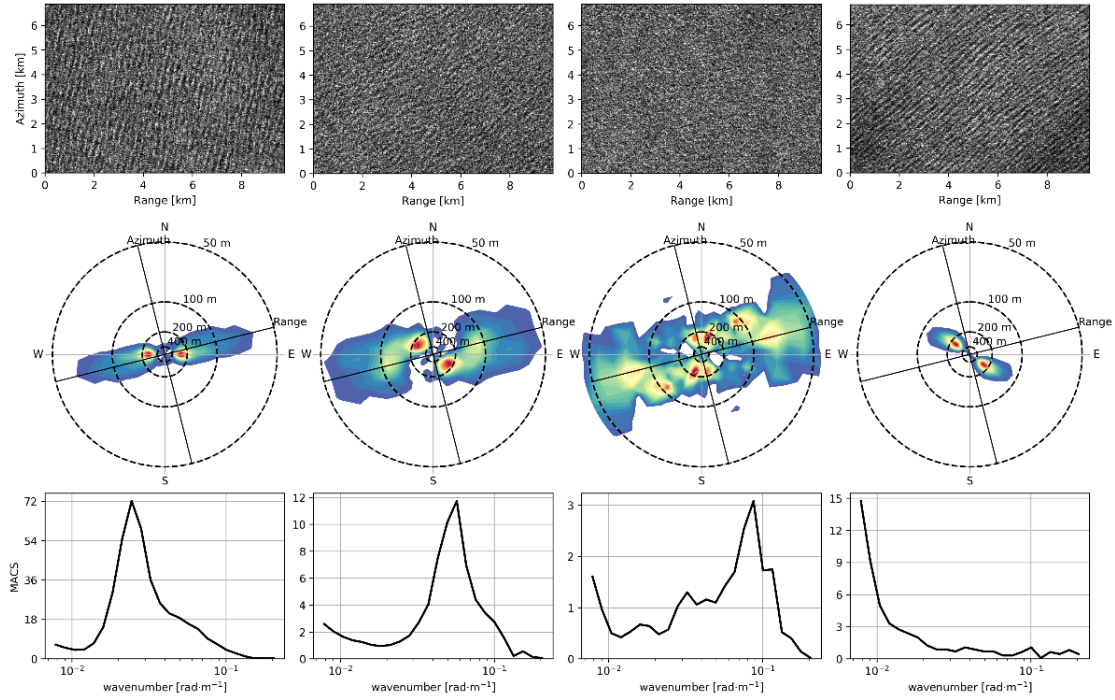


Figure 7.2: Examples of ENVISAT/ASAR wave mode images for definition of range MACS profile. (Top) Normalized backscattering for four cases. (Middle) The corresponding SAR image spectra are plotted. Color represents the normalized image spectral magnitude. The circles from inner to the outer are 400 m, 200 m, 100 m and 50 m respectively. (Bottom) The range MACS profile is extracted relative to wavenumber.

envelope is well preserved by the MACS profile. This capability gradually fades with the peak waves approaching the azimuth. As a quality control and to feature the range-travelling waves, the cases with dominant azimuth traveling waves are detected and filtered out in the following analysis. It is worth pointing out that we focus on the ascending pass data of ASAR wave mode to maintain the wave direction consistent. In the end, there are about 3,000,000 products considered as good cases. In the rest of this chapter, MACS for given wavelength is denoted as MACS_λ , for example, MACS for 62m as MACS_{62} .

Four examples of SAR image and the corresponding extraction of MACS profile are shown in Figure 7.2. In the first three cases, the wave signatures are well preserved for the wave partition close to the range. While this is not the case when the waves are close to the azimuth. In particular, no useful wave signatures are captured if there is only one dominant wave partition as the fourth case in Figure 7.2. This corresponds to a no-peak, which is readily detected. Therefore, all the cases without a peak of MACS profile are excluded in this study.

7.3 MACS variation with wind speed

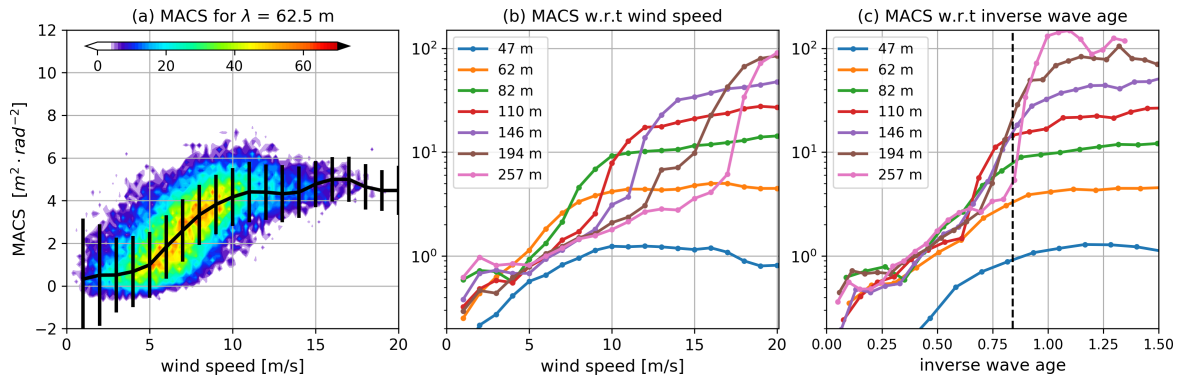


Figure 7.3: MACS derived for various wavelengths. (a) MACS for wavelength of 62.5 m relative to wind speed. Color denotes data counts and solid black line is the mean fit. (b) MACS relative to wind speed for various wavelengths between 47 m and 257 m. (c) MACS variations relative to inverse wave age (wind speed/wave phase speed). Only winds in the radar looking direction (upwind and downwind) with a variation of 2° are included in the analysis.

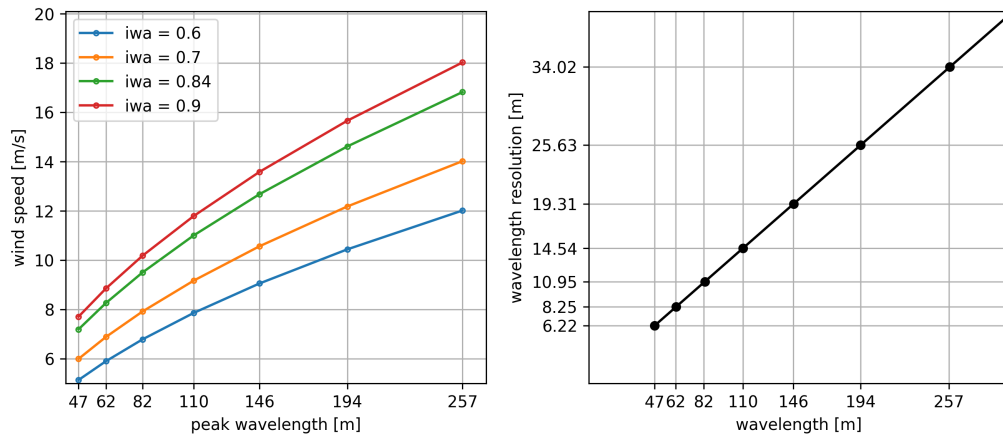


Figure 7.4: (Left) Peak wavelength at given wind speed is plotted for various iwa. Peak wavelength is derived from Elfouhaily spectrum. (Right) Wavelength resolution of Level-1B SAR image spectra products.

Under the impact of local winds, the ocean waves grow over duration and fetch until reached the fully developed sea state. The increase of wave spectral energy for given wavelength accompanies and finally saturates. By definition, MACS is closely associated with the wave spectra. Though indirectly, MACS can still be used to qualitatively study the wave growth relative to the winds. Since MACS only captures wave information in the radar line-of-sight direction, we thus constrain the wind direction in the same direction (both upwind and downwind) with a variation of 3° . Figure 7.3(a) present the increasing $\text{MACS}_{62.5}$ with the wind speed. One finds that $\text{MACS}_{62.5}$ saturates for wind speed higher than 10 m/s. In fact, the saturation is observed for all wavelengths from the

wind sea to the ocean swell, as shown in Figure 7.3(b) that depicts the mean MACS variation from 47 m to 257 m. The saturation wind speed increases with increasing wavelength of interest. From wavelength of 62 m to 194 m, it varies from 10 m/s to 16 m/s.

In reality, the fully developed sea state is rare on the ocean surface. We therefore explore the relationship of MACS increase in terms of the wave maturity through the inverse wave age (iwa). The iwa describes the wave growth under the action of local winds, defined as wind speed divided by phase speed of the ocean waves (Hanley et al., 2010). The iwa of 0.84 is commonly used to characterize the fully developed sea state (Hanley et al., 2010). Otherwise, the ocean swell is dominant for smaller iwa and undeveloped wind sea for larger iwa. As shown in Figure 7.3(c), the sharp increase of MACS occurs at iwa approaching this limit when the local wind becomes dominant in driving the wave growth. For iwa of 0.84 when the wind and waves reach equilibrium, the given wavelength becomes the peak of the wave spectrum. As the iwa increases, the wave spectral energy at this wavelength maintains steady (Elfouhaily et al., 1997), resulting in the saturated MACS. This is also supported by the consistent peak wavelengths for given wind speed with wavelengths of interest here (see Figure SI2(a)). It should be noted that the sharp increase of MACS occurs at slightly greater iwa for ocean swell. This is possibly due to the fact longer ocean swell needs longer temporal duration and larger spatial fetch to be fully developed and therefore, a greater iwa.

The wind speed at which MACS abruptly increases is related to the wind speed at which that wavelength reaches the peak of ocean wave spectrum. Figure 7.4 shows the variation of peak wavelength at different inverse wave age (iwa). For given wind speed, the peak wavelength increases with decreasing iwa. This corresponds to the fetch or duration effect. This is being said, for the same wind, the ocean waves grows bigger for larger fetch or longer duration. Since the fully developed sea is uncommon on the ocean surface, it is widely accepted that iwa increases with wind speed. In other words, the peak wavelength becomes closer to that of fully developed sea with increasing wind. Thus, the wind speed of abrupt increase of MACS is closer to the wind speed at larger iwa for longer wavelength.

7.4 Global wave characteristics from MACS profile

In this section, we first demonstrate the global patterns of MACS at various wavelengths to offer a new way into wave climate by SAR observations. MACS profile is then used to present the seasonal variation of wave features along the latitude. We also show the detection of range peak

wavenumber from MACS profile and the global features. In the end, we carry out an EOF analysis on the detected range peak wavenumber in an effort to decipher its spatio-temporal patterns.

7.4.1 Global MACS at selected wavelengths

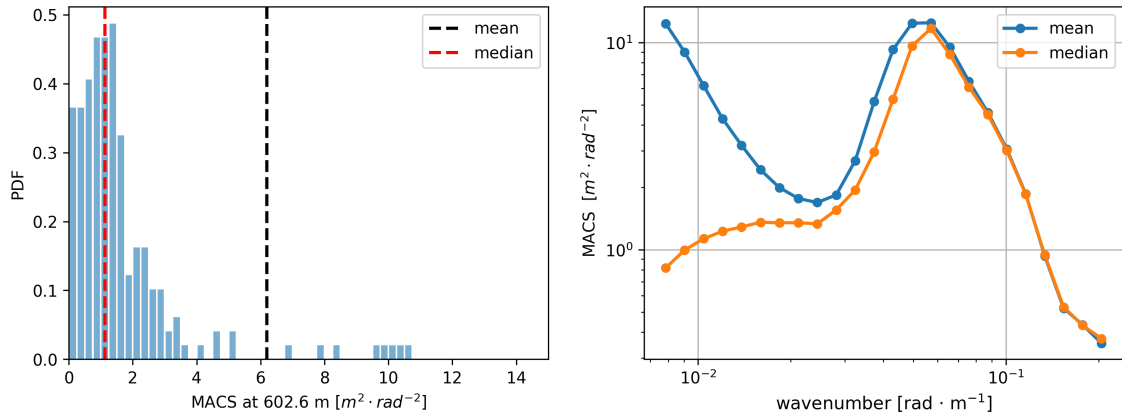


Figure 7.5: (Left) Estimates of averaged MACS for given wavelength. Bars are histogram of MACS at 602.6 m over A2 during the season MAM. Vertical red line indicates the median value and black line is the mean value. (Right) Comparison of range MACS profile using mean and median values.

This figure demonstrates that the mean value differs greatly from the median because the mean is skewed by very large outliers (not shown in the PDF). Since image spectra at low wavenumbers are subject to presence of atmospheric or oceanic phenomena, the impact of skewing is particularly significant for low wavenumbers as shown in the right panel. Based on this demonstration, the median value is finally used to represent the MACS for given wavenumber over a given location and a time period. It is recommended to use median value to represent the sea state over an area because it is more robust against outliers than the mean in (Carter & Cotton, 1995).

Ocean waves cover a wide range of wavelengths from centimeters to hundreds meters (Portilla-Yandún, 2018). Within the wavelength extent resolved by ASAR wave mode, the intermediate waves (~ 50 m) are in higher couple with the local winds than the ocean swell (~ 200 m). To illustrate the difference, seasonal average of global MACS for three selected wavelengths (62.5 m, 168.4 m; 342.0 m) are given in Figure 7.6. As expected, global pattern of $\text{MACS}_{62.5}$ is representative of the global winds (I. Young, 1999). Smaller $\text{MACS}_{62.5}$ are found due to the low wind speed over the Inter Tropical Convergence Zone (ITCZ) (Žagar et al., 2011). Two belts of higher $\text{MACS}_{62.5}$ adjacent to the ITCZ correspond to the trade wind regions. Over the extratropics, $\text{MACS}_{62.5}$ is consistently large because of the high winds. Seasonality of $\text{MACS}_{62.5}$ is also

7.4. Global wave characteristics from MACS profile

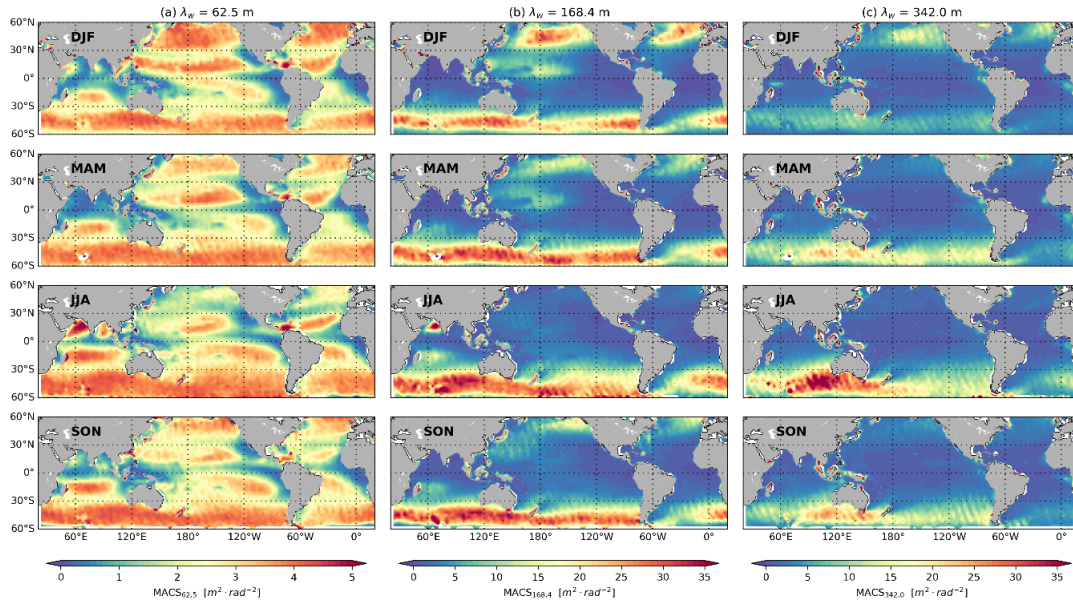


Figure 7.6: Seasonal average of MACS for three selected wavelengths in the panels of (a) 62.50 m; (b) 168.4 m; (c) 342.0 m. Both latitude and longitude are binned into 2.5° by 2.5° . Color denotes MACS and note that the color bar dynamics vary in the three columns. Blank spaces are due to lack of SAR observations.

distinguishing. In the northern extratropics, the maximum activity is during the winter time (DJF) and the minimum in the summer (JJA). The belt of large $\text{MACS}_{62.5}$ in north of the ITCZ extends to the Philippines in DJF while reduces to 180° in JJA. This periodicity is associated with the high winds of winter storms. It is worth mentioning that the two belts exhibit strong asymmetry in DJF and MAM with greater $\text{MACS}_{62.5}$ in the north. In JJA and SON, they become comparable in the magnitude. In addition, the northern Indian Ocean have the largest MACS in JJA, caused by the high winds during the monsoon season. While the minimum MACS is found in MAM, rather than in DJF, consistent with the minimum wind speed in MAM (I. Young, 1999).

The seasonal average of $\text{MACS}_{168.4}$ is presented in Figure 7.6(b). Comparable to the global pattern of $\text{MACS}_{62.5}$, $\text{MACS}_{168.4}$ in the southern extratropics are also consistently high (in red) throughout the year. For its counterpart in the Northern Hemisphere, DJF has the maximum $\text{MACS}_{168.4}$ and the minimum in JJA. Yet, the global pattern of $\text{MACS}_{168.4}$ clearly differs from that of $\text{MACS}_{62.5}$ in the disappearance of the two bright belts over the trade winds, particularly in the south side of ITCZ. This mainly results from the asymmetric winds as shown on $\text{MACS}_{62.5}$. The relatively lower winds (< 7 m/s) in the south of the ITCZ are not sufficiently high to generate ocean waves of 168.4m. In addition, spatial features of $\text{MACS}_{168.4}$ over the northern Indian Ocean are overall weak, except in the Arabian Sea during JJA. While in the Bay of Bengal, $\text{MACS}_{168.4}$ appears to be consistently low. Ocean waves of 168.4 m can be generated by local winds roughly higher than 11 m/s, which is com-

mon in the southern extratropics (Sijp & England, 2009). While ocean waves of 342.0 m can only grow when the wind speed reaches about 18 m/s (K. Hasselmann et al., 1973). In other words, these long waves is usually related to the extreme high winds events. MACS_{342.0} shown in Figure 7.6(c) supports the expectations. Large MACS_{342.0} is mostly observed in the extratropics, particularly in the Southern Hemisphere storm tracks. Due to the blocking impact of the continent, MACS_{342.0} in the west of the continent is much greater than that in the east, particularly for Australia and South America (I. Young & Donelan, 2018). In addition, the winter storms in the northern extratropics are also able to generate these long waves as shown. Given the duration and fetch needed for the long swell to grow, MACS_{342.0} are only observed in the east part, distinguished from the spatially spread MACS in Figure 7.6 (a)(b). As expected, MACS_{342.0} is constantly low in the tropics over the trade winds.

7.4.2 k_{rp} from MACS profile

The ocean waves generated by the local storms can propagate for thousands of kilometers across the whole ocean basin (Collard et al., 2009b). They disperses in space and time, resulting in the smaller wave energy far away from their origins (Stopa et al., 2016). As in Figure 7.6, MACS profile portrays, to an extent, the global distribution of wave spectra for given wavelength. In particular, over the Pacific Ocean (see Figure 7.6), signatures of MACS from the wind sea to the long swell obviously differ. A latitude transect is chosen between 150°W and 145°W to demonstrate the variation of wave signatures across the Pacific Ocean.

Seasonal MACS profile along the latitude is given in Figure 7.7 top panel. From the north to the south, MACS for given wavelength generally decreases to the equator and then increases. This trend is generally consistent with the winds (I. Young, 1999). Along the latitude, four clusters of ocean wave systems are present and evolve with seasons. The one in the northern extratropics reaches the maximum in DJF, spreading between 25°N and 60°N. It reduces to the minimum in JJA and shrinks to 40°N. This pattern is closely related to the impact of winter storms. The long ocean swells generated by the winter storms propagate southward and drives the cluster southward. While in the southern extratropics, the trend is opposite with maximum spread in JJA and minimum in DJF. The two clusters over the trade winds vary in phase with their neighbors in the extratropics.

To highlight the seasonality at given locations, MACS profile at three latitudes are displayed in Figure 7.7(e)-(h). the shape of MACS profile can readily help tell the dominance of swell or local

7.4. Global wave characteristics from MACS profile

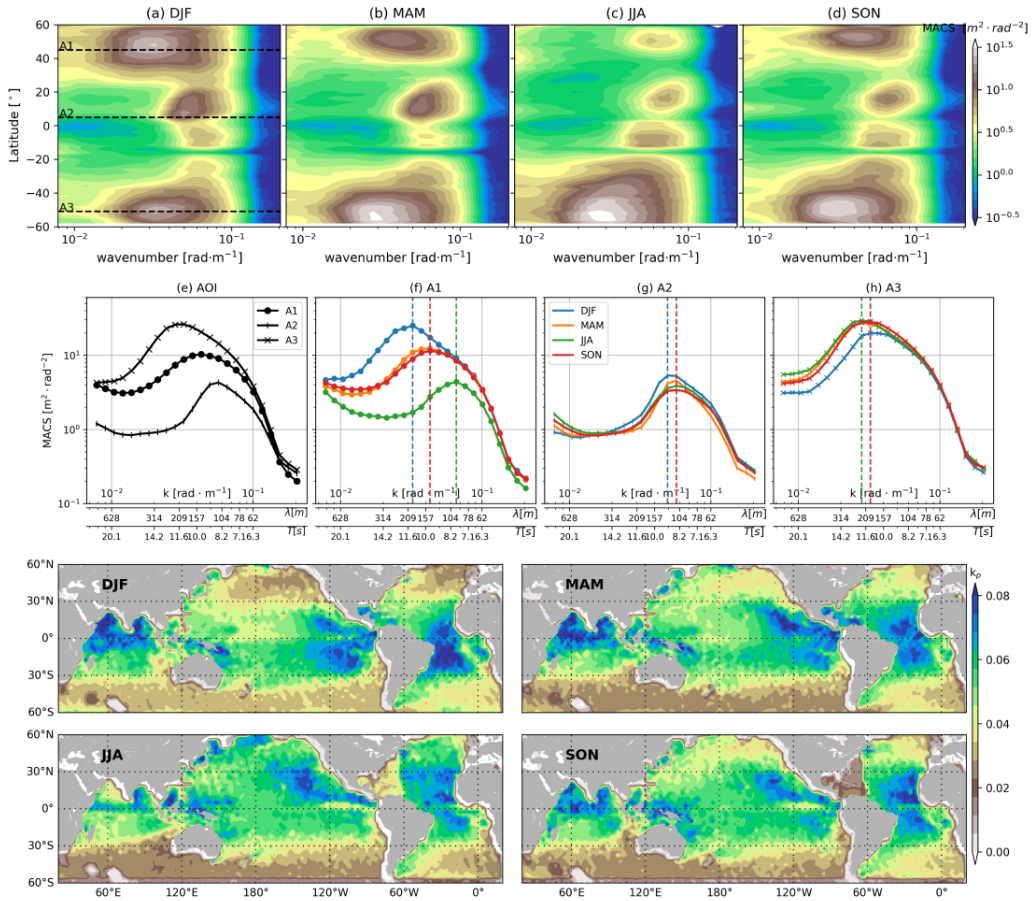


Figure 7.7: (Top) MACS profiles averaged over the Pacific Ocean (150°W-145°W) along latitude are shown for four seasons: (a) DJF; (b) MAM; (c) JJA and (d) SON. Color bar denotes MACS in log scale. (Middle) MACS profile relative to wavenumbers for three latitudes in (a). Total average in (e) and seasonal average for (f) A1; (g) A2; (h) A3. Dashed vertical lines indicates position of detected peak wavenumber with color corresponding to seasons. (Bottom) Seasonal average of global peak wavenumber derived over latitude and longitude bin of 2.5°. Color denotes peak wavenumber k_p [rad · m⁻¹].

wind sea. For example, in Figure 7.7(h), MACS profile roughly follow the wind wave spectra with decreasing magnitude at smaller wavenumber than the peak. While in Figure 7.7(g), MACS remains consistent at longer wavelength than the peak, suggesting the presence of distant ocean swell. In addition, ocean swell is commonly present as suggested by the non-decreasing MACS at long wavelength, which is in agreement with the findings in (Chen et al., 2002). In addition, the range peak wavenumber k_{rp} (vertical dashed lines) of MACS profile is an useful indicator of the sea state. In general, the peak wavelengths in A1 and A3 are around 250 m while it is 120 m over A2. Over A1, DJF has the smallest k_{rp} , namely, the largest peak wavelength. This is caused by the high winds of winter storms during DJF. It is worth noting that SON and MAM have the same k_{rp} , resulting in the overlapping. The low trade winds generate the shorter peak wavelengths over

A2, while the constantly high winds in the southern extratropics for the long wavelengths over A3.

Seasonal average of k_{rp} is presented in the bottom panel of Figure 7.7. The extratropics have smaller k_{rp} (longer wavelength) and the trade winds regions have larger k_{rp} . DJF has minimum k_{rp} (longest waves) in the North Pacific and North Atlantic Ocean between 35°N and 55°N. The smaller k_{rp} almost extends to the equator at longitude of 180°, suggesting the propagation of ocean swell. Over the trade winds region, the k_{rp} are relatively higher, particularly in the Equatorial Pacific Ocean, the Atlantic Ocean and the North Indian Ocean (blue color). Even known as the persistent presence of ocean swell in the equator, the k_{rp} patterns are still closely related to the global winds (I. Young, 1999). With the extinction of winter storms in the northern extratropics, the k_{rp} increases in JJA. Activities in the southern extratropics reaches the maximum and generates the minimum k_{rp} . In addition, a belt of higher k_{rp} compared to the surroundings appears at the equator, extending from 115°W to 90°W. This belt persists into the SON but at reduced extent. Over the Arabian Sea, a cluster of low k_{rp} is obvious. This might be related to the high winds of summer monsoon (I. Young, 1999).

7.4.3 Temporal variation of k_{rp}

The global k_{rp} exhibits strong seasonality, particularly in the northern extratropics. In the following, we choose six areas of interest (A1-A6) to demonstrate the long-term periodicity of k_{rp} . The geographic positions of these six areas are annotated in Figure S5, each covering 5° in both latitude and longitude. Note that A1-A3 are actually overlapped with the three latitude transects in Figure 7.7. All the six areas are chosen by considering the spatial distribution (covering the three Oceans) and maximally consistent acquisitions over that area (see Figure S2).

Figure 7.8 gives the monthly MACS profile with the detected k_{rp} in the left panel. The frequency spectra of temporal series of k_{rp} is accordingly given in the right panel. It should be mentioned that the vertical blank space is due to lack of SAR observations over the area in that month. From the time series of k_{rp} on the Pacific Ocean, A1 exhibits much stronger seasonal changes in comparison to that of A2 and A3. In the winter, long ocean waves are generated by the high winds of the winter storms and the averaged k_{rp} is around 0.025 rad·m⁻¹ (wavelength of 250 m). With the receding winter storms, the winds become lower and the local waves become shorter. As a result, the k_{rp} increases to 0.05 rad·m⁻¹ (wavelength of 125 m) in the summer. This explains the larger k_{rp} in the Northern Hemisphere storm tracks (see Figure 7.7). The strong seasonality of k_{rp} over A1 also

7.4. Global wave characteristics from MACS profile

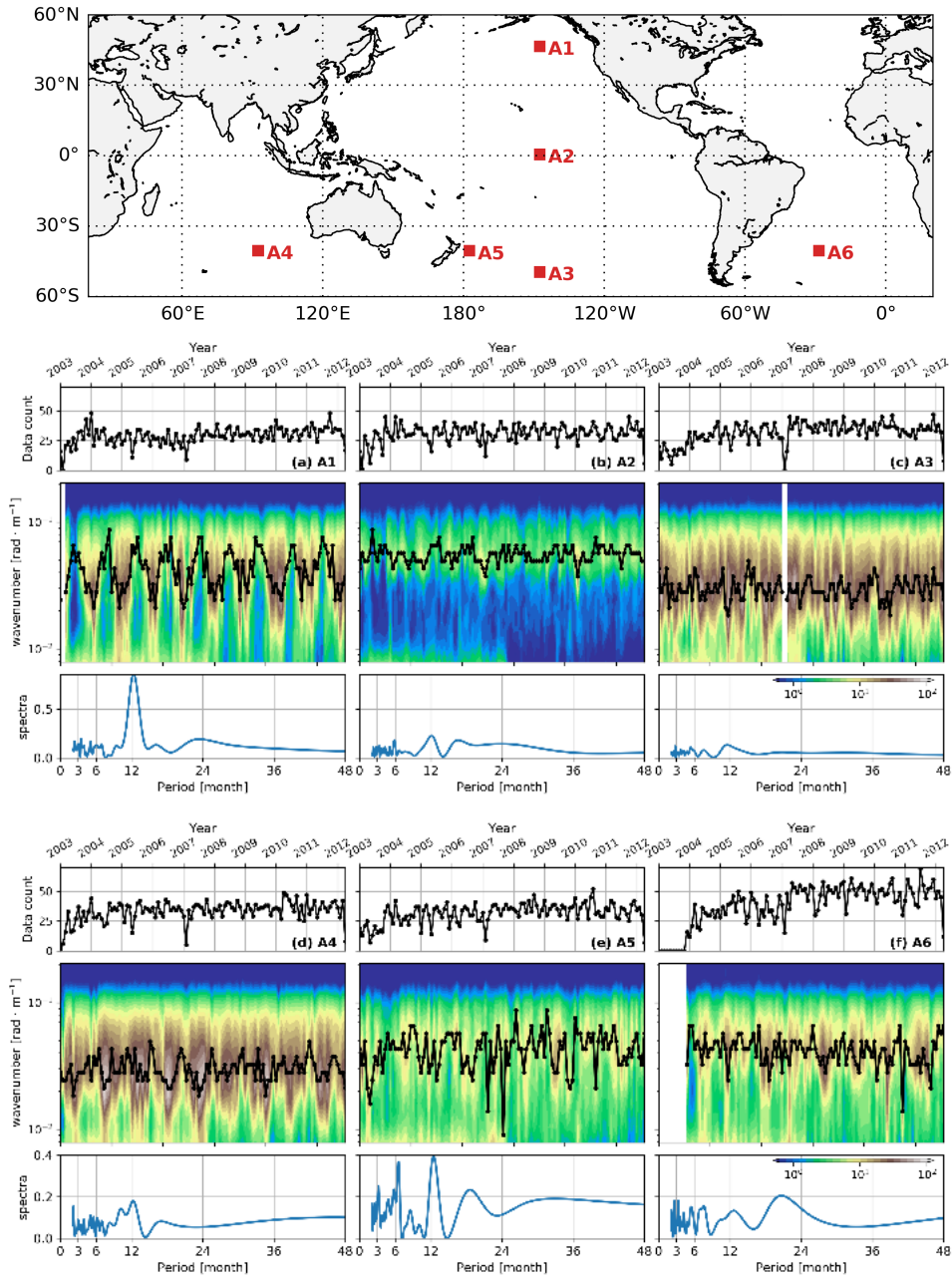


Figure 7.8: (Top) The geographic position of six area of interest. (Left) Monthly time series of MACS profile (color in log scale) over six area of interest (A1-A6) and detected k_{rp} (black solid line). The vertical blank space is due to lack of observations during that month. (Right) The frequency spectra of time series of range peak wavenumber. Note that A1-A3 correspond to the three transects in the Pacific Ocean in Figure 3.

produces the high peak of the frequency spectrum at period of 12 months. By comparison, both A2 and A3 have relatively consistent k_{rp} with weak yearly change, corresponding to the low values of the frequency spectra. But the sea state conditions differ between A2 and A3 in that the average k_{rp} is $0.05 \text{ rad} \cdot \text{m}^{-1}$ for A2 and $0.025 \text{ rad} \cdot \text{m}^{-1}$ for A3. This might be related to the constantly low winds in the trade winds region while high winds in the Southern Ocean throughout the year.

The periodicity of k_{rp} greatly varies even in the Southern Ocean (A3-A6). Among which, time series of k_{rp} over A3 are similar to that of A4, showing k_{rp} of $0.025 \text{ rad} \cdot \text{m}^{-1}$ with minor fluctuations. By comparison, A5 has sharper changes, particularly on a yearly basis. This is also reflected by the higher frequency spectra at periods longer than 15 months. Since A5 is close to the New Zealand, the ocean waves might be subject to the land activities. While A6 has a shorter time series due to lack of data in the beginning of ASAR. There is no clearly annual changes of k_{rp} over A6 and the periodicity is rather dominated by an intra-annual signal.

7.5 Summary

Extensive understanding of the characteristics of ocean waves are significant. The momentum exchange in the air-sea interaction is transferred through the ocean surface waves. A better parameterization of flux transfer by considering the sea state impact is expected to improve the coupled atmosphere-ocean model at global scale (Janssen & Viterbo, 1996). This would advance the interpretation of wave climate in the long term. Enhanced usage of the currently available data to examine the modern wave climate is therefore of priority as pointed in (Hemer et al., 2012).

The spaceborne satellite observations have proven valuable in the investigation of the global wave climate (Chen et al., 2002; Stopa et al., 2015b). In particular, the great potential of high-resolution SAR images that can resolve ocean wave spectral signatures, has probably been underestimated. The ten-year acquisition of Envisat/ASAR wave mode allows one to explore global features of ocean waves. Instead of using the integrated wave variables, we demonstrated encouraging new results obtained focusing only on the range traveling ocean waves.

The ocean waves are mostly in couple with the local wind. As shown by the MACS variation relative to the wind speed, longer ocean waves are in higher degree of coupling with the higher wind speed. From the view of wave growth, the degree of coupling strongly depends on the inverse wave age. Though limited to qualitative interpretations, the wind-wave interaction information provided by MACS is still significant. With the accurate winds independently retrieved from a SAR image, it is feasible to address the global wind-wave interactions. In particular, the wind-wave coupling under tropical cyclones is of great interest.

This study also emphasizes the distinct global signatures of ocean waves from various wavelengths. The results are consistent with the global winds pattern. The short ocean waves well represent the

wind distribution while the long ocean swell mainly exist at high latitude storm tracks. The other variable of range peak wavenumber also shed light on the swell propagation route across the ocean basin. In addition, the temporal periodicity of ocean waves is distinguished, depending on the local wind patterns.

The spatio-temporal patterns of ocean waves are desired to advance the climate model. The preliminary results of temporal range peak wavenumber portray the distinct changes across the ocean. Benefiting from the consistent acquisition of Sentinel-1 constellation (A and B now, C and D in 2020), this study can be readily extended to at least the ocean basin scale. With an more accurate wave spectra inversion algorithm, we might study the wave climate using a combination of both integral wave variables and the spectral variables.

Chapter 8

Conclusion and perspectives

Contents

7.1	Introduction of wave spectra climate	103
7.2	Extraction of the MACS profile	104
7.2.1	Envisat/ASAR wave mode	104
7.2.2	MACS profile extraction	105
7.3	MACS variation with wind speed	107
7.4	Global wave characteristics from MACS profile	108
7.4.1	Global MACS at selected wavelengths	109
7.4.2	k_{rp} from MACS profile	111
7.4.3	Temporal variation of k_{rp}	113
7.5	Summary	115

8.1 Conclusion

Since the launch of the first spaceborne SAR, Seasat-A in 1978, SAR observations have helped improve our understanding on many oceanic and atmospheric phenomena. As the most common elements on the sea surface, ocean winds and waves mutually interact with each other and both are significant to regulate the air-sea flux transfer. Their fine features on the sub-mesoscale (1-10 km) are as yet to be addressed with proper measurements. Spaceborne SAR is an effective means of providing winds and waves observations at resolution up to hundreds meters. It is thus of great interest to accurately derive winds and waves information from SAR images. In this thesis, the SAR observations of winds and waves are presented from several aspects.

SAR backscattering mainly responds to the sea surface roughness composed of capillary waves, commonly quantified by NRCS. Calibration is an essential process to obtain the proper NRCS

from the raw radar signal. An accurate NRCS is critical to inferring the wind speed. Thus, S-1 WV NRCS is first evaluated in this thesis. It is found that WV1 is well calibrated while it is not the case for WV2. Given this result, two re-calibration methods: rain forest calibration and ocean calibration are carried out and accordingly assessed. It is found that the ocean calibration method is more efficient to perform with slightly higher calibration accuracy. In addition to that, since it only needs several days' acquisitions over the global ocean, the operational status of NRCS calibration can be monitored over time. Subsequently, the retrieved wind speed based on the re-calibrated NRCS is demonstrated to improve in comparison to the ESA products. Yet challenges still remain and two aspects of work, at least, are needed to advance the SAR wind observation. One is to compensate the sea state impact in the wind retrieval. The other being a brand new algorithm to independently infer wind speed and direction from SAR observations.

Azimuth cutoff is another parameter that has been used to refine wind retrieval from SAR images. It is advantageous in that it is directly estimated from SAR image spectra and free of the calibration. Azimuth cutoff obtained from single-polarized SAR images has shown similar dependence on winds as NRCS does. With increasing availability of polarimetric data, it is possible to investigate the features of polarized azimuth cutoff. Based on the analyses of Radarsat-2 and Gaofen-3 data, azimuth cutoff is found to be polarization dependent. The general trend of VH larger than HH than in turn larger than VV is observed for both data sets. The comparison of azimuth cutoff between SAR measurements and simulations shows that the present SAR mapping theory is roughly sufficient to represent the co-polarized observations. In contrast, the cross-polarization needs further studies to formulate the transformation from ocean wave spectra to SAR image spectra. As a matter of fact, the distinguished azimuth cutoff of cross-polarization is kind of expected. It has been well documented that cross-polarized signal is more sensitive to the breaking waves on the sea surface, which have faster orbital velocity than the regular ocean waves. In a sense, the velocity bunching part is supposed to be revisited by taking the wave breaking into account, which is expected to lead to a larger azimuth cutoff in cross-polarization.

Either NRCS or azimuth cutoff represent an ensemble response to the imaged ocean waves of all scales. The SAR image spectra calculated from the variance of NRCS, however, reflects the modulation of the small-scale roughness by various wave scales. This lays the basis for inversion of the ocean waves spectra. On contrary to inverting the wave spectra and inferring the integrated parameters, in this thesis, the SAR image cross-spectra of the isolated wavelengths are extracted and termed as MACS. From the Envisat/ASAR to S-1, MACS is defined by filtering the cross-

spectra around the range axis.

On one hand, benefiting the complex nature of SAR cross-spectra, MACS is also a complex number with both real and imaginary component. Since the intermediate ocean waves are in strong coupling with the winds, MACS defined over wavelength of 20 m is found closely related to the local winds. In particular, IMACS provides fruitful information on the wind direction as demonstrated using both S-1 WV and wide swath images. Global analysis of IMACS shows good agreement yet advanced features than the global winds. Its directionality reveals the seasonal migration of intertropical convergence zone. To first order, IMACS is valuable to constrain an independent wind retrieval scheme (wind speed and direction) solely from SAR measurements.

Apart from that, magnitude of MACS (MMACS) is also documented relative to radar configurations (incidence angle, polarization) and the winds (wind speed and direction). It shows greater up-downwind asymmetry particularly at larger incidence angle of (36°). The comparison of MMACS between SAR measurements and the simulations using the nonlinear SAR transformation is found to show great deviations. Assuming a quasi-linear mapping relation of MACS, the RAR MTF is then derived by adjusting the simulations to be consistent with SAR measurements for combination of polarizations and incidence angles.

In comparison to NRCS and azimuth cutoff, MACS highlights the SAR signatures of ocean waves at isolated scales. As outlined above, MACS defined for 20 m waves is examined based on S-1 WV data. Considering that MACS varies with incidence angle, the ten-year acquisitions by Envisat/ASAR wave mode used to investigate the global variation of MACS for various wave scale. Another reason to select this data set is its relatively long duration allows to look into the temporal trend of MACS. Locally speaking, it provides qualitative yet promising evidence on the wind-wave coupling. The growth of ocean waves under the forcing of sea surface winds varies with wave scales: longer waves response strongly to higher winds. In addition to the integrated wave parameters, MACS offers a new means to studying the global wave spectral climate. The global distribution of ocean waves from 60 m to 320 m greatly differs, featuring the typical wind conditions from low to high winds. On top of that, the sea state can also be well derived from the MACS profile through the range peak wavenumber. It not only characterizes the dominant wave systems over the SAR passing time, but depicts the propagation of ocean swell at a broader scale across the ocean basin. This analysis can still be extended to longer time duration as there will be much more and routine acquisitions by the S-1 constellation and Radarsat-2 constellation mission in the

coming 10-20 years. The corresponding results shall contribute a new perspective into the global ocean waves in addition to the integrated variables.

8.2 Future Work

The present thesis reviewed the commonly used SAR variables in wind/wave observations and explored the new perspectives to enhance the capacities of high-resolution SAR images. The analyses presented in this thesis are expected to benefit several aspects of future studies.

First, an independent wind retrieval algorithm from SAR images is feasible given the distinct dependence of IMACS on wind direction. Now the retrieval methods mostly rely on the *a priori* wind direction (model or others) to infer the wind speed. However, the coarse resolution of input wind direction restricts the applications of SAR images in addressing the variation of wind dynamics at high-resolution. Taking advantage of the self-sufficient retrieval, wind changes at sub-mesoscale $O(1\text{ km})$ shall be addressed, such as the wind across the atmospheric or oceanic front et al. As such, the response of wind changes to other impact factors can be better examined.

Similarly, the RAR MTF derived in Chapter 6 requires further validation. This might be achieved by applying the refined RAR MTF in the operational wave inversion algorithm and then comparing the obtained variables such as significant wave height with buoy measurements. In fact, a more thorough look-up-table of RAR MTF can be built as function of winds without the simplification of MMACS formulae. A better RAR MTF shall also be helpful to complement the SAR imaging formulation in a quantitative way.

As in Chapter 7, the coupling between ocean waves and winds is presented by the MACS profile. Though limited to qualitative interpretations, the wind-wave interaction information provided by MACS is still significant. With the accurate winds independently retrieved from a SAR image, it is feasible to address the global wind-wave interactions. A climatology of global wind-wave interaction can therefore be derived based on the SAR data archive. This shall make full use of SAR measurements on simultaneous observations of wind and waves. In particular, this would aid in interpreting the wind-wave coupling under extremely high winds such as tropical cyclones at high spatial resolution. It is worth noting that the SWIM sensor aboard the recently launched CFOSAT (October 2018) is capable of measuring the two-dimensional ocean wave spectrum without nonlinear distortion. The combination of SWIM and existing/coming SAR sensors shall greatly advance

the global waves studies.

Now cross-polarized images are mainly involved in monitoring extreme events considering its high sensitivity at high winds. Its utility in observing ocean wave field has often been overlooked mostly due to lack of consistent observations. To date the SAR imaging theory of ocean waves by VH/HV polarization is barely investigated. Azimuth cutoff gives measure to non-linearity of SAR mapping transformation. In this sense, higher non-linearity of VH imaging process in comparison to that of VV is evidenced. Now, a major challenge in the inversion algorithm is to accurately estimate and remove the nonlinear image spectra component of velocity bunching. The present estimate algorithm is biased since it is computed from input of *a priori* including sea surface wind and wave age. The highly nonlinear image spectra of VH polarization and the negligible RAR modulation can be directly approximated as the nonlinear component in the co-polarized SAR image spectra. This would reduce the additional bias in ocean wave spectral inversion introduced by the inaccurate estimate of nonlinear part. Certainly, the future study will also focus on the theoretical investigations to better comprehend the SAR mapping principles of cross-polarization.

In addition to the points listed above, there are still a lot of questions remaining unanswered during this thesis. For example, the phase of MACS is found inconsistent with the predicted values in terms of SAR nonlinear mapping, which still needs to be examined. Also the application of MACS in extreme winds conditions is under study. Nevertheless, this thesis is not only a progress summary of the current work, but more like an opening knock to the future studies.

Appendix A

Sea state impact on wind retrieval

Contents

8.1 Conclusion	117
8.2 Future Work	120

A.1 Collocated wind and wave dataset

A match-up dataset is systematically first created by collocating S-1 WV imageries with winds from ECMWF operational forecast model. The ECMWF winds are used to re-calibrate the NRCS as in (H. Li et al., 2018). Thus, the wind speeds can not be used to independently evaluate wind retrieval performance. We then collocate S-1 WV data with NDBC buoys and consider buoy measurements as independent and reference winds. Collocations are limited to 100 km in space and 30 min in time. Figure A.1 shows map of collocation pairs between S-1 WV and buoys. Only buoys with concurrent wind and wave measurements are included in this analysis. There are approximately 2000 pairs for WV1 and WV2, respectively.

Most of the NDBC anemometers measure winds at a height of 2.5-4 m above the sea surface. To be consistent with SAR-measured neutral winds at 10 m, all buoy wind speeds are converted to 10 m neutral winds using a log-profile relation based on the assumption of neutrally stable boundary layer. Throughout rest of this paper, the wind speed refers to neutral wind speed at height of 10 m unless particularly stated and noted U10.

The wave spectra measured by NDBC buoys, is composed of frequency from 0.04 Hz up to 0.4850 Hz (Vandemark et al., 2005). The total significant wave height (H_s) is therefore calculated from two-dimensional frequency spectra by:

$$H_s = 4.0\sqrt{M_0} \tag{A.1}$$

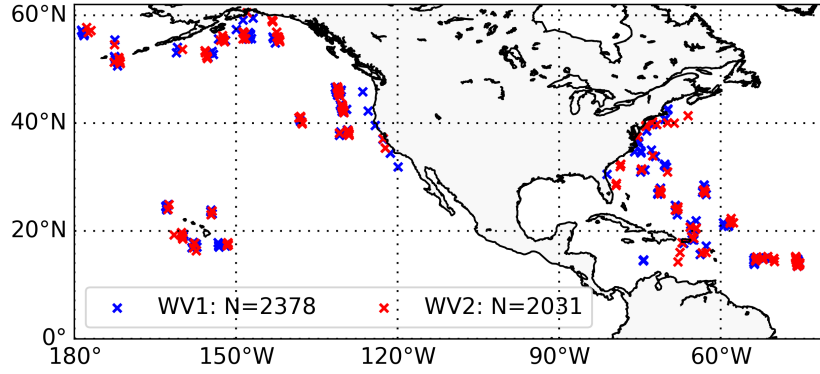


Figure A.1: Map of collocation dataset between S-1 WV and buoys. The red asterisk denotes collocations for WV1 and the blue for WV2. Spatially overlapped WV1 and WV2 do not coincide in time.

where M_i represents the i th moment of the wave spectrum

$$M_i = \int_0^{\infty} f^i S(f) df \quad (\text{A.2})$$

Other sea state parameters such as swell wave height, wave period, wave age have been demonstrated to have subtle impact on wind speed retrieval (Stopa et al., 2017). Thus, we do not include these variables in our analysis and only focus on the U10 relationship with H_s .

A.2 Sea state impact

In this section, U10 retrieved from re-calibrated NRCS is compared with collocated buoy wind speed. The U10 residual is further analyzed relative to buoy wind speed, significant wave height as well as SAR azimuth cutoff.

A.2.1 U10 residuals

U10 retrieval errors are further explored through the U10 residuals ($U10^{SAR} - U10^{Buoy}$). Figure A.2 presents U10 residuals relative to buoy wind speed. The U10 residuals are negatively proportional to buoy wind speed for both WV1 and WV2. This can be explained by the overestimation when buoy U10 is lower than 4 m/s. But the slightly smaller linear fit slope for WV1 is marginally inconsistent with results in (Stopa et al., 2017). They found much weaker wind speed dependence of U10 residual at higher incidence angle using scatterometers observations. This might be because

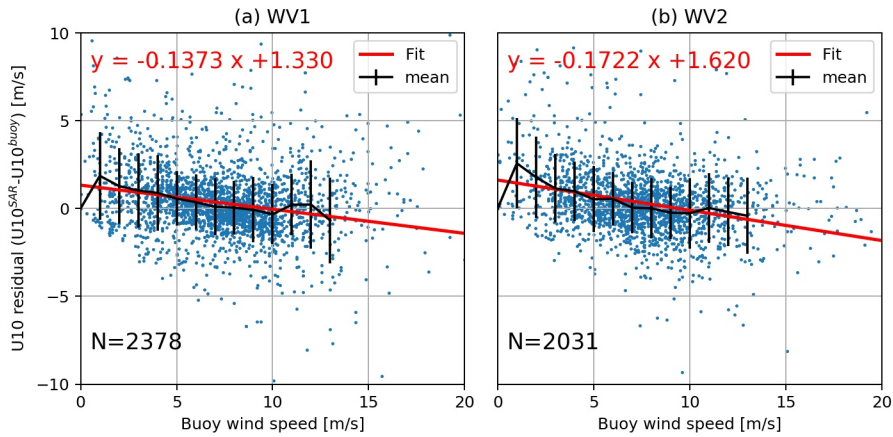


Figure A.2: Wind speed residual ($U^{SAR} - U^{buoy}$) relative to collocated buoy wind speed for (a) WV1 and (b) WV2. The error bars are 1 standard deviation about the average (black solid lines) and red solid lines represent least-squared linear regression. The linear fit slope is annotated on top left corner in red.

ASCAT winds vectors are inferred based on the merged three NRCS from three azimuth look angles. This merge is expected to resolve wind field more accurately even at higher incidence angle. In addition, larger U10 errors are found at low and high wind speeds for both WV1 and WV2. This is consistent with results in (Stopa et al., 2017). By comparison, the overall least-squared regression slope is much smaller in (Stopa et al., 2017) (see their Figure 6). In addition, the U10 residual at higher wind speed (> 12 m/s) for both WV1 and WV2 requires further investigations based on more collocation pairs.

U10 residuals versus collocated buoy H_s are shown in Figure A.3 to document the sea state impact on wind speed retrieval at two incidence angles. Overall, there is distinct relationship between U10 residuals and H_s . U10 residuals proportionally increase with H_s for both WV1 and WV2. The larger slope of U10 residual with H_s for WV1 is comparable to results of ENVISAT/ASAR (Stopa et al., 2017) since they operate at similar incidence angles. As expected, U10 residuals show much weaker dependence on sea state at higher incidence angle for WV2. Linear-regression slope of WV2 (0.128) is almost half that of WV1 (0.305). Since U10 residual dependence on H_s at higher incidence angle of scatterometer was not shown in (Stopa et al., 2017), a direct comparison is not available. Therefore, we computed Pearson correlation coefficient between U10 residual and buoy H_s . They are 0.08459 for WV1 and 0.01334 for WV2. By comparison, the correlation coefficient of sea state is less marked in the S-1 data than in the ASAR data. This might be associated with the larger footprint of S-1, averaging out more contributions from long ocean waves. This can also explain the less pronounced sea state impact of S-1 than scatterometer at incidence angle of WV2. In addition, a larger variability of U10 residual at low sea state ($H_s < 1$ m) is presented for

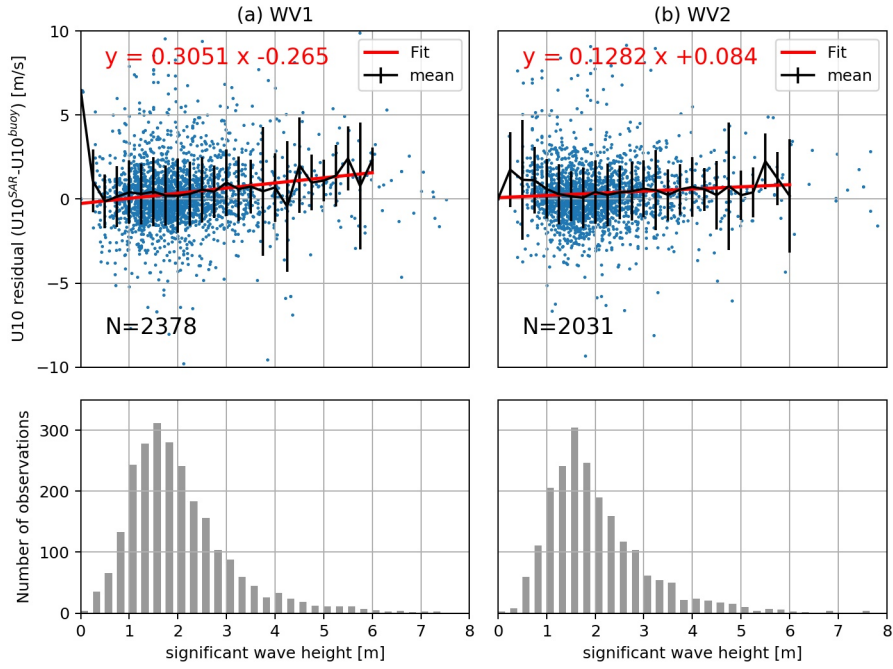


Figure A.3: (Top) Wind speed residual ($U10^{SAR} - U10^{buoy}$) is shown relative to collocated buoy H_s for (a) WV1 and (b) WV2. The error bars are 1 standard deviation about the average (black solid lines) and red solid lines represent linear regression. (Bottom) Histogram with bin of 0.25 m for WV1 in (c) and WV2 in (d), respectively.

both WV1 and WV2. This impact needs to be compensated in order to obtain more accurate wind speed, particularly at low and high wind speed.

The relationship between U10 residuals and collocated H_s indicates the necessity of compensating sea state to improve the wind retrieval. However, this requires *a priori* from external source and cannot estimate from SAR observations. Therefore, relating U10 residuals to a SAR-measured variable is essential to improve the operational SAR wind retrieval. A SAR takes advantage of Doppler history to achieve high along-track resolution, in other words, effect of local sea surface on Doppler echo is also recorded (Chapron et al., 2001). This restricts the imaging of azimuth-traveling waves to minimum wavelength corresponding to azimuth cutoff (Kerbaol et al., 1998a). It can be estimated by minimizing a Gaussian fitted function to cross-correlation function from standard SAR image cross-spectral analysis (Kerbaol et al., 1998a).

Analytically, azimuth cutoff can be calculated directly from ocean wave spectrum using (Kerbaol et al., 1998a; Stopa et al., 2015b)

$$\lambda_c = \pi \frac{R}{V} \sqrt{\int \omega^2 (\sin^2 \theta \sin^2 \phi + \cos^2 \theta) S(\mathbf{k}) d\mathbf{k}} \quad (\text{A.3})$$

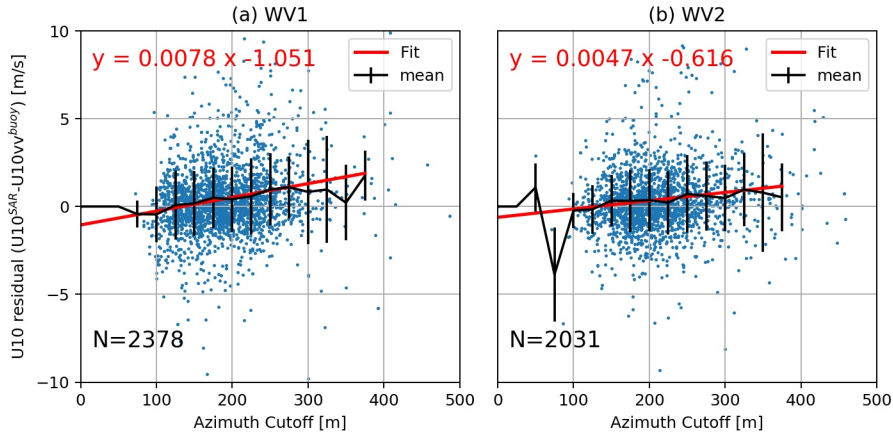


Figure A.4: Wind speed residual ($U^{SAR}-U^{buoy}$) relative to azimuth cutoff for (a) WV1 and (b) WV2. Error bars are 1 standard deviation about the average (black solid lines) and red solid lines represent linear regression.

where R/V is slant range-to-velocity ratio of SAR sensor, ω is angular frequency of ocean waves given by $\omega = \sqrt{gk}$ in deep water conditions. θ is SAR incidence angle and ϕ is wave propagation direction relative to SAR line-of-sight. As given in Eq.(A.1), H_s is zeroth-order moment of ocean wave spectrum while azimuth cutoff is a measure of second-order moment. By this definition, azimuth cutoff and H_s are intercorrelated with the former being more strongly influenced by the high frequency wave components. Several studies have demonstrated the feasibility to estimate H_s through azimuth cutoff (Beal et al., 1983; Shao et al., 2016b; Stopa & Mouche, 2017c). (Vachon et al., 1994) showed that azimuth cutoff has an empirical relationship on the square root of H_s . (Stopa et al., 2015b) reported the climate pattern of wave orbital velocity derived from azimuth cutoff is consistent with H_s using ten-year data of ASAR. This builds the basis of replacing H_s with azimuth cutoff to compensate the sea state impact on wind retrieval.

Figure A.4 presents U10 residuals relative to azimuth cutoff. As the azimuth cutoff increases, the U10 residuals increase proportionally. Slopes of linear regression are 0.0078 for WV1 and 0.0047 for WV2, respectively. This decreasing trend with increasing incidence angle is very similar to the trend observed when applying U10 residual versus H_s (see Figure A.3). Since azimuth cutoff can be obtained from high-resolution SAR images, this parameter is an indicator of the sea state and can potentially be used to account for the sea state impact on the wind speed retrieval without an ancillary dataset.

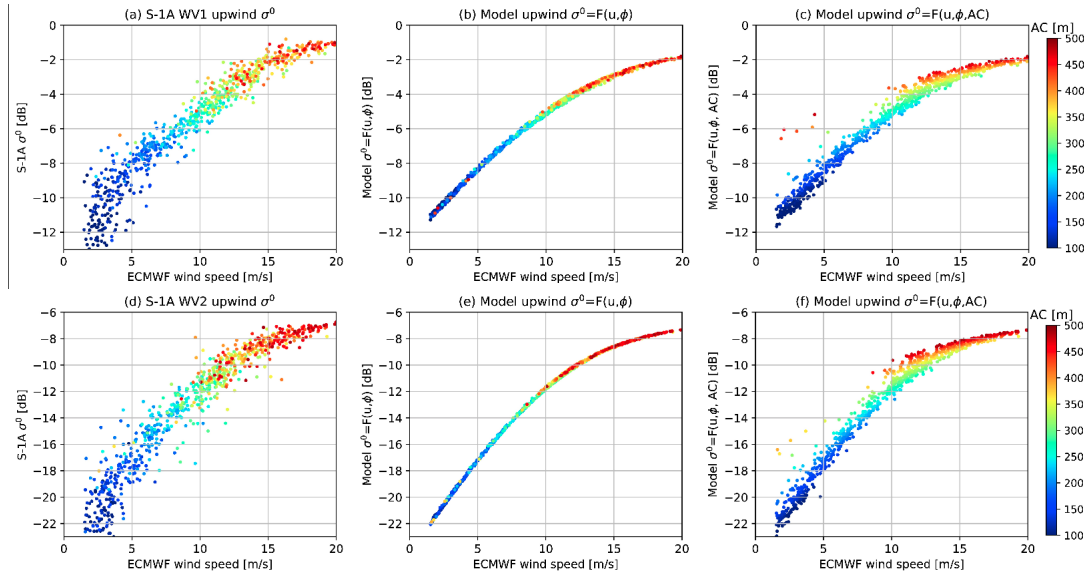


Figure A.5: NRCS as function of wind speed WV1/WV2 at top/bottom (only upwind direction with variation of $\pm 5^\circ$). (a)/(d) S-1A observations; (b)/(e) the predicted using a neural network with wind speed and wind direction as input; and (c)/(f) the predicted using a neural network with wind speed, wind direction and azimuth cutoff as input. The color denotes azimuth cutoff [m]. Bias and RMSE are calculated by the predicted NRCS relative to the S-1A observations.

A.2.2 NRCS with azimuth cutoff

In this section, we propose to assess the possibility of using both NRCS and azimuth cutoff for wind speed retrieval. Given the limited number of SAR-buoy collocations, we use SAR-ECMWF match-ups to demonstrate this feasibility. We restrain the ECMWF wind directions to be upwind with a variation of $\pm 5^\circ$. This is to highlight the impact of sea state in modifying radar NRCS. The deviation 5° is chosen to limit the NRCS variation with wind direction for given wind speed as well as to maintain a certain number of observations. We also choose the incidence angle of $24.2^\circ \pm 0.1^\circ$ for WV1 and $37.2^\circ \pm 0.1^\circ$ for WV2 to avoid the NRCS variation with incidence angle. It ends up with about 6,000 data points for both WV1 and WV2. A three-layer neural network is then used to train the GMF, which relates NRCS to winds and winds plus azimuth cutoff, respectively. This is realized based on the deep learning Python Keras library, publicly available (<https://keras.io/>). By default, the selected dataset is divided into two parts, one for training (70%) and one for validation (30%). Considering both accuracy and computation time, the number of epochs is set to be 50 to train the model after a series of tests. Two types of GMFs are trained, one is to relate NRCS only as function of wind speed and direction and the other relates NRCS to both winds and azimuth cutoff.

Figure A.5 illustrates NRCS from S-1 measurements and two types of GMFs. On the top, Figure A.5(a) presents the S-1 measured NRCS for WV1 relative to wind speed. The color denotes the corresponding azimuth cutoff. It is worth noting that the wind direction has been limited to upwind in order to better demonstrate the NRCS modification by sea state for given wind speed. Figure A.5(b) is the first trained GMF, relating NRCS to only wind speed and wind direction. While NRCS predicted by the second trained GMF as function of both wind and azimuth cutoff is then presented in Figure A.5(c). The results for WV2 are accordingly shown in Figure A.5(d)(e)(f). Note that the two types of GMF are trained separately for WV1 and WV2.

SAR-measured NRCS shows variability for given wind speed at upwind, up to 4 dB at low wind speed for both WV1 and WV2 as shown in Figure A.5(a)(d), respectively. This variability is partly consistent with variation of azimuth cutoff: larger azimuth cutoff corresponds to larger NRCS. This relationship resembles the sea state impact represented by H_s in (Stopa et al., 2017), showing larger H_s for larger NRCS. However, when only wind information is included to train a GMF (see Figure A.5(b)(e)), NRCS does not exhibit any variability at given wind speed. This implies that this GMF is insufficient to account for the NRCS modification by sea state. By comparison, the GMF in Figure A.5(c)(f) by involving the azimuth cutoff can partly resolve the NRCS variability with smaller NRCS bias and RMSE in Figure A.5(c)(f). For given wind speed, NRCS increases with azimuth cutoff rather than a constant predicted by $F(u, \phi)$. For example, at wind speed of 10 m/s in Figure A.5(c), the predicted NRCS increases from -5.5 dB to -3.8 dB with azimuth cutoff varying from 250 m to 400 m. The variation of 1.7 dB corresponds to wind retrieval error of about ± 1.5 m/s at 10 m/s wind speed. As a result, sea state impact is significant and needs to be compensated. This preliminary demonstration confirms the feasibility to train an advanced NRCS GMF with azimuth cutoff and accordingly account for the sea state impact.

References

- Alpers, K. W. and Hasselmann. (1978). The two-frequency microwave technique for measuring ocean-wave spectra from an airplane or satellite. *Boundary-Layer Meteorology*, 13(1), 215–230. Retrieved from <http://dx.doi.org/10.1007/BF00913873> doi: 10.1007/BF00913873
- Alpers, W. (1983, February). Monte carlo simulations for studying the relationship between ocean wave and synthetic aperture radar image spectra. *Journal of Geophysical Research: Oceans*, 88(C3), 1745-1759. Retrieved from <https://agupubs.onlinelibrary.wiley.com/doi/abs/10.1029/JC088iC03p01745> doi: 10.1029/JC088iC03p01745
- Alpers, W., & Rufenach, C. (1979, September). The effect of orbital motions on synthetic aperture radar imagery of ocean waves. *IEEE Transactions on Antennas and Propagation*, 27(5), 685-690. doi: 10.1109/TAP.1979.1142163
- Alpers, W. R., & Bruening, C. (1986, Nov). On the relative importance of motion-related contributions to the sar imaging mechanism of ocean surface waves. *IEEE Transactions on Geoscience and Remote Sensing*, GE-24(6), 873-885. doi: 10.1109/TGRS.1986.289702
- Alpers, W. R., Ross, D. B., & Rufenach, C. L. (1981). On the detectability of ocean surface waves by real and synthetic aperture radar. *Journal of Geophysical Research: Oceans*, 86(C7), 6481–6498. Retrieved from <http://dx.doi.org/10.1029/JC086iC07p06481> doi: 10.1029/JC086iC07p06481
- Ardhuin, F., Aksenov, Y., Benetazzo, A., Bertino, L., Brandt, P., Caubet, E., ... Xie, J. (2018). Measuring currents, ice drift, and waves from space: the sea surface kinematics multiscale monitoring (skim) concept. *Ocean Science*, 14(3), 337–354. Retrieved from <https://www.ocean-sci.net/14/337/2018/> doi: 10.5194/os-14-337-2018
- Ardhuin, F., Collard, F., Chapron, B., Girard-Ardhuin, F., Guitton, G., Mouche, A., & Stopa, J. E. (2015). Estimates of ocean wave heights and attenuation in sea ice using the sar wave mode on sentinel-1a. *Geophysical Research Letters*, 42(7), 2317–2325. Retrieved from <http://dx.doi.org/10.1002/2014GL062940> (2014GL062940) doi: 10.1002/2014GL062940
- Ardhuin, F., Rogers, E., Babanin, A. V., Filipot, J.-F., Magne, R., Roland, A., ... et al. (2010, Sep). Semiempirical dissipation source functions for ocean waves. part i: Definition, calibration, and validation. *Journal of Physical Oceanography*, 40(9), 1917-1941. Retrieved from <http://dx.doi.org/10.1175/2010JPO4324.1> doi: 10.1175/2010jpo4324.1
- Atlas, R., Hoffman, R. N., Bloom, S. C., Jusem, J. C., & Ardizzone, J. (1996). A multiyear global surface wind velocity dataset using ssm/i wind observations. *Bulletin of the American Meteorological Society*, 77(5), 869-882. Retrieved from [https://doi.org/10.1175/1520-0477\(1996\)077<0869:AMGSWV>2.0.CO;2](https://doi.org/10.1175/1520-0477(1996)077<0869:AMGSWV>2.0.CO;2) doi: 10.1175/1520-0477(1996)077<0869:AMGSWV>2.0.CO;2
- Bamler, R. (1992, July). A comparison of range-doppler and wavenumber domain sar focusing algorithms. *IEEE Transactions on Geoscience and Remote Sensing*, 30(4), 706-713. doi: 10.1109/36.158864
- Bao, M., & Alpers, W. (1998, May). On the cross spectrum between individual-look synthetic aperture radar images of ocean waves. *IEEE Transactions on Geoscience and Remote Sensing*, 36(3), 922-932. doi: 10.1109/36.673683
- Barrick, D. (1968, July). Rough surface scattering based on the specular point theory. *IEEE Transactions on Antennas and Propagation*, 16(4), 449-454. doi: 10.1109/TAP.1968.1139220
- Barrick, D. (1972, Sept). Remote sensing of sea state by radar. In *Ocean 72 - iee international conference on engineering in the ocean environment* (p. 186-192). doi: 10.1109/OCEANS.1972.1161190
- Beal, R., Tilley, D. G., & Monald, F. M. (1983). Large and small scale spatial evolution of digitally processed ocean wave spectra from seasat synthetic aperture radar. *Journal of Geophysical Research: Oceans*, 88(C3), 1761-1778. Retrieved from <https://agupubs.onlinelibrary.wiley.com/doi/abs/10.1029/JC088iC03p01761> doi: 10.1029/JC088iC03p01761
- Bentamy, A., Grodsky, S. A., Chapron, B., & Carton, J. A. (2013). Compatibility of c- and ku-band scatterometer winds: Ers-2 and quikscat. *Journal of Marine Systems*, 117-118, 72 - 80. Retrieved from <http://www.sciencedirect.com/science/article/pii/S092479631300033X> doi: <https://doi.org/10.1016/j.jmarsys.2013.02.008>

References

- Bourassa, M. A., Vincent, D. G., & Wood, W. L. (2001). A sea state parameterization with nonarbitrary wave age applicable to low and moderate wind speeds. *Journal of Physical Oceanography*, 31(10), 2840-2851. Retrieved from [https://doi.org/10.1175/1520-0485\(2001\)031<2840:ASSPWN>2.0.CO;2](https://doi.org/10.1175/1520-0485(2001)031<2840:ASSPWN>2.0.CO;2) doi: 10.1175/1520-0485(2001)031(2840:ASSPWN)2.0.CO;2
- Brown, G., Stanley, H., & Roy, N. (1981, April). The wind-speed measurement capability of spaceborne radar altimeters. *IEEE Journal of Oceanic Engineering*, 6(2), 59-63. doi: 10.1109/JOE.1981.1145484
- Camus, P., Losada, I. J., Izaguirre, C., Espejo, A., Menendez, M., & Prez, J. (2017). Statistical wave climate projections for coastal impact assessments. *Earth's Future*, 5(9), 918-933. Retrieved from <https://agupubs.onlinelibrary.wiley.com/doi/abs/10.1002/2017EF000609> doi: 10.1002/2017EF000609
- Carter, D. J. T., & Cotton, P. (1995). Applications of waves statistics estimated from altimeter data. In *Ers applications, proceedings of the second international workshop* (p. 57-60). European Space Agency.
- Carvajal, G. K., Eriksson, L. E. B., & Ulander, L. M. H. (2014, May). Retrieval and quality assessment of wind velocity vectors on the ocean with c-band sar. *IEEE Transactions on Geoscience and Remote Sensing*, 52(5), 2519-2537. doi: 10.1109/TGRS.2013.2262377
- Chapron, B., Collard, F., & Arduin, F. (2005). Direct measurements of ocean surface velocity from space: Interpretation and validation. *Journal of Geophysical Research: Oceans*, 110(C7), 1-17. Retrieved from <http://dx.doi.org/10.1029/2004JC002809> (C07008) doi: 10.1029/2004JC002809
- Chapron, B., Johnsen, H., & Garello, R. (2001, Nov 01). Wave and wind retrieval from sar images of the ocean. *Annales Des Télécommunications*, 56(11), 682-699. Retrieved from <https://doi.org/10.1007/BF02995562> doi: 10.1007/BF02995562
- Chen, G., Chapron, B., Ezraty, R., & Vandemark, D. (2002). A global view of swell and wind sea climate in the ocean by satellite altimeter and scatterometer. *Journal of Atmospheric and Oceanic Technology*, 19(11), 1849-1859. Retrieved from [https://doi.org/10.1175/1520-0426\(2002\)019<1849:AGVOSA>2.0.CO;2](https://doi.org/10.1175/1520-0426(2002)019<1849:AGVOSA>2.0.CO;2) doi: 10.1175/1520-0426(2002)019(1849:AGVOSA)2.0.CO;2
- Collard, F., Arduin, F., & Chapron, B. (2009a). Monitoring and analysis of ocean swell fields from space: New methods for routine observations. *Journal of Geophysical Research: Oceans*, 114(C7), 1-15. Retrieved from <http://dx.doi.org/10.1029/2008JC005215> (C07023) doi: 10.1029/2008JC005215
- Collard, F., Arduin, F., & Chapron, B. (2009b). Monitoring and analysis of ocean swell fields from space: New methods for routine observations. *Journal of Geophysical Research: Oceans*, 114(C7), 1-15. Retrieved from <https://agupubs.onlinelibrary.wiley.com/doi/abs/10.1029/2008JC005215> doi: 10.1029/2008JC005215
- Collecte Localisation Satellites. (2018). *Release note of s-1 ipf for end users of sentinel-1 products*. Retrieved from <https://sentinel.esa.int/documents/247904/2142675/S-1-IPF-Sentinel-1-products-Release-Note.pdf> (Accessed on Jan 16, 2018)
- Collecte Localisation Satellites (CLS). (2017). *Sentinel-1a and -1b annual performance report 2016* (Tech. Rep. Nos. MPC-0366, 2017). Brest, France: CLS.
- Corcione, V., Grieco, G., Portabella, M., Nunziata, F., & Migliaccio, M. (2018). A novel azimuth cutoff implementation to retrieve sea surface wind speed from sar imagery. *IEEE Transactions on Geoscience and Remote Sensing, in press*, 1-10. doi: 10.1109/TGRS.2018.2883364
- Crapolicchio, R., Chiara, G. D., Elyouncha, A., Lecomte, P., Neyt, X., Paciucci, A., & Talone, M. (2012, July). Ers-2 scatterometer: Mission performances and current reprocessing achievements. *IEEE Transactions on Geoscience and Remote Sensing*, 50(7), 2427-2448. doi: 10.1109/TGRS.2011.2179808
- Crapolicchio, R., & Lecomte, P. (1999, October). On the stability of amazon rainforest backscattering during the ers-2 scatterometer mission lifetime. In *Proceedings of the sar workshop: Ceos committee on earth observation satellites*. Toulouse, France.
- Crombie, D. D. (1955). Doppler spectrum of sea echo at 13.56 mc./s. *Nature*, 175(4459), 681.
- Cumming, I. G., & Wong, F. H.-c. (2005). *Digital processing of synthetic aperture radar data*. Artech House.

References

- Doyle, J. D. (2002). Coupled atmosphereocean wave simulations under high wind conditions. *Monthly Weather Review*, 130(12), 3087-3099. Retrieved from [https://doi.org/10.1175/1520-0493\(2002\)130<3087:CAOWSU>2.0.CO;2](https://doi.org/10.1175/1520-0493(2002)130<3087:CAOWSU>2.0.CO;2) doi: 10.1175/1520-0493(2002)130<3087:CAOWSU>2.0.CO;2
- Elfouhaily, T., Chapron, B., Katsaros, K., & Vandemark, D. (1997). A unified directional spectrum for long and short wind-driven waves. *Journal of Geophysical Research: Oceans*, 102(C7), 15781-15796. Retrieved from <https://agupubs.onlinelibrary.wiley.com/doi/abs/10.1029/97JC00467> doi: 10.1029/97JC00467
- Engen, G., & Johnsen, H. (1995, Jul). Sar-ocean wave inversion using image cross spectra. *IEEE Transactions on Geoscience and Remote Sensing*, 33(4), 1047-1056. doi: 10.1109/36.406690
- Engen, G., Vachon, P. W., Johnsen, H., & Dobson, F. W. (2000, Jan). Retrieval of ocean wave spectra and rain rate from dual-polarization sar data. *IEEE Transactions on Geoscience and Remote Sensing*, 38(1), 391-403. doi: 10.1109/36.823935
- European Space Agency. (2017). *Level-1 radiometric calibration*. Retrieved from <https://sentinels.copernicus.eu/web/sentinel/radiometric-calibration-of-level-1-products> ([Online; accessed 11-December-2017])
- European Space Agency. (2018). *User guide*. <https://sentinel.esa.int/web/sentinel/user-guides/sentinel-1-sar/acquisition-modes/wave>. Retrieved from <https://sentinel.esa.int/web/sentinel/user-guides/sentinel-1-sar/acquisition-modes/wave>
- Franceschetti, G., Iodice, A., Riccio, D., Ruello, G., & Siviero, R. (2002, Sept). Sar raw signal simulation of oil slicks in ocean environments. *IEEE Transactions on Geoscience and Remote Sensing*, 40(9), 1935-1949. doi: 10.1109/TGRS.2002.803798
- Franceschetti, G., Migliaccio, M., & Riccio, D. (1998, Jan). On ocean sar raw signal simulation. *IEEE Transactions on Geoscience and Remote Sensing*, 36(1), 84-100. doi: 10.1109/36.655320
- Freilich, M. H., & Dunbar, R. S. (1999). The accuracy of the nscat 1 vector winds: Comparisons with national data buoy center buoys. *Journal of Geophysical Research: Oceans*, 104(C5), 11231-11246. Retrieved from <https://agupubs.onlinelibrary.wiley.com/doi/abs/10.1029/1998JC900091> doi: 10.1029/1998JC900091
- Grieco, G., Lin, W., Migliaccio, M., Nirchio, F., & Portabella, M. (2016). Dependency of the sentinel-1 azimuth wavelength cut-off on significant wave height and wind speed. *International Journal of Remote Sensing*, 37(21), 5086-5104. Retrieved from <https://doi.org/10.1080/01431161.2016.1226525> doi: 10.1080/01431161.2016.1226525
- Gupta, M., Sharma, A., & Kartikeyan, B. (2017, Apr 01). Evaluation of risat-1 sar radiometric calibration using extended amazon rainforest. *Journal of the Indian Society of Remote Sensing*, 45(2), 195-207. Retrieved from <https://doi.org/10.1007/s12524-016-0582-5> doi: 10.1007/s12524-016-0582-5
- Hagfors, T. (1964). Backscattering from an undulating surface with applications to radar returns from the moon. *Journal of Geophysical Research*, 69(18), 3779-3784. Retrieved from <https://agupubs.onlinelibrary.wiley.com/doi/abs/10.1029/JZ069i018p03779> doi: 10.1029/JZ069i018p03779
- Hanley, K. E., Belcher, S. E., & Sullivan, P. P. (2010). A global climatology of windwave interaction. *Journal of Physical Oceanography*, 40(6), 1263-1282. Retrieved from <https://doi.org/10.1175/2010JP04377.1> doi: 10.1175/2010JP04377.1
- Hansen, M. W., Kudryavtsev, V., Chapron, B., Brekke, C., & Johannessen, J. A. (2016, Nov). Wave breaking in slicks: Impacts on c-band quad-polarized sar measurements. *IEEE Journal of Selected Topics in Applied Earth Observations and Remote Sensing*, 9(11), 4929-4940. doi: 10.1109/JSTARS.2016.2587840
- Hasselmann, K., Barnett, T., Bouws, E., Carlson, H., Cartwright, D., Enke, K., ... Walden, H. (1973). *Measurements of wind-wave growth and swell decay during the joint north sea wave project (jonswap)* (Part of collection: Hydraulic Engineering Reports Nos. A(8), 12). Hamburg, Germany: Deutsches Hydrographisches Institut.
- Hasselmann, K., Chapron, B., Aouf, L., Ardhuin, F., Collard, F., Engen, G., ... Schulz-Stellenfleth, J.

References

- (2012). *The ers sar wave mode – a breakthrough in global ocean wave observations* (Vol. SP-1326). ESA. Retrieved from <https://elib.dlr.de/77565/>
- Hasselmann, K., & Hasselmann, S. (1991a). On the nonlinear mapping of an ocean wave spectrum into a synthetic aperture radar image spectrum and its inversion. *Journal of Geophysical Research: Oceans*, 96(C6), 10713–10729. Retrieved from <http://dx.doi.org/10.1029/91JC00302> doi: 10.1029/91JC00302
- Hasselmann, K., & Hasselmann, S. (1991b, June 15). On the nonlinear mapping of an ocean wave spectrum into a synthetic aperture radar image spectrum and its inversion. *J. Geophys. Res.*, 96(C6), 10713–10729. Retrieved from <http://dx.doi.org/10.1029/91jc00302> doi: 10.1029/91jc00302
- Hasselmann, K., Raney, R. K., Plant, W. J., Alpers, W., Shuchman, R. A., Lyzenga, D. R., ... Tucker, M. J. (1985a). Theory of synthetic aperture radar ocean imaging: A marsen view. *Journal of Geophysical Research: Oceans*, 90(C3), 4659–4686. Retrieved from <http://dx.doi.org/10.1029/JC090iC03p04659> doi: 10.1029/JC090iC03p04659
- Hasselmann, K., Raney, R. K., Plant, W. J., Alpers, W., Shuchman, R. A., Lyzenga, D. R., ... Tucker, M. J. (1985b, May 20). Theory of synthetic aperture radar ocean imaging: A MARSEN view. *J. Geophys. Res.*, 90(C3), 4659–4686. Retrieved from <http://dx.doi.org/10.1029/jc090ic03p04659> doi: 10.1029/jc090ic03p04659
- Hasselmann, S., Brning, C., Hasselmann, K., & Heimbach, P. (1996). An improved algorithm for the retrieval of ocean wave spectra from synthetic aperture radar image spectra. *Journal of Geophysical Research: Oceans*, 101(C7), 16615–16629. Retrieved from <https://agupubs.onlinelibrary.wiley.com/doi/abs/10.1029/96JC00798> doi: 10.1029/96JC00798
- Hawkins, R., Attema, E., Crapolicchio, R., Lecomte, P., Closa, J., Meadows, P., & Srivastava, S. (1999, October). Stability of amazon backscatter at c-band: Spaceborne results from ers-1/2 and radarsat-1. In *Proceedings of the sar workshop: Ceos committee on earth observation satellites*. Toulouse, France.
- Heimbach, P., Hasselmann, S., & Hasselmann, K. (1998). Statistical analysis and intercomparison of wam model data with global ers-1 sar wave mode spectral retrievals over 3 years. *Journal of Geophysical Research: Oceans*, 103(C4), 7931–7977. Retrieved from <https://agupubs.onlinelibrary.wiley.com/doi/abs/10.1029/97JC03203> doi: 10.1029/97JC03203
- Hemer, M. A., Wang, X. L., Weisse, R., & Swail, V. R. (2012). Advancing wind-waves climate science. *Bulletin of the American Meteorological Society*, 93(6), 791–796. Retrieved from <https://doi.org/10.1175/BAMS-D-11-00184.1> doi: 10.1175/BAMS-D-11-00184.1
- Hersbach, H. (2008, April). *Cmod5.n: A c-band geophysical model function for equivalent neutral wind*. (Technical Memorandum No. 554). ECMWF.
- Hersbach, H., Stoffelen, A., & de Haan, S. (2007). An improved c-band scatterometer ocean geophysical model function: Cmod5. *Journal of Geophysical Research: Oceans*, 112(C3), n/a–n/a. Retrieved from <http://dx.doi.org/10.1029/2006JC003743> (C03006) doi: 10.1029/2006JC003743
- Hoffman, R. N., & Louis, J.-F. (1990). The influence of atmospheric stratification on scatterometer winds. *Journal of Geophysical Research: Oceans*, 95(C6), 9723–9730. Retrieved from <https://agupubs.onlinelibrary.wiley.com/doi/abs/10.1029/JC095iC06p09723> doi: 10.1029/JC095iC06p09723
- Horstmann, J., Koch, W., Lehner, S., & Tonboe, R. (2002). Ocean winds from radarsat-1 scansar. *Canadian Journal of Remote Sensing*, 28(3), 524–533. Retrieved from <https://doi.org/10.5589/m02-043> doi: 10.5589/m02-043
- Horstmann, J., Schiller, H., Schulz-Stellenfleth, J., & Lehner, S. (2003, Oct). Global wind speed retrieval from sar. *IEEE Transactions on Geoscience and Remote Sensing*, 41(10), 2277–2286. doi: 10.1109/TGRS.2003.814658
- Husson, R., Mouche, A., Chapron, B., Johnsen, H., Collard, F., Vincent, P., ... Gaultier, L. (2016, July). Taking advantage of sentinel-1 acquisition modes to improve ocean sea state retrieval. In *2016 IEEE International Geoscience and Remote Sensing Symposium (IGARSS)* (p. 3886–3889). doi: 10.1109/IGARSS.2016.7730009
- Hwang, P. A., Stoffelen, A., van Zadelhoff, G.-J., Perrie, W., Zhang, B., Li, H., & Shen, H. (2015). Cross-

References

- polarization geophysical model function for c-band radar backscattering from the ocean surface and wind speed retrieval. *Journal of Geophysical Research: Oceans*, 120(2), 893–909. Retrieved from <http://dx.doi.org/10.1002/2014JC010439> doi: 10.1002/2014JC010439
- Jackson, C. R., & Apel, J. R. (2004, September). Synthetic aperture radar marine user's manual [Computer software manual].
- Jacobsen, S., & Hgda, K. A. (1994). Estimation of the real aperture radar modulation transfer function directly from synthetic aperture radar ocean wave image spectra without a priori knowledge of the ocean wave height spectrum. *Journal of Geophysical Research: Oceans*, 99(C7), 14291–14302. Retrieved from <http://dx.doi.org/10.1029/94JC00633> doi: 10.1029/94JC00633
- Jagdish, Kumar, S. V. V. A., Chakraborty, A., & Kumar, R. (2018). Validation of wind speed retrieval from risat-1 sar images of the north indian ocean. *Remote Sensing Letters*, 9(5), 421–428. Retrieved from <https://doi.org/10.1080/2150704X.2018.1430392> doi: 10.1080/2150704X.2018.1430392
- Janssen, P. A. E. M., & Viterbo, P. (1996). Ocean waves and the atmospheric climate. *Journal of Climate*, 9(6), 1269–1287. Retrieved from [https://doi.org/10.1175/1520-0442\(1996\)009<1269:OWATAC>2.0.CO;2](https://doi.org/10.1175/1520-0442(1996)009<1269:OWATAC>2.0.CO;2) doi: 10.1175/1520-0442(1996)009<1269:OWATAC>2.0.CO;2
- Jiang, H., & Chen, G. (2013). A global view on the swell and wind sea climate by the jason-1 mission: A revisit. *Journal of Atmospheric and Oceanic Technology*, 30(8), 1833–1841. Retrieved from <https://doi.org/10.1175/JTECH-D-12-00180.1> doi: 10.1175/JTECH-D-12-00180.1
- Johannessen, J. A., Chapron, B., Collard, F., Kudryavtsev, V., Mouche, A., Akimov, D., & Dagestad, K.-F. (2008). Direct ocean surface velocity measurements from space: Improved quantitative interpretation of envisat asar observations. *Geophysical Research Letters*, 35(22), 1–6. Retrieved from <https://agupubs.onlinelibrary.wiley.com/doi/abs/10.1029/2008GL035709> doi: 10.1029/2008GL035709
- Johnsen, H. (2005). *Envisat asar wave mode product description and reconstruction procedure* (Tech. Rep. No. 1/2005). Tromso, Norway: Norut.
- Johnsen, H., & Collard, F. (2009). *Sentinel-1 ocean swell wave spectra (osw) algorithm definition* (Tech. Rep. No. S1-TN-NRT-52-7450). Tromso, Norway: Norut.
- Johnsen, H., Engen, G., & Guitton, G. (2008, Nov). Sea-surface polarization ratio from envisat asar ap data. *IEEE Transactions on Geoscience and Remote Sensing*, 46(11), 3637–3646. doi: 10.1109/TGRS.2008.2001061
- Jones, W. L., Boggs, D. H., Bracalente, E. M., Brown, R. A., Guymer, T. H., Shelton, D., & Schroeder, L. C. (1981). Evaluation of the seasat wind scatterometer. *Nature*, 294(5843), 704707. doi: 10.1038/294704a0
- Juszko, B.-A., Marsden, R. F., & Waddell, S. R. (1995). Wind stress from wave slopes using phillips equilibrium theory. *Journal of Physical Oceanography*, 25(2), 185–203. Retrieved from [https://doi.org/10.1175/1520-0485\(1995\)025<0185:WSFWSU>2.0.CO;2](https://doi.org/10.1175/1520-0485(1995)025<0185:WSFWSU>2.0.CO;2) doi: 10.1175/1520-0485(1995)025<0185:WSFWSU>2.0.CO;2
- Kerbaol, V. (1997). *Analyse spectrale et statistique vent-vagues des images radar ouverture synthique : application aux donnes satellites ers-1/2* (Unpublished doctoral dissertation). Universit de Rennes 1.
- Kerbaol, V., Chapron, B., & Vachon, P. W. (1998a). Analysis of ers-1/2 synthetic aperture radar wave mode imagettes. *Journal of Geophysical Research: Oceans*, 103(C4), 7833–7846. Retrieved from <http://dx.doi.org/10.1029/97JC01579> doi: 10.1029/97JC01579
- Kerbaol, V., Chapron, B., & Vachon, P. W. (1998b). Analysis of ers-1/2 synthetic aperture radar wave mode imagettes. *Journal of Geophysical Research: Oceans*, 103(C4), 7833–7846. Retrieved from <http://dx.doi.org/10.1029/97JC01579> doi: 10.1029/97JC01579
- Krogstad, H. E., Samset, O., & Vachon, P. W. (1994). Generalizations of the nonlinear oceansar transform and a simplified sar inversion algorithm. *Atmosphere-Ocean*, 32(1), 61–82. Retrieved from <https://doi.org/10.1080/07055900.1994.9649490> doi: 10.1080/07055900.1994.9649490
- Kudryavtsev, V., Akimov, D., Johannessen, J., & Chapron, B. (2005). On radar imaging of current features: 1. model and comparison with observations. *Journal of Geophysical Research: Oceans*, 110(C7). Retrieved from <https://agupubs.onlinelibrary.wiley.com/doi/abs/10.1029/2004JC002505> doi: 10.1029/2004JC002505

References

- Kudryavtsev, V., Chapron, B., & Makin, V. (2013). Impact of wind waves on the airsea fluxes: A coupled model. *Journal of Geophysical Research: Oceans*, 119(2), 1217-1236. Retrieved from <https://agupubs.onlinelibrary.wiley.com/doi/abs/10.1002/2013JC009412> doi: 10.1002/2013JC009412
- Kudryavtsev, V., Hauser, D., Caudal, G., & Chapron, B. (2003). A semiempirical model of the normalized radar cross section of the sea surface, 2. radar modulation transfer function. *Journal of Geophysical Research: Oceans*, 108(C3), 1–24. Retrieved from <https://agupubs.onlinelibrary.wiley.com/doi/abs/10.1029/2001JC001004> doi: 10.1029/2001JC001004
- Kudryavtsev, V., Kozlov, I., Chapron, B., & Johannessen, J. A. (2014, September 1). Quad-polarization SAR features of ocean currents. *J. Geophys. Res. Oceans*, 119(9), 6046–6065. Retrieved from <http://dx.doi.org/10.1002/2014jc010173> doi: 10.1002/2014jc010173
- Kudryavtsev, V., Yurovskaya, M., Chapron, B., Collard, F., & Donlon, C. (2017). Sun glitter imagery of surface waves. part 2: Waves transformation on ocean currents. *Journal of Geophysical Research: Oceans*, 122(2), 1384-1399. Retrieved from <https://agupubs.onlinelibrary.wiley.com/doi/abs/10.1002/2016JC012426> doi: 10.1002/2016JC012426
- Lehner, S., Horstmann, J., Koch, W., & Rosenthal, W. (1998). Mesoscale wind measurements using recalibrated ers sar images. *Journal of Geophysical Research: Oceans*, 103(C4), 7847-7856. Retrieved from <https://agupubs.onlinelibrary.wiley.com/doi/abs/10.1029/97JC02726> doi: 10.1029/97JC02726
- Lehner, S., Schulz-Stellenfleth, J., Schättler, B., Breit, H., & Horstmann, J. (2000). Wind and wave measurements using complex ers-2 sar wave mode data. *IEEE Transactions on Geoscience and Remote Sensing*, 38(5), 2246–2257. doi: 10.1109/TGRS.2003.814658
- Li, H., Chapron, B., Mouche, A., & Stopa, J. E. (2019). A new ocean sar cross-spectral parameter: definition and directional property using the global sentinel-1 measurements. *Journal of Geophysical Research: Oceans*, in press. Retrieved from <https://agupubs.onlinelibrary.wiley.com/doi/abs/10.1029/2018JC014638> doi: 10.1029/2018JC014638
- Li, H., Mouche, A., Stopa, J. E., & Chapron, B. (2018). Calibration of the normalized radar cross section for sentinel-1 wave mode. *IEEE Transactions on Geoscience and Remote Sensing*, 1-9. Retrieved from <https://doi.org/10.1109/TGRS.2018.2867035> doi: 10.1109/TGRS.2018.2867035
- Li, J.-G., & Holt, M. (2009). Comparison of envisat asar ocean wave spectra with buoy and altimeter data via a wave model. *Journal of Atmospheric and Oceanic Technology*, 26(3), 593-614. Retrieved from <https://doi.org/10.1175/2008JTECH0529.1> doi: 10.1175/2008JTECH0529.1
- Li, J.-G., & Saulter, A. (2012). Assessment of the updated envisat asar ocean surface wave spectra with buoy and altimeter data. *Remote Sensing of Environment*, 126, 72 - 83. Retrieved from <http://www.sciencedirect.com/science/article/pii/S0034425712003318> doi: <https://doi.org/10.1016/j.rse.2012.08.018>
- Li, X., Lehner, S., & Bruns, T. (2011, Jan). Ocean wave integral parameter measurements using envisat asar wave mode data. *IEEE Transactions on Geoscience and Remote Sensing*, 49(1), 155-174. doi: 10.1109/TGRS.2010.2052364
- Li, X.-M. (2016). A new insight from space into swell propagation and crossing in the global oceans. *Geophysical Research Letters*, 43(10), 5202-5209. Retrieved from <https://agupubs.onlinelibrary.wiley.com/doi/abs/10.1002/2016GL068702> doi: 10.1002/2016GL068702
- Lin, H., Xu, Q., & Zheng, Q. (2008). An overview on sar measurements of sea surface wind. *Progress in Natural Science*, 18(8), 913 - 919. Retrieved from <http://www.sciencedirect.com/science/article/pii/S1002007108001755> doi: <https://doi.org/10.1016/j.pnsc.2008.03.008>
- Liu, B., & He, Y. (2016, Oct). Sar raw data simulation for ocean scenes using inverse omega-k algorithm. *IEEE Transactions on Geoscience and Remote Sensing*, 54(10), 6151-6169. doi: 10.1109/TGRS.2016.2582525
- Long, D. G., & Skouson, G. B. (1996, Mar). Calibration of spaceborne scatterometers using tropical rain forests. *IEEE Transactions on Geoscience and Remote Sensing*, 34(2), 413-424. doi: 10.1109/36.485119
- Lu, Y., Zhang, B., Perrie, W., Mouche, A. A., Li, X., & Wang, H. (2018, July). A c-band geophysical

- model function for determining coastal wind speed using synthetic aperture radar. *IEEE Journal of Selected Topics in Applied Earth Observations and Remote Sensing*, 11(7), 2417-2428. doi: 10.1109/JSTARS.2018.2836661
- Madsen, S. N. (1989, March). Estimating the doppler centroid of sar data. *IEEE Transactions on Aerospace and Electronic Systems*, 25(2), 134-140. doi: 10.1109/7.18675
- Martin, A. C., Gommenginger, C. P., & Quilfen, Y. (2018). Simultaneous ocean surface current and wind vectors retrieval with squinted sar interferometry: Geophysical inversion and performance assessment. *Remote Sensing of Environment*, 216, 798 - 808. Retrieved from <http://www.sciencedirect.com/science/article/pii/S003442571830292X> doi: <https://doi.org/10.1016/j.rse.2018.06.013>
- Martin, A. C. H., Gommenginger, C., Marquez, J., Doody, S., Navarro, V., & Buck, C. (2016). Wind-wave-induced velocity in ati sar ocean surface currents: First experimental evidence from an airborne campaign. *Journal of Geophysical Research: Oceans*, 121(3), 1640-1653. Retrieved from <https://agupubs.onlinelibrary.wiley.com/doi/abs/10.1002/2015JC011459> doi: 10.1002/2015JC011459
- Montgomery, M. T., & Farrell, B. F. (1992). Polar low dynamics. *Journal of the Atmospheric Sciences*, 49(24), 2484-2505. Retrieved from [https://doi.org/10.1175/1520-0469\(1992\)049<2484:PLD>2.0.CO;2](https://doi.org/10.1175/1520-0469(1992)049<2484:PLD>2.0.CO;2) doi: 10.1175/1520-0469(1992)049<2484:PLD>2.0.CO;2
- Mouche, A., & Chapron, B. (2015a). Global c-band envisat, radarsat-2 and sentinel-1 sar measurements in copolarization and cross-polarization. *Journal of Geophysical Research: Oceans*, 120(11), 7195–7207. Retrieved from <http://dx.doi.org/10.1002/2015JC011149> doi: 10.1002/2015JC011149
- Mouche, A., & Chapron, B. (2015b). Global c-band envisat, radarsat-2 and sentinel-1 sar measurements in copolarization and cross-polarization. *Journal of Geophysical Research: Oceans*, 120(11), 7195–7207. Retrieved from <http://dx.doi.org/10.1002/2015JC011149> doi: 10.1002/2015JC011149
- Mouche, A. A., Chapron, B., Reul, N., & Collard, F. (2008). Predicted doppler shifts induced by ocean surface wave displacements using asymptotic electromagnetic wave scattering theories. *Waves in Random and Complex Media*, 18(1), 185-196. Retrieved from <https://doi.org/10.1080/17455030701564644> doi: 10.1080/17455030701564644
- Mouche, A. A., Chapron, B., Reul, N., Hauser, D., & Quilfen, Y. (2007a). Importance of the sea surface curvature to interpret the normalized radar cross section. *Journal of Geophysical Research: Oceans*, 112(C10), 1–12. Retrieved from <https://agupubs.onlinelibrary.wiley.com/doi/abs/10.1029/2006JC004010> doi: 10.1029/2006JC004010
- Mouche, A. A., Chapron, B., Reul, N., Hauser, D., & Quilfen, Y. (2007b). Importance of the sea surface curvature to interpret the normalized radar cross section. *Journal of Geophysical Research: Oceans*, 112(C10). Retrieved from <https://agupubs.onlinelibrary.wiley.com/doi/abs/10.1029/2006JC004010> doi: 10.1029/2006JC004010
- Mouche, A. A., Chapron, B., Zhang, B., & Husson, R. (2017, Dec). Combined co- and cross-polarized sar measurements under extreme wind conditions. *IEEE Transactions on Geoscience and Remote Sensing*, 55(12), 6746-6755. doi: 10.1109/TGRS.2017.2732508
- Mouche, A. A., Collard, F., Chapron, B., Dagestad, K. F., Guitton, G., Johannessen, J. A., . . . Hansen, M. W. (2012, July). On the use of doppler shift for sea surface wind retrieval from sar. *IEEE Transactions on Geoscience and Remote Sensing*, 50(7), 2901–2909. doi: 10.1109/TGRS.2011.2174998
- Mouche, A. A., Hauser, D., Daloze, J. ., & Guerin, C. (2005, April). Dual-polarization measurements at c-band over the ocean: results from airborne radar observations and comparison with envisat asar data. *IEEE Transactions on Geoscience and Remote Sensing*, 43(4), 753-769. doi: 10.1109/TGRS.2005.843951
- Mouche, A. A., Hauser, D., & Kudryavtsev, V. (2006a). Radar scattering of the ocean surface and sea-roughness properties: A combined analysis from dual-polarizations airborne radar observations and models in c band. *Journal of Geophysical Research: Oceans*, 111(C9), 1–18. Retrieved from <https://agupubs.onlinelibrary.wiley.com/doi/abs/10.1029/2005JC003166> doi:

References

- 10.1029/2005JC003166
- Mouche, A. A., Hauser, D., & Kudryavtsev, V. (2006b). Radar scattering of the ocean surface and sea-roughness properties: A combined analysis from dual-polarizations airborne radar observations and models in c band. *Journal of Geophysical Research: Oceans*, 111(C9). Retrieved from <https://agupubs.onlinelibrary.wiley.com/doi/abs/10.1029/2005JC003166> doi: 10.1029/2005JC003166
- Nilsen, V., Engen, G., & Johnsen, H. (2018). *A novel approach to sar ocean wind retrieval*. Presentation on SeaSAR 2018, ESA-ESRIN, Frascati (Rome), Italy, 2018. Retrieved from <http://seasar2018.esa.int/files/presentation145.pdf>
- Nouguier, F., Chapron, B., Collard, F., Mouche, A. A., Rascle, N., Ardhuin, F., & Wu, X. (2018, Oct). Sea surface kinematics from near-nadir radar measurements. *IEEE Transactions on Geoscience and Remote Sensing*, 56(10), 6169-6179. doi: 10.1109/TGRS.2018.2833200
- Ocean and Sea Ice SAF. (2016, June). *Algorithm theoretical basis document for the osi saf wind products* [Technical Memorandum]. KNMI.
- PCS Team. (1999). *Ers-2 wind scatterometer cyclic report: from 28th june 1999 to 2nd august 1999 cycle 44* (Tech. Rep. No. APP-ADQ/PCS/WS00-001). ESA ESRIN, Frascati, Italy: ESA ESRIN.
- Phalippou, L., & Enjolras, V. (2007, July). Re-tracking of sar altimeter ocean power-waveforms and related accuracies of the retrieved sea surface height, significant wave height and wind speed. In *2007 IEEE International Geoscience and Remote Sensing Symposium* (p. 3533-3536). doi: 10.1109/IGARSS.2007.4423608
- Phillips, O. M. (1977). *The dynamics of the upper ocean* (2nd ed.). Cambridge-London-New York-Melbourne: Cambridge University Press.
- Phillips, O. M. (1985). Spectral and statistical properties of the equilibrium range in wind-generated gravity waves. *Journal of Fluid Mechanics*, 156, 505531. doi: 10.1017/S0022112085002221
- Plagge, A. M., Vandemark, D., & Chapron, B. (2012). Examining the impact of surface currents on satellite scatterometer and altimeter ocean winds. *Journal of Atmospheric and Oceanic Technology*, 29(12), 1776-1793. Retrieved from <https://doi.org/10.1175/JTECH-D-12-00017.1> doi: 10.1175/JTECH-D-12-00017.1
- Portilla-Yandún, J. (2018). The global signature of ocean wave spectra. *Geophysical Research Letters*, 45(1), 267-276. Retrieved from <https://agupubs.onlinelibrary.wiley.com/doi/abs/10.1002/2017GL076431> doi: 10.1002/2017GL076431
- Portilla-Yandún, J., Salazar, A., & Cavaleri, L. (2016). Climate patterns derived from ocean wave spectra. *Geophysical Research Letters*, 43(22), 11,736-11,743. Retrieved from <https://agupubs.onlinelibrary.wiley.com/doi/abs/10.1002/2016GL071419> doi: 10.1002/2016GL071419
- Queffelec, P., & Bentamy, A. (2007). Analysis of wave height variability using altimeter measurements: Application to the mediterranean sea. *Journal of Atmospheric and Oceanic Technology*, 24(12), 2078-2092. Retrieved from <https://doi.org/10.1175/2007JTECH0507.1> doi: 10.1175/2007JTECH0507.1
- Quilfen, Y., & Bentamy, A. (1994, Aug). Calibration/validation of ers-1 scatterometer precision products. In *Geoscience and remote sensing symposium, 1994. igarss '94. surface and atmospheric remote sensing: Technologies, data analysis and interpretation., international* (Vol. 2, p. 945-947 vol.2). doi: 10.1109/IGARSS.1994.399308
- Quilfen, Y., Chapron, B., Bentamy, A., Gourrion, J., El Fouhaily, T., & Vandemark, D. (1999). Global ers 1 and 2 and nscat observations: Upwind/crosswind and upwind/downwind measurements. *Journal of Geophysical Research: Oceans*, 104(C5), 11459-11469. Retrieved from <http://dx.doi.org/10.1029/1998JC900113> doi: 10.1029/1998JC900113
- Quilfen, Y., Chapron, B., Collard, F., & Vandemark, D. (2004). Relationship between ers scatterometer measurement and integrated wind and wave parameters. *Journal of Atmospheric and Oceanic Technology*, 21(2), 368-373. Retrieved from [https://doi.org/10.1175/1520-0426\(2004\)021<0368:RBESMA>2.0.CO;2](https://doi.org/10.1175/1520-0426(2004)021<0368:RBESMA>2.0.CO;2) doi: 10.1175/1520-0426(2004)021<0368:RBESMA>2.0.CO;2
- Raney, R. K., Runge, H., Bamler, R., Cumming, I. G., & Wong, F. H. (1994, July). Precision sar processing using chirp scaling. *IEEE Transactions on Geoscience and Remote Sensing*, 32(4), 786-799. doi:

References

- 10.1109/36.298008
- Reguero, B. G., Losada, I. J., & Méndez, F. J. (2019). A recent increase in global wave power as a consequence of oceanic warming. *Nature Communications*, *10*(1), 205. Retrieved from <https://doi.org/10.1038/s41467-018-08066-0> doi: 10.1038/s41467-018-08066-0
- Reul, N., Chapron, B., Zabolotskikh, E., Donlon, C., Mouche, A., Tenerelli, J., ... Kudryavtsev, V. (2017). A new generation of tropical cyclone size measurements from space. *Bulletin of the American Meteorological Society*, *98*(11), 2367-2385. Retrieved from <https://doi.org/10.1175/BAMS-D-15-00291.1> doi: 10.1175/BAMS-D-15-00291.1
- Rice, S. O. (1951). Reflection of electromagnetic waves from slightly rough surfaces. *Communications on Pure and Applied Mathematics*, *4*(23), 351-378. Retrieved from <https://onlinelibrary.wiley.com/doi/abs/10.1002/cpa.3160040206> doi: 10.1002/cpa.3160040206
- Rouault, M. J., Mouche, A., Collard, F., Johannessen, J. A., & Chapron, B. (2010). Mapping the agulhas current from space: An assessment of asar surface current velocities. *Journal of Geophysical Research: Oceans*, *115*(C10), 1–14. Retrieved from <https://agupubs.onlinelibrary.wiley.com/doi/abs/10.1029/2009JC006050> doi: 10.1029/2009JC006050
- Said, F., Johnsen, H., Chapron, B., & Engen, G. (2015, Dec). An ocean wind doppler model based on the generalized curvature ocean surface scattering model. *IEEE Transactions on Geoscience and Remote Sensing*, *53*(12), 6632-6638. doi: 10.1109/TGRS.2015.2445057
- Schulz-Stellenfleth, J., Knig, T., & Lehner, S. (2007). An empirical approach for the retrieval of integral ocean wave parameters from synthetic aperture radar data. *Journal of Geophysical Research: Oceans*, *112*(C3), 1-14. Retrieved from <https://agupubs.onlinelibrary.wiley.com/doi/abs/10.1029/2006JC003970> doi: 10.1029/2006JC003970
- Schulz-Stellenfleth, J., & Lehner, S. (2002). Spaceborne synthetic aperture radar observations of ocean waves traveling into sea ice. *Journal of Geophysical Research*, *107*(C8). doi: 10.1029/2001jc000837
- Schulz-Stellenfleth, J., & Lehner, S. (2005, July). A noise model for estimated synthetic aperture radar look cross spectra acquired over the ocean. *IEEE Transactions on Geoscience and Remote Sensing*, *43*(7), 1443-1452. doi: 10.1109/TGRS.2005.846871
- Schwerdt, M., Schmidt, K., Ramon, N. T., Alfonzo, G. C., Dring, B. J., Zink, M., & Prats-Iraola, P. (2016, March). Independent verification of the sentinel-1a system calibration. *IEEE Journal of Selected Topics in Applied Earth Observations and Remote Sensing*, *9*(3), 994-1007. doi: 10.1109/JSTARS.2015.2449239
- Shao, W., Zhang, Z., Li, X., & Li, H. (2016a). Ocean wave parameters retrieval from sentinel-1 sar imagery. *Remote Sensing*, *8*(9). Retrieved from <http://www.mdpi.com/2072-4292/8/9/707> doi: 10.3390/rs8090707
- Shao, W., Zhang, Z., Li, X., & Li, H. (2016b). Ocean wave parameters retrieval from sentinel-1 sar imagery. *Remote Sensing*, *8*(9). Retrieved from <http://www.mdpi.com/2072-4292/8/9/707> doi: 10.3390/rs8090707
- Sharma, S., Dadhich, G., Rambhia, M., Mathur, A. K., Prajapati, R., Patel, P., & Shukla, A. (2017). Radiometric calibration stability assessment for the risat-1 sar sensor using a deployed point target array at the desalpar site, rann of kutch, india. *International Journal of Remote Sensing*, *38*(23), 7242-7259. Retrieved from <https://doi.org/10.1080/01431161.2017.1371858> doi: 10.1080/01431161.2017.1371858
- Shimada, M., Isoguchi, O., Tadono, T., & Isono, K. (2009). Palsar radiometric and geometric calibration. *IEEE Transactions on Geoscience and Remote Sensing*, *47*(12), 3915–3932.
- Shimura, T., Mori, N., & Mase, H. (2015). Future projections of extreme ocean wave climates and the relation to tropical cyclones: Ensemble experiments of mri-agcm3.2h. *Journal of Climate*, *28*(24), 9838-9856. Retrieved from <https://doi.org/10.1175/JCLI-D-14-00711.1> doi: 10.1175/JCLI-D-14-00711.1
- Sijp, W. P., & England, M. H. (2009). Southern hemisphere westerly wind control over the ocean's thermohaline circulation. *Journal of Climate*, *22*(5), 1277-1286. Retrieved from <https://doi.org/10.1175/2008JCLI2310.1> doi: 10.1175/2008JCLI2310.1
- Smirnova, J. E., Golubkin, P. A., Bobylev, L. P., Zabolotskikh, E. V., & Chapron, B. (2015). Polar low

References

- climatology over the nordic and barents seas based on satellite passive microwave data. *Geophysical Research Letters*, 42(13), 5603-5609. Retrieved from <https://agupubs.onlinelibrary.wiley.com/doi/abs/10.1002/2015GL063865> doi: 10.1002/2015GL063865
- SMITH, A. M. (1991). A new approach to range-doppler sar processing. *International Journal of Remote Sensing*, 12(2), 235-251. Retrieved from <https://doi.org/10.1080/01431169108929650> doi: 10.1080/01431169108929650
- Staabs, C., & Bauer, E. (1998). Statistical comparison of global significant wave heights from topex and ers-1 altimeter and from operational wave model wam. *Physics and Chemistry of the Earth*, 23(5), 581 - 585. Retrieved from <http://www.sciencedirect.com/science/article/pii/S0079194698000731> doi: [https://doi.org/10.1016/S0079-1946\(98\)00073-1](https://doi.org/10.1016/S0079-1946(98)00073-1)
- Sterl, A., Komen, G. J., & Cotton, P. D. (1998). Fifteen years of global wave hindcasts using winds from the european centre for medium-range weather forecasts reanalysis: Validating the reanalyzed winds and assessing the wave climate. *Journal of Geophysical Research: Oceans*, 103(C3), 5477-5492. Retrieved from <https://agupubs.onlinelibrary.wiley.com/doi/abs/10.1029/97JC03431> doi: 10.1029/97JC03431
- Stoffelen, B. A., & Anderson, D. (1997). Ambiguity removal and assimilation of scatterometer data. *Quarterly Journal of the Royal Meteorological Society*, 123(538), 491-518. Retrieved from <https://rmets.onlinelibrary.wiley.com/doi/abs/10.1002/qj.49712353812> doi: 10.1002/qj.49712353812
- Stopa, J. E., Ardhuin, F., Chapron, B., & Collard, F. (2015a). Estimating wave orbital velocity through the azimuth cutoff from space-borne satellites. *Journal of Geophysical Research: Oceans*, 120(11), 7616–7634. Retrieved from <http://dx.doi.org/10.1002/2015JC011275> doi: 10.1002/2015JC011275
- Stopa, J. E., Ardhuin, F., Chapron, B., & Collard, F. (2015b). Estimating wave orbital velocity through the azimuth cutoff from space-borne satellites. *Journal of Geophysical Research: Oceans*, 120(11), 7616–7634. Retrieved from <http://dx.doi.org/10.1002/2015JC011275> doi: 10.1002/2015JC011275
- Stopa, J. E., Ardhuin, F., Husson, R., Jiang, H., Chapron, B., & Collard, F. (2016). Swell dissipation from 10years of envisat advanced synthetic aperture radar in wave mode. *Geophysical Research Letters*, 43(7), 3423-3430. Retrieved from <https://agupubs.onlinelibrary.wiley.com/doi/abs/10.1002/2015GL067566> doi: 10.1002/2015GL067566
- Stopa, J. E., Cheung, K. F., Tolman, H. L., & Chawla, A. (2013). Patterns and cycles in the climate forecast system reanalysis wind and wave data. *Ocean Modelling*, 70, 207 - 220. Retrieved from <http://www.sciencedirect.com/science/article/pii/S1463500312001503> (Ocean Surface Waves) doi: <https://doi.org/10.1016/j.ocemod.2012.10.005>
- Stopa, J. E., & Mouche, A. (2017a). Significant wave heights from sentinel-1 sar: Validation and applications. *Journal of Geophysical Research: Oceans*, 122(3), 1827–1848. Retrieved from <http://dx.doi.org/10.1002/2016JC012364> doi: 10.1002/2016JC012364
- Stopa, J. E., & Mouche, A. (2017b). Significant wave heights from sentinel-1 sar: Validation and applications. *Journal of Geophysical Research: Oceans*, 122(3), 1827-1848. Retrieved from <https://agupubs.onlinelibrary.wiley.com/doi/abs/10.1002/2016JC012364> doi: 10.1002/2016JC012364
- Stopa, J. E., & Mouche, A. (2017c, mar). Significant wave heights from sentinel-1 SAR: Validation and applications. *Journal of Geophysical Research: Oceans*, 122(3), 1827–1848. doi: 10.1002/2016jc012364
- Stopa, J. E., Mouche, A. A., Chapron, B., & Collard, F. (2017, May). Sea state impacts on wind speed retrievals from c-band radars. *IEEE Journal of Selected Topics in Applied Earth Observations and Remote Sensing*, 10(5), 2147-2155. doi: 10.1109/JSTARS.2016.2609101
- Stopa, J. E., Sutherland, P., & Ardhuin, F. (2018). Strong and highly variable push of ocean waves on southern ocean sea ice. *Proceedings of the National Academy of Sciences*, 115(23), 5861–5865. Retrieved from <https://www.pnas.org/content/115/23/5861> doi: 10.1073/pnas.1802011115
- Toba, Y. (1972, Jun 01). Local balance in the air-sea boundary processes. *Journal of Oceanography*, 28(3),

- 109–120. Retrieved from <https://doi.org/10.1007/BF02109772> doi: 10.1007/BF02109772
- Torres, R., Snoeij, P., Geudtner, D., Bibby, D., Davidson, M., Attema, E., ... Rostan, F. (2012). Gmes sentinel-1 mission. *Remote Sensing of Environment*, 120(Supplement C), 9 - 24. Retrieved from <http://www.sciencedirect.com/science/article/pii/S0034425712000600> (The Sentinel Missions - New Opportunities for Science) doi: <https://doi.org/10.1016/j.rse.2011.05.028>
- TUCKER, M. J. (1985). Review article. the imaging of waves by satellite-borne synthetic aperture radar: the effects of sea-surface motion. *International Journal of Remote Sensing*, 6(7), 1059-1074. Retrieved from <http://dx.doi.org/10.1080/01431168508948263> doi: 10.1080/01431168508948263
- Ulaby, F. T. (1982). *Microwave remote sensing active and passive. vol 2, radar remote sensing and surface scattering and emission theory*. Addison-Wesley.
- Žagar, N., Skok, G., & Tribbia, J. (2011). Climatology of the itcz derived from era interim reanalyses. *Journal of Geophysical Research: Atmospheres*, 116(D15), 1–6. Retrieved from <https://agupubs.onlinelibrary.wiley.com/doi/abs/10.1029/2011JD015695> doi: 10.1029/2011JD015695
- Vachon, P. W., Krogstad, H. E., & Paterson, J. S. (1994). Airborne and spaceborne synthetic aperture radar observations of ocean waves. *Atmosphere-Ocean*, 32(1), 83-112. Retrieved from <http://dx.doi.org/10.1080/07055900.1994.9649491> doi: 10.1080/07055900.1994.9649491
- Valenzuela, G. (1967, July). Depolarization of em waves by slightly rough surfaces. *IEEE Transactions on Antennas and Propagation*, 15(4), 552-557. doi: 10.1109/TAP.1967.1138962
- Valenzuela, G. R. (1976). The growth of gravity-capillary waves in a coupled shear flow. *Journal of Fluid Mechanics*, 76(2), 229250. doi: 10.1017/S0022112076000608
- Valenzuela, G. R. (1978, Jan 01). Theories for the interaction of electromagnetic and oceanic waves — a review. *Boundary-Layer Meteorology*, 13(1), 61–85. Retrieved from <https://doi.org/10.1007/BF00913863> doi: 10.1007/BF00913863
- Vandemark, D., Chapron, B., Elfouhaily, T., & Campbell, J. W. (2005). Impact of highfrequency waves on the ocean altimeter range bias. *Journal of Geophysical Research: Oceans*, 110(C11), 1–12. Retrieved from <https://agupubs.onlinelibrary.wiley.com/doi/abs/10.1029/2005JC002979> doi: 10.1029/2005JC002979
- Verspeek, J., Portabella, M., Stoffelen, A., & Verhoef, A. (2013). *Calibration and validation of ascat winds* (Tech. Rep. No. SAF/OSI/KNMI/TEC/TN/163). De Bilt, The Netherlands: Ocean and Sea Ice SAF.
- Violante-Carvalho, N., Robinson, I. S., & Schulz-Stellenfleth, J. (2005). Assessment of ers synthetic aperture radar wave spectra retrieved from the max-planck-institut (mpi) scheme through intercomparisons of 1 year of directional buoy measurements. *Journal of Geophysical Research: Oceans*, 110(C7). Retrieved from <https://agupubs.onlinelibrary.wiley.com/doi/abs/10.1029/2004JC002382> doi: 10.1029/2004JC002382
- Wang, H., Wang, J., Yang, J., Ren, L., Zhu, J., Yuan, X., & Xie, C. (2018). Empirical algorithm for significant wave height retrieval from wave mode data provided by the chinese satellite gaofen-3. *Remote Sensing*, 10(3). Retrieved from <http://www.mdpi.com/2072-4292/10/3/363> doi: 10.3390/rs10030363
- Wang, H., Yang, J., Mouche, A., Shao, W., Zhu, J., Ren, L., & Xie, C. (2017). Gf-3 sar ocean wind retrieval: The first view and preliminary assessment. *Remote Sensing*, 9(7). Retrieved from <http://www.mdpi.com/2072-4292/9/7/694> doi: 10.3390/rs9070694
- Wang, X. L., Feng, Y., & Swail, V. R. (2014). Changes in global ocean wave heights as projected using multimodel cmip5 simulations. *Geophysical Research Letters*, 41(3), 1026-1034. Retrieved from <https://agupubs.onlinelibrary.wiley.com/doi/abs/10.1002/2013GL058650> doi: 10.1002/2013GL058650
- Wang, X. L., Zwiars, F. W., & Swail, V. R. (2004). North atlantic ocean wave climate change scenarios for the twenty-first century. *Journal of Climate*, 17(12), 2368-2383. Retrieved from [https://doi.org/10.1175/1520-0442\(2004\)017<2368:NAOWCC>2.0.CO;2](https://doi.org/10.1175/1520-0442(2004)017<2368:NAOWCC>2.0.CO;2) doi: 10.1175/1520-0442(2004)017<2368:NAOWCC>2.0.CO;2
- Wingham, D. J., Phalippou, L., Mavrocordatos, C., & Wallis, D. (2004, Oct). The mean echo and echo cross product from a beamforming interferometric altimeter and their application to elevation measurement. *IEEE Transactions on Geoscience and Remote Sensing*, 42(10), 2305-2323. doi: 10.1109/TGRS.2004

References

.834352

- Wright, J. (1968, March). A new model for sea clutter. *IEEE Transactions on Antennas and Propagation*, 16(2), 217-223. doi: 10.1109/TAP.1968.1139147
- Wu, C., y. Liu, K., & Jin, M. (1982, Sept). Modeling and a correlation algorithm for spaceborne sar signals. *IEEE Transactions on Aerospace and Electronic Systems*, AES-18(5), 563-575. doi: 10.1109/TAES.1982.309269
- Young, I. (1999). Seasonal variability of the global ocean wind and wave climate. *International Journal of Climatology*, 19(9), 931-950. Retrieved from <https://rmets.onlinelibrary.wiley.com/doi/abs/10.1002/%28SICI%291097-0088%28199907%2919%3A9%3C931%3A%3AAID-JOC412%3E3.0.CO%3B2-0> doi: 10.1002/(SICI)1097-0088(199907)19:9<931::AID-JOC412>3.0.CO;2-O
- Young, I., & Donelan, M. (2018). On the determination of global ocean wind and wave climate from satellite observations. *Remote Sensing of Environment*, 215, 228 - 241. Retrieved from <http://www.sciencedirect.com/science/article/pii/S0034425718302840> doi: <https://doi.org/10.1016/j.rse.2018.06.006>
- Young, I. R., Zieger, S., & Babanin, A. V. (2011). Global trends in wind speed and wave height. *Science*, 332(6028), 451-455. Retrieved from <http://science.sciencemag.org/content/332/6028/451> doi: 10.1126/science.1197219
- Zhang, B., & Perrie, W. (2012). Cross-polarized synthetic aperture radar: A new potential measurement technique for hurricanes. *Bulletin of the American Meteorological Society*, 93(4), 531-541. Retrieved from <https://doi.org/10.1175/BAMS-D-11-00001.1> doi: 10.1175/BAMS-D-11-00001.1
- Zhang, B., Perrie, W., & He, Y. (2010). Validation of radarsat-2 fully polarimetric sar measurements of ocean surface waves. *Journal of Geophysical Research: Oceans*, 115(C6), 1-11. Retrieved from <https://agupubs.onlinelibrary.wiley.com/doi/abs/10.1029/2009JC005887> doi: 10.1029/2009JC005887
- Zhang, B., Perrie, W., & He, Y. (2011a). Wind speed retrieval from radarsat-2 quad-polarization images using a new polarization ratio model. *Journal of Geophysical Research: Oceans*, 116(C8), 1-13. Retrieved from <http://dx.doi.org/10.1029/2010JC006522> (C08008) doi: 10.1029/2010JC006522
- Zhang, B., Perrie, W., & He, Y. (2011b). Wind speed retrieval from radarsat-2 quad-polarization images using a new polarization ratio model. *Journal of Geophysical Research: Oceans*, 116(C8), 1-13. Retrieved from <https://agupubs.onlinelibrary.wiley.com/doi/abs/10.1029/2010JC006522> doi: 10.1029/2010JC006522
- Zhang, G., Perrie, W., Zhang, B., Khurshid, S., & Warner, K. (2018). Semi-empirical ocean surface model for compact-polarimetry mode sar of radarsat constellation mission. *Remote Sensing of Environment*, 217, 52 - 60. Retrieved from <http://www.sciencedirect.com/science/article/pii/S0034425718303717> doi: <https://doi.org/10.1016/j.rse.2018.08.006>
- Zhao, Y., Mouche, A. A., Chapron, B., & Reul, N. (2018, June). Direct comparison between active c-band radar and passive l-band radiometer measurements: Extreme event cases. *IEEE Geoscience and Remote Sensing Letters*, 15(6), 897-901. doi: 10.1109/LGRS.2018.2811712

Observations globales des vents et des vagues de surface de l'océan à l'aide de mesures de radars à synthèse d'ouverture spatiaux

Par Huimin LI

Thèse présentée et soutenue à Plouzane, le 7 juin, 2019

Unité de recherche : LabSTICC

Thèse N° : 2019IMTA0138

Mots clés : Radar à synthèse d'ouverture, vents et vagues océaniques

Abstract : Les radars à synthèse d'ouverture (SAR) spatioportés ont fait la preuve de leur valeur inestimable dans l'observation des vents et des vagues océaniques mondiaux. Les images SAR acquises par plusieurs capteurs sont utilisées, notamment Sentinel-1 (S-1), Envisat/ASAR, Gaofen-3 et Radarsat-2. Cette thèse passe en revue les paramètres SAR couramment utilisés dans la première partie. Une série d'étapes d'étalonnage sont nécessaires pour obtenir un NRCS approprié et une évaluation du NRCS est effectuée pour le mode d'onde S-1 (WV). Il s'avère que WV est mal calibré et est donc recalibré pour obtenir un NRCS précis. Il a été démontré que la coupure de l'azimut est complémentaire du NRCS et peut expliquer l'impact de l'état de la mer sur l'extraction du vent. D'après les produits SAR entièrement polarimétriques disponibles, la coupure de l'azimut varie considérablement en fonction des polarisations. La transformation actuelle de la cartographie SAR est suffisante pour interpréter la coupure azimutale copolarisée, mais pas pour la polarisation croisée. Compte tenu des limites de l'imagerie SAR, un nouveau paramètre est proposé et défini en fonction du spectre croisé de l'image SAR, appelé MACS. La partie imaginaire de MACS est une quantité signée par rapport à la direction du vent. Compte tenu de cette dépendance, on s'attend à ce qu'un algorithme indépendant de récupération du vent en bénéficie. L'ampleur du MACS peut aider à estimer la fonction de modulation de la cartographie SAR. De plus, la MACS donne également des résultats prometteurs en ce qui concerne les études globales sur les vagues. Les signatures globales du MACS à différentes longueurs d'onde sont bien représentatives de la distribution spatiale et saisonnière des vents. Les MACS des vagues longues montrent des valeurs plus élevées sur les trajectoires des tempêtes alors que les vagues plus courtes sont principalement dans les vents des tradar. Ces résultats devraient aider à évaluer les résultats du modèle et compléter les études ultérieures sur le climat spectral global des vagues.

Resume:

L'océan joue un rôle important dans la formation des caractéristiques de la Terre. L'océan contrôle les conditions météorologiques et les régimes climatiques à long terme de la Terre. Elle a également de grandes répercussions sur nos sociétés par le biais de l'approvisionnement en eau et en nourriture et de la livraison de produits. Ce n'est qu'en étudiant les caractéristiques et la dynamique de l'océan que nous pourrions mieux projeter son influence sur l'humanité. Parmi les nombreuses techniques d'exploration, le radar à synthèse d'ouverture (SAR) spatial, indépendant de l'illumination solaire et de la couverture nuageuse, a été largement utilisé pour observer les phénomènes atmosphériques et océaniques. Les interactions air-mer régissent la rugosité de la surface de la mer (ondes gravitationnelles-capillaires) qui détermine l'amplitude de la rétrodiffusion radar. Bien que complexe et non linéaire, la modulation de la rugosité de la surface de la mer par les ondes océaniques est également cartographiée sur les images SAR, fournissant une source unique de mesures bidimensionnelles du spectre de houle océanique depuis l'espace. Par conséquent, de nombreuses applications différentes, comme le suivi de la houle, l'assimilation des spectres de vagues dans les systèmes opérationnels de prévision des vagues ou, plus récemment, les études sur les interactions vagues-glace, ont bénéficié des observations SAR. Toutefois, depuis Envisat/ASAR (2002-2012), qui prévoyait des acquisitions sur 10 ans en haute mer, les systèmes SAR ont été considérablement améliorés, offrant de nouvelles perspectives pour les applications océaniques. Cette thèse porte sur le potentiel de ces nouvelles missions à exploiter pleinement leurs capacités et, éventuellement, à fournir des orientations pour de futures missions conceptuelles.

Dans ce but, cette thèse porte principalement sur la dernière constellation Sentinel-1(S-1) (S-1A en avril 2014 et S-1B en avril 2016) de la constellation européenne (programme Copernicus). Ces deux SAR en bande C assurent la continuité avec les missions européennes précédentes pour la mesure des vagues grâce à ce que l'on appelle le mode Wave et à de nouvelles capacités. En particulier, le mode d'onde S-1 acquiert des vignettes SAR au-dessus de l'océan mondial à une résolution supérieure à celle d'Envisat/ASAR et alternativement à deux angles d'incidence différents pour augmenter l'échantillonnage par houle. Cette thèse explore également le GaoFen-3 (mission chinoise) et Radarsat-2 (mission canadienne) afin d'étendre la gamme des angles d'incidence et d'étudier les avantages de la diversité de polarisation. Enfin, les données d'Envisat/ASAR sur 10 ans sont également prises en compte pour explorer la tendance temporelle des vents et des vagues dans le monde.

Dans la partie I, les paramètres SAR couramment utilisés sont examinés, y compris la section transversale normalisée du radar (NRCS) et la coupure de l'azimut. Le NRCS a été largement utilisé dans le domaine de la télédétection hyperfréquence pour décrire l'ampleur de la rétrodiffusion de la zone imagée. Une série d'étapes d'étalonnage sont nécessaires pour obtenir le NRCS approprié. Ainsi, avant toute application géophysique, le NRCS des acquisitions en mode vague (WV) en mode Sentinel-1 (S-1) est d'abord évalué. Cette thèse montre que le WV NRCS est mal calibré, en particulier pour le WV2 à un angle d'incidence plus grand. Cela s'explique par le fait qu'il n'y a pas d'acquisitions stratégiques sur les réflecteurs d'angle pour étalonner de façon constante le NRCS. Deux méthodes de recalibrage différentes : le calibrage de la forêt tropicale humide et le calibrage de l'océan sont effectués et tous deux ont atteint des performances comparables. L'étalonnage de l'océan s'avère plus efficace et plus facile à mettre en œuvre du point de vue opérationnel. Après le réétalonnage du NRCS, la vitesse du vent est ensuite dérivée à l'aide d'une direction du vent d'entrée et comparée aux produits S-1 de niveau 2. Il montre une meilleure concordance avec la vitesse du vent de la bouée colocalisée, en particulier dans la plage des vents faibles. Malgré l'amélioration de la qualité du NRCS grâce au réétalonnage, le NRCS est toujours soumis à d'autres facteurs d'impact, tels que la présence de phénomènes géophysiques et le rapport signal/bruit.

La coupure d'azimut est un autre paramètre qui s'est avéré utile dans la récupération du vent. La coupure d'azimut est avantageuse parce qu'elle est directement estimée à partir des spectres d'images SAR et qu'elle ne comporte pas d'étapes d'étalonnage. Il peut être considéré comme un complément au NRCS et tient compte de l'impact de l'état de la mer sur la vitesse du vent. En plus de sa dépendance au vent, le seuil d'azimut est également analysé en fonction de sa dépendance à la polarisation en fonction des données acquises par Radarsat-2 et Gaofen-3. En général, la coupure de l'azimut est plus grande en VH qu'en HH, qui à son tour est plus grande que VV. La comparaison du seuil d'azimut entre les mesures SAR et la simulation à partir de spectres de vagues océaniques colocalisés est effectuée au cas par cas. Le désaccord statistique réside principalement dans la coupure d'azimut à polarisation croisée selon laquelle les mesures du SAR montrent des valeurs plus élevées. La plus grande coupure d'azimut est spéculée pour s'associer à la plus grande sensibilité de la polarisation croisée à la rupture de l'onde. D'autres études théoriques sont nécessaires pour interpréter pleinement les principes de la cartographie SAR pour les mesures de polarisation croisée. Cela doit permettre de quantifier les contributions de la rupture des vagues en combinant la coupure d'azimut polarisée.

L'une des principales limites du système SAR existant est son angle de vision unique. Pour résoudre ce problème, on peut combiner des paramètres radar complémentaires (sensibilité différente à l'angle de visée azimutal). Par exemple, l'utilisation de l'anomalie centroïdale Doppler (DCA) et du NRCS s'est avérée utile pour limiter la vitesse et l'inversion de direction du vent. Toutefois, en raison de problèmes dans les systèmes d'attitude du S-1, sa précision est encore en cours d'amélioration. Une autre solution possible serait d'adopter des concepts de mission SAR plus avancés, comme STEREOID, pour obtenir à la fois la diversité des angles de visée et des paramètres radar. Ici, sur la base du SAR existant, un nouveau paramètre SAR est défini pour compléter le NRCS et le seuil d'azimut. De plus, il pourrait éventuellement remplacer le DCA, car les exigences actuelles des missions SAR ne correspondent guère à la précision obligatoire exigée par le Doppler pour les applications océaniques. Ce nouveau paramètre est appelé MACS et est défini à partir de l'image SAR croisée Spectra. La partie II de cette thèse est consacrée à ce nouveau paramètre.

La MACS est d'abord définie en filtrant les spectres croisés autour des vagues océaniques intermédiaires (15-20 m) qui voyagent à grande distance, car ces vagues sont fortement couplées avec les vents locaux. Par définition, on s'attend à ce que le MACS reflète à la fois l'amplitude et la direction des vagues intermédiaires cartographiées. Il s'agit d'une quantité complexe qui dépend des configurations radar (fréquence centrale du radar, polarisations et angles d'incidence). La partie imaginaire de MACS (IMACS) est une quantité signée par rapport à la direction du vent (du près au vent arrière). L'IMACS montre également une asymétrie par rapport à la direction de la ligne de visée radar. Tout comme le DCA, le MACS peut être utilisé avec le NRCS pour établir un algorithme de vent indépendant. Les vents auto-dérivés à partir des mesures SAR bénéficieront d'autres études, telles que l'inversion des vagues, l'évaluation de l'interaction entre le vent, les vagues et les courants à échelle finie, et autres.

Dans le cadre d'une étude de suivi de la dépendance de l'IMACS à l'égard des vents, la possibilité d'utiliser le MACS pour examiner la fonction de transfert de modulation (MTF) entre la rétrodiffusion SAR et les vagues océaniques est également examinée. À cette fin, l'ampleur du MACS (MMACS) est documentée en ce qui concerne le vent de surface de la mer (dépendance de la direction du vent, asymétrie ascendante et descendante du vent) et les configurations radar (angles d'incidence et polarisation). La comparaison des MMACS obtenus à partir des

mesures et des simulations du DAS montre des désaccords, en particulier pour les petits angles d'incidence. En supposant une cartographie linéaire pour le MMACS, le MTF du radar à ouverture réelle (RAR) est donc dérivé en ajustant la simulation pour qu'elle soit cohérente avec les mesures. Le rapport entre le MTF dérivé et le MTF RAR initial augmente avec la vitesse du vent. Et pour une vitesse de vent donnée, ce rapport est légèrement plus grand en HH qu'en VV et beaucoup plus grand à petit angle d'incidence. Il sera utilisé pour affiner l'inversion spectrale des ondes et éventuellement pour compléter la modulation d'inclinaison basée sur le GMF du NRCS.

Plus concrètement, le MACS offre de nouvelles perspectives pour l'analyse des vents et des vagues à partir d'acquisitions courantes et globales de R-S, mais aussi pour mieux caractériser des phénomènes atmosphériques complexes. Les données de la WV S-1 sur un an sont utilisées pour démontrer les variations globales et saisonnières de l'IMACS. En général, les schémas globaux des IMACS sont en accord avec les vents globaux. L'IMACS présente des signes opposés, des alizés aux vents d'ouest. Son ampleur est beaucoup plus grande dans les trajectoires des tempêtes respectives, ce qui est associé à des vents constamment forts. Complémentaire au NRCS, l'IMACS est capable de saisir les variations saisonnières de la direction du vent. De plus, la faisabilité d'utiliser le MACS calculé à haute résolution spatiale pour mesurer le champ de vent à la surface de la mer à partir d'acquisitions SAR en mode large bande est également démontrée dans le cas d'une dépression polaire. Dans ce contexte, l'IMACS devrait être avantageusement utilisé pour aider à limiter les schémas locaux de récupération du vent à partir de diverses mesures SAR et pour aider à examiner les structures fines du champ de vent par rapport aux événements de vent locaux.

Comme décrit, MACS est défini pour mettre en évidence les propriétés spectrales de l'image des différentes échelles d'onde. L'application principale du MACS sera d'étudier la distribution globale des ondes océaniques à différentes longueurs d'onde. Tirant parti des acquisitions décennales du mode à ondes Envisat/ASAR, cet aspect est étudié avec les résultats suivants. Le MACS pour différentes longueurs d'onde présente une tendance à la hausse par rapport à la vitesse du vent, correspondant au couplage onde-vent. Le degré de couplage dépend de la longueur d'onde : plus les ondes sont longues, plus le couplage est élevé, plus les vents sont forts. Et du point de vue du climat des vagues, les modèles globaux de MACS diffèrent des vagues de vent intermédiaires (60 m) aux longues vagues océaniques (300 m). Les signatures

représentent bien la distribution globale des vents, dans l'espace et en fonction des saisons. De plus, on constate que les longueurs d'onde les plus énergétiques sont étroitement liées aux vents locaux. En particulier, les signatures MACS des vagues plus longues se trouvent sur les trajectoires des tempêtes alors que les vagues relativement plus courtes (~100 m) sont dans les alizés. On s'attend à ce que les signatures globales des vagues représentées par MACS aident à évaluer les résultats du modèle et complètent les études sur le climat spectral des vagues. La poursuite de l'étude S-1 au cours des dix prochaines années permettra à cette étude de s'étendre vers une analyse temporelle plus longue.

Sur la base des résultats présentés dans cette thèse, des études futures sont prévues à plusieurs égards. Premièrement, étant donné la dépendance distincte du MACS à l'égard de la direction du vent, un système indépendant d'extraction du vent combinant le NRCS et le MACS permettra certainement d'améliorer l'utilisation des images SAR. On s'attend également à ce que cette méthode fonctionne avec des images SAR à large bande et à ce que l'on puisse examiner la structure fine du champ de vent lors de divers événements météorologiques. Cette technique d'analyse peut ensuite être facilement appliquée aux observations SWIM à bord du satellite CFOSAT, qui est capable de fournir les spectres bidimensionnels complets des vagues océaniques. Le MACS doit être étendu à toutes les directions des vagues puisque la SWIM n'est pas soumise à la cartographie non linéaire comme un SAR. En outre, l'analyse spectrale des échelles d'ondes individuelles peut servir de référence pour le traitement des données des missions conceptuelles à venir, telles que STEREOID et SKIM. Le MACS proposé ouvrira une nouvelle voie à l'analyse des données afin d'améliorer l'utilité des observations SAR ainsi que d'autres capteurs.

Titre: Observations globales des vents et des vagues de surface de l'océan à l'aide de mesures de radars à synthèse d'ouverture spatiaux

Mots clés : Radar à synthèse d'ouverture, vents et vagues océaniques

Abstract :

Les radars à synthèse d'ouverture (SAR) spatioportés ont fait la preuve de leur valeur inestimable dans l'observation des vents et des vagues océaniques mondiaux. Les images SAR acquises par plusieurs capteurs sont utilisées, notamment Sentinel-1 (S-1), Envisat/ASAR, Gaofen-3 et Radarsat-2. Cette thèse passe en revue les paramètres SAR couramment utilisés dans la première partie. Une série d'étapes d'étalonnage sont nécessaires pour obtenir un NRCS approprié et une évaluation du NRCS est effectuée pour le mode d'onde S-1 (WV). Il s'avère que WV est mal calibré et est donc recalibré pour obtenir un NRCS précis. Il a été démontré que la coupure de l'azimut est complémentaire du NRCS et peut expliquer l'impact de l'état de la mer sur l'extraction du vent. D'après les produits SAR entièrement polarimétriques disponibles, la coupure de l'azimut varie considérablement en fonction des polarisations. La transformation actuelle de la cartographie SAR est suffisante pour interpréter la coupure azimutale copolarisée, mais pas pour la polarisation croisée.

Compte tenu des limites de l'imagerie SAR, un nouveau paramètre est proposé et défini en fonction du spectre croisé de l'image SAR, appelé MACS. La partie imaginaire de MACS est une quantité signée par rapport à la direction du vent. Compte tenu de cette dépendance, on s'attend à ce qu'un algorithme indépendant de récupération du vent en bénéficie. L'ampleur du MACS peut aider à estimer la fonction de modulation de la cartographie SAR. De plus, la MACS donne également des résultats prometteurs en ce qui concerne les études globales sur les vagues. Les signatures globales du MACS à différentes longueurs d'onde sont bien représentatives de la distribution spatiale et saisonnière des vents. Les MACS des vagues longues montrent des valeurs plus élevées sur les trajectoires des tempêtes alors que les vagues plus courtes sont principalement dans les vents des trader. Ces résultats devraient aider à évaluer les résultats du modèle et compléter les études ultérieures sur le climat spectral global des vagues.

Title Global observations of ocean surface winds and waves using spaceborne synthetic aperture radar measurements

Keywords : Synthetic aperture radar, ocean winds, ocean waves

Abstract :

Spaceborne synthetic aperture radar (SAR) has been demonstrated invaluable in observing the global ocean winds and waves. SAR images acquired by multiple sensors are employed, including Sentinel-1 (S-1), Envisat/ASAR, Gaofen-3 and Radarsat-2. This thesis reviews the commonly used SAR parameters (NRCS and azimuth cutoff) in the first part. A series of calibration steps are required to obtain a proper NRCS and assessment of NRCS is carried out for S-1 wave mode (WV). It turns out that WV is poorly calibrated and is thus re-calibrated to obtain accurate NRCS. Azimuth cutoff is demonstrated to be complementary to NRCS and can account for the sea state impact on the wind retrieval. Based on the available fully polarimetric SAR products, azimuth cutoff is found to vary greatly with polarizations. The present SAR mapping transformation is sufficient to interpret the co-polarized azimuth cutoff, while not for the cross-polarization.

With the limitations of SAR imaging in mind, a new parameter is proposed and defined based on the SAR image cross-spectra, termed as MACS. The imaginary part of MACS is found to be a signed quantity relative to the wind direction. Given this dependence, an independent wind retrieval algorithm is expected to benefit. The magnitude of MACS is able to aid for estimate of modulation function of SAR mapping. In addition, MACS also gives promising results regarding the global wave studies. The global signatures of MACS at various wavelengths are well representative of the winds distributions, spatially and seasonally. MACS of long waves shows greater values over the storm tracks while the shorter waves are mostly within the trader winds. These results are expected to help evaluate the model outputs and complement further studies of the global wave spectral climate. Data continuity in the coming 10 years shall extend the study towards longer duration.